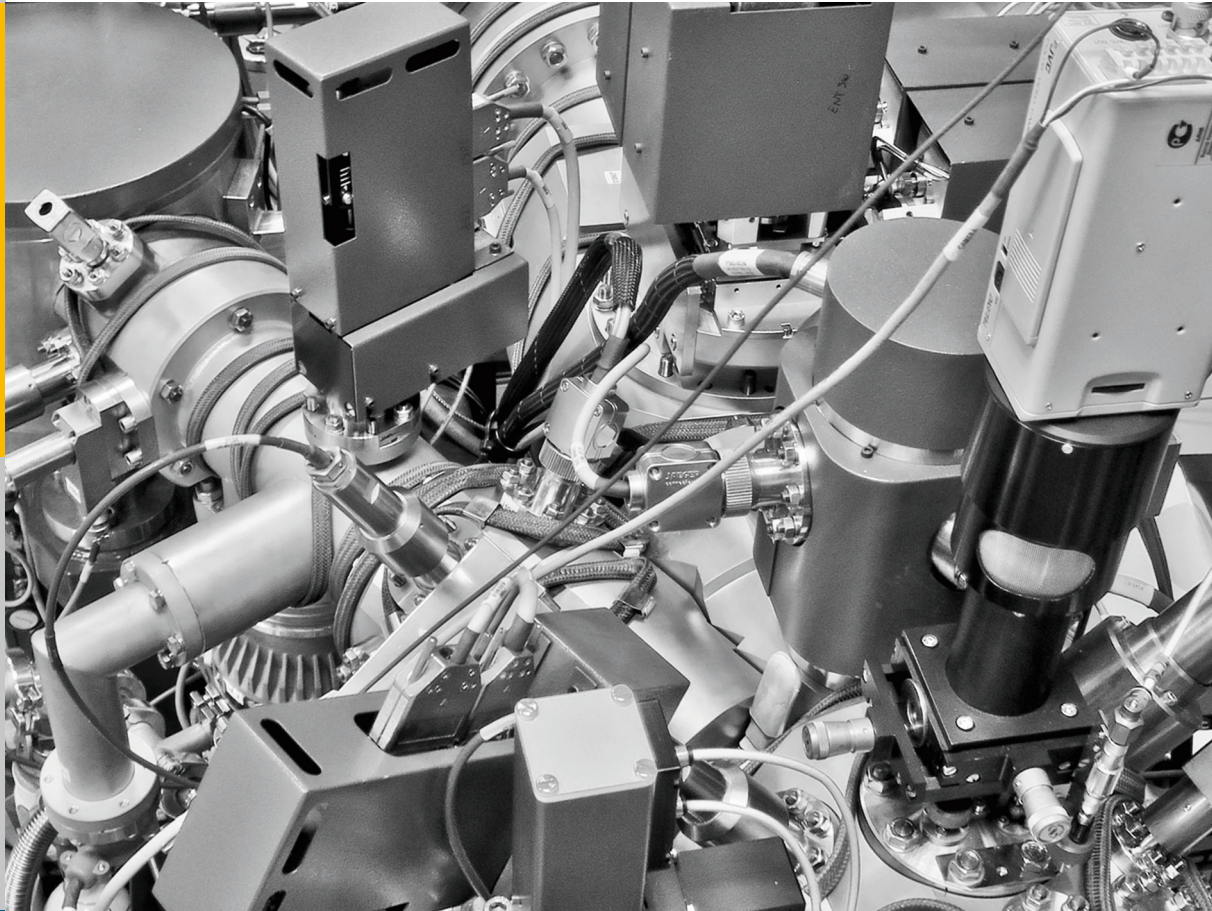


# Production and Characterization of Monodisperse Uranium Particles for Nuclear Safeguards Applications

Alexander Knott



Energie & Umwelt /  
Energy & Environment  
Band / Volume 336  
ISBN 978-3-95806-172-9





Forschungszentrum Jülich GmbH  
Institut für Energie- und Klimaforschung  
Nukleare Entsorgung und Reaktorsicherheit (IEK-6)

# **Production and Characterization of Monodisperse Uranium Particles for Nuclear Safeguards Applications**

Alexander Knott

Schriften des Forschungszentrums Jülich  
Reihe Energie & Umwelt / Energy & Environment

Band / Volume 336

---

ISSN 1866-1793

ISBN 978-3-95806-172-9

Bibliographic information published by the Deutsche Nationalbibliothek.  
The Deutsche Nationalbibliothek lists this publication in the Deutsche  
Nationalbibliografie; detailed bibliographic data are available in the  
Internet at <http://dnb.d-nb.de>.

Publisher and  
Distributor: Forschungszentrum Jülich GmbH  
Zentralbibliothek  
52425 Jülich  
Tel: +49 2461 61-5368  
Fax: +49 2461 61-6103  
Email: [zb-publikation@fz-juelich.de](mailto:zb-publikation@fz-juelich.de)  
[www.fz-juelich.de/zb](http://www.fz-juelich.de/zb)

Cover Design: Grafische Medien, Forschungszentrum Jülich GmbH

Printer: Grafische Medien, Forschungszentrum Jülich GmbH

Copyright: Forschungszentrum Jülich 2016

Schriften des Forschungszentrums Jülich  
Reihe Energie & Umwelt / Energy & Environment, Band / Volume 336

D 82 (Diss. RWTH Aachen University, 2016)

ISSN 1866-1793  
ISBN 978-3-95806-172-9

The complete volume is freely available on the Internet on the Jülicher Open Access Server (JuSER)  
at [www.fz-juelich.de/zb/openaccess](http://www.fz-juelich.de/zb/openaccess).



This is an Open Access publication distributed under the terms of the [Creative Commons Attribution License 4.0](https://creativecommons.org/licenses/by/4.0/),  
which permits unrestricted use, distribution, and reproduction in any medium, provided the original work is properly cited.

*"Everything will turn out right, the world is built on that."*

Mikhail A. Bulgakov - The Master and Margarita

To my father and mother



# Table of Contents

<b>Table of Contents</b> .....	<b>3</b>
<b>Abbreviations</b> .....	<b>A</b>
<b>Abstract</b> .....	<b>C</b>
<b>Kurzzusammenfassung</b> .....	<b>E</b>
<b>Acknowledgments</b> .....	<b>G</b>
<b>1. Introduction</b> .....	<b>1</b>
1.1 Needs and Goals .....	3
<b>2. Scope of the Thesis</b> .....	<b>4</b>
(1) Particle Production .....	4
(2) Characterization Efforts .....	5
<b>3. Scientific and Theoretical Background</b> .....	<b>7</b>
3.1 Particle Production .....	7
3.1.1 Approaches for Particle Production .....	7
3.1.2 Aerosol Droplet Generation .....	9
3.1.3 Droplet to Particle Conversion Kinetics and Thermodynamics .....	12
3.2 Particle Transport .....	19
3.2.1 Phenomena of Particle Transport Mechanisms .....	20
3.2.2 Particle Collection - Sampling, Cut-Off Diameter .....	27
3.3 Micro-Analytical Techniques .....	29
3.3.1 Scanning Electron Microscopy (SEM) .....	29
3.3.2 Secondary Ionization Mass Spectrometry (SIMS) .....	31
3.3.3 Raman Spectroscopy .....	34
<b>4. Materials and Methods</b> .....	<b>39</b>
4.1 Aerosol Solutions and Particle Production .....	39
4.1.1 Aerosol Solution .....	39
4.1.2 Particle Production .....	40
4.1.3 Particle Transfer Techniques .....	46
4.2 Analytical Methods .....	49
4.2.1 Microscopy: Scanning Electron Microscopy and Optical Microscopy .....	49
4.2.2 SE-Computation .....	50
4.2.3 Focused Ion Beam and Time of Flight SIMS .....	52
4.2.4 Micro-Raman Spectroscopy .....	52
4.2.5 SIMS Analysis .....	54
<b>5. Results and Discussion</b> .....	<b>56</b>
5.1 Particle Collection .....	56
5.1.1 Assessment on the Efficiency of the "One Stage Inertial Impactor" .....	56
5.1.2 Modified Inertial Impactor .....	60

5.1.3	<i>Cyclone Impactor</i> .....	63
5.1.4	<i>Conclusion</i> .....	64
5.2	<b>Characterization of Particle Size and Morphology</b> .....	64
5.2.1	<i>Overview</i> .....	64
5.2.2	<i>Particle Size Distribution</i> .....	65
5.2.3	<i>Characterization of Internal Particle Morphology</i> .....	71
5.2.4	<i>Conclusion SEM Characterization</i> .....	85
5.3	<b>Particle Characterization with Micro-Raman Spectroscopy</b> .....	88
5.3.1	<i>Reference Raman Spectra on Particulate Material</i> .....	88
5.4	<b>Particle Characterization with Secondary Ionization Mass Spectrometry</b> .....	98
5.4.1	<i>Isotopic Analysis</i> .....	98
5.4.2	<i>Direct Comparison to existing QC-Materials and CRMs</i> .....	103
5.4.3	<i>Assessment of Hydride Correction</i> .....	106
5.4.4	<i>Total Evaporation Experiments</i> .....	109
<b>6.</b>	<b>Conclusions and Outlook</b> .....	<b>117</b>
<b>7.</b>	<b>Appendix</b> .....	<b>i</b>
7.1	<b>Size Distribution Histograms</b> .....	<b>i</b>
7.1.1	<i>SG150312_05A, SG150401_14A, SG150413_03A and SG150429_02A</i> .....	<i>i</i>
7.2	<b>Shape Descriptors: Circularity</b> .....	<b>iii</b>
7.2.1	<i>SG150312_05A, SG150401_14A, SG150413_03A and SG150429_02A</i> .....	<i>iii</i>
7.3	<b>Focused Ion Beam</b> .....	<b>v</b>
7.3.1	<i>Auxiliary Focused Ion Beam analysis on SG150401_14</i> .....	<i>viii</i>
7.4	<b>EDX-Spectra</b> .....	<b>xi</b>
7.4.1	<i>Polydisperse Batch: SG140521_02</i> .....	<i>xi</i>
7.4.2	<i>Uniform Batches: SG141027_12A, SG150312_05A, SG150401_14A, SG150413_03A and SG150429_02A</i> .....	<i>xii</i>
7.5	<b>Micro-Raman Spectroscopy</b> .....	<b>xiv</b>
7.5.1	<i>Uranyl nitrate Hexahydrate Spectra</i> .....	<i>xiv</i>
7.5.2	<i>Raman Spectra of selected number of particles originating from CEA and TUW with a total spectral range of 100-3200cm<sup>-1</sup></i> .....	<i>xvi</i>
7.5.3	<i>Raman Spectra of UO<sub>2</sub>F<sub>2</sub> – Double band at 867cm<sup>-1</sup></i> .....	<i>xviii</i>
7.5.4	<i>Raman Spectra of SG140521_02</i> .....	<i>xviii</i>
7.5.5	<i>Raman Spectra of SG141027_12A</i> .....	<i>xix</i>
7.5.6	<i>Raman Spectra of SG141027_12A from CEA vs TUW</i> .....	<i>xix</i>
7.5.7	<i>Raman Spectra of SG150401_14A</i> .....	<i>xx</i>
7.5.8	<i>Direct comparison of selected uranium compounds to particles produced at FZJ</i> .....	<i>xxi</i>
7.6	<b>SIMS spectra</b> .....	<b>xxii</b>
7.6.1	<i>Abundances of <sup>234</sup>U, <sup>235</sup>U and <sup>236</sup>U of a selected number of particles originating from SG1040521_02 and SG141027_12A</i> .....	<i>xxii</i>
7.6.2	<i><sup>238</sup>U-intensity plot for NBS-U010, IRMM-9073, SG140521_02 and SG141027_12A</i> .....	<i>xxiii</i>
7.6.3	<i>Certificate: NBS U010</i> .....	<i>xxiv</i>

7.6.4	<i>Certificate: IRMM 9073</i> .....	xxv
7.6.5	<i>TE-Spectra of SG141027_12A, ITU and IRMM-9073</i> .....	xxvi
7.6.6	<i>Total Evaporation</i> .....	xxviii
<b>8.</b>	<b>Eidesstattlich Erklärung</b> .....	<b>i</b>
<b>9.</b>	<b>Disclaimer</b> .....	<b>i</b>
<b>I.</b>	<b>Table of Figures</b> .....	<b>ii</b>
<b>II.</b>	<b>References</b> .....	<b>vii</b>



# Abbreviations

AcV	Accelerating Voltage
ADU	Ammonium Diuranat
AP	Additional Protocol
APM	Automated Particle Measurement
BLPI	Berner Low Pressure impactor
BMW <i>i</i>	Federal Ministry of Economic Affairs and Energy
BSE	Back-Scattered Electron
CA	Complementary Access
COM	Center of Mass
CR	Certified Reference Material
DMT-Model	Deryagin, Muller, Toporov-Model
DPRK	Democratic People's Republic of Korea
DU	Depleted Uranium
ECAS	Enhancing Capabilities of the Safeguards Analytical Services
EDX	Energy dispersive X-Ray Spectroscopy
EELS	Electron Energy Loss Spectroscopy
ESL	Environmental Sample Laboratory
EXAFS	Extended X-Ray Absorption Fine Structure
FIB	Focused Ion Beam
FZJ	Forschungszentrum Jülich GmbH
GC	Glassy Carbon
IAEA	International Atomic Energy Agency
IDMS	Isotope Dilution Mass Spectrometry
ID-TIMS	Isotope Dilution Thermal Ionization Mass Spectrometry
IP	Ion Probe
IRMM	Institute of Nuclear Material Management
ISO	International Organization for Standardization
ITU	Institute for Transuranium Elements
JKR-Model	Johnson, Kendall Roberts Model
JRC	Joint Research Centre
LG-SIMS	Large Geometry Secondary Ionization Mass Spectrometry
LMD	Laser Micro Dissection
MCP	Micro-Channel Plate
MII	Modified Inertial Impactor
MP	Microprobe
NIST	National Institute of Standards and Technology
NPT	Non Proliferation Treaty
NNWS	Non-Nuclear-Weapon State

NU	Natural Uranium
NUSIMEP	Nuclear Signatures Interlaboratory Measurement Evaluation Program
NWAL	Network of Analytical Laboratory
NWS	Nuclear Weapon States
PIB	Polyisobutylen-Nonane
PILS	Particle Into Liquid Sampling
POI	Particle of Interest
ppb	Parts Per Billion
ppm	Parts Per Million
QC	Quality Control material
RM	Reference Material
RSD	Relative Standard Deviation
SE	Secondary Electron
SEM	Scanning Electron Microscopy
SGAS	Safeguards Analytical Services
SI	International System of Units
SIMS	Secondary Ionization Mass Spectrometry
SLS	Swiss Light Source
STD	Standard Deviation
TIMS	Thermal Ionization Mass Spectrometry
TUW	Technical University of Vienna
UNH	Uranyl Nitrate-Hexahydrate
VOAG	Vibrating Orifice Aerosol Generator
WDX	Wavelength Dispersive X-Ray Spectroscopy
XANES	X-Ray Absorption Near Edge Structure
XAS	X-Ray Absorptions Spectroscopy
XRD	X-Ray Diffraction spectroscopy
YC	Yellow Cake

## Abstract

The International Atomic Energy Agency (IAEA) is the official body to apply nuclear safeguards to verify compliance with existing legal bilateral or multilateral safeguards agreements [a]. Environmental sampling is a very effective measure to detect undeclared nuclear activities. Generally, samples are taken as swipe samples on cotton. These swipes contain minute quantities of particulates which have an inherent signature of their production and release scenario. These inspection samples are assessed for their morphology, elemental composition and their isotopic vectors. Mass spectrometry plays a crucial role in determining the isotopic ratios of uranium. Method validation and instrument calibration with well-characterized quality control (QC)-materials, reference materials (RMs) and certified reference materials (CRMs) ensures reliable data output. Currently, the availability of suitable well defined microparticles containing uranium and plutonium reference materials is very limited. Primarily, metals, oxides and various uranium and plutonium containing solutions are commercially available. Therefore, the IAEA's Safeguards Analytical Services (SGAS) cooperates with the Institute of Nuclear Waste Management and Reactor Safety (IEK-6) at the Forschungszentrum Jülich GmbH in a joint task entitled "Production of Particle Reference Materials". The work presented in this thesis has been partially funded by the IAEA, Forschungszentrum Jülich GmbH and the Federal Ministry of Economic Affairs and Energy (BMWi) through the "Joint Program on the Technical Development and Further Improvement of IAEA Safeguards between the Government of the Federal Republic of Germany and the IAEA" (in brief: German Support Program, GER SP).

In order to strengthen the IAEA's analytical capabilities, a broad range of tailor-made uranium and plutonium containing particles with consistent characteristics are needed: (1) monodisperse particles with a certified value on the number of atoms per particle (2) mixed particles sizes and (3) artificial QC samples by embedding various monodisperse particle populations with different particle sizes onto swipe samples (these swipes could additionally contain a "dirt" matrix to simulate real-life samples). In the long run, these particles are targeted to be used for quality assurance, method validation and interlaboratory performance evaluations and finally as reference materials or even certified reference materials. The first step towards monodisperse microparticles was the development of pure uranium oxide particles made from certified reference materials.

This work in this thesis represents the efforts and results made during the last three years. A comprehensive outlook will be given later on. The focus of the dissertation is (1) the implementation of a working setup to produce monodisperse uranium oxide particles and (2) the characterization of these particles towards the application as QC-material.

A successful working setup was implemented at IEK-6. Monodisperse uranium oxide particles were produced by spray pyrolysis. Spray pyrolysis is the production of aerosols and the subsequent thermal conversion to its corresponding oxides: A dilute hydro-alcoholic solution made from certified uranyl nitrate solutions was used to produce monodisperse aerosol droplets. Monodisperse aerosol droplets were generated using a vibrating orifice aerosol generator (VOAG). Particles were dried and thermally converted to uranium oxide within a preheating system and a four zone oven and after cooling they are removed from the system by inertial collection. All in all, the entire setup was designed to be a closed system that can even be operated inside a glove box. All components were designed to be easily replaceable. As cost-effective connections and tubes, Swagelok and KF connectors and flanges were used, which ensure a gas tight connection.

[a] Treaty of Rarotonga, Treaty of Tlatelolco, Treaty on a Nuclear-Weapon-Free-Zone in Central Asia (CANWFZ), Bangkok Treaty, Comprehensive Nuclear-Test-Ban Treaty, etc.

It was demonstrated that the particle size can be controlled primarily by the aerosol precursor solution and the production parameters during the aerosol generation - in particular the liquid feed rate and the frequency of the orifice. The final particle morphology is controlled by the precipitation conditions during the conversion from aerosol droplets to solid entities. Small changes to these parameters have a significant influence on the final geometry, size and morphology.

The second part of this thesis deals with the characterization of microparticles. A selection of particles was chosen to present the developments over a period of 12 months. Scanning Electron Microscopy coupled with Energy Dispersive X-Ray Spectroscopy (SEM-EDX) was used for various applications, e.g. to verify the elemental content and to assess the size and geometry of the particles. Furthermore, automated particle assessments over large areas were performed. It was demonstrated that the particle batches show an almost monodisperse size distribution. Combined Focused Ion Beam (FIB-SEM) studies revealed the presence of a porous inner structure for all solid particles. Hence, the resulting overall density was less than expected. Time of Flight Secondary Ionization Mass Spectrometry (TOF-SIMS) studies evaluated the elemental content and demonstrated the need for cleanliness since minute quantities of contaminations could be found in single particles. Micro Raman investigations were used to determine the crystallinity, crystal orientation and uranium species. The measurements showed that particles primarily consist of  $U_3O_8$ . Parts consist of Meta-schoepite and U(IV)-hydroxide which indicates residual water inside the crystal lattice. Micro Raman investigations were performed at CEA (Ile de France) and at the TU-Vienna. SIMS measurements were performed at Safeguards Analytical Services – Environmental Sample Laboratory (SGAS-ESL) on the Large Geometry-SIMS (LG-SIMS) with the scope to assess their performance as a QC material. Particles produced at Jülich were also compared directly against existing QC- and reference materials. Investigations and characterization assays on monodisperse microparticles indicate reproducible results and LG-SIMS investigations indicate equal or even better performance than existing reference materials. It can be concluded that SIMS-experiments indicate a consistent uranium mass per particle. Furthermore, SIMS analysis implies consistent and predictable performance regarding the isotopic content, hydride formation rate, total evaporation profiles and a better performance than existing certified reference materials (CRMs).

# Kurzzusammenfassung

Die Internationale Atomenergie-Organisation (IAEO) ist die offizielle Institution zur Überwachung der Einhaltung des Atomwaffensperrvertrages und anderen internationalen Vereinbarungen auf Basis von bilateralen oder multilateralen Safeguards-Vereinbarungen, siehe [a]. Seit den frühen 1990ern wird „Environmental Sampling“ genutzt, um verdeckten nuklearen Aktivitäten auf die Spur zu kommen. Environmental Sampling beschreibt ein Teilgebiet der nuklearen Forensik, das sich auf das Detektieren und Charakterisieren von kleinsten Mengen an radioaktivem Material in der Umgebung von kerntechnischen Anlagen beschäftigt. Environmental Sampling hat sich seit seiner Einführung als wirkungsvollste Methode im Kampf gegen die Verbreitung von nuklearem Material entwickelt. Durch sogenannte Wischtests können selbst kleinste Partikel aufgenommen, detektiert und gemessen werden. Diese Partikel lassen durch geeignete Untersuchungen wichtige Rückschlüsse zu, z.B. über die Prozesse, die zu ihrer Herstellung oder Freisetzung beigetragen haben. Es ist daher wichtig, die Partikel auf ihre elementare Zusammensetzung, die Morphologie und die Isotopenzusammensetzung zu untersuchen. Um verlässliche Ergebnisse garantieren zu können, ist eine vorangehende Verifizierung und Kalibrierung der Geräte unerlässlich. Qualitätskontrolle (QC), Referenz- und zertifizierten Referenz-Materialien kommt hier eine Schlüsselbedeutung zu. Da die Auswahl an geeigneten nuklearen Referenz-Materialien begrenzt ist, gilt deren Verbesserung als zentrale Herausforderung. Hier kooperieren das Institut für Nukleare Entsorgung und Reaktorsicherheit (IEK-6) des Forschungszentrums Jülich GmbH und die Safeguards Analytical Services (SGAS) der IAEO in einem gemeinsamen Projekt namens "Production of Particle Reference Materials". Die vorliegende Arbeit wurde zu Teilen von der IAEO, dem Forschungszentrum Jülich GmbH und dem Bundesministerium für Wirtschaft und Energie (BMWi) im Rahmen des deutschen IAEO-Unterstützungsprogramms (dem sogenannten „Joint Programme on the Technical Development and Further Improvement of IAEA Safeguards between the Government of the Federal Republic of Germany and the IAEA“ - kurz GER SP) finanziert. Um die analytischen Fähigkeiten der IAEO zu verbessern, bedarf es der Entwicklung von maßgeschneiderten Mikropartikeln. Der Fokus lag dabei auf einer monodispersen Größenverteilung, was zu einem konstanten Wert für die Anzahl der Atome pro Partikel führt. Die hier präsentierte Arbeit beschreibt die Vorgänge und Ergebnisse der letzten drei Jahre, deren Fokus auf der Setupentwicklung im Forschungszentrum Jülich und der Charakterisierung von Partikeln lag. Dabei galt es zu ermitteln, ob die Qualität der produzierten Partikel ausreicht, um als QC-Material genutzt werden zu können. In den vergangenen 15 Monaten wurde am IEK-6 ein funktionierender Prototyp aufgebaut, der nach dem Funktionsprinzip der Spray-Pyrolyse monodisperse Uranpartikel produzieren kann. Dabei wird eine verdünnte hydro-alkoholische Lösung, hergestellt aus zertifiziertem Referenz-Material, durch einen Schwingblenden-Aerosolgenerator (VOAG) geleitet. Im Anschluss werden die verwendeten Partikel in einem Ofen, im Luftstrom, kalziniert und nach dem Abkühlen mittels Trägheitsimpaktoren eingesammelt. Bei der Entwicklung wurde darauf geachtet, dass alle Komponenten sich einfach austauschen lassen und die Apparatur gasdicht verschlossen ist.

Es konnte nachgewiesen werden, dass die finale Partikelgröße primär von der Urankonzentration der Ausgangslösung und den Einstellungen während der Aerosolproduktion (wie der Liquid Feed Rate und der Frequenz der Schwingblende) abhängt. Damit lässt sich die Partikelgröße einfach kontrollieren. Die gewünschte Partikelmorphologie wird durch eine homogene Präzipitation während der Konversion von den Aerosolprekursoren zu festen, unkalzinierten Vorstufen von Partikeln befördert. Geringe Änderungen an den Umwandlungsbedingungen haben einen signifikanten Einfluss auf die Partikelgröße und Morphologie.

Der zweite Teil der Arbeit widmet sich der Charakterisierung der entwickelten Partikel. Es wurde festgestellt, dass sich die Mikropartikel als QC-Material eignen und die bestehende IAEO-Analytik unterstützen können. Anhand einer Auswahl von Partikeln konnte der Fortschritt über einen Zeitraum von 12 Monaten protokolliert werden. Dabei wurde festgestellt, dass die Partikelgrößenverteilung annähernd monodispers ist und die Partikel primär aus  $U_3O_8$  bestehen. Focused Ion Beam (FIB) oder

Ionenfeinstrahl-Untersuchungen konnten zeigen, dass die Partikel eine poröse Innenstruktur aufweisen. Mittels Rasterelektronenmikroskopie (REM) konnte die Größen- und Partikelverteilung auf dem Substrat nachgewiesen werden; mittels energiedispersiver Röntgenspektroskopie (REM-EDX) wurde die Elementarzusammensetzung verifiziert. Time-of-Flight-Sekundärionen-Massenspektrometrie-Messungen (TOF-SIMS) konnten nachweisen, dass kleinste Verunreinigungen aus dem System sich in den Partikeln nachweisen lassen. Mikro-Raman-Messungen konnten die Kristallstruktur und Uranphasen nachweisen: Die Partikel bestehen hauptsächlich aus  $U_3O_8$  mit Anteilen an Meta-Schöpit and U(IV)-Hydroxid. Um die Kristallstrukturen der Uranspezies zu bestimmen wurden Mikro-Raman-Untersuchungen an der CEA (Ile de France) und an der TU-Wien durchgeführt. Diese ließen darauf schließen, dass sich noch Wasser in der Kristallstruktur verbirgt. Im „Safeguards Analytical Service – Environmental Sample Laboratory“ (SGAS-ESL) in Seibersdorf wurden an der Large Geometry-SIMS (LG-SIMS) durchgeführt – diese hatten das Ziel festzustellen, in wie weit sich die Partikel als QC-Material eignen. Dazu wurden die Partikel in mehreren Messungen direkt gegen existierende QC- und Referenzmaterialien eingesetzt. Es konnte nachgewiesen werden, dass durch die monodispersen Eigenschaften reproduzierbare und konsistentere Ergebnisse abgeliefert werden konnten. Die neuen Mikropartikel schnitten im Vergleich zu existierenden Referenz-Materialien vergleichbar gut oder sogar deutlich besser ab.

## Acknowledgments

The Institute for Nuclear Waste Management and Reactor Safety (IEK-6) at the Forschungszentrum Jülich GmbH (FZJ) and the International Atomic Energy Agency's Office of Safeguards Analytical Services Environmental Sample Laboratory (IAEA, SGAS-ESL) cooperate in a common project to produce monodisperse uranium oxide particles. This dissertation project is a direct result of this joint venture which started in early 2012. Within eighteen months, a working prototype setup was developed at IEK-6 and the assessment and characterization of these particles was performed in Germany and Austria.

I would like to express my gratitude to my doctoral supervisor Prof. Dirk Bosbach for offering me the opportunity to write my dissertation with the IEK-6 and his steady support and insightful comments and encouragements. I am also grateful to my second assessor Prof. Georg Roth for his interest in my work and providing valuable support.

My deepest gratitude is to my advisors Dr. Martin Dürr (FZJ) in Germany and Dr. Stephan Vogt (IAEA) in Austria. I am very fortunate to have had two excellent advisors who supported me all the way through. Martin is responsible for the implementation of the setup and the particle production process at IEK-6. Stephan is the driving force behind this project at the IAEA. Without their active contributions, this project would not have been feasible. Their guidance, openness and knowledge helped me on many occasions and it led the project on a successful track. I cannot overstate the importance of their willingness to engage in dialogue, for their feedback and listening to my ideas.

I would like to say a special word of thank you to Mr. Ernesto Chinea-Cano (IAEA) and Dr. Dariusz Wegrzynek (IAEA). I am deeply grateful for their guidance and support. Both were among the best teachers I have ever had. I am in debt to them for their continuous encouragement and input. Ernesto taught me valuable lessons; i.e. analytical techniques, 3D printing, microscopy, computational simulations and of course his gin support to lift my spirits and motivation.

Thanks to Ms. Naida Dzidal (IAEA) for being a great colleague and friend. Naida and I are fellow PhD candidates at the IAEA. We worked on numerous occasions and projects. The overlap of our PhD-projects was a very helpful and beneficial fact for both of us. I wish Naida all the best with her dissertation and future endeavors. Additionally, I would like to acknowledge Mr. Ronald Middendorp's valuable contributions to my dissertation project including aerosol solution preparation, ICP-MS measurements, improving the setup, etc. Without his efforts, my job would have been undoubtedly more difficult. Ronald also a fellow PhD candidate and he is my successor on the particle production setup in Jülich. I wish him all the best for his dissertation and his future endeavors.

I am grateful to Dr. Irmgard Niemeyer (FZJ) for including me to her working group and for her support and insightful comments.

I am in debt to the members of the Micro Particle Analysis Team at SGAS-ESL in particular to Dr. Jane Poths, Dr. Laure Sangely, Thippatai Tanpraphan, Olivier Bildstein and Dr. Madvej Aleshin for their extensive support with supplies, granting me a lot of time and freedom to perform multiple time-consuming measurements on the Large Geometry Secondary Ionization Mass Spectrometer (LG-SIMS), operating this amazing apparatus for me, helping me with the huge amounts of data and for a lot of fun. Thank you to Thip, Olivier and especially Laure for devoting countless hours and even weekends for this project. I am truly in debt and humbled for your support.

I would like to express my deepest gratitude to all people working at IEK-6 and SGAS with whom I have interacted during the last three years. Thank you very much receiving me with open arms and for their encouragement and help. I would like to acknowledge some colleagues and friends in particular for their support: Dr. Martina Klinkenberg (FZJ) for her outstanding support with SEM-EDX and FIB, Christian Schreinemachers (FZJ) for introducing me particle chemistry and his support, Dr. Sergei

Boulyga (IAEA) for his encouragement and support, Dr. Zsuzsanna Mácsik (IAEA) for introducing me to IAEA's analytical chemistry and to Vienna, Clemens Listner (FZJ), Dr. Philip Kegler (FZJ), Denis Nidrée (FZJ), Dr. Felix Brandt (FZJ), Mathieu Rosenzweig (IAEA), Franz Sturm (IEAE), Catherine Mansoux (IAEA), Dr. Stefanie Konegger-Kappel (IAEA), Ala Kist (IAEA), Maria Hedberg (IAEA), Dr. Beata Varga (IAEA), Islam Amirul (IAEA) and many more.

Dr. Ingo Spahn for his efforts and time spent reading carefully my various iterations of this manuscript. I am grateful to William Kings for his valuable support proof-reading my thesis.

I was introduced to the world of Nuclear Safeguards by Dr. Gabriele Voigt (IAEA) and Dr. David Donohue (IAEA). I am highly grateful for the trust and the opportunity I was given by both to prove myself in this thrilling and exciting work environment. Furthermore, I would like to acknowledge Dr. Yusuke Kuno's (IAEA) efforts in supporting and pursuing this project.

I am also thankful to Anton Nirschl (IAEA) and Gerhard Ritz (FZJ) and their teams for their support and expertise.

I would like to express my appreciation for Dr. Fabien Pointurier for his support with the  $\mu$ -Raman measurements and the preparation to visit the CEA DAM Ile de France facility (Commissariat à l'énergie atomique et aux énergies alternatives Direction des Applications Militaires). I would like to thank him for his hospitality and the very productive work environment. I am also grateful to Professor Bernhard Lendl at the Institute of Chemical Technologies and Analytics (Division: Environmental and Process Analytics) at the Vienna University of Technology (TUW) for his support with Raman Spectroscopy. I would like to acknowledge in particular Dr. Johannes Ofner (TUW) efforts in granting me short dated access to the  $\mu$ -Raman instrument. And I am thankful to Mrs. Karin Wieland for her efforts and times spend together.

I am thankful to numerous people for their support, valuable contributions and encouragement Dr. Yetunde Aregbe (IRMM), Dr. Rozle Jakopič (IRMM), Dr. James Tushingham, Dr. Uri Admon, Dr. Stefan Buerger (IAEA), Dr. Ylva Ranebo (IRMM), Dr. Monia Kraiem (IAEA), Dr. Anne-Laure Fauvre (CEA), Olivier Marie (CEA), Dr. Amélie Hubert (CEA), Wolfgang Trautwein (BMW/GER SP), Dr. Bernd Richter, Dr. Gotthard Stein, Dr. Canty Morton, Dr. Arnold Rezniczek (all GER SP).

The thesis was partly sponsored by the Federal Ministry of Economic Affairs and Energy (BMW) through the Joint Program on the Technical Development and Further Improvement of IAEA Safeguards between the Government of the Federal Republic of Germany and the IAEA (in brief: German Support Program, GER SP) under the GER SP Task A1961, and the IAEA. From July 2012 until June 2015 I was supported through a Special Service Agreement by the IAEA.

Finally, I would like to thank my girlfriend, family and friends for their support and encouragement throughout the entire time.

# 1. Introduction

The International Atomic Energy Agency's (IAEA) dates back to US President Eisenhower's speech "Atoms for Peace" to the General Assembly of the United Nations in 1953. After many modifications and negotiations, his proposal formed the basis for the Statute of the International Atomic Energy Agency (IAEA) that entered into force in 1957. Eisenhower's speech put forward a proposal promoting peaceful use of nuclear energy and fostering scientific and technological exchange as means of contributions for peace, health and prosperity under the control of an international authority, as well as achieving and sustaining nuclear disarmament at the same time. The Statute requires that IAEA safeguards are to be applied to nuclear facilities and materials. Since the 1960s, legal safeguards arrangements between the IAEA and individual member states exist and they have been gradually adapted to the changing political reality. – They are documented in published agreements INFCIRC/26, INFCIRC/66, and INFCIRC/153 [1]. The "Treaty on the Proliferation of Nuclear Weapons" (NPT); also known as INFCIRC/140 [2] was signed in 1968 and entered into force in 1970. The NPT is a multilateral treaty which is not just related to safeguards issues, but also to the peaceful use of nuclear energy and nuclear disarmament by nuclear weapon states (NWS). It has proven to be a pillar of the global nuclear non-proliferation regime. As of today, 191 states including the five nuclear-weapon states have signed the NPT, including the Democratic People's Republic of Korea (DPRK), but neither India, Israel, Pakistan nor South Sudan. The NNWS party to the NPT are obliged to accept safeguards as set down in bilateral or multilateral agreements with the IAEA, in accordance with the IAEA Statute and safeguards system.

The nuclear safeguards regime is predominantly based on the control of nuclear material flow and inventories which obliges member states to establish a nuclear material accountancy system. The IAEA conducts verification of operators' declarations, e.g. by conducting measurements inter alia performed by the IAEA Safeguards Analytical Laboratory in Seibersdorf, Austria, or by the use of containment and surveillance. In 1991, after the first Gulf War, the international community learned about Iraq's large scale clandestine nuclear program, which was neither declared nor detected by the IAEA. In 1990s, safeguards inspections in the DPRK revealed inconsistencies with the declared plutonium stock. The DPRK refused additional access and information to resolve the situation. This implied a deterioration of the situation which in 1994 led to the DPRK's withdrawal from its IAEA membership. These experiences highlighted the need for the IAEA to review the effectiveness of its current safeguards system. Nuclear material accountancy, the main pillar of this program, provided the IAEA with the means of verifying the correctness of the declared activities the state provided on its nuclear program. The IAEA, however, was not well equipped to detect undeclared nuclear material and activities in signatory States, i.e. an assessment of the completeness of a State's declarations. At the end of 1993, as a direct effect the IAEA launched a broad program (so-called Program "93+2") to further strengthen safeguards implementation by enhancing its ability to consider a state as a whole. In 1997, the "93+2" program eventually led to the implementation of the Model Additional Protocol (AP) or INFCIRC/540 [3], which is aimed at improving the IAEA's ability to detect undeclared activities in states with comprehensive safeguards agreements. One of these new measures aimed at strengthening the safeguards system was environmental sampling (ES), which was implemented as collection of swipe samples inside of nuclear facilities. ES provides indication, i.e. on the absence of undeclared nuclear materials and activities as the analysis of swipe samples probes for nuclear signatures and traits which are not part of the facility's and state's declarations. To this end, the Safeguards Analytical Laboratory's capabilities were enhanced by adding a clean room facility ("Clean Laboratory", today part of the Office of Safeguards Analytical Services' Environmental Sample Laboratory) to provision clean sampling kits and the analysis of ultra-trace amounts of nuclear materials collected on the swipe samples. Environmental swipe samples returned from inspections to the Environmental Sample Laboratory (ESL) are screened using non-destructive analytical techniques, such as Gamma-Ray and X-Ray spectroscopy, followed by more detailed, destructive analyses. Destructive analyses are divided into (a) so-called "bulk" analytical techniques,

where the entire swipe sample is decomposed and analyzed for its elemental and isotopic composition of nuclear material traces. And (b) there are “particle” analytical methods with which individual uranium and plutonium bearing particles from a swipe sample are characterized.

In particle analysis, the measurement of the major ( $^{235}\text{U}/^{238}\text{U}$ ) and minor (in particular for  $^{236}\text{U}/^{238}\text{U}$ ) isotopic ratios of uranium are of key interest because they are strong indicators for inherent process procedures, a technique which also finds application in nuclear forensics. Various references such as Betti et al. (1999) [4], Pajo et al. (2001) [5], Erdmann et al. (2003) [6], Baude et al. (2005) [7], Pointurier (2011) [8] describe different methodologies used in nuclear forensics to identify, relocate and measure single microparticles (normally in the size range of a few micrometer to a several hundred micrometers). Donohue et al. (2002) [9] (2008) [10] describe a series of micro analytical techniques used at IAEA to investigate the size, morphology and elemental- and isotopic content of single spherical particles in the size range of 9 - 12  $\mu\text{m}$  which were recovered from a swipe sample taken from a nuclear facility under safeguards: Particles were identified by SEM/EDX, relocated and transferred under an optical microscope and SIMS was used to determine the isotopic content, focused ion beam (FIB) was used to investigate the inner structures. Pidduck et al. (2006) [11] describe techniques specifically targeted for the IAEA’s need to characterize micrometer-sized uranium particulates. Shinonaga et al. (2008) [12] describe the analysis of single uranium particles with SEM-EDX, ICP-MS and TIMS analysis. Particles were transferred from cotton swipes via inertial impaction and by micromanipulation onto suitable substrates. Artificial uranium bearing entities and micrometer-sized uranium particulates for method development, validation and quality assurance are of particular interest for particle analysis users in the evolving field of international safeguards and nuclear forensics. For example, such synthetic and well characterized test particles come into play when existing technologies are adapted to the current needs and which need to be validated; see Kappel et al. (2012) [13] and (2013) [14].

In recent years, a number of Ph.D. projects focused on the synthesis of microparticles for nuclear safeguards related issues have been published: Stetzer (2001) [15] presents the production of monodisperse uranium oxide particles for fission track detection techniques whereas Kips (2007) [16] describes the production of polydisperse uranium oxyfluoride particles by  $\text{UF}_6$  hydrolyzation in a controlled environment. While others depict specific methodologies for sampling such as Ithantola (2009) [17], others describe methodologies for determining the isotopic and morphological content of nuclear particulate; see Ranebo et al. (2009) [18] [19], Kappel (2012) [13], Warneke (2012) [20] and Macsik (2013) [21].

As for any analytical method, certified reference (CRM) and QC materials are required for instrument calibration, method validation, and internal/external QC programs and proficiency testing. For bulk analytical techniques, a wide range of CRMs are available from authorized laboratories, i.a. the Joint European Commission’s (JRC) Institute of Reference Materials and Measurements (IRMM), or the United States Department of Energy’s New Brunswick Laboratory (NBL), the United States National Institute of Standards and Technology (NIST) and the French Commission d’Etablissement des Methodes d’Analyse (CETAMA). However, for particle analysis techniques, only a very limited number of such materials are available: JRC-IRMM’s  $\text{UO}_2\text{F}_2$  particles, in limited quantities and just distributed to a hand-picked number of laboratories JRC-ITU’s monodisperse uranium oxide particles, VTT’s polydisperse particles and microparticles supported by the UK support program to the IAEA, see more detailed information in Chapter 3.1.1.

Particles with a broad range of characteristics are needed to ensure and improve reliability of analytical results measured from single particles. For safeguards related analyses, uranium and plutonium containing particles of various isotopic compositions and sizes are needed. Some examples for the needs in safeguards and nuclear forensics are: (1) Monodisperse particles with a known number of atoms per particle are needed mainly for instrument calibrations, (2) mixed particle sizes are needed for QC materials to better reflect field samples, as are particles of mixed elemental and/or isotopic

composition, and (3) QC samples, i.e. swipes doped with particles of various sizes, compositions and relative proportions thereof.

A working prototype setup has been developed at FZJ and is successfully producing monodisperse uranium oxides particles since May 2014. The approach described in this dissertation is based on the generation of monodisperse aerosol precursor, made from certified reference materials, who are thermally converted into solid species. The aim of this publication is to describe the generation process and the subsequent characterization efforts. This approach assumes that the certified isotope ratios of the bulk material are preserved in the final particles, which has indeed been confirmed in independent measurements of isotope ratios of the synthetically produced particles. However, characterization of the particles from these experiments showed that the density within a microparticle varies considerably and is much lower than theoretically anticipated for the pure oxides. In conclusion, based on the various requirements on particulate material for quality assurance purposes in particle analysis, the main focus was put on the consistency of the quantity of uranium per particle - density, morphology and geometry / size were of secondary priority.

The Institute of Nuclear Waste Management and Reactor Safety (IEK-6) at the Forschungszentrum Jülich GmbH (FZJ) and the Federal Ministry of Economic Affairs and Energy (BMWi) through the Joint Program on the Technical Development and Further Improvement of IAEA Safeguards between the Government of the Federal Republic of Germany and the IAEA (in brief: German Support Program, GER SP) cooperate with the IAEA's Department of Safeguards on particle reference material production. The name of this project under the GER SP task A1961 is entitled "Production of Particle Reference Materials".

## 1.1 Needs and Goals

At the beginning of this project, a catalogue of requirements was set up. Uranium oxide particles should to be used for various (non)-destructive analytical techniques for particle analysis for nuclear safeguards applications such as scanning electron microscopy and energy dispersive X-ray spectroscopy / wavelength dispersive X-ray spectroscopy (SEM-EDX/WDX) for size distribution, morphology and elemental verification,  $\mu$ -Raman spectroscopy to assess the morphology of single particles, mass spectrometry - in particular SIMS, ICP-MS and TIMS for the determination of the isotopic content and many more assays. Therefore, it was agreed that micrometer-sized, monodisperse particles are the favored species for this new kind of reference material. Monodisperse particles offer the advantage of consistent and homogeneous particle properties. The most important feature is the constant amount of uranium per particles. Other particle attributes are of secondary importance. These are: (i) tailored isotopic content, (ii) particle size, geometry, density and morphology. If the characterization efforts prove to be promising, a certification process would require additional authentication. Beyond the homogeneity assessment traceability to the international system of units (SI) is a prerequisite. It was decided that the approach using a VOAG showed the most promising potential of all reported particle production approaches, see Chapter 3.1.1. The system was designed in a way to (a) reduce the risk of cross contaminations, (b) easy access and maintenance ability to ensure safe handling and handling inside glove boxes and most importantly (c) improved particle collection.

## 2. Scope of the Thesis

This work describes the efforts of a joint program between the Institute of Nuclear Waste Management and Reactor Safety (IEK-6) at the Forschungszentrum Jülich GmbH and the Department of Safeguards at the International Atomic Energy Agency (IAEA). The scope of this thesis covers two objectives: (1) the development and implementation of a working setup to produce monodisperse uranium microparticles and (2) the characterization towards application as a QC-material and (C)RM material.

### (1) Particle Production

The needs and goals are a good starting point to describe the basic structure of the particle production theme in this dissertation: to have (1) well defined microparticles with a known number of atoms per particle, (2) consistent particle-size distribution, (3) homogenous particle morphology throughout the particle batch and (4) reproducibility of these properties. Monodisperse uranium oxide particles were produced by spray pyrolysis. The particle production is an integrated two-step process: (1) generation of monodisperse aerosol precursor-droplets using a vibrating-orifice aerosol generator (VOAG) and (2) subsequent drying and calcination of droplets to the corresponding oxides. Particles are generally collected via inertial impaction on glassy carbon disks. The entire setup consists of a closed system to prevent the spread of radioactive aerosol particles into the environment and to prevent contamination. It was agreed to develop a prototype out of commercially available components such as the VOAG, the furnace, the pumps, the KF-flanges and Swagelok systems, etc. with the focus on accessibility and ease of exchangeability.

The introduction in Chapter 1 situates this dissertation project into the context of IAEA's nuclear safeguards regimen: as part of their efforts to improve their analytical capabilities and to outsource R&D to an external research facility (the IEK-6 at the Forschungszentrum Jülich GmbH). Also the "Needs and Goals" for this project are indicated. This forms a bridge between the basics and theory of particle production (Chapter 3.1) and associated issues such as particle transport (Chapter 3.2) and micro-analytical techniques (Chapter 3.3): The part of the thesis that comprises the particle production is divided into several parts: (1) other microparticle projects, (2) theory of precursor production, (3) theory of thermal conversion, (4) the collection of microparticles and their behavior in laminar and non-laminar air streams and (5) the evolution of the particle production setup at IEK-6. Chapter 3.1.1 describes the different approaches and aims of producing microparticles for nuclear safeguards application and it exemplifies why we chose to the VOAG approach. Chapter 3.1.2 describes the theory behind producing monodisperse aerosol droplets by using a vibrating orifice. Subsequently, after the precursor generation, the thermal conversion takes place, see Chapter 3.1.3. Due to the complexity of the particle formation a sound theoretical model calculation is difficult to be amenable because the final morphology and geometry are both determined by the temperature, dwell time and air flow which prevail during the conversion step from aerosol precursors to solid entities. Nevertheless, a phenomenological description of this specific formation dynamics helps to shed light into the particle generation mechanics inside the setup which is deployed at IEK-6.

The last step in the evolution process of the particle generation is the collection from the system. In order to understand the particle collection, a prior brief introduction to the basics of particle adhesion and re-entrainment are described in Chapter 3.2.1. These basics are necessary to understand the issues related to particle collection in the beginning of this project as well as to understand how an inertial impaction works, see Chapter 3.2.2. And Chapter 3.3 briefly discusses the most important analytical techniques used in this dissertation: from scanning electron microscopy to secondary ionization mass spectrometry.

The Chapter 4 “Materials and Methods” contains two important pieces of information: (1) the evolution process during the first 1.5 years towards a successful implementation of the microparticle production setup at IEK-6 and (2) the materials and methods applied in this project. The first part is important because it covers the major part of the first half of my dissertation project. It also includes the Chapter “Particle Transfer Techniques” (Chapter 4.1.3) which describes a procedure of existing and newly developed methods (custom grid- and reference point engraving using a laser micro dissection system) to identify and relocate single particles on a large area. This technique was extensively used for combined SEM / LG-SIMS investigations during my time at SGAS-ESL. An important step between particle production and characterization are appropriate particle transfer techniques and the choice of a suitable substrate for sampling. The underlying idea was to have a particle production setup that offers flexibility in terms of particles size distribution and functionality: particles can be collected onto various substrates or into multiple suspensions via inertial impaction techniques. Triangulation helps to relocate single microparticles within a bigger matrix.

## (2) Characterization Efforts

This chapter aims to describe how microparticles produced in Jülich perform in comparison to existing (C)RMs and why they are suitable candidates for application as QC-material and even as (C)RM.

The second part deals with the characterization of a selected number of uranium oxide particles batches. These particles depict a cross section of the evolution process of uranium particles from May 2014 until April 2015.

The Chapter “Results and Discussion” starts off with a brief characterization of the existing one stage inertial impactors. These devices are extensively used at SGAS-ESL and also during this project. But, so far no real characterization had been made. For the  $\mu$ -Raman spectroscopy investigation uranium reference materials were deposited onto graphite substrates using a modified inertial impactor, which was designed to mimic the size distribution of the microparticle generation setup developed at IEK-6. These reference materials were used as a calibration standard as well for comparison. And in Chapter 5.1.3 a cyclone impactor designed at SGAS-ESL is introduced which allows efficient sampling at high air flows. This device was developed during the first half of my dissertation project when the collection yield was not sufficient.

Chapter 5.2.3 takes a deeper look at the inner structure of the particles of interest. It could be demonstrated by using non-destructive computational means that the inflated species are hollow and their existence is in congruence with references, see Chapter 5.2.3.1. The solid particle species was investigated by using a Focused Ion Beam instrument coupled to a Time of Flight Secondary Ionization Mass Spectrometer (FIB-TOF-SIMS). It was shown that these particles have a porous inner structure, see Chapter 5.2.3.2. Quantitative SEM-EDX analysis on all particle species proved to be not meaningful due to the small size of the particles. Nevertheless uranium could be identified easily.

The crystal structure and orientation and the composition were evaluated using  $\mu$ -Raman spectroscopy, see Chapter 5.3.  $\mu$ -Raman spectroscopy indicated the existence of a uranium compound that was expected:  $U_3O_8$  but different uranium compounds were also identified which indicate an inconsistent uranium species distribution within a single micro particle. The characterization of the physico-chemical particle properties plays an important role, however thorough research into this domain is not within the scope of this dissertation. In this respect, combined X-ray diffraction and X-ray absorption near edge structure and extended X-ray absorption fine structure (XRD and XANES/EXAFS) performed on single micrometer-sized particles promises to provide detailed insight.

Chapter 5.4 describes the characterization efforts performed a Cameca 1280, Large Geometry SIMS investigations (LG-SIMS). These experiments demonstrate the aptitude of the microparticles as a future reference material, especially in terms of particle homogeneity,  $m(U)/\text{particle}$ , density and mechanical

stability during ion beam bombardment. SIMS experiments on selected batches were used to (1) assess the isotopic content and compare it with the original data and (2) assess the performance of uranium particles against existing QC-materials and calibration standards. The latter point addresses LG-SIMS specific characteristics, such as the hydride correction, total evaporation and redistribution profiles plus the assessment of the useful yield and the beam profiles of the  $^{238}\text{U}$  intensities all of which are indicators for future usage as a reference material.

## 3. Scientific and Theoretical Background

### 3.1 Particle Production

#### 3.1.1 Approaches for Particle Production

Nuclear reference materials normally occur as solutions, metals, ceramics or oxides. Most (certified) reference materials can be purchased as oxides, ceramics or solutions; in particular nitrate solutions containing uranium or plutonium. Reference materials play an important role in the performance assessment of analytical laboratories which is evaluated within interlaboratory comparison exercises, e.g. the Nuclear Signatures Interlaboratory Measurement Evaluation Program (NUSIMEP) organized by the JRC-IRMM. NUSIMEP-6 and 7 [22], [23] were conducted in 2006 and 2011 respectively. These round-robin exercises were used to assess the performance of each laboratory in determining the isotopic amount ratios of uranium particles. However, the availability of tailor-made reference materials for particle analysis with specific properties such as consistent morphology, isotopic and elemental background and amount of fissile material per unit is very limited. So far there are no microparticles commercially available as QC or (C)RM. Over the last decade, several programs have been initiated to produce uranium, plutonium containing microparticles with different properties. These programs will be discussed briefly in this chapter.

Uranium-doped glasses were developed at JRC-IRMM by Raptis et al. (2002) [24]. Seven different uranium-doped glass powders with 5 mass-% uranium with various <sup>235</sup>U abundances, from natural to highly enriched uranium, were produced for the IRMMs support program to the IAEA and for the external NUSIMEP-program. These particles should mimic real-life particles embedded in an inactive matrix of glass. Particles were produced by blending fine, high-purity borosilicate powders and U<sub>3</sub>O<sub>8</sub> (U<sub>3</sub>O<sub>8</sub> was obtained by hydrolysis of certified UF<sub>6</sub>) together. The mixtures were melted together at 1450 °C and then milled. The mean particle size was between 10 – 20 µm. Particles showed sharp-edged, irregular surface structures and homogenous morphology. The final yield of uranium was between 30 – 40 g of uranium glass per 1 kg of matrix glass. All glasses have been certified as RMs for isotopic determinations of uranium, see Kappel et al. (2012) [25]. The inactive glass matrix simulates for dust, soil or sediment which is collected in every swipe-sample.

Another program was started at JRC-IRMM: Uranium particles with certified isotopic abundances made from UF<sub>6</sub> were produced at IRMM by a controlled hydrolyzation reaction of UF<sub>6</sub> gas inside an aerosol deposition chamber. This JRC-IRMM development produces uranium-oxyfluoride particles by hydrolyzing UF<sub>6</sub> in a controlled environment. These particles were designed to mimic UF<sub>6</sub> hydrolysis products found in conversion and enrichment plants.



This project is based on the work of Lux (1982) [26], Carter and Hembree (1998) [27] and Kemp (2006) [28] who studied the emergence, production, release scenarios and effects of UF<sub>6</sub> and UO<sub>2</sub>F<sub>2</sub> to the environment. A working installation was build and developed at JRC-IRMM, see Kips et al. (2007) [29] and (2012) [30]. UF<sub>6</sub> was released into a vessel by mechanically breaking a UF<sub>6</sub> glass vial. By controlling the internal humidity levels within the vessel, a controlled reaction was achieved. Particles were sampled via gravitational deposition on glassy carbon planchets. The morphology of these particles ranged from chain-like agglomerates to single particles, all in the range micrometers. The formation of agglomerations is very much dependent on the interaction between the humidity level and the temperature inside the deposition chamber. Combined TEM-Electron Energy Loss Spectroscopy (EELS) measurements revealed that the surface of single particles was composed of uranium and oxygen. Fluorine was also detected underneath the surface layer. Electron diffraction patterns of single particles

indicated a cubic lattice structure. Morphology, chemical- and isotopic composition of these particles was investigated by SEM-EDX and SIMS, see Kips et al. (2007) [16] and [29] and Kips et al. (2009) [31].

Between 2006 and 2009, the Technical Research Center of Finland (VTT) contributed to the SG-ESL. The work is documented in a series of internal reports, Kaerkela et al. (2006) [32] and (2007) [33], Ziliacus et al. (2008) [34] and Hokkinen et al. (2010) [35]. Polydisperse actinide oxide particles were produced by spray pyrolysis. Particles were produced using an aerosol generator called an Atomizer (TSI, Model 3076). Aerosol solutions consisting of nitrate solution of uranium, plutonium and cerium and water were used to produce polydisperse particles. Particles were sampled onto aluminum foil covered with an adhesive (Apiezon) via multiple-stage inertial impaction - a device called the "Bernier low pressure impactor" (BLPI). Uranium, plutonium and cerium particles in the range  $\leq 1.0 \mu\text{m}$  were produced. Unfortunately, these particles were not suitable for safeguards applications, as the particles were collected on aluminum foils using Apiezon-L. The high amount of adhesive made single particle transfer impossible also the removal of excess adhesive introduced massive hurdles for elemental and isotopic analysis and interfering with SEM studies.

The UK Safeguards Support Programme to the IAEA chose a different approach of producing polydisperse uranium particles. Microparticles were produced by spray pyrolysis and aerosol precursor droplets were generated by means of a spinning-top aerosol generator. The system uses a compressed air to rotate the spinning disk. Aerosol droplets are generated by directing a liquid jet of a uranium containing solution on to the spinning disk causing the dispersion of the liquid into micro-droplets. The aerosol droplets are carried away by a steady air stream and an internal particle removal system removes the vast majority of unwanted aerosol - in order to generate a monodisperse size distribution. The precursor aerosol particles are converted into uranium oxide particles in a furnace at temperatures of up to  $1200 \text{ }^\circ\text{C}$ . Subsequently, the particles were collected on PTFE filters and analyzed with SEM-EDX, TEM and SIMS, as reported in internal reports by Tushingham and Taylor (1998 - 2000) [36], [37], [38] [39]. Particles with three different enrichments were produced: natural uranium, low enriched uranium (3 - 5 % U-235) and high-enriched uranium ( $> 20 \%$ , U-235). The mean diameter for all particle batches was  $1 \mu\text{m}$ . Particles were designed to have consistent properties with regard to their density, size and mass, but with different isotopic content thus to be used as QC-materials. SEM/EDX and SIMS investigation indicated insufficient consistency regarding particle morphology and polydisperse size distribution; thus resulting in an inconsistent mass of U per particle. SEM investigations revealed the existence of hollow particles, particle shells, disintegrated particles and agglomerations of particle shells. Particles from these experiments were applied to the swipe matrix used in the IAEA's sampling kits and used as QC swipes. Several sets of these QC materials were used to administer a QA/QC program to check on the reliability of the Network of Analytical Laboratories performance. The project was not further pursued.

In 2000, Nicole Erdmann and her working group at the Joint Research Center - Institute for Transuranium Elements (JRC-ITU) started to develop a system to produce monodisperse uranium and plutonium particles, see Stetzer (2001) [15] and Erdmann et al. (2000) [40]. Particles were produced by spray pyrolysis. Precursor aerosol droplets were produced by using dilute hydro-alcoholic solutions made from uranyl nitrate hexahydrate (UNH). The aerosol was produced by using a vibrating-orifice aerosol generator (VOAG). The mean diameter of these particles was in the range of a few micrometers. Particle size is predominantly controlled by the UNH-concentration. The final particles were collected on Nuclepore filters and aliquot pieces were cut out for further analysis, see Erdmann et al. (2000) [40], and Stetzer et al. (2004) [41]. Multiple batches of uranium and plutonium containing particles were produced and analyzed in order to assess the characteristics, i.e. morphology, size distribution,  $m(\text{U})/\text{particle}$ , isotopic composition and mass spectrometry specific behavior with SIMS, see Ranebo et al. (2007) [42], (2008) [43], (2009) [18], (2010) [44]. Kraiem et al. (2012) [45] quantified the uranium mass in single micron particles by isotope dilution thermal ionization mass spectrometry (ID-TIMS). They investigated the two different particle batches with comparable size distributions. ID-MS

measurements revealed a significant variance of the uranium mass per particle and the uranium mass density between those two batches. An average uranium mass value per particle for batch (1) [U100] of  $2.80 \pm 0.28$  pg ( $k = 2$ ) was determined and for batch (2) [U020-A]  $1.83 \pm 0.15$  pg ( $k = 2$ ). The variance of the corresponding uranium mass density is also significant between batch (1)  $5.63 \pm 1.04$  g/cm<sup>3</sup> and  $4.48 \pm 0.92$  g/cm<sup>3</sup> for batch (2). Kraiem et al. (2012) [45] state that the lower mass density is caused by the presence of more voids on the outer structure which are detected by SEM and more voids on the inside, undetectable for SEM. In direct comparison to naturally grown, Kraiem et al. (2012) [45] also state that the molecular composition is not exactly known (UO<sub>2</sub>, U<sub>3</sub>O<sub>8</sub>, UO<sub>3</sub>, U-O mixture). The project was not pursued any further despite the promising results obtained.

The existing particle production programs show that uniform particle characteristics with regard to the uranium mass content and morphology can only be achieved by monodisperse microparticles, i.e. consistent mass of uranium per particle, density and consistent particle morphology. Uranium-doped glasses were developed to simulate soil, sediment or dust matrixes, but lacked in consistency of uranium mass per particle since the size distribution was polydisperse. Hydrolyzed UF<sub>6</sub> microparticles were produced to simulate particles found in enrichment and conversion plants. These microparticles were in the range of a few micrometers, but they were erratically shaped thus resulting in inconsistent uranium mass content. Particles produced at VTT showed a much more consistent size distribution, but these particles were deposited onto an adhesive layer which prevented any further investigation. By using a Berner Impactor, the size discrimination was sufficient but by NIST standards not monodisperse. Actinide oxide particles produced at VTT were investigated at SGAS-ESL by SEM-EDX. The investigations were hampered by the adhesive coating, but it could be shown that these microparticles showed some significant ageing effects. In 1998, the UK support program to the IAEA started a particle production program which was terminated after about two years because the particle morphology could not be controlled in a satisfactory manner and the particle size distribution was polydisperse. SEM investigations revealed the presence of particle shells and debris simultaneously side by side with intact microspheres. Erdmann et al. (2000) [40] and Stetzer (2001) [15] showed the potential of a working prototype to produce monodisperse microparticles by using a vibrating orifice-aerosol generator. Extensive studies by JRC-IRMM and JRC-ITU indicate that, if the particle production parameters are under control, acceptable quality can be produced. That is why the JRC-ITU approach was taken and further developed for IAEA's particle production program.

### 3.1.2 Aerosol Droplet Generation

The first step in the production of monodisperse particles is the production aerosol droplets. This is achieved with an aerosol generator called the Vibrating Orifice Aerosol Generator (VOAG). The Vibrating-Orifice Aerosol Generator (VOAG) was developed by Berglund and Liu (1973) [46] at the University of Michigan. In 1974 [47] the VOAG was patented. They developed a system that was able to produce monodisperse aerosol particles by pressing a hydro-alcoholic solution through a small orifice. The core of the VOAG is the orifice which is mounted onto a piezoelectric crystal. Two fittings below the orifice provide the feed solution and a transportation/dispersion stream of filtered air. As a feed solution a 1 : 1 mixture of water and alcohol is used.

The aqueous fraction of this mixture contains a certain amount of a non-volatile species which determines the particle's composition. In order to obtain uranium bearing particles this is achieved e.g. by adding uranyl-nitrate solution. The functional principle of generating aerosol droplets with a precisely defined diameter is based on the instability of a liquid jet. Such a liquid jet is unstable by nature and has therefore a strong tendency to turn into droplets. Under normal conditions, this droplet evolution is random and erratic and leads to non-uniform droplets. In order to control the droplet formation process, a frequent disturbance is imposed on the system. This is accomplished by using a piezo electric element which oscillates with modulating frequency. With every turn of the disturbance-cycle, one droplet is formed.

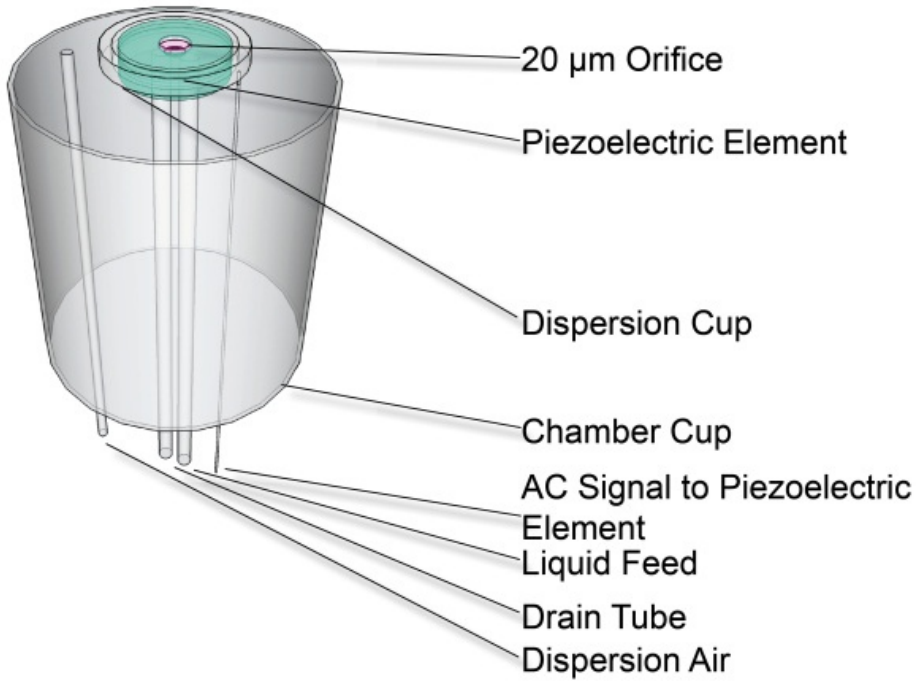


**Figure 1: Schematics of the core unit of the vibrating orifice aerosol generator.**

Plateau (1873) [48] derived a minimum wavelength for a disturbance to be unstable. The minimum disturbance induced wavelength " $\lambda_{min}$ " is a proportional to the diameter of the ejected liquid jet " $d_j$ ":

$$\lambda_{min} = \pi d_j \quad (2)$$

According to Rayleigh et al. (1878) [49] (1879) [50] the optimal wavelength " $\lambda_{opt}$ " is an empirical value which is determined by a factor 4.508 of the ejected liquid jet. If these conditions are met the liquid is jet is expected to be most unstable.

$$\lambda_{opt} = 4.508 d_j \quad (3)$$

Studies by Schneider et al. (1964) [51] indicate a feasible wavelength range for the production of monodisperse droplets:

$$3.5 d_j < \lambda < 7.0 d_j \quad (4)$$

The wavelength range derived by Schneider et al. (1964) [51] can be modified with the expression of the minimum flow rate " $q_{j,min}$ ".

$$3.5 d_j < \frac{q_j}{f} < 7 d_j \quad (5)$$

According Lindblad et al. (1965) [52] the minimum flow rate is the square root of the ratio between the surface tension " $\alpha$ " and the product of the density of the solution and the diameter of the ejected liquid jet:

$$v_{j,min} = \left( \frac{8\alpha}{\rho d_j} \right)^{1/2} \quad (6)$$

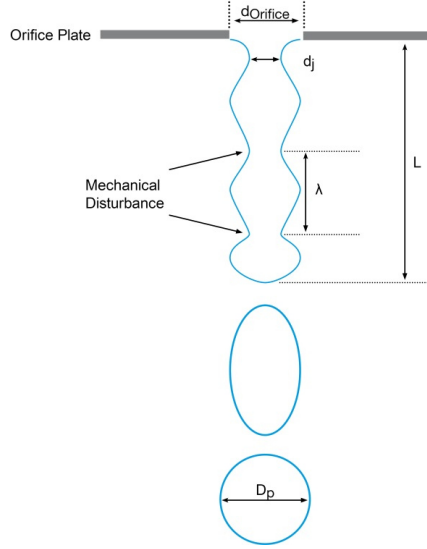


**Figure 2: Diagram of liquid jet break up cycle induced by piezo electric disturbance.**

The mixture is then pressed in a very precise manner through the orifice fitting which provides the feed solution – this will be referred to as the Liquid-Feed-Rate, “ $Q$ ”.

The orifice is directly connected via Luer-Lock connectors to a disposable syringe which contains the aerosol solution. The syringe is compressed by a stepper motor which can be adjusted in order to control the amount of liquid being ejected. This ejected volume provides the feed solution and will be referred to as the Liquid-Feed-Rate “ $Q$ ”. By imposing a frequent disturbance, the droplet formation process monodisperse droplets can be generated. The droplet diameter “ $d_{Droplet}$ ” size can be derived by the droplet volume “ $V_{Droplet}$ ” right after it exits the orifice and no evaporation has occurred. The volume of each droplet can be expressed as the quotient of the liquid flow rate “ $Q$ ” which is the amount of liquid solution in volume per time unit and the frequency of the disturbance “ $\nu$ ”.

$$V_{Droplet} = \frac{Q}{\nu} \quad (7)$$

The droplet diameter “ $d$ ” and the droplet volume are connected in the following manner:

$$V_{Droplet} = \frac{1}{6} * \pi * D_{Droplet}^3 \quad (8)$$

$$D_{Droplet} = \sqrt[3]{\frac{V_{Droplet} * 6}{\pi}} = \sqrt[3]{\frac{6 * Q}{\pi * \nu}} \quad (9)$$

Under typical operation procedures the VOAG emits droplets with diameters of 40  $\mu\text{m}$ . The decisive feature of the VOAG is that the amount of uranyl-nitrate in the liquid feed is the defining parameter for the amount of uranium in each particle and thus also the final diameter of the particles. The elemental content in the particle is dependent on the choice of the density of the feed solution “ $\rho$ ”, the frequency of the orifice “ $\nu$ ” and the Liquid-Feed-Rate “ $Q$ ”, since

$$N_{Droplet} = N_{particle} = V_{Droplet} * \rho * N_A / M = \frac{Q}{\nu} * \rho * N_A / M \quad (10)$$

“ $N_A$ ” is the Avogadro constant, and “ $M$ ” is the molar mass of the respective element.

After leaving the orifice, the droplets immediately start to shrink due to the evaporation of the volatile part until the droplets are fully evaporated and converted to precursor particles. The air streams serve four functions: (a) disperse the aerosol droplets into a bigger volume, (b) dilute the aerosol

droplets to prevent coagulations, (c) drying of the precursor droplets and (d) transportation throughout the entire system until the final particles are collected from the air streams. The final precursor particle diameter " $D_{Pre}$ " can be expressed as a function of the concentration and the droplet diameter. The volatile part of the solution evaporates and leaves behind the non-soluble part of the aerosol solution. With " $c_{Vol}$ " the volume concentration of the non-volatile solute in the solution:

$$D_{Pre} = c_{Vol}^{1/3} * D_{Droplet} \quad (11)$$

All non-volatile impurities represent an error in the subsequent particle diameter. " $c_{Vol}$ " has to be modified by a correctional term " $I$ " to account for the volumetric concentration of the non-volatile impurities, thus resulting in corrected term for the diameter of the precursor particles " $D_{corr}$ ":

$$D_{corr} = (c_{Vol} + I)^{1/3} D_{Droplet} = \left( \frac{c_{Mass}}{\rho} + I \right)^{1/3} D_{Droplet} \quad (12)$$

The corrected particle diameter is dependent from the " $\rho$ " density of the dried uranium speciation, " $I$ " the correctional term for all the non-volatile impurities in the aerosol solution and from " $c_{Mass}$ " the mass concentration of the aerosol solution. In order to generate particle of approximately 1  $\mu\text{m}$  in diameter, non-volatile concentrations in the area of  $10^{-4}$  g/ml are used.

For small particles such as those a few micrometers in diameter, impurities may represent an issue. For instance, an impurity of 10 ppm (0.001 %) leads to bigger precursor particle diameter in the scale of 2.6%. Therefore, it is important to use high purity reagents for the production of the particles.

### 3.1.3 Droplet to Particle Conversion Kinetics and Thermodynamics

The mechanics and kinetics of droplet-to-particle conversion are very complex. It is advisable to bear in mind that the whole spray pyrolysis process takes place in less than 15s, including (1) aerosol production, (2) evaporation, (3) dehydration, (5) nucleation, (4) first thermal treatment, (5) second thermal treatment, (6) oxidation, (7) sintering, (8) cooling and (9) sampling. Depending on the conditions during generation and conversion, different final particle species can evolve. All references presented in this thesis investigating the dehydration and decomposition of uranyl nitrate hexahydrate do not discuss the conversion of micrometer particles on short time scales, but deal with bulk amounts, i.e. few grams, with treatment durations in the range of hours and days.

The conditions during the early stages of evaporation and decomposition play a crucial role in the transformation process to the final product. The most important parameters are the dwell time, the temperature profile, the precursor / aerosol solution concentration, the ratio of volatile to non-volatile part, morphology and density of the microparticles. Sefiane et al (2003) [53] describe the evaporation of sessile water-ethanol droplets. They investigate the differences in evaporation kinetics of pure substances and mixtures. They state that the observed kinetics differ from the anticipated values which is due to the energy and mass transfer during evaporation. Tonini and Cossali (2013) [54] derived a mathematical model to describe the mass transport in small spherical droplets. According to Tonini and Cossali et al. the energy transfer for infinitely small particles/droplets is almost instant. The main concern with spray pyrolysis processes is the inability to control the particle morphology. According to Kodas et al. 1989 [55] and Pratsinis et al. (2011) [56], solid particle formation is an empirical matter in which certain conditions allow the formation of solid particles. If these criteria are not met less dense, inflated particles are formed, as described by Kingery et al. (1976) [57]. Therefore, the most important step is the control over the precursor conversion. Messing et al. (1993) [58] demonstrated that high solubility and low solution concentrations favor the formation of solid particles. They investigated the formation of ZrO<sub>2</sub>-particles which were produced by spray pyrolysis using a VOAG. Different precursor solutions were used such as ZrOCl<sub>2</sub>, ZrO(NO<sub>3</sub>)<sub>2</sub> or ZrO(OH)Cl. Messing et al. (1993) [58] also stated that the formation of solid particles depends not only on the precursor solution concentration, but also on the precursor species as well.

This observation concurs with the investigations of Kodas et al. (1993) [59] who states that, even though a large number of references exist that depict the conversion process during spray pyrolysis is too complex for, a consistent trend to have emerged so far. The first step is the droplet evaporation from the surface thus changing the air temperature and humidity. The droplet size decreases and the solvent concentration increases with further evaporation. Eventually, nucleation occurs due to super-saturation and crystal growth takes place. For every droplet diameter " $d_{\text{Droplet}}$ ", one can calculate the solution concentration at the droplet surface by solving five differential equations. The following paragraph depicts the derivation of these conclusions, see Xiong and Kodas et al. (1993) [60]. Figure 3 depicts the schematics of particles entrapped inside a laminar air flow during spray pyrolysis. The droplet-to-particle evolution starts at time " $t_0=0$ " with an initial droplet diameter " $d_{\text{Droplet}}$ " and a solution molality " $m_0$ ". The conversion takes place at ambient pressure  $p = 101.325 \text{ kPa}$ , with a relative humidity " $R.H.^0$ " and a flow rate " $Q$ " [l/min]. The reactor vessel has a length " $L$ " and a diameter " $d$ " or radius " $r$ ". For the following consideration, five assumptions have to be made: (1) a laminar flow, (2) the Kelvin effect [b] (see La Mer and Gruen (1952) [61]) can be neglected (particles are  $\gg 0.1 \mu\text{m}$ ), (3) free convection is not important and the heat conduction in the axial direction are negligible compared to the convection, (4) only mass transport due to evaporation and vapor diffusion to the reactor walls at steady state. Effects such as coagulations, diffusion are not important and (5) the temperature of the air stream and the droplet changes along the length of the reactor vessel. However, the temperature remains uniform within the droplets. The aerosol residence time " $dt/dx$ " within in the reaction vessel and the change in droplet diameter " $dd_{\text{Precursor}}/dx$ " can be given as:

$$\frac{dt}{dx} = \frac{0.06\pi r^2}{Q} \left( \frac{T_0}{T} \right) \frac{(1-y_w)}{(1-y_w^0)} \quad (13)$$

$$\frac{dd_{\text{Precursor}}}{dx} = \left( \frac{dd_{\text{Precursor}}}{dt} \right) \left( \frac{dt}{dx} \right) = \frac{4D_v m_1}{\rho_{\text{Droplet}}} (n - n_s) \left( \frac{dt}{dx} \right) \quad (14)$$

With " $t$ " the residence time in [s], " $x$ " the axial reactor axis, " $T$ " is the air temperature, " $y_w$ " the water vapor mole fraction in the air. The last term " $(1-y_w)/(1-y_w^0)$ " is a correctional factor to account for the change in the vapor content as a result of the droplet evaporation.

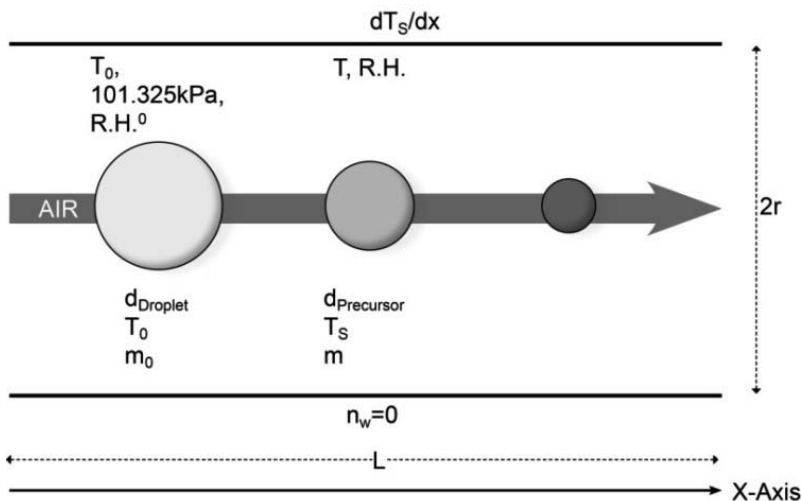


Figure 3: Schematic of spray pyrolysis: evolution of droplet-to-particle conversion in a heated flow reactor.

[b] Kelvin-Effect: The vapor pressure over a bent surface is bigger than over a plane surface.

" $D_v$ " is the vapor diffusion coefficient in air at T, " $m_l$ " is the mass of a water molecule, " $n$ " and " $n_s$ " are the vapor concentrations [#molecules/cm<sup>3</sup>] at the surface at T or T<sub>s</sub> and " $\rho_{\text{droplet}}$ " as the droplet density. The equation for the water vapor concentration accounts for the introduction of water vapor into the air and is subtracted by the term which accounts for the vapor loss due to diffusion to the reactor walls.

$$\frac{dn}{dx} = \left(\frac{dn}{dt}\right) \left(\frac{dt}{dx}\right) = \left(-2\pi d_{\text{precursor}} D_v N_0 (n - n_s) - \frac{2K_m(n-n_w)}{r}\right) \left(\frac{dt}{dx}\right) \quad (15)$$

" $N_0$ " is the droplet number concentration [#droplets cm<sup>-3</sup>], " $n_w$ " is the vapor concentration at the reactor wall and " $K_m$ " is the vapor mass transfer coefficient for a laminar flow. The change in droplet temperature " $T_s$ " along the x-axis is induced by the heat transfer of the surrounding air and by the latent heat " $H_L$ " of the water evaporation.

$$\frac{dT_s}{dx} = \left(\frac{dT_s}{dt}\right) \left(\frac{dt}{dx}\right) = \left(\frac{1}{C_p d_p}\right) \left(3H_L \frac{dd_{\text{precursor}}}{dt} + \frac{6h_s}{\rho_p} (T - T_s)\right) \left(\frac{dt}{dx}\right) \quad (16)$$

" $C_p$ " is the heat capacity of the droplet and " $h_s$ " is the heat transfer coefficient around the droplet. The air temperature is accounted for by the heat transfer. With " $F$ " as the molar flow rate, " $C_{\text{wet air}}$ " as the heat capacity of the wet air and " $h_w$ " as the heat transfer coefficient at the reactor wall.

$$\frac{dT}{dx} = \frac{1}{F C_{\text{wet air}}} \left(-\pi^2 R^2 d_p^2 \text{precursor} N_0 h_s (T - T_s) + 2\pi r h_w (T_w - T)\right) \quad (17)$$

As discussed, before a concentration gradient during evaporation occurs, the highest concentrations can be found at the surface of the precursor droplets. Under the assumption that the change of the droplet diameter " $d_{\text{droplet}}$ " is constant, a radial dependence " $r$ " of the concentration " $c$ " can be derived; before precipitation occurs.

$$c = c_0 \exp\left[\left(\frac{K}{4D_L}\right) \left(\frac{r}{r_{\text{droplet}}}\right)^2\right] \quad (18)$$

$$K = \frac{2D_v m_1 (n_s - n)}{\rho_p} \quad (19)$$

" $c_0$ " is the concentration at the droplet center, " $r_{\text{droplet}}$ " is the droplet radius and " $D_L$ " is the solute diffusion coefficient and the constant " $K$ ". The concentration " $c_s$ " at the droplet surface is the following, while the mean droplet concentration " $c_{\text{mean}}$ " is given by the subsequent equation:

$$c_s = c_0 \exp\left[\left(\frac{K}{4D_L}\right)\right] \quad (20)$$

With  $r = r_{\text{droplet}}$  and  $R_{\text{droplet}} = r_{\text{droplet}}$

$$c_{\text{mean}} = 3c_0 \int_0^1 R_{\text{droplet}}^2 \exp\left[\left(\frac{K}{4D_L}\right) R_{\text{droplet}}^2\right] dR_{\text{droplet}} \quad (21)$$

The solute concentration at the surface can be modified to:

$$c_s = c_{\text{mean}} \frac{\exp\left[\left(\frac{K}{4D_L}\right)\right]}{3 \int_0^1 R_{\text{droplet}}^2 \exp\left[\left(\frac{K}{4D_L}\right) R_{\text{droplet}}^2\right] dR_{\text{droplet}}} \quad (22)$$

For small " $K/4D_L$ " Equation (21) and (22) can be expressed as followed; with " $\rho_s$ " the solute density and " $d_{ps}$ " the equivalent sphere diameter of a dried precursor:

$$c_s = c_{\text{mean}} \left(1 + 0.4 \left(\frac{K}{4D_L}\right)\right) \quad (23)$$

$$c_{\text{mean}} = \left(\frac{d_{ps}}{d_{\text{droplet}}}\right)^3 \rho_s \quad (24)$$

### 3.1.3.1 Particle Formation Mechanism

As previously discussed, the conditions during evaporation and decomposition play a crucial role in the formation of the final product and determine its final properties, such as particle size, shape and external and internal morphology including crystal structure, density variation, phase variances, etc. Stebelkov (2005) [62] describes the characteristics such as size distribution, morphology and elemental and isotopic content of the single particles which are routinely found on swipe and environmental swipes collected by nuclear safeguards inspectors. These particles have an inherent signature due to their generation, release scenario and environmental conditions. However, particles that are synthesized under controlled laboratory conditions have different properties. Pratsinis and Vemury (1996) [63] gives a broad overview the formation processes during spray pyrolysis and how the dynamics of droplet-to-particle conversion affect the final morphology. Even though it does not describe the formation of actinide micro-particles, it provides the basics of droplet evaporation, nucleation and sintering. During the droplet-to-particle conversion, a mass and energy transfer occurs. Hopkins and Reid (2005) [64] investigated the evolution of the evaporation of ethanol-water droplets and their coagulation behavior. They concluded that rapid evaporation of volatile species leads to non-isothermal behavior.

The precursor surface cools down faster and more than the core of the droplet until equilibrium between the energy transfer between particle and surrounding gas phase is reached. Hopkins and Reid (2005) [64] also stated that the particles which were produced with a VOAG showed unsteady evaporation after 1ms of droplet generation. According to Schluender (1964) [65], who studied the evaporation of quasi stationary systems, the temperature and mass change can be calculated, theoretical and experimental data showing a strong correlation. Messing et al. (1993) [58] describe in detail the conversion process and how evaporation and nucleation mechanics affect the final product. They also state that the production rates are limited for particles size smaller than 5  $\mu\text{m}$ . Reuge et al. (2008) [66] [67] investigated the influence of evaporation kinetics, nucleation and sintering processes and came up with a scheme of the formation of micro- and nanometer sized particles and fragments, see Figure 5). Both Messing et al. (1993) [58] and Reuge et al. (2008) [67] state that the exact kinetics and mechanics are not fully understood.

#### Homogenous Precipitation

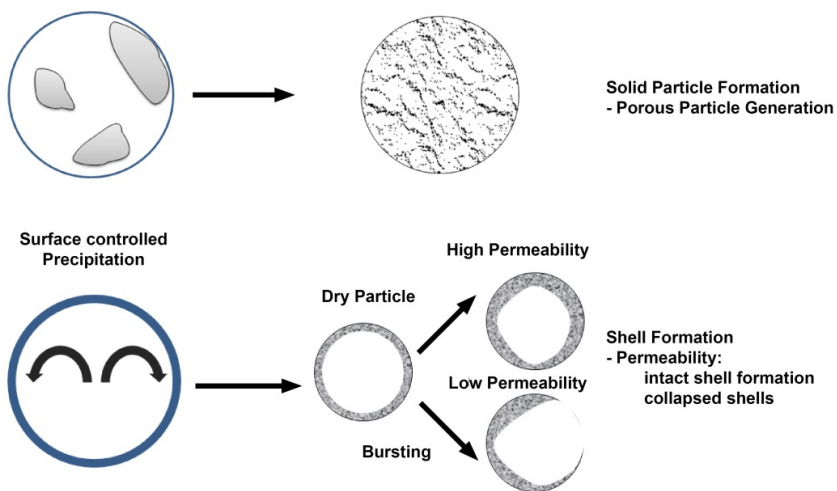
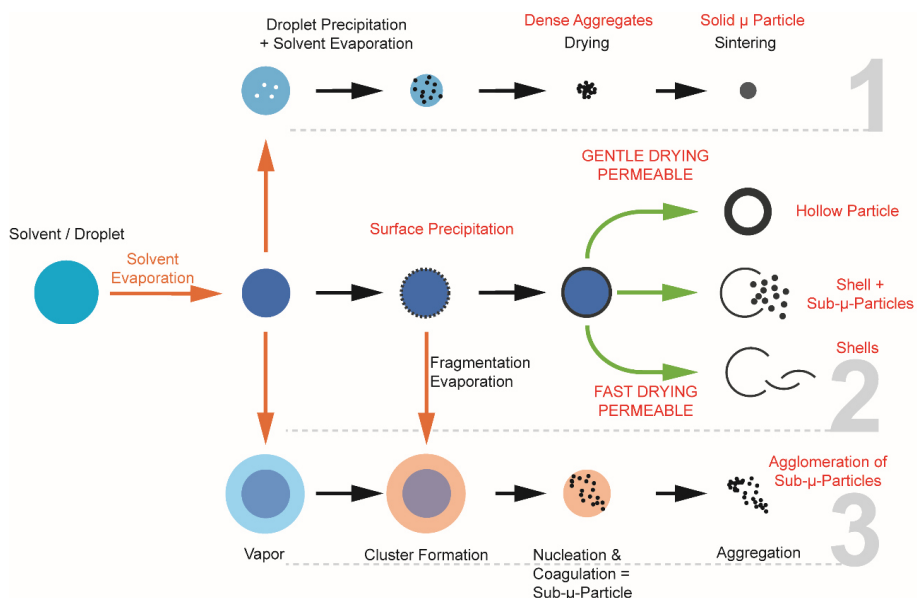


Figure 4: Precipitation schematics for homogenous and surface controlled precipitation.

In theory, five different particle species can be obtained: (1) solid  $\mu$ -particles, (2) hollow, bloated particles, (3) a combination of very thin shells and sub- $\mu$ -particles, (4) thin shells and (5) an aggregation of sub- $\mu$ -particles – see Messing et al. (1993) [58] and Reuge et al. (2008) [66]. They also deliver a comprehensive model for the nucleation process occurring to explain the precipitation system. Basically two different nucleation mechanics can occur: (1) homogenous precipitation or (2) surface controlled precipitation, see Figure 4 and Figure 5. (1) If internal precipitation occurs homogeneously, the overall salt-concentration (including uranyl nitrate plus salt-contamination content) is evenly distributed and precipitation takes place at random points. These randomly occurring “precipitation-islands” have a steady growing interface layer to the surrounding solution. Re-diffusion of uranyl nitrate into the solution takes place [c]. Gaseous pressure of a droplet depends on the surrounding temperature and its salt concentration. The density and porosity of the final particle is determined by the evaporation and denitration speed. According to Reuge et al. (2008) [66] [67] no experimental data exists on this dependence. Surface controlled precipitation is dictated by super-saturation in the outer layer of the droplets which is induced by the external heat field of the furnace. This results in the formation of an outer crust or shell. Depending on the conditions, a permeable, semi-permeable or low-permeable shell is formed.

A permeable crust leads normally to an inflated particle due to the internal evaporation pressure and a semi-permeable to low permeable shell leads to a partial collapse of the particle structure. The formation of a non-permeable crust might even lead to the formation of sub-micron particle debris. It can be concluded that, during the first stage of the spray pyrolysis, two phenomena occur simultaneously: (1) droplet evaporation from the surface, (2) diffusion of the volatile part into the gaseous phase, (3) droplet volume reduction, (4) change in the droplet temperature and (5) diffusion of solute towards the droplet center.



**Figure 5: Schematics of droplet-to-particle morphology evolution during thermolysis, see Messing et al. (1993) [58] and Reuge et al. (2008) [66] [67].**

[c] Re-diffusion is a relatively slow process and can therefore be neglected for fast conversions such as in spray pyrolysis processes.

According to Xiong and Kudas et al. (1993) [68], the diffusion of the volatile part proceeds the fastest and reaches a steady state much earlier before volume reduction due to shrinkage occurs. The mean concentration of the dissolved salt " $c_m$ " increases simultaneously while the droplet volume shrinks. The following equation depicts the mathematical context of the initial concentration " $c_0$ " and droplet diameter " $d_0$ ". The concentration nevertheless is not totally homogenous throughout the evaporation process.

$$c_m = c_0 \left( \frac{d_0}{d} \right)^3 \quad (25)$$

The loss due to solvent evaporation from the surface is bigger than solute diffusion thus creating a higher solute concentration at the droplet surface. The concentration dependency of the droplet radius can be expressed as a partial differential equation; with " $c$ " as the solute concentration and " $r$ " and " $t$ " as the radial components. The following assumptions that at  $t = 0$  the initial concentration " $c_0$ " is equal to  $c$ . And at  $r = 0$  there is no change in concentration. The determination of the concentration as a function of the radius and accounting for droplet shrinkage is a very complex matter. Van der Lijn (1976) [69] gave a solution for the partial differential equation, but the equation is still not very effective because it does not consider diffusivity changes of the solute concentration. The evaporation rate and temperature change of liquid droplets can be expressed as a function droplet size change. The change in droplet size is a function of the temperature " $T$ " and the relative humidity in the initial stage. The evaporation rate of a droplet which is moving with the same velocity as the carrier gas or atmosphere can be expressed as followed as a change of mass in dependence of the temperature: " $dm/dT$ ".

$$\frac{dm}{dt} = \frac{2\pi d_{Droplet} D_v M}{R} \left( \frac{p_{\infty}}{T_{\infty}} - \frac{p_{Surface}}{T_{Surface}} \right) = \frac{2\pi d_{Droplet} D_v M}{R} \left( \frac{\Delta p}{\Delta T} \right) \quad (26)$$

" $p_{\infty}$ " and " $T_{\infty}$ " are the surrounding vapor pressure and temperature of the reaction stage, while the subscript " $_{Surface}$ " refers to the parameter at the droplet surface. " $M$ " is the molecular weight of the gas, " $R$ " is the gas constant and " $d_{Droplet}$ " is the initial droplet diameter. The initial stage of drying and surface evaporation is comparable to the pure liquids. But the vapor pressure of the liquid decreases as a result of the solute in the droplet. The product of the solute mole fraction " $\gamma$ " at the droplet surface and the activity coefficient of the solute " $\chi$ " are equal to the ratio of the vapor pressure " $p_{Sol}$ " and the saturated vapor pressure " $p_{Sat}$ " of the solvent. Under the assumption that the gas phase is ideal and that the activity coefficient for the solute is also ideal  $\gamma = 1$ .

$$\frac{p_{Sol}}{p_{Sat}} = \chi \quad (27)$$

Messing (1993) [58] also states that the activity coefficient can vary significantly. During evaporation the droplet also loses heat. But if the temperature of the surrounding atmosphere is greater than the droplet temperature it gains heat. The temperature change can be expressed as such:

$$4\pi R K \Delta T + \lambda \frac{dm}{dt} = m S \frac{dT_{Surface}}{dt} \quad (28)$$

With " $K$ " as the thermal conductivity, " $\lambda$ " the latent heat of the evaporation of the solvent and " $S$ " the specific heat of the liquid, this equation can be used to describe salt solutions if the specific and latent heat do not differ significantly from the pure solvent. During the evaporation conversion, the droplet temperature increases from ambient temperature to the saturated solution temperature " $T_{Sat}$ ". Xiong and Kudas et al. (1993) [68] state that low evaporation rates, small droplet sizes, low solution concentrations, long residence times favor the formation of solid particles. But they also state that the mechanisms are not still fully understood and that particle formation processes can differ from substance to substance massively. SEM studies performed at FZJ and SGAS-ESL on uranium oxide particles which were produced at FZJ during 2014 underpin the mechanics described by Kudas, Messing and Reuge. Due to operational conditions and technical issues (hardware failures), the final morphology of a single batch of uranium oxide particles significantly varied, which is a good indication of the sensitivity of the production process towards any influences. In conclusion, the final form and phase of



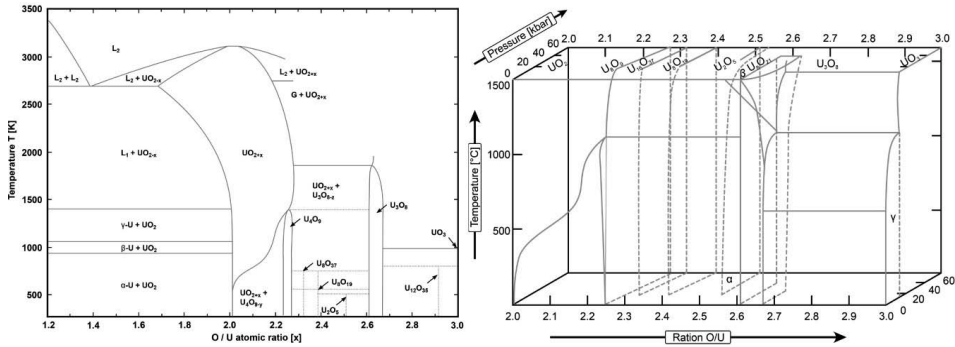


**Figure 7: Left: Phase diagram of the O-U system. Right: U-O phase diagram in O/U ratio range 2.0-3.0 in dependence of the pressure, see Morss et al. (2011) [92].**

According to Dash et al. (1999) [76],  $\text{UO}_3\text{H}_{1.17}$  is a hydrogen insertion of  $\text{UO}_3$  which Lodding et al. (1965) [71] referred to as  $\text{UO}_2(\text{OH})_x$ . Dash et al. (1999) [76] also state that the overlapping processes of the evaporation and the decomposition lead to a surface dominated kinetic control and thus to random nucleation. During thermal treatment, the uranyl nitrate precursors are converted gradually to the corresponding oxides. The calcination of uranium in oxygen containing atmospheres is very well documented. Calcination of uranium in oxygen containing atmospheres takes place at temperature between 450 - 1500°C, see Scott and Harrison (1963) [77]. Depending on the amount of oxygen present and the temperature, different uranium speciation develop. At temperatures above 500 °C, in ambient pressure it is expected to form  $\text{U}_3\text{O}_8$ . At these temperatures and these short dwell times, mixed oxides of uranium (III and IV) are expected, see Peakall et al (1960) [78], Wheeler et al. 1964 [79], Cordfunke (1969) [80], Loopstra (1970) [81] [82], Labroche (2003) [83] and Felker et al. (2008) [84]. According to Hoekstra et al. (1961) [85], the structures of  $\alpha\text{-UO}_3$  and  $\text{U}_3\text{O}_8$  are very similar and indicate a possible solid solution between these compounds. This has not been experimentally confirmed. Grønvold et al (1955) [86] investigated the  $\text{UO}_2 - \text{U}_3\text{O}_8$  region. They indicate that, due to the complexity the different uranium oxides and their phases are very similar and therefore difficult to distinguish. Kulyako et al. (2013) [87] converted UNH solution in the presence of hydrazine hydrate into  $\text{UO}_3$  at 440 °C and into  $\text{U}_3\text{O}_8$  at temperatures of 570 – 800 °C. The phase transition of the uranium-oxygen system is a target of interest for many years: Rand et al. (1978) [88] assessed the thermodynamic data and compiled a phase diagram depicting the dependence of the different uranium phases depending on the O/U ratio. According to Chevalier et al. (2002) [89], Guéneau (2002) [90] and Labroche et al. (2003) [91], the data has to be re-assessed in order to account for the uncertainties of the previously published data. Figure 7 depicts the updated phase diagram of the uranium U-O system which derived from the Katz, Seaborg and Morss et al. (2011) [92]. According to Sweet et al. (2013) [93], the formation routes of  $\text{UO}_3$  and  $\text{UO}_3\text{-H}_2\text{O}$  are not fully characterized, even though they are considered part of the nuclear fuel cycle. Different production routes for the several polymorphic phases of  $\text{UO}_3$  have been investigated. This property does not only apply to  $\text{UO}_3$  but at least to  $\text{U}_3\text{O}_8$  respectively, see Senanayake et al. (2005) [94].

## 3.2 Particle Transport

This chapter describes the basic theory and phenomena associated with the transport, re-entrainment and collection of particles inside idealized air flows. A brief introduction into the mechanism of particle adhesion and detachment/re-entrainments will be given. Adhesion and re-entrainments effects are significantly important for the development of the setup: in particular during (i) particle collection with inertial impactors (see Chapter 5.1) and (ii) for particle transfer techniques (see Chapter 4.1.3). Particle collection via inertial impactors played a crucial role in the sampling regime during this entire project. Inertial impactors offer an easy, fast and cheap way to conveniently collect

sufficient numbers of particles for subsequent analysis. Particles were directly deposited onto Si-wafer substrates or glassy carbon substrates. The adhesion and re-entrainment forces associated with the collection of microparticles will be discussed in the following sub-chapter. Additionally, particle-transfer techniques play an important role in the subsequent particle-handling procedure. Micromanipulation techniques (inside the SEM or under an optical microscope) were extensively used for the preparation of the single microparticles to be assessed by SEM-EDX, SIMS and  $\mu$ -Raman spectroscopy measurements. Micromanipulation with small entities is a challenge. This chapter will give a comprehensive introduction into the basics to better understand the phenomena discuss in this project.

### 3.2.1 Phenomena of Particle Transport Mechanisms

The aerodynamic diameter is a quantity of particles within a surrounding gas. When a particle is accelerated through drag- or gravitational force in the medium, at a certain point in time it reaches equilibrium velocity, i.e. the accelerating force and the friction force are in equilibrium. The equilibrium velocity depends on the shape, the size and the density of the particle. The aerodynamic diameter " $d_A$ " is referenced as an idealized rigid, spherical particle with a density of 1 g/cm<sup>3</sup>. An idealized particle and a real particulate which have the same aerodynamic diameter have the same settling velocity under standard conditions (298.15 K and 101 kPa), but not the same geometric diameters.

$$d_A = d \sqrt{\frac{\rho_{Particle}}{\rho_{Fluid}}} \quad (29)$$

An important property in describing the behavior of gases is the mean free path " $\lambda$ ". It is the mean path of a single particle without any interaction with another particle. The mean path is dependent on the particle density " $n$ " which accounts for the number of particles per volume, the diameter of a molecule " $d$ " (in air under standard conditions,  $d = 3.7 \cdot 10^{-10}$  m; 298.15 K and 100 kPa) and the gross cross section " $\sigma$ ". In equilibrium state derived from the Maxwell velocity distribution " $\lambda$ " can be formulated as:

$$\lambda = \frac{1}{\sqrt{2}n\sigma} \quad (30)$$

The Reynolds number " $Re$ " is another parameter to describe the dynamic properties of the flow and is important in evaluating an inertial impactor system. It is a dimensionless number and describes the ratio of the inertial forces " $\rho v d$ " to the viscous ones " $\eta$ " in steady, laminar flow environments.

$$Re = \frac{\rho v d}{\eta} \quad (31)$$

Here, " $\rho$ " is the characteristic density of the Newtonian fluid, " $v$ " is the characteristic flow rate and " $d$ " is the characteristic length of the object. " $d$ " is also called reference length. With  $\eta = \rho \cdot \vartheta$  equation (2) changes to:

$$Re = \frac{\rho v d}{\eta} = \frac{v d}{\vartheta} \quad (32)$$

" $\vartheta$ " is the kinematic viscosity of the fluid. For smaller Reynolds numbers it can be assumed that the flows are laminar until they reach a certain threshold " $Re_{Thres}$ ". This is the transition point from laminar to turbulent flow:  $Re > Re_{Thres}$ . For small Reynolds number in laminar flows, the viscosity forces are most dominant for turbulent flows. At higher Reynolds numbers, the inertial force dominates the flow behavior.

$$d_A = \sqrt{\frac{9\pi\eta D^3}{4V\rho}} \quad (33)$$

According to Ihtola (2009) [17], the Reynolds number in a laminar flow, such in a pipe, describes an average flow behavior, whereas the Reynolds number calculated for a single particle characterizes the streamlines near the surface. Mc Donald and Fox (1985) [95] state that air flow is considered laminar when " $Re < 2300$ " and turbulent if " $Re > 4000$ ". The region in-between is called a transitional region where the flow characteristics depend upon the surface roughness and various other parameters. To calculate the Reynolds number for a single particle, one can use equation (4) as well. The flow velocity around the particle is important and  $d$  is the parameter for the particle diameter. According

to Ihanola (2009) [17] as well as McDonald and Fox" the flow is considered laminar if  $Re < 1$ . With increasing Re-number the flow becomes more turbulent due to the generation of flow vortices and stalling of the airflow. The settling velocity of an aerosol at low Reynolds numbers can be expressed by the rate at which particles settle in steady air conditions. The settling velocity " $v_{set}$ " is equal to the terminal velocity when only gravitational forces are applied. That means that the drag force " $f_{drag}$ " is equal to the gravity force " $f_{grav}$ ". These forces are dependent on the mass of the settling particle:

$$m_{Particle} = V_{Particle} * \rho_{Particle}.$$

$$F_{Drag} = m_{particle} * g \quad (34)$$

" $g$ " is the gravitational acceleration. The settling velocity can be derived by equation 34 and accounts for the particle diameter " $d$ ", the density " $\rho$ ", the viscosity component " $\eta$ " and the Cunningham slip correction factor (to be described in the following chapter):

$$v_{Set} = \frac{\rho_{Particle} * d_{Particle}^2 * \chi_C}{18\eta} \quad (35)$$

The particle drag force is described by the Stokes equation. Assuming that the particles are very small compared to the mean free path and that the surrounding gas does not interact with the particle movement, the resisting forces depend on the fluid characteristics. Also assuming that the viscous forces dominate and that no walls interact, with a velocity " $v$ " and the fluid velocity at the surface is zero. The Stokes equation for the friction force " $F_{Fric}$ " describes the dependence of " $F_{Fric}$ " of spherical bodies with a defined velocity " $v$ " to their radius " $r$ " involving the dynamic viscosity " $\eta$ " of the fluid:

$$F_{Fric} = 6 * \pi * r * \eta * v \quad (36)$$

Cunningham slip correction factor " $\chi_C$ " is a correction term for the Stokes friction equation. It has to be applied when the particle diameter is in the range of the mean free path " $\lambda$ ". " $A_{1/2/3}$ " are constants which are depending on the fluid and " $d$ " is the particle diameter:

$$\chi_C = 1 + \frac{2\lambda}{d} * \left( A_1 + A_2 + e^{-\frac{A_3 * r}{\lambda}} \right) \quad (37)$$

Inserting the slip correction factor in equation 37 gives:

$$F_{Fric} = 6\pi r \eta v \left( 1 + \frac{\lambda}{r} * \left( A_1 + A_2 + e^{-\frac{A_3 * r}{\lambda}} \right) \right)^{-1} \quad (38)$$

For fluids such as air it can be simplified to:

$$F_{Fric} \approx 6\pi r \eta v \left( 1 + \frac{1.63 * \lambda}{r} \right)^{-1} \quad (39)$$

This is important to derive a formula for the stationary sedimentation velocity " $v_{sed}$ " - for spherical bodies in a fluid:

$$v_{Sed} = \frac{2r^2 g (\rho_{Particle} - \rho_{Fluid})}{9\eta} \quad (40)$$

With: " $g$ " gravitational force, " $r$ " radius of spherical object, " $\rho_{particle}$ " density of the particle, " $\rho_{fluid}$ " density of the fluid and " $\eta$ " the dynamic viscosity.

In order to describe particles in laminar and turbulent flow, a dimensionless number, the so-called Stokes number " $Stk$ " is used. This Stokes number can also be used to deduct the cut-off diameter of an inertial impactor:

$$d_{50} = \sqrt{\frac{9\pi\eta D Stk}{4V\rho_{Particle}\chi_C}} \quad (41)$$

The cut off diameter " $d_{50}$ " of a round one stage impactor can be calculated with equation 41: with " $D$ " the nozzle diameter of the impactor, " $\eta$ " represents the dynamic viscosity of air, " $V$ " is the volume flow rate, " $\chi_C$ " is the Cunningham slip correction factor, " $\rho_{Particle}$ " is the particle density and " $Stk$ " is the Stokes number.

### 3.2.1.1 Adhesion Forces

Adhesion forces are the most important forces that determine the efficiency of an inertial impactor and are necessary to understand its basic functionality. Adhesion forces are also important to describe particle transfer techniques e.g. micromanipulation.

This chapter is designed to give a brief and comprehensive introduction into the basics of particle adhesion. Micrometer-sized particles which are deposited on a flat and even surface can show some interesting behavior and the whole theory is rather complex, for example, when particle deformation needs to be taken into account. To explain the particle adhesion, different mathematical models are used. Each model describes the adhesion process partially and cannot account for all factors involved.

The JKR-model [96] by Johnson, Kendall and Roberts and the DMT-model [97] by Derjaguin, Muller and Toporov are widely used to describe the adhesion and deformation forces induced by van der Waals interaction, neglecting electrostatic forces. According to Mueller et al. (2000) [98], the van der Waals- and electrostatic forces are the dominant adhesion factors. Ideal particles do not deform when placed on a plane surface thus creating only one point of contact with their convex surface. In general the contact area becomes bigger, and short-range adhesion forces govern the finite contact area. Long-range adhesion forces rule the perimeter of the contact area. In these cases, only the elastic deformation of the particles is considered because it predicts the shape of the sphere in contact with the substrate, the pressure distribution within, the contact area and the force necessary to pick up the particle. In 1890, Hertz [99] derived an equation describing the maximal tension or contact pressure " $p_{max}$ " between two elastic bodies, seen from the center of the contact area. If two ideal, rigid bodies with convex surfaces touch there is only one point of contact. Since they are not ideal and those particles have a certain elasticity, the contact area flattens and becomes much bigger. The contact area experiences a force the so called contact pressure. In case of a spherical object and a plane the contact area is elliptically shaped. " $F$ " is the force between the two objects, " $E$ " is the elasticity constant, " $\nu_{1/2}$ " Poisson number for object (1) and (2), " $x_{1/2}$ " is constant for the contact area of bend surfaces and " $k$ " for the bending.

$$F_{Hertz} = \frac{1}{x_1 * x_2} * \sqrt[3]{\frac{3F * E^2 (\sum k)^2}{8\pi^3 (1-\nu^2)^2}} \quad (42)$$

The Van der Waals force is a non-covalent interaction between atoms or molecules. Compared to atomic- or ionic bonds they are weak forces. Electron fluctuations in non-polar molecules or atom cause an instant dipole-momentum  $p_i$  with an electric field  $E_i \sim r^{-3}$ . The first dipole-momentum induces a second dipole-momentum at the second molecule/atom:  $p_j = \alpha E_i$ . Its interaction energy " $W$ " decreases by the sixth degree with the distance of the two interaction objects:  $W = 1/r^6$ . Also quadrupole-dipole interactions occur but they are mostly neglected. The term Van der Waals forces includes three forces: (1) the Keesom force which is the electrostatic force between two permanent dipoles (2) Debye force which is the force between a permanent dipole and an induced dipole and (3) the London dispersion force which describes the force between two interacting, induced dipoles. Bowling (1998) [100] describes that the Van der Waals force is the primary force for particle, smaller than 50  $\mu\text{m}$ , adhesion on surfaces. These Van der Waals forces can differ depending on deformations either on particles or on the surface. According to Bowling (1998) [100] an increase of the Van der Waals forces leads to an increase in the contact area. Particles smaller than 1  $\mu\text{m}$  in diameter can be retained on the surface by forces attaining forces up to 100  $\text{gcm/s}^2$ . The adhesion force on the particle can therefore exceed the gravitational force up to a factor of  $10^6$ .

The electrostatic force can be described by Coulomb's law. It is the interaction force " $F$ " between two point charges " $q_1$ " and " $q_2$ ". " $F$ " is proportional to the arithmetic product of " $q_1$ " and " $q_2$ " and reciprocal proportional to the square of its distance from the spherical center " $r$ " and " $\epsilon_0$ " the electric permittivity of free space.

$$F = \frac{1}{4\pi\epsilon_0} * \frac{q_1 * q_2}{r^2} \quad (43)$$

Particles can either be attracted by electrostatic forces by external charging and/or by charge transfer between two layers (double-layer force). Bowling (1998) [100] described that particles with a diameter of less than 20  $\mu\text{m}$  the double-layer force plays the most dominant part of electrostatic forces.

The JKR-model derived by Johnson, Kendall and Roberts in 1971 [96] is an extension of the Hertz theory and includes the effects of elastic deformation. These adhesion effects and the broadening of the contact area are regarded as surface energy induced. Adhesive forces are restricted to the finite contact area. Adhesive stresses in the non-contact areas are neglected. According to Johnson et al. (1971) [96] the edges of the contact area tensile and the center of the particle is compressible. This compressibility is dependent upon particle properties such as hardness, crystal structure, density and particle diameter.

The equation for the JKR model includes the component for the stored elastic energy, the mechanical potential energy and the surface energy. The following paragraph describes a comprehensive derivation of the JKR model. For this assumption, each particle is under a certain pressure " $p$ " and therefore adheres with a force " $F_A$ " to the surface. The contact radius " $a$ " is significantly smaller than the particle radius " $r$ ". Based on this assumptions one can derive the equations for the contact radius " $a$ ", the area of the contact " $A$ " and the pressure " $p$ " which bears on the particle - the so-called "Hertz Pressure". " $K$ " is the elastic modulus or Young's modulus it measures the force needed to deform a solid object. Equation 44 and 45 show the dependence of the contact radius " $a$ " and contact area " $A$ " - with the variables " $m_1$ " for the particle and " $m_2$ " for the flat, solid substrate.

$$a = \left[ \frac{3F_A R}{4K} \right]^{\frac{1}{3}} \quad (44)$$

$$A = \pi a^2 = \pi \left[ \frac{3F_A R}{4K} \right]^{\frac{2}{3}} \quad (45)$$

The corresponding maximum pressure " $p_{max}$ " and the mean pressure " $p_m$ " can be derived with an elastic infinite half-space analysis:

$$p = \frac{3F_A}{2\pi a^2} = \frac{3}{2} p_m \left[ \frac{6F_A D K}{\pi^3 R^2} \right]^{\frac{1}{3}} \quad (46)$$

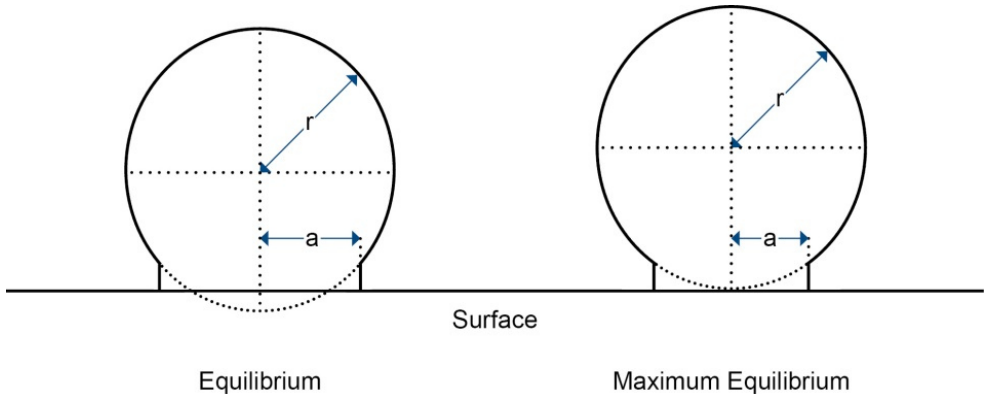
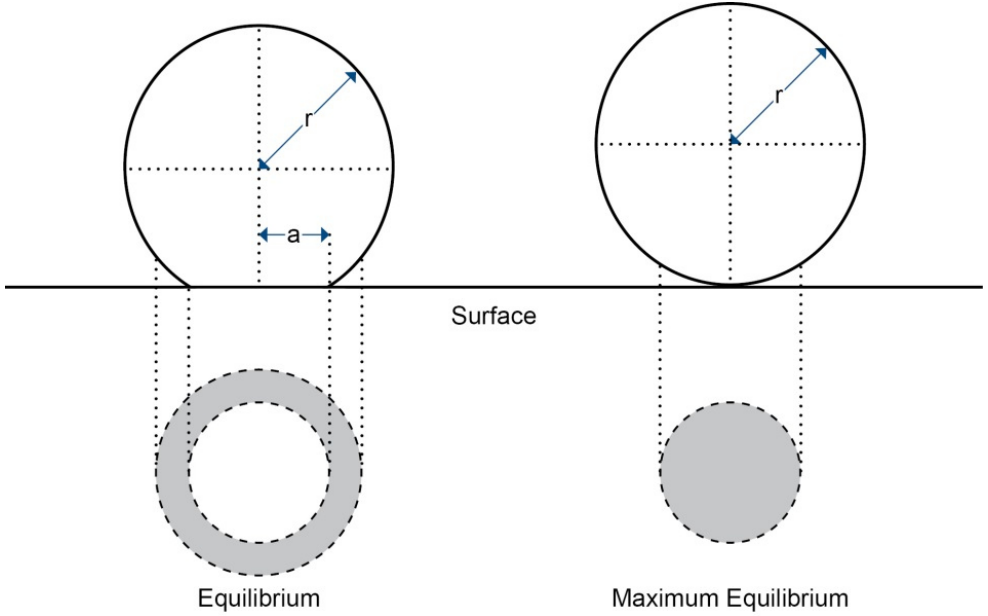


Figure 8: JKR model depicting particle deformation in contact area.



**Figure 9: DMT-model depicting adhesion forces with the affected zones and contact area (marked grey).**

With the Poisson ratio “ $\nu$ ”, the elastic modulus can be expressed as:

$$K = \left[ \frac{1-\nu_{m1}^2}{K_{(m1)}} + \frac{1-\nu_{m2}^2}{K_{(m2)}} \right]^{-1} \quad (47)$$

Based on the JKR-model, the area of contact can be easily derived from the contact radius.

$$a = \left[ \frac{3R}{4K} \left( F_A + 3\pi R W_a + (6\pi R W_a F_A + (3\pi R W_a)^2)^{\frac{1}{2}} \right)^{\frac{1}{3}} \right] \quad (48)$$

“ $W_a$ ” is the thermodynamic work of adhesion per unit area. The JKR-model also gives an equation for the pull-off force “ $F_{POF}^{JKR}$ ” which is proportional to the particle radius “ $r$ ”.

$$F_{POF}^{JKR} = \frac{3}{2} \pi r W_a \quad (49)$$

The DMT model uses a different approach which accounts for the Van der Waals interaction outside the elastic contact area. For the contact area itself, a Hertzian stress profile is assumed. In 1975, Derjaguin and Muller [97] demonstrated that the adhesion force between two convex surfaces depends on their curvature and their relative orientation towards each other. The total force of adhesion is the difference between the molecular attraction and elastic repulsion. According to the DMT-model, the contact pressure acts also in the vicinity of the contact area due to molecular attraction; this area is marked grey in Figure 9. This molecular attraction causes a flattening of the particle until it reaches equilibrium with the elastic repulsion force. The maximum adhesion force on the particle is described in equation 50. This force is determined by the particle diameter “ $d$ ” and the surface energy of the adhesion “ $\gamma$ ”. It is also the force needed to detach the particle.

$$F_A^{DMT} = \pi \gamma d \quad (50)$$

The pull-off force for the DMT-model is given by:

$$F_{POF}^{DMT} = 2\pi r W_a \quad (51)$$

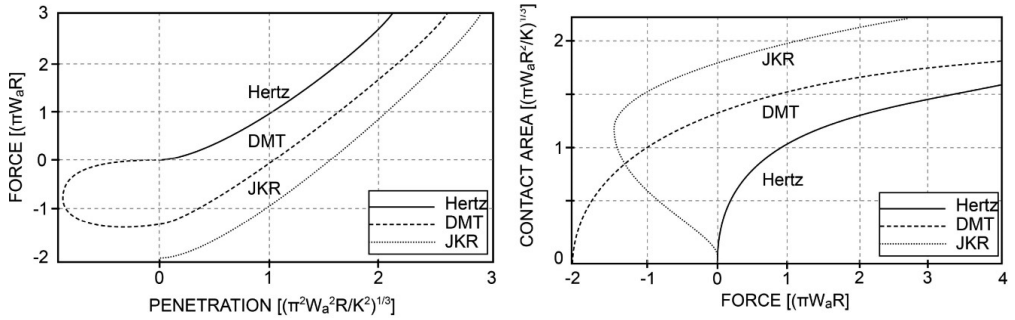


**Figure 10: Contact relations for the Hertz-, DMT- and JKR-models.**

The applicability of the Hertz-, DMT- and JKR model is restricted to specific types of interactions between surfaces. JKR- and DMT model lack a comprehensive description on how to deal with border areas. The JKR model applies to softer or compliant solids. These particles have a low elastic modulus, large radius of curvature and large adhesion energy or surface energy. The DMT model on the other hand is used to describe hard or stiffer solids. These particles generally have small curvature radius and a much weaker surface energy.

### 3.2.1.2 Particle Detachment

The following paragraph briefly describes the most common interaction forces that lead to particle detachment. Particle detachment processes can occur during particle collection inside an inertial impactor. These re-entrainment processes are the main reason for a significant loss of collection yield. The main reasons for this are excessive air flows which lead to a significant re-entrainment process. Detachment and re-entrainment processes are also needed to understand the basics of micromanipulation and of other particle transfer techniques. The most difficult part of micromanipulation is the deposition of the microparticle onto the new substrate.

The preceding chapters explain the adhesion-forces that act on a sphere that is in a stationary equilibrium on the surface. " $F_A$ " is the surface force, " $F_T$ " which is directed tangentially to the surface and the external normal force to surface " $F_N$ ". The gravitational force " $F_G$ " is much lower for micrometer sized particles because the adhesion force surpasses it, sometimes even up to a factor of  $10^6$ . According to Phares et al. (2000) [101], the particle size is a very important property when it comes to particle detachment or re-entrainment. Corn et al. (1965) [102] and Kousaka et al. (1980) [103] investigated the re-entrainment of small particles by air from flat surfaces. They found out that the predominant detachment mechanisms were rolling motions caused by shear stresses and due to particle-to-particle collisions. An insignificantly low number of particles was detached due to lift-offs. The correlation of air velocity and particle diameter is very important. The relation between " $F_G$ ", adhesion force " $F_A$ ", external tangential to surface " $F_T$ " and external force normal to surface " $F_N$ " and contact area radius " $a$ " is given in equation 52.

$$\tau F_T + a F_N > a F_A \quad (52)$$

The force required to detach a particle can be expressed by the following equation which is derived from equation 52 and auxiliary components which in turn are derived from the JKR-model (49) and the Stoke equation (36).

$$\frac{d}{4} \pi \tau d^3 + 1.15 a \tau d^3 > \frac{3}{4} a \pi \eta d \quad (53)$$

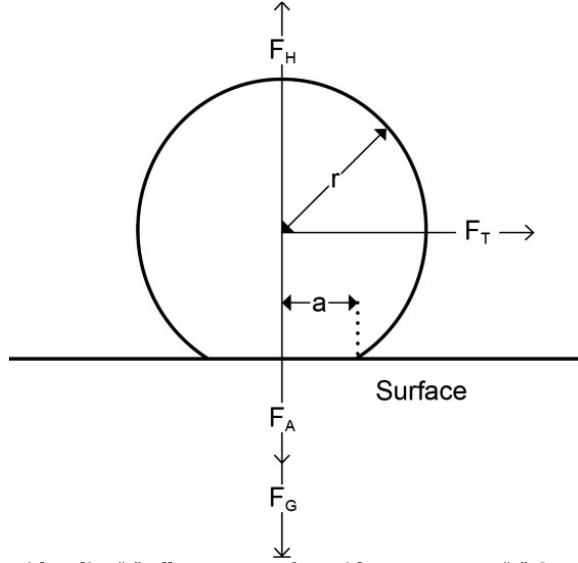


**Figure 11: Particle with radius “r” adherent on surface with a contact area “a”. Several forces act on the particle including: gravitational force “ $F_G$ ”, adhesion force “ $F_A$ ”, external tangential to surface “ $F_T$ ” and external force normal to surface “ $F_N$ ”.**

With “ $\eta$ ” the dynamic viscosity of the gas and „ $d$ ” the particle diameter. The shear stress “ $\tau$ ” to detach a particle is expressed:

$$\tau > \frac{\frac{3}{4}a\pi\eta}{\frac{3}{4}\pi d^2 + 1.15ad^2} \quad (54)$$

Smedley et al. (1999) [104] state the flow close to a stagnation point of an impinging jet can be described by laminar boundary layer theory. The maximum shear stress “ $\tau_{max}$ ” is within a radial distance which is correlated to the jet height above the surface “ $H$ ”. “ $\tau_{max}$ ” can be expressed as a function of the Reynolds number “ $Re$ ”, the nozzle-to-surface distance “ $S$ ”, the nozzle diameter “ $W$ ”, the gas density at the nozzle exit “ $\rho_g$ ”, the average flow velocity at nozzle exit “ $v$ ” [d] and a correctional term for the gas compressibility “ $f(M)$ ” which is a function of the Mach number “ $M$ ”; see equation 55 and 56.

$$\tau_{max} = \frac{44.6(\rho_g v^2)(1+f(M))}{Re^2 \left(\frac{S}{W}\right)^2} \quad (55)$$

The empirical function for the Mach number for air jets was derived by and Phares et al. (2000) [105]:

$$f(M) = 0.66M - 3.2M^2 + 3.9M^3 \quad (56)$$

Phares et al. (2000) [101] state that the detachment mechanics just apply to the area around the impinging point up to “ $r_{max}$ ”. The transition to turbulent boundary layer conditions at radial distances beyond “ $r_{max}$ ” is the beginning of the wall region where the detachment model does not work. Particle entrainment can occur with the amplitude of the fluctuations of these shear stresses. Detachment of particles in the size range of a few micrometers is more difficult than detaching larger particles. The particle size is actually more important as the particle material for the detachment process. Also the particle substrate interaction plays an important role. All depicted detachment models share a common characteristic: they are based on the assumption that a force balance in a viscous sub-layer of the plane and all models predict a sudden release of particles when a certain threshold in the flow velocity is

[d] The product of the gas density and the average flow density is called the dynamic pressure: “ $p_{dyn} = \rho g \cdot v$ ”

exceeded. A derivation of the detachment due to shear stresses is the detachment by tangential drag forces, which can be considered as a special case of the previously mentioned case. Particles that are impacted on the surface are not exposed to the constant air flow field; therefore the Reynolds equation cannot be applied. The flow speed varies dramatically and is dependent on the distance to the surface and the location relative to the air-flow. Gaseous air flows close to the surface have to be considered viscous. The Reynolds number plays an important role in describing the particle behavior in a gaseous flow. For low Reynolds numbers the tangential force can equal the Stoke or Newton drag forces. According to Leighton et al. (1985) [106] the tangential drag forces can be calculated by the Stoke drag force; with “ $\tau$ ” as the shear stress. This equation can be applied under the assumption that the gaseous flow is uniform:

$$F = \frac{3}{2}\pi\tau d^2 \quad (57)$$

Leighton et al. (1985) [106] also investigated the forces necessary to lift a particle off a surface. Particles which are deposited on a surface are exposed to a certain amount of lift forces even when the fluid inertia can be considered negligible.

$$F = 0.576(\tau d^2) \left(\frac{\tau d^2}{v\eta}\right) \quad (58)$$

With “ $v$ ” the flow speed at the center plane of the particle, “ $\eta$ ” the dynamic viscosity of the gas and “ $d$ ” is the particle diameter. Equation 58 can be simplified by assuming a linear velocity profile over the particle height:

$$F = 1.15\tau d^3 \quad (59)$$

### 3.2.2 Particle Collection – Sampling, Cut-Off Diameter

Inertial impaction proved to be the most efficient method to collect microparticles from the air stream. IAEA uses a self-developed one-stage design to collect microparticles for (non)-destructive particle analysis, see Figure 12. Particles were collected within a few minutes yielding in a sufficient number of microparticles. All particles were collected directly onto the substrate: in the beginning, when the installation was not fully adjusted due to conversion work, the collection yield was not sufficient enough to perform subsequent analysis. Therefore, some substrates were covered with an adhesive organic layer, either PIB-nonane or Apiezon-L grease. Later on, with a fully adjusted system, no adhesive layers on the substrate surface were needed obtain a sufficient collection yield.

According to the studies of Marple and Willeke (1976) [107] and Juric and Wang (1993) [108], there a few key properties for round, one stage inertial impactors that ensure an efficient sampling. They recommend an “ $S/W$ ” ratio of 1.0. “ $S$ ” is the jet to substrate distance and “ $W$ ” is the nozzle diameter; another feature is the “ $T/W$ ” ratio. “ $T$ ” is the nozzle throat length. Particles entering the nozzle adapt their speed according to the nozzle diameter and length. A critical component in the assessment of the impactor efficiency is the Reynolds number “ $Re$ ” and the so called cut-off diameter. The collection efficiency curve is a very important characteristic feature of an impactor.

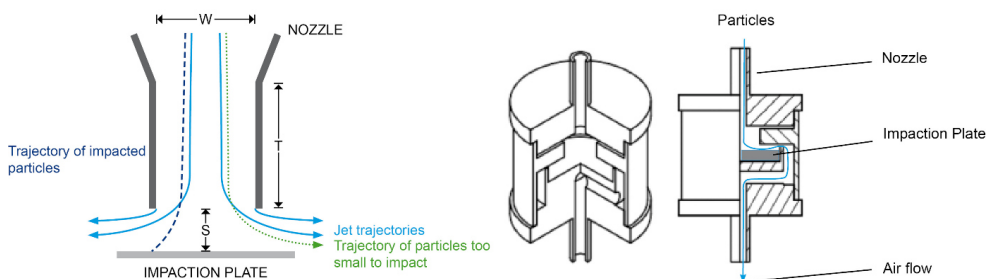


**Figure 12: Left: Jet trajectories for an inertial impactor (see Marple et al. (1976) [107]), Right: Schematics of inertial impactor used at SGAS-ESL.**

It depicts the percentage of particles that are impacted onto the impaction stage, depending on their aerodynamic diameter / respectively by their inertia. An ideal efficiency curve has a very distinct turning point thus a “sharp” cut-off diameter; in theory, every particle with a diameter smaller than the cut-off diameter is not impacted, see Figure 13.

In reality, undersized particles are collected to a certain degree and oversized particles are not - Figure 13 depicts the ideal and the actual collection efficiency curve. The cut-off diameter “ $d_{50}$ ” is defined as the threshold for the particle size where the collection efficiency is 50 % and it represents the mid-way point of the collection efficiency curve. Factors such as the nozzle diameter, the air flow rate, re-entrainment effects, interstage losses and the “S/W” and “T/W” ratios affect the actual impactor efficiency. One way to increase the collection efficiency is to use a so-called cascade impactor, which consists of multiple stages consecutively mounted. That means a small sub-micrometer cut-off diameter requires a small nozzle and high air flow velocities. According to Ensor (2011) [109], the limitations for inertial impactors cut-off diameters are in the range of 0.2 - 0.3  $\mu\text{m}$ . With the usage of micro orifices these limitations can be extended down to 0.05 - 0.06  $\mu\text{m}$ .

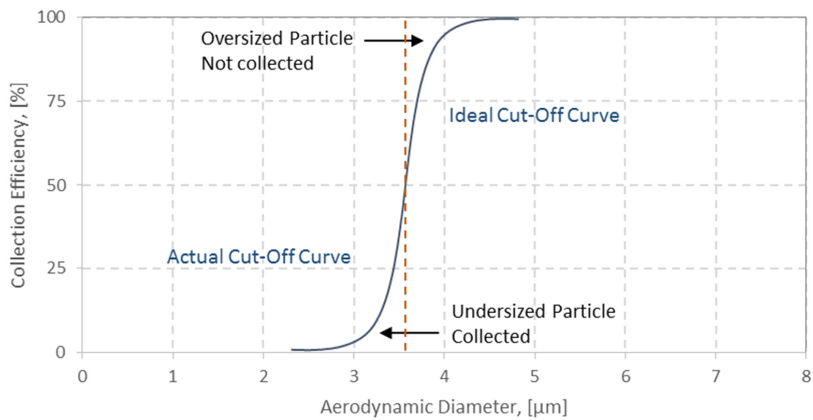


**Figure 13: Determination of the cut-off diameter by plotting the collection efficiency curve.**

## 3.3 Micro-Analytical Techniques

### 3.3.1 Scanning Electron Microscopy (SEM)

SEM instruments were used extensively in this work. They were used to assess the geometry, the size distribution, the morphology and the elemental composition of bulk quantities and of single microparticles. All uranium microparticles were directly assessed inside the SEM. No further particle preparation was performed. Even at  $Acv > 15$  keV, no particle movements could be observed. Particles were routinely investigated with SEM instruments using Tungsten and LaB<sub>6</sub> electron guns. Elemental composition was verified using energy dispersive X-Ray spectrometers (EDX) detectors made by Oxford Instruments and their native software. SE and BSE images were taken manually or in an automated sequence with or without elemental verification via EDX analysis. Large areal scans were derived from single SE/BSE images which were belatedly composed together with image acquisition software (FIJI and IMAGEJ).

Scanning Electron Microscopy (SEM) is the preferred tool for imaging objects at in a wide range of magnifications (10 - 10.000 x). In SEM, the area of interest is irradiated with a focused electron beam. The area of interest can either be rastered or a single point can be investigated using a static signal. The interaction of the electron beam with the sample causes various interactions with the emission of secondary electrons, backscatter electrons, characteristic x-rays and other photons of various energies. The volume which interacts with the electron beam is called "interaction volume" and it can be used to determine characteristics like surface topography, crystallography, elemental composition, size, geometry, density, etc. Another important feature of SEM imaging is the large depth of field in comparison to a normal optical microscope, providing more information about the specimen. A SEM instrument uses a beam of high energy electrons focused at the specimen surface to generate an artificial effigy of specimen. This "image" is not an actual image. It is a visual representation of the sequential point by point (rastering) illumination of the specimen surface with the electron beam probe. The strength of the signal generated from each point varies due to topographical or compositional reasons.

A standard scanning electron microscope (SEM) consists of six main components: (1) electron gun (2) a column through which the electron beam travels and which houses a series of lenses in order to shape and focus the electron beam – the so-called "electron column", (4) a specimen chamber, (5) detectors and (6) a processing / operating unit. All of the equipment from (1) – (5) is kept under vacuum and a schematic layout is depicted in Figure 14. Electron guns generate a beam of electrons which is subsequently used to investigate the specimen. During this project, only thermoionic electron guns made from Tungsten and LaB<sub>6</sub> were used. After leaving the gun, the electron beam passes into the so-called electron column which consists of a variety of lenses and coils. A basic setup for an electron column consists of a condenser lens, scanning coils and an objective lens. The condenser lens controls the electron beam intensity. The scanning coils can deflect the electron beam in both horizontal and vertical direction. This is applied when the sample surface is rastered with an electron beam hence the name "scanning electron microscope". The objective lens focuses the electron beam on the specimen and can de-magnify it. When the electron beam interacts with matter, the electrons dissipate their kinetic energy into the target by elastic or inelastic scattering or absorption and a bulb like interaction volume is created. As a consequence of this interaction, electrons and electromagnetic radiation is emitted. This can be detected and be processed and pictorialized. Two types of X-rays are emitted: (1) Bremsstrahlung or continuum or background X-rays and (2) characteristic X-rays. Characteristic X-Rays, continuous X-Rays and fluorescent X-Rays are emitted from deeper within the interaction volume. The size of this interaction volume is dependent on the accelerating voltage, on the atomic number of the target and its density. Depending on these parameters the interaction volume varies significantly.

## SEM LAYOUT

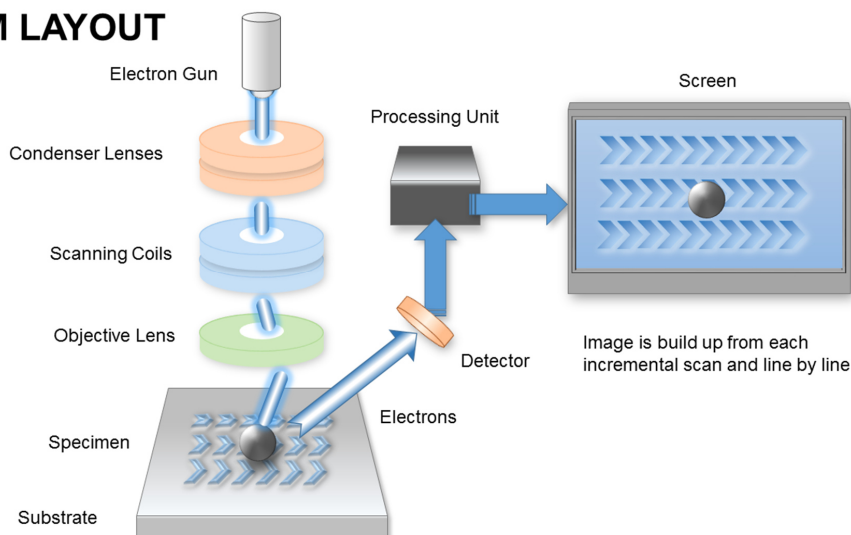


**Figure 14: Layout of a Scanning Electron Microscope.**

The primary electron beam generates secondary electrons such as Auger electrons close to the surface (about  $10 \text{ \AA}$  from the surface). Low energy ( $< 50 \text{ eV}$ ) electrons are generated from a layer-depth of up to  $10 \text{ nm}$ . These electrons can be detected by an Everhart-Thornley detector which is basically a scintillator tube and a photomultiplier. These secondary electrons (SE) show the topographical contrast of the surface because the detected intensity is dependent on the angle of the incident beam and the sample surface. Electrons that originate from deeper within the sample are of higher energy and are called backscattered electrons (BSE). The intensity of those BSE is comparatively speaking poorer than those of SE. But BSE are common used in SEM studies. The brightness of a backscattered image increases with its atomic number. SEM analysis requires a conducting surface, which is why uranium particle are deposited directly onto Si-wafer chips or graphite disks, no additional conductive coating had to be applied to the particles. There are various ways to transfer multiple or bulk materials of microparticles onto an appropriate substrate. For instance, Donohue et al. (2008) [10] used a conductive tape attached to an SEM-stub or particles were directly collected onto Nuclepore filters, see Erdman et al. (2000) [40]. Most commonly at SGAS-ESL particles are transferred via inertial impaction, see Boulyga et al. (2015) [110]. Energy Dispersive X-ray Spectroscopy (EDX) is a qualitative and quantitative X-ray micro-analytical technique that is coupled with a SEM hence SEM-EDX. SEM-EDX can provide information about the elemental composition and works for elements with an atomic number " $Z$ "  $Z > 3$ . The X-rays are detected by an energy dispersive detector: thus a spectrum can be derived which is an intensity distribution over the energy scale. The characteristic X-rays allow the elements to be identified while the intensities of these characteristic X-rays may allow quantification. The spatial resolution of the EDX analysis is determined by the size of the interaction volume in other words by the accelerating voltage, the atomic number of the sample and the density of the sample. For EDX the depth resolution is just a few microns. For instance, a Monte Carlo simulation performed with DTSA-II on  $1.0 \text{ \mu m}$   $\text{U}_3\text{O}_8$  particle (with a homogenous density of  $8.3 \text{ g/cm}^3$ ,  $\text{AcV} = 25 \text{ keV}$ ) revealed a depth resolution of about  $0.4 \text{ \mu m}$ . The detection limit of EDX analysis is substantially dependent on the sample composition and density, but it generally in the order of  $0.1$   $0.5 \text{ wt\%}$ . It therefore lacks the sensitivity used in ultra-trace analysis, see Chapter 5.2.3.3. SEM-EDX was used extensively to verify the existence of uranium in microparticles. A combination of SEM-EDX is routinely used for the elemental verification of micro entities in nuclear safeguards related research, see Donohue et al. (2008) [10], Kips et al. (2007-2011) [29] [30] [31], Pointurier et al. (2010) [135] and many more.

### 3.3.2 Secondary Ionization Mass Spectrometry (SIMS)

Secondary Ionization Mass Spectrometry (SIMS) is a very effective technique to determine isotopic abundances of bulk material and single micrometer sized particulates. In particular, high resolution SIMS machines with large sector fields are able to distinguish minor and major isotopic abundance more precisely than ever before. All elements and compounds that are solid and stable under high vacuum conditions can be measured. SIMS is used for various applications, e.g. geochemistry, material and life sciences, microelectronics and nuclear forensics to name but a few.

In principle, a SIMS uses a focused ion beam to bombard the sample. This primary ion beam dissipated its energy on impact. Two things occur: (1) a thin surface layer of about 0.1 - 2.0 nm is ionized and (2) sputtering occurs. The primary beam interaction leads to the formation of secondary ions. The secondary ions are positively or negatively charged, depending on polarity of the primary ion beam. Just a small fraction of the secondary ions is extracted and further accelerated and transferred to a magnetic analyzer. The complete mechanism of secondary ionization is not yet fully understood giving rise to a variety of phenomena when the elemental and isotopic composition or properties of the sample is studied.

SIMS methodologies offer a large variety of measurement procedures such as elemental and isotopic analysis. Bulk material or single particulates can be measured as well. SIMS is able to perform depth profiling, ion imaging and even ion tomography of three dimensional objects (the lateral resolution generally is between 5.0 - 50.0  $\mu\text{m}$ ). The basic schematics of the LG-SIMS are depicted in Figure 15: including the duoplasmatron, the primary column and the analyzer and detection system - taken from the Cameca users guide, courtesy of Cameca.

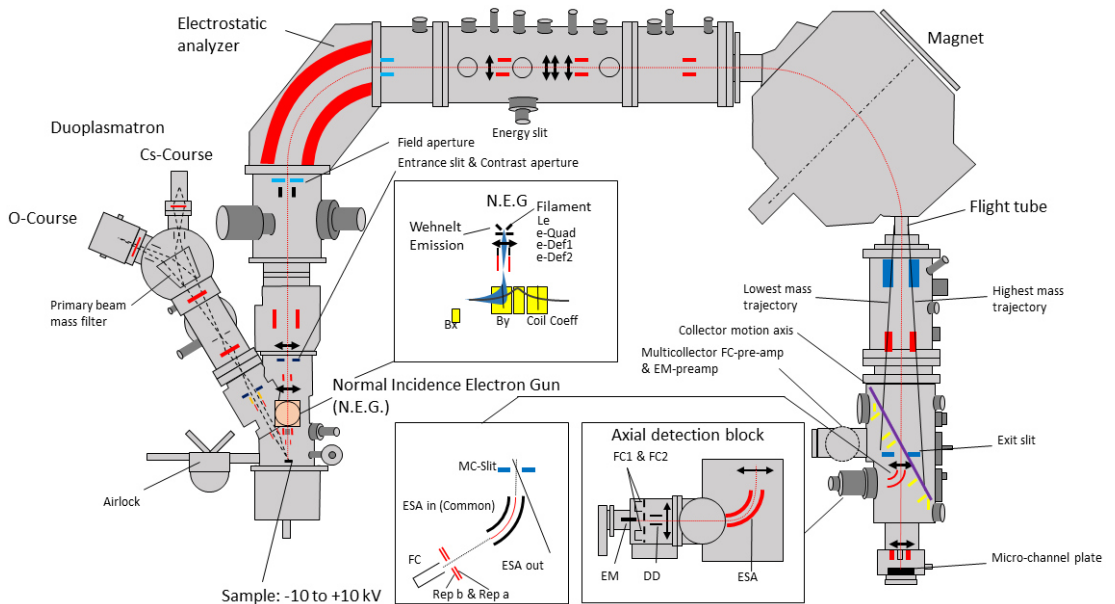


Figure 15: Schematics of Cameca's IMF1280 LG-SIMS, courtesy of CAMECA.

The IAEA operates a CAMECA 1280 LG-SIMS strictly for Nuclear Safeguards applications. It is used specifically for (1) the identification and detection of single micrometer sized particles embedded into different matrixes (“Needle in the haystack”) and (2) the measurement of selected individual particles to assess their uranium isotopic ratios. Those particles originate predominantly from the vicinity of nuclear facilities (“environment”) and they are normally collected with a piece of cotton cloth – called swipes – by nuclear safeguards inspectors. They have an inherent signature which is correlated to the processes performed at the nuclear installation. For identification, large area mappings can be performed up to 500 x 500  $\mu\text{m}^2$ . IAEA nuclear safeguards inspectors routinely collect around 900 environmental samples from the nuclear facilities world-wide and around one third are analyzed using SIMS. Cameca’s IMS 1280 (HR) is the successor of the IMS 1270 and an upgraded, up-scaled version of the IMS 4 – IMS 7f. The introduction of the CAMECA IMS 1280 was an important step forward in SIMS technology to the Nuclear Safeguards Community, see Ranebo (2009) [18] [19]. Its increased mass resolution power leads to an increase in sensitivity by up to a factor of ten. Multicollector usage enables the user to save time in comparison to peak-jump mode. The IMS 1280 (HR) is equipped with an array of five moveable detectors (either Faraday Cups or Electron multipliers). Most IMS 1280 (HR) devices which are dedicated for nuclear safeguards applications feature a multicollector system including five electron multipliers. The IMS 1280 (HR) offers the ability to measure all uranium isotopes simultaneously. SIMS is the established technique of choice at SGAS-ESL for uranium isotopic detection, identification and measurements due to its high sensitivity, large field mapping capabilities and performing in-situ microanalysis. The IMS 1280 (HR) offers several features such as two ion sources (Cs and O) and the duoplasmatron ion source can provide positive and negative primary ions. Depending on the primary beam polarity, the accelerating voltage can charge the sample positively or negatively. The primary beam can be shaped like Gaussian distribution through demagnification of the ion source or the beam can be shaped with an aperture. The secondary ions are extracted via an immersion lens. The double focusing spectrometer is stigmatic. The name large geometry SIMS is derived by the large magnet radius: 585 mm. This increased radius results in a higher mass resolution thus an increased mass dispersion.

Two important correction factors are to be considered when performing SIMS analysis: (1) the fractionation mass bias and (2) the hydride correction: (1) the fractionation mass bias effect or mass bias is derived from the differential ion transmission during the ionization process until the detection. According to Habfast (1998) [111], the measured isotopic ratio changes slightly over the time. A CRM has a certified value on the isotopic ratios. The discrepancy between the real value and the measured value is considered the mass bias effect. The real value can be derived using the fractionation law that accounts for the degree of depletion as a function of time and sample evaporation. (2) The hydride correction accounts for the conflicting emergence of interfering hydride-ion-species. For ions with a mass/charge ration “ $m/Q$ ” of  $m/Q(236)$  the  $^{235}\text{UH}^+$  ion can significantly interfere with the  $^{236}\text{U}^+$  ions. In order to overcome this issue CRM’s are used as a calibration to evaluate a correctional factor – the so-called hydride correction – to account for this interference.

### 3.3.2.1 Fundamentals of SIMS

The following section gives an introduction to secondary ionization mass spectrometry, which was derived from the sub-chapter “Secondary Ion Mass Spectrometry” by Sangely et al. (2014) [112] taken from the book “Sector Field Mass Spectrometry for Elemental and Isotopic Analysis – New Developments in Mass Spectrometry” edited by Prohaska et al. (2014): A primary ion beam transfers parts of its energy onto the surface of the sample resulting in a change of impulse both for the projectile and the target, whereas the target atom is recoiled into the sample lattice and the projectile is recoiled. These recoiled particles become themselves second generation projectiles. This subsequently leads to a cascade of recoiled particles and fragments until the transferred energy falls below a certain threshold value. The accepted basic principle for the sputtering process is based to a series of subsequent collisions, referred to as “collision cascade”. Sputtering occurs when the transferred energy is higher than the surface

binding energy of the target. In general, the origin of the sputtered fragments is from the first very first nm of the surface. The sputter yield “ $S$ ” is defined as the number of particles removed from the sample per impacting primary ion. Depending on the sample property such as the atomic number “ $Z$ ”, binding energy, crystal orientation and the properties of the primary ion beam such as mass, energy, incident angle the sputter yield ranges between  $5 \leq S \leq 25$ . The total sputter yield in multicomponent materials equals to the sum of the partial sputter yields of the constituent atoms. Different phenomena can occur, for example, the ratio of two different species does not equal the concentration ratio found on the active surface. In fact, the near surface region tends to be depleted in elements which have a higher sputter yield and is enriched with elements that have a lower sputter yield, and this phenomenon is called preferential sputtering phenomena. The interaction of sputtered particles originating from the upper surface layer with underneath lying particle can be traced down a few nm into the sample; this interaction volume is called “*damage volume*”. Inside this damage volume the structure and composition of the sample is strongly altered due to the implantation of primary ions and the transport of atoms from one layer to another. The depth of the damage volume depends on the sample properties ( $Z$ , density, crystal orientation) and the primary beam properties (mass, energy, incident angle). The majority of the sputtered material consists of neutral atoms. In order to describe the formation of secondary ions “ $W_{Sec.Ions}$ ” equation 60 is used:

$$W_{Sec.Ions} = \frac{\text{Number of ions formed}}{\text{Total number of atoms of the same species}} \quad (60)$$

The ionization probability is defined as the ratio between the number of ions being formed and the total number of atoms (molecules) of the same species initially present. The ionization probability is generally between a few tenths of % to a few %. The ionization rate is a critical SIMS parameter because it is correlates directly to its sensitivity. A positive ion formation rate tends to increase with the ionization potential and the negative ion formation rate tends to increase with the electron affinity. The use of oxygen as a primary ion source enhances the positive ion formation and cesium sources tend to favor formation of negative ions. Ionization efficiency depends on the chemical environment of the sputtered species. Oxygen bombardment leads to the implantation of oxygen ions into the surface layer and to the formation of metal-oxygen bonds. These metal-oxide bounds break during the sputtering and the oxygen reduces, captures one electron due to its high electron affinity while the sample constituent is positively charged.

When the bombardment of the sample starts, the concentration of implanted ions increases dramatically: from zero to a saturation level. The saturation level is defined as the number of newly implanted primary ions equal to the number of primary ions leaving the damage volume due to recoil- and sputtering effects. Due to preferential sputtering, the ratio between sample elemental and isotopic composition changes over the time to a point of maximum alteration. This point is reached once the active surface reaches a depth that is exceeded by the damage volume. This time span is called transition or pre-equilibrium state. It is characterized by a short run sputter yield, ionization rate and sample surface composition that compromises the use of common calibration methods. There are two different methodologies to compensate for this limitation: (1) static SIMS and (2) dynamic SIMS:

- (1) Static SIMS refers to a methodology where the primary ion fluence “ $\Phi$ ” (number of particle per area) is kept below a certain threshold to ensure that the emitted ions do not originate from a former sputter area and are therefore not affected by this event. The active surface is therefore very thin and is just composed out of the first outer surface layers. Static SIMS is a technique strictly limited for surface analysis and is often used in time of flight (ToF) analyzers.
- (2) In dynamic SIMS, the ion fluence is adjusted to the bombarded area and high enough to etch layer by layer of the surface. Analysis is restricted to layers where the equilibrium state prevails (few nm – few hundred  $\mu\text{m}$  from the surface). During the equilibrium state, the sputter yield and the ionization rates are constant and the chemical, elemental and isotopic composition of the sputtered

material is expected to resemble the composition of a fresh sample. On a microscopic level, the dynamic SIMS leads to the formation of craters that deepens at a constant sputter rate (sputter rate: 0.5 – 5 nm/s<sup>2</sup>). The sputter rate is dependent on the primary ion beam density and the sputter yield. Since the sputter yield varies as a function of the crystal orientation the craters in polycrystalline materials tend to be grinded at the bottom.

Rare-earth elements and uranium and thorium form already ions with the primary ion or the matrix; under oxygen bombardment positive oxides and dioxide ions are formed. Secondary ions are sputtered in all directions their translational kinetic energy ranges from a few eV to a several hundreds of eV. Since the ionization rates vary from element to element and isotope to isotope, the measurement of trace elements and their isotopic composition is highly dependent on the availability of suitable reference materials; to match the sample matrix, elemental-, isotopic composition, chemical environment, etc. Solid samples can be analyzed by SIMS under the assumption that they are deposited on a flat and conductive surface and that they can withstand ultra-high vacuum conditions – high precision isotopic analysis requires a mirror-polished surface. Non-conductive specimens have to be coated with gold or carbon (comparable to SEM) and a charged combination for the primary and secondary polarities. Cameca 1280(HR) has the option of performing “ion microscopy”: on the IMS 1280 the optics were constructed in such a way that the extracted secondary ions converge into the transfer optics by forming a stigmatic optical system. Which means an image of the sample surface which is in the focal plane is generated in which the ions of the selected mass converge into a single image point. If the ion beam is defocused or a rastered primary beam is used, such a mass filtered ion image can be projected onto an appropriate detector at the end of the mass spectrometer such as a micro-channel plate (MCP). This method is generally used for elemental and isotopic mapping. For ion microscopy, a maximal lateral resolution of ~ 2.0 μm for analyte concentrations down to 100 μg/g can be achieved. Microprobe is an additional imaging capability of all SIMS instruments and is an in situ micro analysis tool for the detection of trace elements with detection limits in the ppm – ppb range: a focused ion beam is used to raster the sample surface. A two dimensional intensity distribution is generated out of the time-dependent intensity profile of the electron multipliers generated by the secondary ions. In microprobe mode, the lateral resolution depends on the primary beam cross-section in the focal plane. Normally, a static beam with low intensities is used, nevertheless small volumes of a few μm<sup>3</sup> can be sputtered in a few minutes.

### 3.3.3 Raman Spectroscopy

Raman Spectroscopy was used to identify the uranium-oxide composition, the crystallinity and crystal orientation of selected single uranium particles. In order to measure single, micrometer sized uranium particles, confocal Raman Spectroscopy instruments by Renishaw and Vitec were used.

#### 3.3.3.1 Fundamentals of Raman Spectroscopy

According to Dietzek et al. (2011) [113], an induced molecular dipole moment is generated as a reaction of the molecules to an incident electromagnetic wave. That interaction generates an oscillating dipole moment which emits radiation – it scatters light. The basis of that dipole moment is the polarizability which depends on the nuclear coordinates and therefore on the vibrations of the molecule. The molecular polarizability is the ease with which the electron density distribution of the molecule can be distorted by an electric field. The electric dipole moment of a molecule is induced by electromagnetic interaction. The induced dipole moment is a vector and can be written as followed:

$$\vec{P} = \tilde{\alpha}\vec{E} \quad (61)$$

The induced dipole moment „ $P$ “ is a vector, such as the induced electric field „ $E$ “ while the polarizability tensor „ $\alpha$ “ is a 2<sup>nd</sup> rank 3 x 3 tensor.

$$\begin{bmatrix} P_x \\ P_y \\ P_z \end{bmatrix} = \begin{bmatrix} \alpha_{xx} & \alpha_{xy} & \alpha_{xz} \\ \alpha_{yx} & \alpha_{yy} & \alpha_{yz} \\ \alpha_{zx} & \alpha_{zy} & \alpha_{zz} \end{bmatrix} \begin{bmatrix} E_x \\ E_y \\ E_z \end{bmatrix} \quad (62)$$

The polarizability of the molecule can be described mathematically as a Taylor expansion that includes the static polarizability and a factor to take account for small vibrational displacements:

$$\alpha = \alpha_0 + \frac{\partial \alpha}{\partial Q} Q + \dots \quad (63)$$

With „ $\alpha_0$ “ the static/equilibrium polarizability, „ $Q$ “ is a vibrational coordinate and the expression „ $\partial \alpha / \partial Q$ “ as a vibrational modulation or molecular polarizability. The polarizability is expressed as a function of the vibrational coordinates of the investigated molecule.

$$Q = Q_0 \cos(2\pi \nu_{vib} t) \quad (64)$$

“ $Q$ ” can be expressed as a cos-function of the vibrational state and it is a normal vibrational coordinate with “ $Q_0$ ” as the maximum value of “ $Q$ ”. The Taylor Expansion describing polarizability tensor can be modified to the following equation - This equation is limited to the static, linear polarizability in the vibrational modulation.

$$\alpha = \alpha_0 + \frac{\partial \alpha}{\partial Q} Q_0 \cos(2\pi \nu_{vib} t) \quad (65)$$

When monochromatic, highly polarized laser light – with an oscillating electric field “ $E$ ” - interacts with the molecules of the target, it induces an oscillating molecular dipole moment at the frequency of the incident radiation “ $\nu$ ”.

$$E = E_0 \cos(2\pi \nu t) \quad (66)$$

The induced oscillating dipole moment emits radiation with a lower frequency/energy than the incident radiation:  $E = h\nu > E' = h\nu'$ ; scattering in different directions occurs. The expanded expressions for the static and vibrational components of the polarizability tensor “ $\alpha$ ” can be integrated into the initial expression for the induced dipole moment:

$$P(t) = \alpha_0 E_0 \cos(2\pi \nu t) + \frac{\partial \alpha}{\partial Q} Q_0 E_0 \left( (\cos(2\pi \nu t)) (\cos(2\pi \nu_{vib} t)) \right) \quad (67)$$

“ $\alpha_0 E_0 \cos(2\pi \nu t)$ ” is the term to express the induced dipole moment at the frequency of the incident radiation. The second term combines the incident radiation frequency with the vibrational frequency of the molecule and the vibrational modulation of the polarizability. Applying a trigonometric identity equation 62 can be converted to the following expression to describe light scattering from oscillating molecular dipole moments:

$$P(t) = \alpha_0 E_0 \cos(2\pi \nu t) + \frac{\partial \alpha}{\partial Q} \frac{Q_0 E_0}{2} [\cos(2\pi(\nu - \nu_{vib})t) + \cos(2\pi(\nu + \nu_{vib})t)] \quad (68)$$

The different components of this equation are easily identified: the static value for the Rayleigh Scattering can be expressed as the following term “ $\alpha_0 E_0 \cos(2\pi \nu t)$ ”, and the combined Stokes Raman Scattering component – which is the subtractive component - “ $\cos(2\pi(\nu - \nu_{vib})t)$ ” and Anti-Stokes Raman Scattering component “ $\cos(2\pi(\nu + \nu_{vib})t)$ ” – which is the additive component - to account for the vibrational modulation induced by the incident radiation “ $\frac{\partial \alpha}{\partial Q} \frac{Q_0 E_0}{2} [\cos(2\pi(\nu - \nu_{vib})t) + \cos(2\pi(\nu + \nu_{vib})t)]$ ”.

The number of Raman scattering components depends on the number of Raman active nuclei. A change in the polarizability has the effect that atomic bonds start to vibrate: vibrational states can be symmetric stretches, asymmetric stretches, scissoring (in and out of plane vibrational modes). Whether a molecule is Raman active or non-active is determined by the change of the polarizability. Inelastic

scattered light derives from non-zero derivative of the polarization at the equilibrium. This means that, if the polarizability of a vibrational mode around the equilibrium position is not equal to zero ( $\delta\alpha/\delta Q \neq 0$ ), then this vibrational mode is Raman active.

$$I \propto |\vec{\alpha} \cdot \vec{E}_S \cdot \vec{E}_i|^2 \quad (69)$$

This expression can be considered an intuitive “selection rule” for Raman scattering. When a molecule is Raman active the emitted Raman signature is dependent on the magnitude of the Raman polarizability tensor. The allowance of a Raman mode is strictly dictated by “ $\vec{\alpha}$ ”: if “ $\vec{\alpha} \neq 0$ ” if these criterion is met a molecule is considered Raman active. The intensity is proportional to the scalar product of the vector of the incident polarization “ $\vec{E}_i$ ” times the collection polarization (the orientation at which the incident radiation is collected) and time the polarizability tensor. Raman scattering is basically the difference between a ground state “ $E_0$ ” and an excited state “ $E_1$ ” and is basically an inelastic scattering of a photon off a molecular bond. The scattered Raman intensities are dependent from the incident radiation energy and frequency. For simplicity reason the energy and frequency dependence of the scattered Raman intensities is exemplified by Stokes radiation. Starting from equation 69 which describes the induced, oscillating dipole moment:

$$P(t) \propto \left(\frac{\partial\alpha}{\partial Q}\right)^2 \cos[(v - v_{vib})t] E_0 \quad (70)$$

Each oscillating dipole serves also as a Hertzian dipole - generating secondary oscillation. The total scattered Raman intensity “ $I_{Stokes}$ ” is proportional to the emitted power by the induced dipole moment.

$$I_{Stokes} \propto \left(\frac{\partial\alpha}{\partial Q}\right)^2 (\propto -v_{vib})^4 E_0^2 \quad (71)$$

Equation 79 shows the proportionality of Raman scattering with excitation wavelength:  $I_{Raman} \propto \nu^4$ . Another feature of the laser wavelength “ $\lambda$ ” is the fact that the shorter the wavelength the higher the lateral resolution “ $\Delta x$ ”:

$$\Delta x = 0.61 \frac{\lambda}{N_A} \quad (72)$$

The lateral resolution depends on the excitation wavelength and on the numerical aperture “ $N_A$ ” of the objective. For shorter wavelengths (< 350 nm), the number of appropriate objectives with suitable  $N_A$  is limited, but Raman excitation is high. At shorter wavelengths, the energy per quantum is high and can start damaging the sample. At longer wavelengths, lateral resolution decreases, but the Raman efficiency drops and fluorescence effects are less likely to occur. Picking a suitable laser is therefore crucial. In general, a laser should have a Gaussian beam profile with a very line shape to ensure broadening of the emitted Raman bands, have a stable frequency, be linearly polarized and be stable in intensity output.

### 3.3.3.2 $\mu$ -Raman Spectroscopy

$\mu$ -Raman investigations of micrometer-sized uranium entities offer additional, valuable information for nuclear safeguards applications, especially with regards to micrometer sized uranium particles. However, the analytical techniques have to be extremely sensitive as those particles contain pg-level of uranium. Uranium compounds have been investigated routinely with Raman analysis in geological and forensics studies for over 40 years in order to assess the morphology and crystal structure of microcrystalline entities, see Manara et al. (2003) [114], Mellini et al. (2005) [115] and Maya and Begun (1981) [116], Allen et al. (1987) [117] and Butler et al. (1988) [118] – The following references are notable mentioning: Rao et al. (1990) [119], Roeper et al. (2006) [120], Blumenroeder et al. (1988) [121], Amme et al. (2002) [122], Graves (1990) [123] and Morris et al. (1996) [124]. There is a significant number of references citing the use of (Micro) Raman spectroscopy on the uranium oxygen system with (sub-) stoichiometric oxides ratios; see Winer et al. (1986) [125], Palacios et al. (2000) [126], Hoekstra

et al. (1961) [85] and [127], Guéneau et al. (2002) [90], Labroche et al. (2003) [128] and [91], Peakall et al. (1960) [78], Grønvold (1955) [129], McEachern and Taylor (1998) [130], Thein and Bereolos (2000) [131] and more recently Nipruk et al. (2011) [132]. In particular, uranyl compounds are of special interest for nuclear waste and disposal research since they can exist in natural mineral formations. Micro Raman Spectroscopy is a well-established technique to investigate the complexity of the uranium oxygen system, see Biwer et al. (1990) [133]. MRS is elaborately used in nuclear forensics related research, e.g. see Pidduck et al. (2006) [11] and (2008) [134] and Kips et al. (2009) [31]. Since the late 1980's micro-Raman spectroscopy is used to detect and distinguish uranium compounds. Generally bulk materials of polydisperse uranium species are measured. Very rarely single micrometer-sized particles are investigated. Pointurier and Marie et al. (2010) [135] and (2013) [136] or Stefaniak et al. (2006) [137], (2008) [138] and (2013) [139] demonstrated the benefits of MRS for nuclear safeguards applications. They used standalone and coupled SEM-Raman devices to detect certified uranium compounds and artificial micrometer-sized uranium particles. According to Pointurier and Marie (2010) [135,] MRS offers a spatial resolution of  $< 1 - 10 \mu\text{m}$  which is superior to micro-infrared (spatial resolution:  $20 - 400 \mu\text{m}$ ) and micro-XRF (spatial resolution:  $50 - 3000 \mu\text{m}$ ). However the analysis of micrometer sized uranium entities by MRS is difficult due to fluorescence and intense coloration. Also laser induced sample heating can actually lead to a degradation / oxidation of existing U-species as reported by Pointurier et al. (2010) [135] and Jégou et al. (2010) [140].

In the course of this work, several uranium compounds will be discussed, e.g. 1)  $\text{UO}_2\text{F}_2$ , (2)  $\text{U}_3\text{O}_8$ , (3)  $\text{UO}_2$ , (4) Uranyl nitrate Hexahydrate (UNH) and (5) Ammonium Diuranate (ADU).  $\text{UO}_3$  was not measured because it was not available; therefore a small introduction into the behavior and spectra analysis will be given:  $\text{UO}_3$  exists in different crystalline phases:  $\alpha$ -,  $\beta$ -,  $\gamma$ -,  $\delta$ -,  $\epsilon$ - and an amorphous  $\text{UO}_3$ , see Hoekstra et al. (1961) [85] and [127]. All six  $\text{UO}_3$ -modifications have different hydration states - e.g.:  $\text{UO}_3 \cdot 0.5 \text{H}_2\text{O}$ ,  $\text{UO}_3 \cdot 0.7 \text{H}_2\text{O}$ ,  $\text{UO}_3 \cdot 0.8 \text{H}_2\text{O}$ ,  $\text{UO}_3 \cdot 2 \text{H}_2\text{O}$ ,  $\text{UO}_3 \cdot 2.9 \text{H}_2\text{O}$  and many more. According to Dawson et al. (1956) [141] and Sobry et al. (1973) [142], the U-O system is rather complex and leads to the formation of various stoichiometric and non-stoichiometric uranium-oxide species. According to Wheeler et al. (1964) [79] and Weller et al. (1999) [143], the two most common hydrolysis products of  $\text{UO}_3$  are  $\alpha\text{-UO}_3(\text{OH})_2$  and meta-schoepite ( $\text{UO}_2)_4\text{O}(\text{OH})_6 \cdot 5 \text{H}_2\text{O}$ . Sweet et al. (2013) [93] describe the  $\text{UO}_3$  hydrate state as a "complex situation".

According to Wheeler et al. (1964) [79],  $\alpha\text{-UO}_3$  is formed by thermal treatment of amorphous  $\text{UO}_3$  at temperatures around  $450 \text{ }^\circ\text{C}$ . Not only  $\alpha\text{-UO}_3$  can be formed but also sub-stoichiometric  $\text{U}_{2.9}$ . The crystal structure of  $\alpha\text{-UO}_3$  has, according to Cordfunke et al. (1969) [144], an orthorhombic structure whereas Wheeler et al. (1964) [79] claim to have found indications for a hexagonal structure. The formation to  $\beta$ - and  $\gamma\text{-UO}_3$  is formed at  $500 - 550 \text{ }^\circ\text{C}$  in air while a fast heating rate of  $\geq 35 \text{ }^\circ\text{C}/\text{min}$  leads to  $\beta\text{-UO}_3$  while slower heating rates  $\sim 3 - 5 \text{ }^\circ\text{C}/\text{min}^{-1}$  result in the formation of  $\gamma\text{-UO}_3$ . According to Hoekstra et al. (1961) [85] ( $\alpha$ -,  $\beta$ -,  $\gamma$ -)  $\text{UO}_3$  decomposes directly to  $\text{U}_3\text{O}_8$  at temperatures  $550 - 680 \text{ }^\circ\text{C}$ .  $\text{UO}_3$  was not measured due to the lack of appropriate reference material. Nevertheless, reference data on  $\text{UO}_3$  obtained by the very same machine by Pointurier and Marie exists and is used for comparison. According to Pointurier et al. (2010) [135], the 785 nm laser provides better results because the fluorescence is minimized in comparison to the 514 nm laser. Pointurier measured an intense band at  $845 \text{ cm}^{-1}$  and a weaker one at  $1052 \text{ cm}^{-1}$  (with a 785 nm laser) which corresponds with Pidduck et al. (2006) [145] with a band at  $830 \text{ cm}^{-1}$  and  $840 \text{ cm}^{-1}$  with a 514 nm laser. Additional reference from Canizarès et al. (2012) [146] indicates a band at  $840 \text{ cm}^{-1}$ . Palacios et al. (2000) [126] report two peaks at  $768 \text{ cm}^{-1}$  and  $846 \text{ cm}^{-1}$  with a 514nm laser. Investigation on  $\gamma\text{-UO}_3$  and hydrated  $\text{UO}_3$  (Meta-Schoepite:  $\alpha\text{-UO}_2(\text{OH})_2$ ) with a 785 nm laser by Sweet et al. (2013) [93] show peaks at  $220 \text{ cm}^{-1}$  (weak),  $339 \text{ cm}^{-1}$  (strong),  $\sim 380 \text{ cm}^{-1}$  (weak),  $484 \text{ cm}^{-1}$  (middle) and a strong one at  $767 \text{ cm}^{-1}$  for  $\gamma\text{-UO}_3$  and  $\sim 280 \text{ cm}^{-1}$  (weak),  $\sim 370 \text{ cm}^{-1}$  (strong),  $\sim 430 \text{ cm}^{-1}$  (weak) and a strong peak at  $840 \text{ cm}^{-1}$ . According to Sweet (2013) et al. [93], meta Schoepite shows a strong peak at  $841 \text{ cm}^{-1}$ ,  $\alpha\text{-UO}_2(\text{OH})_2$  has one peak at  $840 \text{ cm}^{-1}$  (strong) and  $\gamma\text{-UO}_3$  has three peaks:  $339 \text{ cm}^{-1}$  (strong),  $484 \text{ cm}^{-1}$  (middle) and  $767 \text{ cm}^{-1}$  (strong). All results are listed in Table 1.

**Table 1: Raman bands identification for UO<sub>3</sub> based on references.**

Wavelength, [cm <sup>-1</sup> ]		Reference	
1	830-845	s	UO <sub>3</sub> : Pidduck et al. (2006) (830cm <sup>-1</sup> & 840cm <sup>-1</sup> ) (514nm Laser), Pointurier et al. (2010) (845cm <sup>-1</sup> ) (785nm Laser), Canizarès et al. (2012) (840 cm <sup>-1</sup> ), Palacios et al. (2000) (846cm <sup>-1</sup> )
2	1052	w	UO <sub>3</sub> : Pointurier et al. (2010)
3	768	m	UO <sub>3</sub> : Palacios et al. (2006)
4	220	w	Meta Schoepite, Sweet et al. (2013)
5	484	m	Meta Schoepite, Sweet et al. (2013)
6	767	s	Meta Schoepite, Sweet et al. (2013)
7	339	s	γ-UO <sub>3</sub> : Sweet et al. (2013)
8	484	m	γ-UO <sub>3</sub> : Sweet et al. (2013)
9	767	s	γ-UO <sub>3</sub> : Sweet et al. (2013)

## 4. Materials and Methods

### 4.1 Aerosol Solutions and Particle Production

#### 4.1.1 Aerosol Solution

##### 4.1.1.1 Precursor preparation and Dilution Steps

Certified uranyl nitrate solution from IRMM-183 was used as the source material for preparing the uranium input solution for production of particles. IRMM-183 has a nominal uranium concentration of 148.9 mg/g. ICP-MS measurements determined a concentration of 124 mg/g. Starting from IRMM-183, several dilutions have been prepared with ultrapure water (18.2 mΩ). Dilutions have been prepared by gravimetric and volumetric means. All uncertainties are given with a coverage factor of  $k = 1$ . After adjusting the uranium concentration to about 200  $\mu\text{g/g}$  an equivalent volume of ultrapure ethanol (analytical grade, Merck Germany) is added.

**Table 2: Uranium concentrations of a relevant dilutions and solution – determined by ICP-MS or gravimetric and volumetric calculations.**

	ICP-MS $c(\text{U}), [\mu\text{g g}^{-1}]$	( $k=1$ ) $\Delta c(\text{U}), [\mu\text{g g}^{-1}]$
IRMM-183	123900	1616.0
Dilution 1	2238	222.0
Dilution 2	1876	47.0
Dilution 3	293	11.0
Dilution 4 (mixture, no ICP-MS)	215	10.0
Solution 1a [e]	216.6	18.1
Solution 1b	263.5	6.6
Solution 1c	224.4	6.3
Solution 1d	264.2	4.8
Solution 1g	326.2	27.2

Table 2 depicts the main dilution-steps and the solutions. The solution concentration refers to the diluted solution without ethanol being added. ICP-MS measurements were performed at IEK-6 on a quadrupole ICP-MS (Perkin Elmer, SCIEX Elan 6100 DRC). For the production of uranium particles, the following solution were used: Solution 1d, 1g, and Dilution 4. Dilution 4 was made of the residues of the aerosol solutions of Solution 1c, 1d and 3a and no ICP-MS measurement was performed for Dilution 4, see Table 2. The precursor solution was prepared from a certified reference material IRMM-183 which was purchased from the Joint Research Centre Institute of Reference Materials and Measurements (JRC-IRMM). IRMM-183 is a CRM for depleted uranium (DU) with a relatively high mass fraction of  $^{236}\text{U}$ . The mass and amount fractions of IRMM-183 are depicted in Table 3.

**Table 3: Weight-, Amount- and Amount of Substance Fractions of IRMM 183.**

Mass Fraction ( $\cdot 100$ )	Amount Fraction ( $\cdot 100$ )	Isotope Amount Ratio(s)
$m(233\text{U})/m(\text{U}) < 0.000\ 000\ 2$	$n(233\text{U})/n(\text{U}) < 0.000\ 000\ 2$	$n(233\text{U})/n(238\text{U}) < 0.000\ 000\ 002$
$m(234\text{U})/m(\text{U}) 0.001\ 935\ 8(22)$	$n(234\text{U})/n(\text{U}) 0.001\ 968\ 8(22)$	$n(234\text{U})/n(238\text{U}) = 0.000\ 019\ 55(22)$
$m(235\text{U})/m(\text{U}) 0.316\ 45(16)$	$n(235\text{U})/n(\text{U}) 0.320\ 49(16)$	$n(235\text{U})/n(238\text{U}) = 0.003\ 215\ 7(16)$
$m(236\text{U})/m(\text{U}) 0.014\ 661\ 8(54)$	$n(236\text{U})/n(\text{U}) 0.014\ 785\ 8(54)$	$n(236\text{U})/n(238\text{U}) = 0.000\ 148\ 58(54)$
$m(238\text{U})/m(\text{U}) 99.666\ 95(16)$	$n(238\text{U})/n(\text{U}) 99.662\ 76(17)$	

[e] No ICP-MS measurement available, value was evaluated by gravimetric attenuation.

IRMM-183 is delivered as a nitrate solution in a sealed glass ampule. The mass of sealed vial was weighted beforehand as a redundant measure:  $m(\text{CRM}) = 6.7155 \pm 0.0001 \text{ g}$ . The volume was approximately 5.0 ml. IRMM-183 was delivered with a certified value for the uranium isotopic abundances for the  $^{233}\text{U}$ ,  $^{234}\text{U}$ ,  $^{235}\text{U}$ ,  $^{236}\text{U}$ , and  $^{238}\text{U}$  isotopes and the molar mass  $M_{\text{CRM}}$  of 238.0407716 g/mol but not for the concentration. IRMM-183 has a calculated uranium concentration of 148.9 mg/g but the true value was determined by ICP-MS and found to be  $1.239 \cdot 10^5 \pm 1.616 \cdot 10^3 \text{ } [\mu\text{g/g}]$ .

**Table 4: Specifications of IRMM-183.**

$M_{\text{CRM}}$	238.0407716	[g/mol]
$m(\text{CRM})$	$6.7155 \pm 0.0001$	[g]
$V_{\text{CRM}}$	5.0	[ml]
$c(\text{U})_{\text{CRM}}$	123.890	[mg/g]
$\rho(\text{CRM})$	1.343	[g/ml]

Weighing was performed with a Mettler Toledo XP-205DR scale, and all liquid transfer was performed using Eppendorf Research Plus pipettes with 10 - 5000  $\mu\text{L}$  volume. The aerosol precursor solution was prepared by mixing a 1:1 mixture of Suprapure water, and analytical grade Ethanol (EtOH was purchased by Merck, Germany,  $\ll 1 \text{ } \%$ ). An aliquot of the CRM-solution was added to the water-ethanol mixture. Since the orifice vibrates in an ultra-sonic frequency range of about 70 kHz, it can lead to minute quantities of air leaching from the precursor solution. If the precursor solution is not degassed air trapped within the solution can coagulate at the orifice which will hinder or even disturb the aerosol formation process. In order to minimize this risk, all solutions are degassed in an ultrasonic bath for about 10 - 15 min. After degassing, the freshly prepared aerosol solutions are carefully transferred into disposable plastic syringes with Luer-Lock connectors for the particles production.

## 4.1.2 Particle Production

A vibrating orifice aerosol generator (VOAG, model 2450 TSI Inc.) was employed to produce aerosol droplets made from the precursor solutions. For the production of small micrometer sized particles, a standard operating feed rate  $Q = 1.392 \cdot 10^{-1} \text{ cm}^3/\text{min}^1$  is applied when using the 20  $\mu\text{m}$  diameter orifice and a frequency of  $\nu = \sim 70 \text{ kHz}$  was used to generate monodisperse droplets of an approximate volume of  $3.3 \cdot 10^4 \text{ } \mu\text{m}^3$ .

### 4.1.2.1 Aerosol Production and Precursor Particles

Starting procedures include the following steps: In order to prevent heat stasis inside the system, a small constant air flow is applied. After the system is heated up to temperature and the vibrational frequency of the orifice has stabilized, a disposable 60 ml plastic syringe with the aerosol solution is attached to the system. The syringe is attached to the system with a Luer-Lock connection. Before starting the aerosol production, it is important to flush the system carefully in order to remove all access air inside the VOAG.

The compression rate for the syringe is slightly increased to build a sufficient pressure of  $\sim 200 \text{ kPa}$ . After a liquid jet is established, the liquid feed rate " $Q$ " has to be adjusted back to operating conditions in order not over pressurize the system and to maintain a steady and constant aerosol jet. During the jet adjustment, filtered pressurized air is circulating through the system. Both of the air streams, (1) dispersion- and (2) dilution air stream have to be adjusted carefully. During the entire microparticle production process, air streams play an integral part. Basically, two different air streams are applied to the particle formation process: (1) to ensure the dispersion of the droplets an air stream (the so-called dispersion air stream) is introduced to the aerosol generation process. Particles are directly dispersed through the dispersion cup into the drying column. The drying column is a cylindrical volume of ca. 12 cm in diameter and 40 cm in length which is used for droplet evaporation and aerosol droplet dilution to minimize coagulation effects. (2) The dilution of the particles is ensured through the

introduction of a second and more powerful airstream, the so called "dilution air stream". These air streams also function as a transport agent for the particles. The air flows have to be carefully adjusted so the inertial impactors can operate with a maximum yield (see Chapter 4.1.2.4 and 4.1.2.5) and to minimize turbulences inside the system which reduce the particle yield as well.

#### 4.1.2.2 Particle Conversion – Heat Treatment

Up to this point, the precursor droplets have already partially evaporated. The combined air streams generate an air-flow which is too high to be heated to sufficiently high temperatures within the furnace to ensure a proper thermal treatment that guarantees thorough calcination of the particles. The reduction of air-flow is achieved with a component called a virtual impactor. It divides the air-stream exiting the drying column into two different streams. Two different heaters were used to heat the air stream to achieve calcination of the precursor particles. This first was a tubular air heater commercially available for aerosol treatment (Dekati® Pressurized air heater) with a heated region in the range of 300 mm and a final temperature of ca. 590 °C. The second comprised a four zone furnace with a length of in total 1200 mm and a final temperature of 1100 °C. Both heating systems were installed in series and tested individually and in combination for the second major step of particle production, which is the online calcination of the precursor particles. This thermal treatment converts the dried metal nitrates into its oxides. According to the literature on thermal decomposition of bulk amounts of uranyl nitrate, we expect to get mixed oxides of uranium, especially in the oxidation form of +4 and +6. Calcinated particles offer more advantages to the use as RMs as dried particles. Firstly, the actinide oxides are chemically far more stable than in its nitrate form. Secondly, the mechanical properties are better; this means that the integrity of those spheres is much more stable. This fact is quite important because those spheres may have to be manually transferred to another substrate in order to perform particle analysis.

First the particles are diverted through a small pre-heating system and sequentially attached is a four zone furnace. Each zone can be controlled individually. The overall dwell time inside the pre-heating system and the oven is less << 10 s in total. The pre-heating system was installed to gradually increase the temperature and minimize mechanical stress imposed on the integrity of the aerosol particles through sudden heat exposure. To ensure a thorough oxidation process within our setup one has to compensate for the short dwell time in which the particles are exposed to the high temperature fields of the furnaces. Temperatures were set between 500 - 900°C for the preheating system and the furnace.

#### 4.1.2.3 Post Processing

After thermal treatment, the particles are directed into an air-cooled cooling tube before being collected from the air flow by inertial impaction. Both air streams are separately controlled by airflow meters and two separate membrane pumps. In the end those two air streams are filtered separately, each by an ultra-high purity ceramic filter (UHP filter).

These filtered exhaust airstreams are then discharged into a fume-hood. As a consequence of working with radioactive elements such as uranium, it is essential to guarantee a safe handling of the whole apparatus. Therefore, the entire setup was designed to be tightly sealed off to minimize cross contaminations and enhance cleanliness and accessibility during standard operations and for maintenance. Therefore, all components such as the VOAG, the virtual impactor, the pre-heater, the furnace, the cooling unit and the sampling unit are connected via DIN sized, industrial tubing, fittings and flanges. These crucial components of the setup are installed inside a fume hood. The tubing is mainly made of 6mm stainless steel tubes, vacuum flanges and connectors with standard fittings (e.g. Swagelok®). A vibrating-orifice aerosol generator (VOAG, model 2450 TSI Inc.) was employed together with a furnace system for the production of monodisperse uranium particles. Crucial components of the setup are installed inside a fume hood at the IEK-6 in Jülich Germany, see Figure 16. After cooling down the final particles are collected from the air stream by inertial impaction. In general sampling takes about 5 - 10 min per batch.



**Figure 16: Image of the particle production setup at IEK-6 at Forschungszentrum Jülich GmbH, as of December 2014.**

Particles are primarily collected by a one-stage inertial impactor which is a proprietary design of the IAEA. The sampling unit is directly attached to the particle production setup. Particles are impacted onto a 1" diameter glassy carbon disk (Ted Pella Inc.), see Chapter 5.1.

#### **4.1.2.4 Setup Evolution and Particular Features**

The following chapters will discuss the setup evolution until about December 2014. The setup is installed inside a fume hood at the IEK-6 in Jülich Germany. In the last three years, a prototype setup was developed and implemented at the Institute of Nuclear Waste Management and Reactor Safety (IEK-6) at the Forschungszentrum Jülich GmbH. This chapter depicts briefly the evolution of the setup up to the stage of producing uranium oxide particles. Since early 2013, when the first operational prototype was implemented for neodymium particle production many components have been changed, rebuild, modified or even removed. Here are the most important changes in chronological order: Before operating the system with active uranium solutions, it was decided to test the equipment by using a surrogate: neodymium nitrate to produce neodymium oxide particles. The idea was to test the system rather than mimicking the uranium chemistry. The first running prototype was built in early 2013 and was without the heat treatment stage and was used for testing operations of the aerosol generator.

By May 2013, shortly before the installation of the furnace, it became obvious that the particle size can be controlled primarily by the precursor solution concentration. Figure 17 shows at No (1) a neodymium precursor-particle on a glass substrate - see left hand side. The concentration was calculated to yield in  $1\mu\text{m}$  neodymium oxide ( $\text{Nd}_2\text{O}_3$ ) particles. SEM investigations revealed that the de-hydration was not thorough and a lot of residual water was left. Particles were initially collected directly on glass or high grade steel targets. Initially, Nuclepore Filters were used to collect particles. They turned out to have multiple disadvantages: (1) tedious handling caused by curling up of the filter, (2) low particle

retention, (3) intricate handling especially the removal from the sample holder after collection, (4), limited imaging capabilities inside the SEM and (5) particles “jumped-off” the filter material due to electrostatic charging. A more elegant and easier method was needed, thus introducing inertial impaction. Standard inertial impactors developed and used by IAEA (see Chapter 3.2.2) were applied.

Since then particles have been predominantly collected via inertial impaction on glassy carbon disks – so-called “GC-planchets”. Six months later, in November 2013, the first dry neodymium spheres were produced with a nominal diameter of around 3.0  $\mu\text{m}$ . At this stage, the furnace was installed and the setup proved to be operational, see Figure 17 No (2). This setup consisted of an aerosol generator, the virtual impactor, the air heater, a furnace and an inertial impactor sampling system. At this time it was decided to start to produce uranium oxide particles. Since then, the drying column has been shortened to increase the sampling yield.

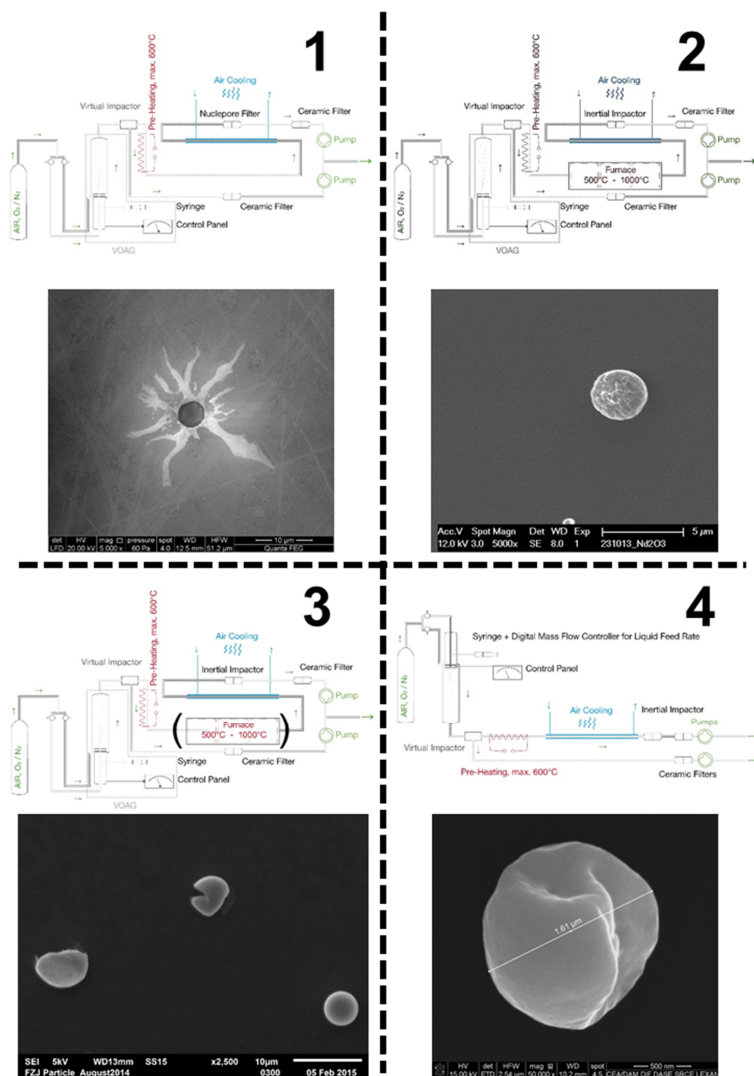


**Figure 17: No (1): First setup with neodymium precursor particles (wet); No(2): First fully operational setup to produce dry neodymium oxide particles; No(3) Uranium oxide particles from SG140521\_02; No(4) latest evolution step of the setup as from December 2014.**

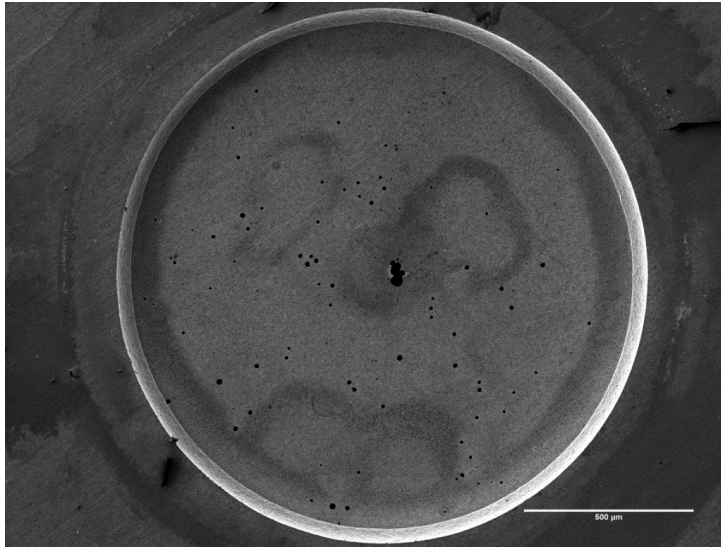


**Figure 18: SE-image of a corroded high grade steel orifice used to produce uranium particles.**

The first uranium test runs were performed in May 2014 and showed some promising results. SEM studies indicated almost monodisperse size distribution. In the time between May and August 2014, technical difficulties occurred. This made it difficult to reproduce the promising results from early 2014. During that difficult time, batch SG140521\_01 was produced, in May 2014, see Figure 17, No (3).

Technical difficulties occurred until August 2014. SEM investigations revealed the existence of various particle sizes and morphologies within single batches. To a large extent, particles size distribution was not uniform due to particles that showed signs of voids or particles that had fragmented and also inflated particles. At this point, it became obvious that the complexity of the mechanics and kinetics of droplet-to-particle conversion needed to be considered and studied. The major cause for malfunction was primarily the degradation of the orifice, which is made of high grade steel. It normally withstands corrosive media and lasts for months of operation – these components are considered routine replacement parts, see Figure 18. Since May 2014, several components have been changed: the orifice was mounted up-side down such that the droplet transport is in direction of the gravitational force hereby increasing the transport efficiency in the drying column. Also an optical particle counter was added to give an online indication about the particle size and particle output. Finally, the heat treatment was limited to a temperature of 500 °C and the large furnace was disassembled. Heat treatment is now accomplished by the compact air-heater. And since April 2015 digital mass flow controllers have been installed to ensure a consistent volume flow to ensure a steady aerosol production. This optimized setup consists of the aerosol generator, the air-heater, a cooling system and the sampling unit, see Figure 17, No (4). This schema depicts the evolution step of January 2015.

Note: In the beginning, the sampling yield of the inertial impaction did not meet our criteria, it was far too low. The excessive loss of particles could be associated to two basic reasons: (1) the great loss of particles due to the complex geometry of the system and (2) an excessive calcination temperature of 900 - 1100 °C. After changing the system by placing the orifice up-side down, shortening the tubing, attenuating sharp angles which acted like impactor sites and adjusting the air flows, the sampling yield could be restored to acceptable levels. Another measure to increase the sampling yield was the introduction of a suitable adhesive. Various organic materials from Si grease, Apiezon-L to Polyisobutylene (PIB) have been investigated. Most of the mentioned adhesive highly interfere with the

analysis or even hinder to perform such: so far PIB proved to be the best solution. It can easily be burnt away by heat treatment of around 300 °C about 30 min.

Nowadays, a sampling process endures about 5 min and about  $21 \cdot 10^6$  particles are generated during that time and about  $10 \cdot 10^3 - 20 \cdot 10^3$  particles are collected on a glassy carbon substrate during that time – depending on the specific working conditions and setup status as of October 2014. This range is more than sufficient for distributing and performing subsequent assays.

#### **4.1.2.5 Particle Collection via Inertial Impaction**

Sampling played a crucial role in the development of the setup. Initially, the sampling yield was too low to guarantee further analysis. During the first 1.5 years different methods were applied to collect particles from the air stream: starting with filtering, electrostatic precipitation and inertial impaction. As discussed earlier, the application of Nuclepore Filters (Whatman, Track Etched Nuclepore Filters) introduced a number of difficulties. Electrostatic precipitators are well-established methodologies for sampling, but are not as effective as inertial impactors. They offer the most promising sampling yield, most user friendly, easy to maintain and very cost effective. IAEA uses a one stage inertial impactor to prepare samples for SEM imaging and LG-SIMS analysis. Particles can be directly deposited onto a suitable substrate; further particle preparation would be reduced to a minimum. In general, particles are sampled with a one stage inertial impactor. This one stage impactor was developed at IAEA. A gaseous jet of particles is passed through a thin nozzle to adjust the impaction speed evenly. Directly below the nozzle is an impaction plate that bends the air stream by 90°. The air flow hits the sampling plate and gets diverted towards the exit. The particles which are present in the air stream try to follow the air-flow, but due to their inherent inertia they are forced to impact on the so-called impaction plate; smaller particles with a smaller inertia stay airborne.

Before particle collection, the impactor was loaded with a clean glassy carbon disk (purchased from TedPella, diameter: 1"). To collect particles from the setup the one-stage inertial impactor used by the IAEA was inserted into the collection air stream by switching a valve which diverts the air stream through the impactor. With appropriate air flow, a sufficient number of particles ( $> 1000$  particles per disk) could be collected. Sampling occurred for about 5 – 10 min in average. Afterwards the carbon disk was carefully removed from the impactor and stored inside a plastic casing.

During the development of the setup, it became apparent that the sampling yield was not sufficient for higher air flows and that the sampling yield could yet be raised. Therefore, a two stage inertial impactor and a cyclone inertial impactor were developed at SGAS-ESL. The two stage inertial impactor was used to collect particles for the  $\mu$ -Raman spectroscopy: basically two one-stage inertial impactors were connected together to form a two stage impactor. By modifying the nozzle diameters, the cut-off diameter of each stage could be adjusted accordingly: the first stage was designed to hold-off particles with aerodynamic diameter well above 5  $\mu\text{m}$  and the second stage was designed to retain particles in the range of a few hundred nanometers up to 5  $\mu\text{m}$ .

#### **4.1.2.6 Final Aerosol Solutions & Production Parameters**

Solution 1d, 1g, and Dilution 4 were used to produce uranium oxide particles. Table 5 shows the production parameters. All particles were produced using a 20  $\mu\text{m}$  orifice. All particles were collected using an inertial impactor either on glassy carbon substrate or on Si-Wafers. Since SG141027\_12A the large high temperature furnace was no longer used because of the low particle yield and the low quality of particles that were treated at temperatures above 500 °C. Instead the air heater with temperature control of the output air temperature up to maximum temperature of  $\sim 570$  °C was used for the calcination process. Also the inertial impactor system was mounted up-side down during sampling. In total six different batches containing uranium particles were produced within the time frame of May 2014 to March 2015. Table 6 below depicts the batches of interest which will be discussed within this thesis. These particle batches represent the evolution of particle production at FZJ.

**Table 5: Frame conditions during particle production of all six batches of interest.**

#	Sample-ID	Details
1	SG140521_02	c(U) = 132.0 ppm, v = 69.00 kHz, Q = 2.32 10 <sup>-9</sup> m <sup>3</sup> s <sup>-1</sup> , T <sub>PH</sub> = 580 °C, T <sub>1-4</sub> ≈ 716 - 750, t = 30 min, GC-disk, Inertial Impactor, coated PIB-Nonane, Impactor normal
2	SG141027_12A	c(U) = 147.0 ppm, v = 69.16 kHz, Q = 2.32 10 <sup>-9</sup> m <sup>3</sup> s <sup>-1</sup> , T <sub>PH</sub> = 560 °C, T <sub>1-4</sub> ≈ removed, t = 5 min, Inertial Impactor, GC-disk, Uncoated, Impactor upside down
3	SG150312_05A	c(U) = 107 ppm, v = 70.28 kHz, Q = 2.32 10 <sup>-9</sup> m <sup>3</sup> s <sup>-1</sup> , T <sub>PH</sub> = 394 °C, T <sub>1-4</sub> ≈ 580 – 900 °C, t = 5 min, Inertial Impactor, 10 x 10 mm Si wafer, uncoated, Impactor upside down
4	SG150401_14A	c(U) = 104.6 ppm, v = 70.36 kHz, Q = 2.32 10 <sup>-9</sup> m <sup>3</sup> s <sup>-1</sup> , T <sub>PH</sub> = 500 °C, T <sub>1-4</sub> ≈ removed, t = 5 min, Vacuum Impactor, Glassy GC-disk, Uncoated, Impactor upside down
5	SG150413_03A	c(U) = 59.9 ppm, v = 70.32 kHz, Q = 2.32 10 <sup>-9</sup> m <sup>3</sup> s <sup>-1</sup> , T <sub>PH</sub> = 500 °C, T <sub>1-4</sub> ≈ removed, t = 5 min, Inertial Impactor, 7 x 5 mm Si wafer, Uncoated, Impactor upside down
6	SG150429_02A	c(U) = 120.0 ppm, v = 40.25 kHz, Q = 2.32 10 <sup>-9</sup> m <sup>3</sup> s <sup>-1</sup> , T <sub>PH</sub> = 500 °C, T <sub>1-4</sub> ≈ removed, t = 5 min, Inertial Impactor, 10 x 10 mm Si wafer, Uncoated, Impactor upside down

Each sample has a unique, identification code: *SG(yy)(mm)(dd)(aa)(b)*: with “(yy)” two digits for the year (i.e. 2014 → “14”), “(mm)” two digits for the month (i.e. January → “01”), “(dd)” two digits for the day, “(aa)” two digits for batch number and “(b)” one digit for the sampling position (position A is before position B) – no digit means just one collection position.

**Table 6: Sample-ID, corresponding uranium concentrations, sampling methodology and temperature profile for the batches of interest.**

#	Sample-ID	c(U), [µg/g]	Δc(U), [µg/g]	Substrate	Preheating, [°C]	Furnace, [°C]
1	SG140521_02	132.1	4.8	GC-Disk	480	737-747
2	SG141027_12A	146.5	11.0	GC-Disk	560	-
3	SG150312_05A	107.5	11.0	Si Wafer (10x10mm <sup>2</sup> )	394	580-900
4	SG150401_14A	104.6	10.0	GC-Disk	500	-
5	SG150413_03A	59.9	6.3	Si Wafer (5x7mm <sup>2</sup> )	500	-
6	SG150429_02A	120.0	12.0	Si Wafer (10x10mm <sup>2</sup> )	500	-

### 4.1.3 Particle Transfer Techniques

Marking techniques using a laser micro dissection system (LMD) was used to engrave reference points on graphite planchets. These could be new planchets or existing ones with an entire batch deposited on top. All particle substrates were retrospectively engraved to re-identify single particles of interest. Initially, this procedure was designed to be applied for combined SEM / LG-SIMS analysis. Particles were first identified inside the SEM and could then be located inside the LG-SIMS and afterwards relocated inside the SEM. The SE-images taken from the totally evaporated particles were recorded with this method; see Figure 86 in Chapter 5.4.4.3.

This principle of particle identification and relocation is applicable not only for idealized, monodisperse microparticles, but also for real-life samples. These samples contain a matrix of other elements in all sizes and shapes. The most important task for nuclear forensics is the identification of particles of interest. So what is actually a single particle? - Answering this question is not as straightforward as one might think. Admon et al. (2009) [147] provide a suitable explanation of what can be defined as a particle: a single particle is an entity which does not disintegrate while being observed. The notion of a single particle however is an arbitrary definition because a particle may be homogenous for a specific property but heterogeneous by another.

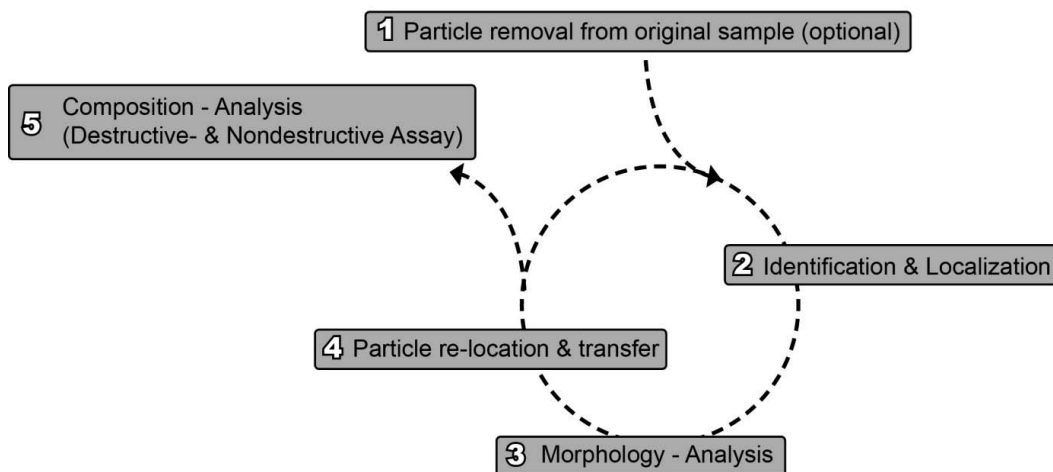


**Figure 19: Particle analysis and re-location scheme, see Admon et al. (2009).**

Admon et al. (2009) [147] conclude that the definition is equivocal and depends on arbitrary connotations. In our case, homogeneity is the main criterion thus making particles easy to identify. Admon et al. (2009) [147] provide an efficient procedure of five of consecutive steps to build up a procedure to first identify particles of interest via a three-point algorithm and then relocate these particles of interest in any given instrument with a high degree of accuracy. (1) if necessary particles have to be transferred to an appropriate substrate, i.e. from cotton swipes to a vitreous graphite substrate (this will be referred to a “glassy carbon planchets or disks”), (2) identification and localization of particles of interest, (3) if necessary a morphology assessment, (4) particle relocation and transfer to a new substrate and (5) re-localization of particle of interest on the new substrate for destructive characterization.

Particle manipulation was performed on either an optical microscope system or within the Jeol JSM 6610 SEM. Two micromanipulation arms (by Klocke Nanotechnik GmbH) are installed inside the SEM chamber of the Jeol JSM 6610 SEM. The arms are driven by piezo motors and are controlled by a proprietary Klocke software package. The optical micromanipulator (M205) is from Suruga-Seiki Company Ltd. and has two arm manipulators by Mitsutoyo Company. This system consists of a micromanipulator system from with two arm-manipulators an optical microscope and a PC to control the manipulation process. The transfer process is monitored with an optical microscope (Zeiss Axioplan) with a max. magnification (x 2.000) attached to the Zeiss microscope is CCD Color Camera (KP-D 20AP, Hitachi Co. with IMAQ 1405 National Instruments). Tungsten fine tip needles were used (tip diameter <<20nm). Reference marks were laser-cut with a laser micro dissection system by MMI. Attached to the laser was an optical microscope by Olympus. Proprietary MMI software controlled the laser cutting process. All reference marks developed by using Microsoft Excel and Notepad++.

#### 4.1.3.1 Three Point Algorithm

The triangulation method offers an easy, fast and reliable method for particle relocation. The substrate has to be prepared with reference marks, preferably beforehand. There are many ways of applying reference marks: either by gluing a mesh, such as transmission electron microscopy (TEM) mesh, carving by hand or by laser micro dissection (LMD). The following passage shows the derivation for an algorithm to relocate single particles with three reference marks which are not collinear. “P” represents the particle of interest, “A, B, C” are three non-collinear reference marks on the substrate, O and O’ are the stage coordinates system (Cartesian). Any point “P” coplanar with A, B, and C can be

expressed as the vector-sum. The components  $\{m_i\}$  are independent of the coordinates system, which means “P” is defined by  $\{m_i\}$  in respect to A, B, C in any coordinates system:  $m_1 + m_2 + m_3 = 1$ .

$$\vec{p} = \sum_{i=1}^3 m_i \vec{r}_i \quad (73)$$

$$\vec{q} = \sum_{i=1}^3 m_i \vec{s}_i \quad (74)$$

The precise determination of a particle of interest on a substrate is vital to re-locate it for further analysis. If  $\{x_i, y_i\}$  and  $\{u_i, v_i\}$  are the measured stage coordinates of the reference marks A, B, C in the source and target instrument respectively. It can be assumed that there is no movement in z-direction, therefore  $z=\text{const}$ . “R” is the reference marks matrix.

$$\begin{pmatrix} x_p \\ y_p \\ 1 \end{pmatrix} = \begin{pmatrix} x_1 & x_2 & x_3 \\ y_1 & y_2 & y_3 \\ 1 & 1 & 1 \end{pmatrix} \begin{pmatrix} m_1 \\ m_2 \\ m_3 \end{pmatrix} = R \begin{pmatrix} m_1 \\ m_2 \\ m_3 \end{pmatrix} \quad (75)$$

The target coordinates of any given point can be calculated if the source coordinates are known. The precision of the relocation algorithm is  $< 10.0 \mu\text{m}$ .

$$\begin{pmatrix} u_p \\ v_p \end{pmatrix} = \begin{pmatrix} u_1 & u_2 & u_3 \\ v_1 & v_2 & v_3 \end{pmatrix} \begin{pmatrix} m_1 \\ m_2 \\ m_3 \end{pmatrix} = \begin{pmatrix} u_1 & u_2 & u_3 \\ v_1 & v_2 & v_3 \end{pmatrix} \begin{pmatrix} x_1 & x_2 & x_3 \\ y_1 & y_2 & y_3 \\ 1 & 1 & 1 \end{pmatrix}^{-1} \begin{pmatrix} x_p \\ y_p \\ 1 \end{pmatrix} \quad (76)$$

At SGAS-ESL two different system were at our disposal: (1) an optical microscope (Zeiss Axioplan) which was connected to two separate, remotely controlled, micromanipulator arms (M205 Micromanipulator from Suruga Seiki Company Ltd.) and (2) JEOL JSM 6610 SEM equipped with two piezo-driven micromanipulators by Klocke Nanotechnik and controlled by Klocke “NanoControl” software.

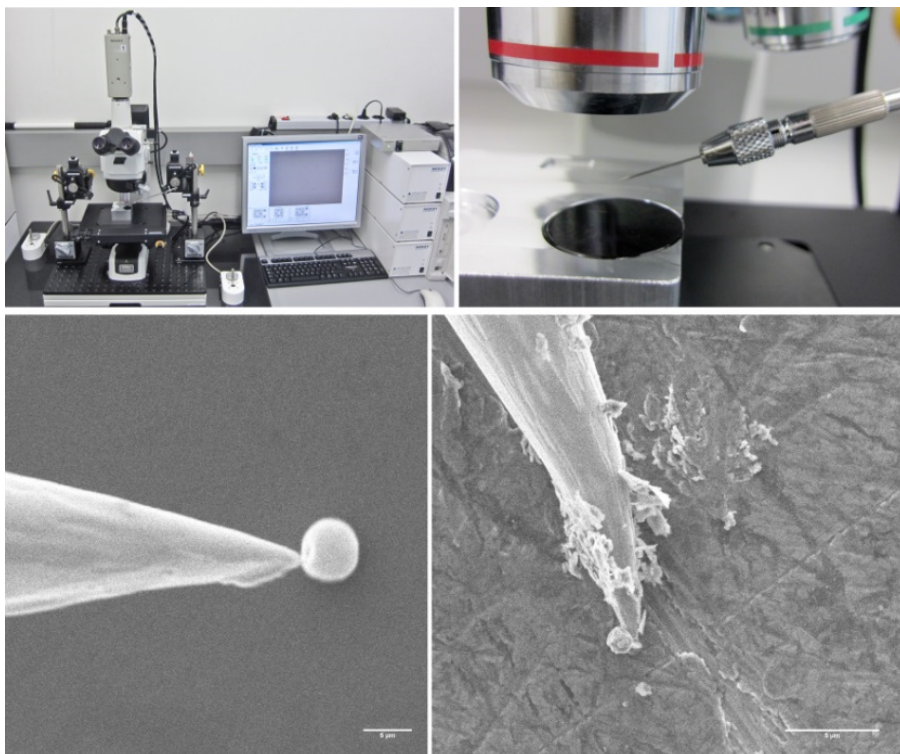


**Figure 20: Top: SURUGA-Particle manipulation system at SAL and bottom: SE-images depicting the transfer of single micrometer sized particles, recorded with Jeol JSM 6610.**

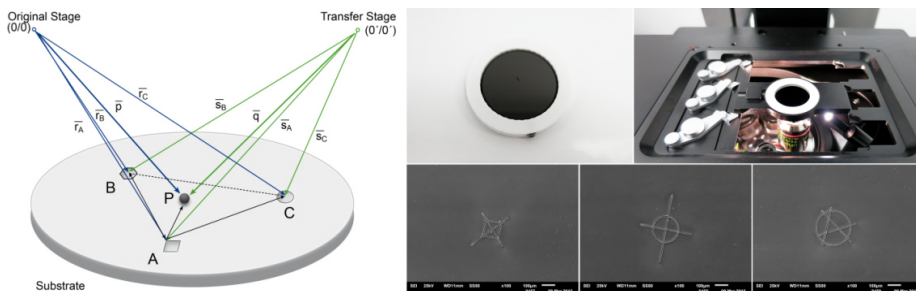


**Figure 21: Left: Vector diagram representing the triangulation method. A, B, C are reference marks, P is the particle of interest, O the source instrument and O' the target instrument. (See Admon, et al. 2005 [9]); Right: Reference marks: (left hand side) either by scratching with a tungsten needle or (right hand side) by LMD.**

Picking up particles can be achieved by carefully approaching a thin tungsten needle above a particle. If the distance is low enough between needle tip and particle, the particle “jumps up” to the needle. Substrates which are coated with an adhesive layer prevent the detachment of particles thus making it impossible as a substrate for micromanipulation. Once the particle adheres to the needle, it can be transferred to the new substrate. The most delicate phase is the deposition of the particle. Particle can be destroyed or maybe displaced on the needle tip thus aggravating the deposition process.

## 4.2 Analytical Methods

### 4.2.1 Microscopy: Scanning Electron Microscopy and Optical Microscopy

Scanning electron microscopy investigations were performed at FZJ and at IAEA respectively. At IEK-6, a FEI Quanta 200 F SEM was used which is equipped with three separate detectors: (1) an Everhart Thornley SE-detector (for high vacuum use) and (2) a gaseous large field SE-detector (for low vacuum mode) and (3) with a backscatter electron detector (BSE) (GAD detector). For EDX an Apollo X Si drift detector (SDD) from EDAX was used. The vast majority of the SEM investigation was performed at SGAS-ESL on a Jeol JSM 6610 SEM. The SEM is also equipped with an EDX, a SE and a BSE detector. Uranium particle manipulation was performed inside the Jeol SEM with tungsten needles. Particles were also analyzed using a SEM Tima SEM equipped with SE, EDX and WDX detectors. Combined FIB analysis and SEM investigations were performed on a Tescan Lyra SEM with ToF detector, SE, BSE, EBSD and EDX.

All SEM were used to investigate the particle morphology and characteristics such as size distribution and shape. SEM investigation were performed on bulk material (a few hundred particles-+) and on single micrometer sized particles. All particles were deposited on glassy carbon disk (Ted Pella Inc., 2" diameter) or on Si wafer chips (7x5 or 10x10mm, Ted Pella Inc.). All investigated particles were deposited onto the substrate by inertial impaction and no adhesive was used. For SEM analysis no coating was necessary. SEM analysis was performed at accelerating voltages (AcV) between 1 - 30kV, in average an AcV between 25 - 30 kV was applied. For EDX analysis a minimal AcV of 25kV was applied respectively.

Amongst other things, microscopy was used to determine the particle size, the morphology and to do an elemental analysis using SEM-EDX/-WDX. The particle size distribution of each batch was derived by image processing of selected SEM-images. The SEM investigations were complemented by optical microscopy (Zeiss Z2m with Axio Vision SE64 software) which can cover larger areas of the substrate and is used for particle mapping. Optical microscopy is not well suited for a precise determination of the microparticle size distribution due to the limitation in resolution even for a high performing optical microscope such as the Zeiss Z2m. Therefore, the optical microscopy was just used for the characterization of the particle distribution over the substrate surface. All image processing was done using FIJI software (Version 1.48c - ImageJ distribution).

#### 4.2.2 SE-Computation

For the computational simulations of secondary electron images CASINO software was used (version 3.3.0.2, 64-bit). CASINO is an easy to use Monte Carlo computation program to simulate electron interaction with matter such as SE- and BSE image simulations, electron (SE and BSE) scatter trajectories and energy dissipation. CASINO was developed by Drouin et al. (2007) [148] at the University of Sherbrooke and is an acronym for “Monte Carlo Simulation of electron trajectory in solid”. CASINO offers the user to create a three-dimensional sample with defined boundary layers which have specific elemental- and stoichiometric compositions, density, shape and geometry. Secondary electron generation is calculated by the Moeller equation and by plasmon theory, see Reimer et al. (1986) [149] and Kotera et al. (1990) [150]. Moeller’s equation is used for the generation of fast secondary electrons while the plasmon theory is used for the generation of slow secondary electrons. Particles investigated in this study originate from one single batch and were initially investigated with SEM and identified as uranium containing particles with energy dispersive X-Ray spectroscopy (SEM-EDX). These uranium particles were produced at FZJ in May 2014 and deposited on a glassy carbon substrate (TedPella, Inc.).

The production of monodisperse micrometer-sized uranium oxide particles with spray pyrolysis is a complex matter. The conditions during evaporation and decomposition play a determining role in the formation of the final product for attributes such as particle size, shape, external and internal morphology including crystal structure, density variation, and phase variances. SEM studies performed at FZJ and IAEA revealed the presence of two distinct particle populations: (i) solid particles with an expected diameter of around 1.3  $\mu\text{m}$  and (ii) an unexpected particle species with mean diameter of  $> 5.5 \mu\text{m}$ . The existence of particle population (ii) can be attributed to a corroded orifice and / or to inconsistencies in the liquid feed rate. In order to understand the formation process including mechanism and kinetics of the droplet-to-particle conversion the morphology, elemental composition, solidity and density of the non-typical species were investigated. The conversion from aerosol droplet precursors to solid entities leads to formation of three basic particle populations: (1) solid submicron particles, (2) hollow, expanded particles (these particles can exist in several forms as (a) intact hollow spheres, (b) shell debris due to impermeable outer shell and (c) combination of shell debris and submicron entities), and (3) agglomerations of submicron particles. The same authors also state that the exact kinetics and mechanisms of particle formation are still not fully understood. Solid particles are formed if internal precipitation sets in and the salt concentration inside the droplet precursors is homogenous; in this case, precipitation occurs randomly throughout the precursor. Due to the fast conversion, the (re-) diffusion effects can be neglected. These precipitation areas have a steady growing interface layer to the surrounding solution which leads to aggregation of dense submicron particles which are sintered together to one entity at higher temperatures. Surface-controlled precipitation is caused by non-steady state conditions of the concentration in the precursor. The formation of a crust or outer shell hinders the ongoing evaporation, which leads to a volume expansion due to evaporation pressure build-up inside the shell. Depending on the permeability of the outer crust, these entities can break apart during thermal treatment - which can result in the above mentioned variations (a)-(c). An intermediate of (1) and (2) is the mechanics in (3) which subsequently end in a large number of agglomerations of polydisperse submicron particles with no specific morphology characteristics.

### 4.2.2.1 Process Description and Operating Conditions

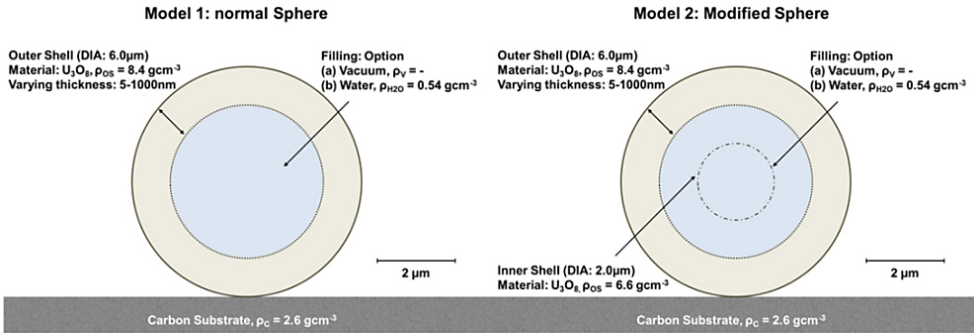


**Figure 22: Left: Model (1) simple  $U_3O_8$  sphere with variable shell thickness. Right: Model (2) modified  $U_3O_8$  sphere with variable outer shell thickness and constant inner cavity.**

For this investigation, CASINO (Version 3.3.0.2, 64-bit) was used to simulate the SE-images at a constant accelerating voltage (AcV). SEM image sequence of particle (1) (Chapter 4.2.3.1.1) was used as a reference; the reference was recorded at a constant AcV = 25 keV. The objective of this investigation was the non-destructive assessment of the inner structure of the inflated intact spheres.

Single, three dimensional spheres containing uranium oxide ( $U_3O_8$ ) were placed on a virtual substrate made of carbon with a density  $\delta_{Carbon} = 2.6 \text{ g/cm}^3$ . A grid of  $\geq 25,000$  points was used to simulate the objects with a max number of 1000 simulated electrons. The beam diameter was 100nm with a spacing of 50 nm. The overall simulation time per object was between 35 - 45 min. Electron trajectory simulations and BSE generation were not of interest for this study just the simulation of SE-images. Image processing was performed with ImageJ and FIJI. Particle morphology was modeled by combining basic three-dimensional objects and planes. Each object is characterized by: (1) position, (2) dimensions and (3) orientation. There are seven basic shapes available in CASINO providing the ability to model complex geometries by combining the shapes. Each object has two defined sides: (a) outside- and (b) inside region.

**Table 7: Parameters for MC-Simulation including shell thickness, particle DIA, AcV, material properties, filling material.**

#	Outer Shell [nm]	Material	Filling	#	Outer Shell [nm]	Material	Filling
1	5	$U_3O_8$	$H_2O$	17	200	$U_3O_8$	$H_2O$
2	5	$U_3O_8$	Vacuum	18	200	$U_3O_8$	Vacuum
3	5	$U_3O_8$	$H_2O$	19	200	$U_3O_8$	$H_2O$
4	5	$U_3O_8$	Vacuum	20	200	$U_3O_8$	Vacuum
5	20	$U_3O_8$	$H_2O$	21	300	$U_3O_8$	$H_2O$
6	20	$U_3O_8$	Vacuum	22	300	$U_3O_8$	Vacuum
7	20	$U_3O_8$	$H_2O$	23	300	$U_3O_8$	$H_2O$
8	20	$U_3O_8$	Vacuum	24	300	$U_3O_8$	Vacuum
9	50	$U_3O_8$	$H_2O$	25	500	$U_3O_8$	$H_2O$
10	50	$U_3O_8$	Vacuum	26	500	$U_3O_8$	Vacuum
11	50	$U_3O_8$	$H_2O$	27	500	$U_3O_8$	$H_2O$
12	50	$U_3O_8$	Vacuum	28	500	$U_3O_8$	Vacuum
13	100	$U_3O_8$	$H_2O$	29	1000	$U_3O_8$	$H_2O$
14	100	$U_3O_8$	Vacuum	30	1000	$U_3O_8$	Vacuum
15	100	$U_3O_8$	$H_2O$	31	1000	$U_3O_8$	$H_2O$
16	100	$U_3O_8$	Vacuum	32	1000	$U_3O_8$	Vacuum

For each region, the elemental composition has to be set – comprising of single elements or multiple elements with the corresponding weight fractions. The mass density can be set automatically or manually. To assess whether these particles are solid or hollow, two different 3-D models were developed: Model (1) and Model (2). Both models share some common attributes for instance each particle object was directly deposited on a Carbon surface and had a distinct boundary layer. It was decided to make the outer shell of each object out of  $U_3O_8$  with a constant density of  $8.4 \text{ g/cm}^3$ . The shell thickness “ $d$ ” for the outer shell was made variable from 5nm to subsequently 1000 nm in total eight iterations. The inside of each object was either filled with water ( $\delta_{H_2O} = 0.5 \text{ g/cm}^3$ ) or with nothing (Vacuum). For each model, two different “fillings” were selected: either no filling = vacuum or water filling to enhance the signal contrast. Model (1) consists just of spherical particle with an outer diameter of  $6.0 \mu\text{m}$  and a variable shell ( $5 \text{ nm} \leq d \leq 1000 \text{ nm}$ ) made of  $U_3O_8$ . Model (2) is a modified version of the latter: it has an additional structure which consists of second shell. This shell forms a spherical cavity around the center of the object and has a total diameter of  $2.0 \mu\text{m}$ . The inner shell is also made of  $U_3O_8$ , but its density is lower and set to  $6.6 \text{ g/cm}^3$ . The reason for the lower density of  $U_3O_8$  is based on SEM studies on solid uranium particles performed at FZJ and IAEA. SEM images show the existence of a thin, denser layer and a density gradient to the center - this is also in accordance to the particle formation mechanics described by Reuge et al. (2008) [66] [67]. Table 7 lists all important features and settings for all 32 simulations.

### 4.2.3 Focused Ion Beam and Time of Flight SIMS

A Lyra3 GM was chosen for the combined FIB-TOF-SIMS investigations. It is a combined SEM / FIB /TOF-SIMS system (TOFWERK, Model C-TOF). A positively charged Gallium beam with a primary current of 577 pA and an AcV = 25 keV was used. The dwell time was  $14 \mu\text{s}$  and a field of view of  $12 \mu\text{m}$  was chosen. Data was analyzed and processed with Mmass (Version 3) and TOF-Sims Explorer (Version 1.0.1.11).

### 4.2.4 Micro-Raman Spectroscopy

Micro Raman Spectroscopy (MRS) measurements were performed at two different institutions:

- (1) At CEA-DAM Ile de France an InVia Renishaw spectrometer (Renishaw, Watton-Under-Edge, UK) was used. The apparatus is a confocal MRS-system which is equipped with two lasers: (1) a green laser with a wavelength of 514 nm and (2) near infrared (NIR) laser with a wavelength of 785 nm. The laser power can be adjusted between 50 – 300 mW as well as the irradiation time. The spectral resolution of the system is  $2 \text{ cm}^{-1}$ . The laser pulses are guided through a sequence of optical filters and condensers, passing through the ocular of the Leica Microscope. The laser is focused on the specimen through an optical fiber. The excited Raman radiation is directed in the opposite direction and is collected by a Peltier cooled CCD detector. The machine was calibrated beforehand with a pure Si sample ( $520 \pm 1 \text{ cm}^{-1}$ ). Particles were identified with an in-build Leica optical microscope at 100 x magnification. Per spectrum, six acquisitions with an acquisition time of 10 s were used. Spectra of the uranium compounds were collected at different laser intensities. Data acquisition was carried out using Renishaw WIRE 3.4 software and data was processed using the Fityk (version 0.9.8) software package.
- (2) At the Technical University of Vienna (TUW) MRS measurements were performed using a Vitec Alpha 300 RSA+ system. Data acquisition and processing was performed on Vitec native software. The system is equipped with 785 nm laser. The stage is controlled by the Vitec Software and allows the stitching of large area scans. The instrument was also calibrated with the silicon band at  $520.5 \text{ cm}^{-1}$ . A mesh size of 300 g/mm was used. Irradiation time and laser power can be adjusted accordingly.

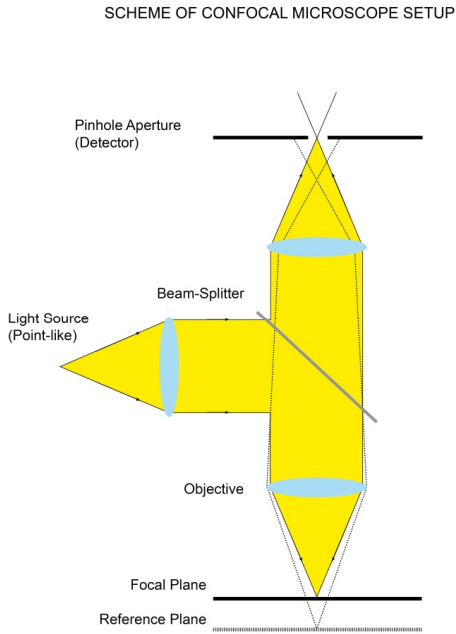
All comparison particles used for MRS were prepared from certified reference materials which were on stock at IAEA. Minute quantities were grinded and transferred via inertial impactation on glassy carbon disks (Ted Pella, 1” diameter). All operations were performed inside a Class 100 laminar bench and inside a Glove Bag.

For the  $\mu$ -Raman Spectroscopy investigations at CEA and TUW, five different references were prepared and measured: (1)  $\text{UO}_2\text{F}_2$ , (2)  $\text{U}_3\text{O}_8$ , (3)  $\text{UO}_2$ , (4) Uranyl nitrate Hexahydrate (UNH) and (5) Ammonium Diuranate (ADU). The following chapter will discuss briefly the results obtained from these references. All samples presented were prepared by using the modified inertial impactor which will be discussed in Chapter 5.1. The uranium reference compounds were prepared by carefully grinding the material and dispersion them on cotton swipes. These particles were transferred to C-substrates via inertial impactation using the modified inertial impactor. Stage 1 was heavily greased to intercept the particles of a larger size; Stage 2 was designed to mimic a size distribution much closer and more comparable to particles produced in Jülich which were also deposited onto C-substrate. These Stage 2 targets were predominantly used to assess all five reference materials; some exceptions were made, e.g. uranyl nitrate hexahydrate was also measured from Stage 1.

All samples were measured with a laser wavelength of 785 nm. Acquisition time for all spectra recorded at CEA and TUW was six iterations à 10 s. For the Vitec device at TUW a mesh of 300 g/mm was used. All samples were recorded using a confocal micro Raman setup and all particulates were recorded using a 100 x magnification. All spectra acquired at TUW have a wider wavelength range from 100 - 3200  $\text{cm}^{-1}$ .

#### 4.2.4.1 Confocal Raman Spectroscopy

Raman scattering is a weak effect. The excitation of molecular bonds with electromagnetic waves leads to a variety of scatter effects and non-resonant interactions. This problem is even enhanced in confocal Raman microscopy because the detection volume is limited to a minimum. This problem is even enhanced in confocal Raman microscopy because the detection volume is limited to a minimum, therefore, a large number of spectra have to be acquired and processed. All spectra were collected through a small pinhole detector. The word confocal is defined as having the same focus. In confocal microscopy it describes the fact that the sample is illuminated through a point-like source and just a point-like area of the sample is illuminated. Both the illumination source and the pinhole aperture are positioned in the same focal plane. An image of the sample is gathered by scanning laser focus points. Since the pinhole aperture prevents most of the scattered light from passing through to the detector, only light originating from the focal plane reaches the detector. Some samples can generate strong fluorescence bands. These bands interfere with Raman measurements. Fluorescence intensity can outnumber the Raman intensities by six orders of magnitude and can overlay the Raman bands; reducing the fluorescence background is therefore important. This can either be accomplished by using an excitation wavelength that generates less fluorescence or by reducing the detection volume. Confocal Raman microscopy offers the advantage of detecting Raman signals where normal optical microscopes would just pick up fluorescence signals due the small detection volume. In wide angle microscopy, the whole sample is illuminated and scatters light in every direction. Common microscopy is therefore limited in terms of spatial resolution and due to the large amount of light scattering. Confocal microscopy, however, overcomes these limitations by introducing a point-like light source and second aperture. The spatial resolution of the focal spot in the focal plane is dependent by the wavelength of the light source and the quality of the image formation. With an appropriate pinhole diameter, the lateral resolution can be increased up to a factor of  $\sqrt{2}$ . The basic difference to a standard wide angle microscope is the idea of illuminating just a small spot. The reflected light is retrieved through a pinhole aperture, see Figure 23. Light which does not come from the focal plane does not enter the pinhole thus intensifying the signal or image contrast. With confocal microscopy, three dimensional images of the sample can be obtained.



LAYOUT OF RAMAN SPECTROMETER CONNECTED TO CONFOCAL MICROSCOPE

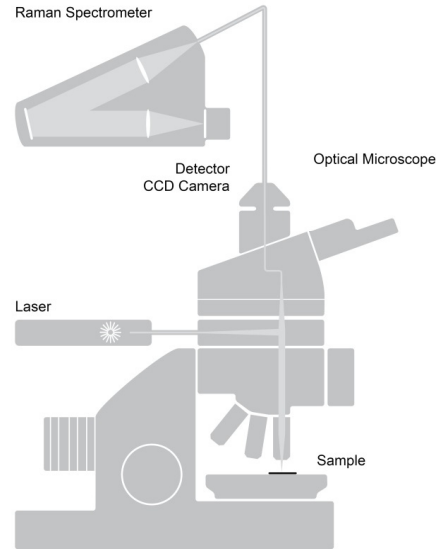


**Figure 23: Basic scheme of a confocal microscope and Layout of a confocal Raman Spectrometer.**

According to Dieing and Hollricher et al. [151], the choice of the pinhole diameter “ $d_0$ ” is very important as well as the lateral position while the focal position is not as critical. The pinhole diameter should not exceed 2.5 x the detector size to avoid loss in resolution in the z-axis. In practice, the pinhole diameter can be up to 4 x the detector size without significant loss of depth resolution and up to 2 x the detector size without significant loss of lateral resolution.

$$\frac{M}{N_A} \geq \frac{\pi d_0}{v_{PMAX} \lambda} \quad (77)$$

The optimal pinhole diameter can be calculated by the following relation where the ratio between the magnification “ $M$ ” and the numerical aperture of the objective “ $N_A$ ” is bigger than the pinhole diameter multiplied with the reciprocal product of the maximal detector size “ $v_{PMax}$ ” with the wavelength of the light source “ $\lambda$ ”.

#### 4.2.5 SIMS Analysis

The LG-SIMS measurements were performed using a Cameca IMS 1280 instrument at the Office of Safeguards Analytical Services Environmental Sample Laboratory (SGAS-ESL). The instrument is calibrated with polydisperse CRM’s obtained from the Joint Research Centre Institute of Reference Materials and Measurements (JRC-IRMM) and the National Institute of Standards and Technology (NIST): these materials are predominantly powdered uranium oxides in “bulk” quantities. These CRM’s were also used in direct comparison to microparticles produced at IEK-6. Additionally, a small section will address microparticles produced at JRC Institute of Transuranium Elements (JRC-ITU) by Erdman, Stetzer et al. [6] [15]. These particles were also used in a small, comprehensive comparison, see Chapter 5.3.4. All particles were deposited on 1” diameter glassy carbon disks, no adhesive was applied.

Cameca IMS 1280 is able to perform large area scans in rastering mode (APM: automated particle measurement) when the primary ion beam raster covers a larger area, APM mode was used to investigate area between 150 x 150  $\mu\text{m}^2$  up to 500 x 500  $\mu\text{m}^2$ . This mode is predominantly used to determine the major isotopic ratios in particular  $^{235}\text{U}$  and  $^{238}\text{U}$ . APM was used to identify single uranium bearing microparticles of interest over a large area. For the investigation of single particles, the MP-

mode (microprobe-mode) was used. All MP values were acquired using a  $10 \times 10 \mu\text{m}^2$  raster. The mass species for " $m/Q$ " -  $m/Q(234)$ ,  $m/Q(235)$ ,  $m/Q(236)$  and  $m/Q(238)$  - were recorded simultaneously with the Multicollector system. A correctional factor for the formation of  $^{235}\text{U}$ -hydride " $^{235}\text{UH}^+$ " had to be applied in order to distinguish it from the  $m/Q(^{236}\text{U}^+)$  signal. The fractionation mass bias or mass bias was determined by the measurement of calibration standards from NIST and IRMM. The corrections account to approximately 0.40 % per atomic mass unit (amu). In order to prevent cross-contamination and to maintain cleanliness, all sample preparation at SGAS-ES was performed in clean environments which correspond to ISO 5/Class 100.

## 5. Results and Discussion

A selected number of particles will be discussed in this chapter which depicts the evolution of the uranium particles in the time range October 2014 – April 2015. First of all, the assessment of inertial impactor designs will be addressed. Subsequently, results on characterization of particles using SEM-EDX in order to investigate the elemental composition, size, geometry and shape will be presented. This part will be complemented by computational means in order to quickly assess the inner composition and density of certain particles and by time of flight SIMS to assess the isotopic and elemental composition as well as the inner morphology of single particles of interest. Finally, this chapter presents results from SIMS analysis, which serves for the evaluation whether these particles are fit to be used as QC or even as RM. Some of the investigations are highly specific to LG-SIMS. The crystal structure will be investigated using  $\mu$ -Raman Spectroscopy.

### 5.1 Particle Collection

Initially, the collection yield of the inertial impactors was not sufficient. This issue exemplifies the importance of a well-adjusted collection system: (a) air flows and (b) impactor design have to be coordinated. Interestingly, the impactors used in this project, IAEA design, were never fully characterized. Since all samples which are discussed in this chapter were prepared using inertial impactors, it is necessary to take a closer look at them. The following sub-chapters evaluate the efficiency and performance of the standard (one stage) and modified (two stage + changed nozzle diameters) designs – the two stage design will be referred to as modified inertial impactor (MII).

#### 5.1.1 Assessment on the Efficiency of the “One Stage Inertial Impactor”

The one stage inertial impactor was designed at SGAS as a disposable component to collect debris from cotton swipes. Its design was derived from empirical studies and experience gained from decades of experience. It is comprised of three basic components: (1) an upper body-part which contains the nozzle and (2) a center body which houses the 1” glassy carbon planchet and redirects the air current to (3) the bottom part of the impactor; the schematics were already depicted in Figure 12. The inertial impactor was initially developed to be used to vacuum swipe samples with average air flow of 6 - 10 l/min. As discussed earlier, the cut-off diameter “ $d_{50}$ ” is a measure for threshold of the aerodynamic diameter that can be collected efficiently.

The inertial impactor was initially developed at SGAS to transfer matrix material from cotton swipes onto glassy carbon substrates at air flows around 4 l/min. The same impactor design was also used as a disposable sampling unit for the production of monodisperse uranium particles at Forschungszentrum Jülich GmbH. Particles were collected at air flows around 6 l/min. Therefore, the impactor efficiency was assessed at various air flows ranging from 4 l/min to 35 l/min. The aim of this assessment is to evaluate the size distribution, the radial distribution and the collection efficiency. For these experiments certified soil matrix was used (Sigma Aldrich, Channel sediment, BCR-320R).

About 0.5 g soil matrix was carefully ground and then transferred onto a cotton swipe. All particles are erratically shaped and of polydisperse distribution. Matrix material was then transferred from the cotton swipe onto a pre-cleaned silicon wafer (purchased from Ted Pella Inc., 3” diameter) using the one stage inertial impactor. The Si-wafer disk had a rectangular shape with an overall area of 25 x 25 mm<sup>2</sup> – reference marks were applied carefully carving by hand before the experiments. A composed areal image was recorded and stitched together from a large number of single images recorded at 5x magnification on an optical Zeiss microscope (Stitching with FIJI and optical microscope: Zeiss Axio-Vision). The covered area of the stitched image accounts for approximately 20.0 x 20.0 mm<sup>2</sup>.



**Figure 24: Target surface after vacuum impaction, with visible score marks.**

For each air flow, a predetermined pattern of five steps was used to vacuum the particle off the target substrate. In total, over 17211 particles were counted with a size distribution range “ $R$ ”  $1.26 \leq R \leq 21.00 \mu\text{m}$ . Therefore, the feret diameter was used as the particle size. For each air flow, the theoretical cut-off diameter was calculated accounting for equation 41, the values are depicted in Table 8. Particles were collected on pre-cleaned glassy carbon disks (purchased from Ted Pella Inc., 1” diameter). After the collection the disks were transferred to an optical microscope (Zeiss Axio Vision) to acquire multiple images (in total over 500) to compose a stitched image – this was performed using FIJI [f] [152]. The number of particles collected and their size distribution was counted using the particle analysis plugin of FIJI. A spherical area of approximately  $7.07 \text{ mm}^2$  was investigated, which accounts for a radial length of  $\sim 15 \text{ mm}$  from the center of each glassy carbon disk. Due to the large amount of data acquired for each stitching, no larger area could be processed. Six different air flows were used for the evaluation of the one stage inertial impactor: 4 l/min, 10 l/min, 15 l/min, 20 l/min, 25 l/min and 35 l/min. The total area which was analyzed on Si wafer surface was about  $400 \text{ mm}^2$ , the Si wafer disk is labelled as “*Target*”. In total 17211 particles were counted using image evaluation software. The matrix material is composed of finely grinded polydisperse entities which have an irregular shape and geometry. Therefore, the feret diameter was used as particle size assessment. Image processing also showed a homogenous particle distribution throughout the whole investigated area. The particle sizes ranged between  $1.26 - 21.00 \mu\text{m}$ .

**Table 8: Test sequence for one-stage inertial impactor design at various air flows ranging from 4 - 35 l/min, investigated area, number of particles found and the resulting yield [%].**

	Substrate	Area, [ $\mu\text{m}^2$ ]	Particle, [#]	Yield, [%]
Target (before)	Si-Wafer	$4.00 \cdot 10^5$	17211	-
4 l/min	Glassy Carbon	$7.07 \cdot 10^3$	1354	8.27
10 l/min	Glassy Carbon	$7.07 \cdot 10^3$	1174	6.98
15 l/min	Glassy Carbon	$7.07 \cdot 10^3$	889	5.22
20 l/min	Glassy Carbon	$7.07 \cdot 10^3$	759	4.41
25 l/min	Glassy Carbon	$7.07 \cdot 10^3$	657	3.85
35 l/min	Glassy Carbon	$7.07 \cdot 10^3$	519	3.01

[f] FIJI is a software distribution of ImageJ: <http://fiji.sc/Fiji>

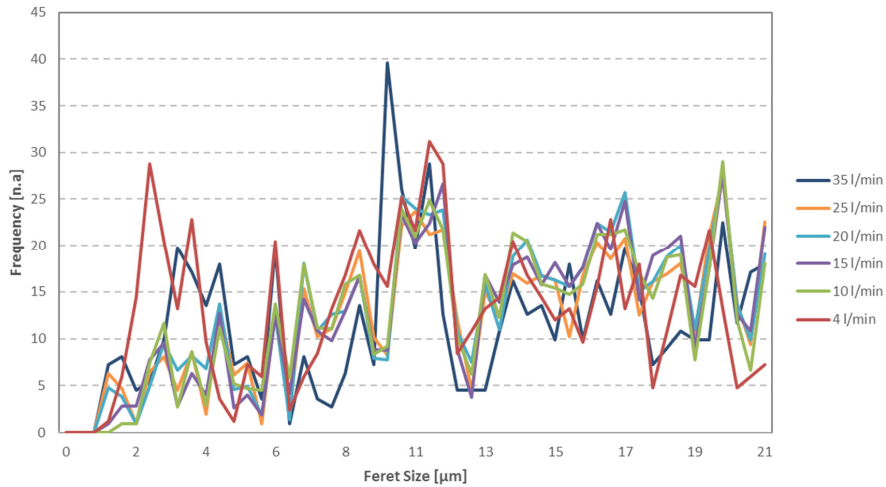


**Figure 25: Histogram depicting the number of particles per size-iteration for each batch from 4 - 35 l/min.**

For each air flow iteration; a theoretical cut-off diameter " $d_{50(theor)}$ " was calculated and compared with the measured values – with increasing air flow the value for the cut-off diameter decreases, see Chapter 2.1.4. The air flow increases almost by a factor of 8.8 while the cut-off diameter decreases by over 36 %. Investigation of the images acquired after the vacuum impaction show that the retention of particles is significant. Particles were detached only in areas where the nozzle had contact or was in close proximity. Figure 24 shows a visible score marks caused by the nozzle tip, just particles in close proximity were detached. In Figure 25 the size distribution of each iteration was plotted as a function of the number of particles collected. The size distribution above " $d_{50}$ " is randomly distributed. But a trend appears: The number of particles collected decreases with increasing air flows.

This phenomenon can be accounted for by two effects which act against one another. A higher air flow increases the number of particles impinging on the surface, on the other hand higher air flows also increase the probability of particles being detachment due to shear-, lift and drag forces. According to Misra et al. (2002) [153], this phenomenon is caused by turbulence and pressure changes over the substrate surface. Misra et al. describe a pressure drop on the surface which is located directly under the nozzle exit. The radial distribution of the particles over an angle of 360° was investigated by image-processing. Stitched, composed images of each glassy carbon disk were investigated using FIJI.

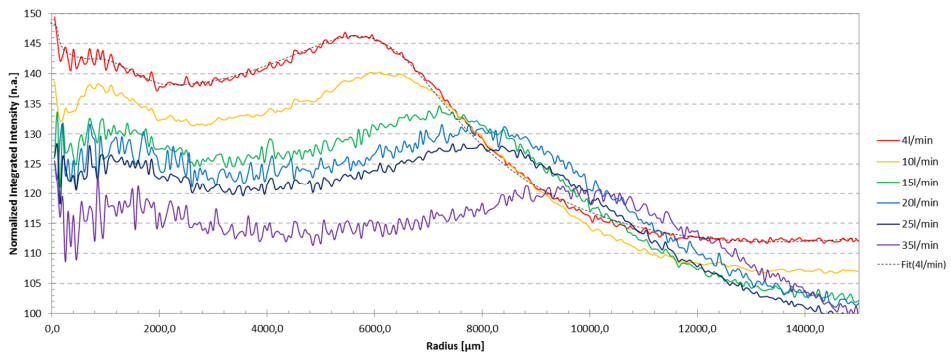


**Figure 26: Radial profile distribution over 360° for all six air flows: 6-35 l/min.**

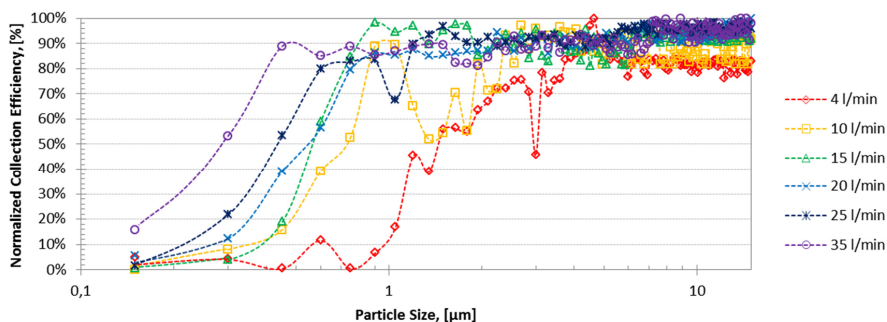


**Figure 27: Normalized collection efficiency curves for each air flow: 4-35 l/min.**

The collection pattern is a unique characteristic for each inertial impactor. The radial distribution depends strongly on the air flow. Increased air flow causes the circular patterns to expand; Figure 26 illustrates this trend. Additionally, the number of particles collected is proportional to the calculated intensities, thus generating an air flow dependent gradient. The data depicts the integrated and normalized intensities which were acquired using the “Radial Profile Angle”-Plug-In in FIJI. This graph also shows the characteristic deposition pattern of this impactor design. It becomes obvious that the radial distribution of the accumulation of particles is dependent on the air flow. The data profile for 4 l/min was chosen as an example to highlight a typical accumulation profile, see the red dotted line in Figure 26. It shows a typically distribution over 15.000  $\mu\text{m}$ : Generally, the accumulation profile shows two distinct maxima: the first one is close to the center and has a rather sharp form. This investigation showed a radial length 130 - 140  $\mu\text{m}$ , for all batches. The fuzziness and tailings can be accounted for by the polydisperse particle distribution and the low number of particles with small sizes. The second maximum is more distinct for each air flow and shows a wider but equally strong signal. The radial distribution of this peak is correlated to the air flow. The radial distance increases with increasing air flow respectively: for 4 l/min it is about 5800  $\mu\text{m}$ , for 10 l/min it is 6150  $\mu\text{m}$ , for 15 l/min it is 7200  $\mu\text{m}$ , for 20 l/min it is 7750  $\mu\text{m}$ , for 25 l/min it is 7900  $\mu\text{m}$  and for 35 l/min it is 9950  $\mu\text{m}$  away from the center.

**Table 9: Theoretical and measured cut-off diameters for the one-stage inertial impactor.**

	$d_{50(\text{theor})}$ , [ $\mu\text{m}$ ]	$d_{50(\text{meas})}$ , [ $\mu\text{m}$ ]	$\Delta$ , [%]
4 l/min	1.17	1.49	27.5%
10 l/min	0.71	0.78	9.86%
15 l/min	0.57	0.60	6.01%
20 l/min	0.48	0.45	6.05%
25 l/min	0.42	0.51	21.14%
35 l/min	0.34	0.39	13.70%

The collection efficiency was derived from the size dependent distribution and the data acquired from the radial profile distribution using FIJI. Figure 27 shows the normalized collection efficiency plotted against the particle size. Values for the measured cut-off diameters “ $d_{50(\text{meas})}$ ” were derived from this plot.

This investigation endorsed the prediction that the cut-off diameter decreases with increasing air flow. Table 9 depicts the discrepancy between the theoretical cut-off diameters “ $d_{50}$ ” and the measured one “ $d_{50(\text{meas})}$ ”. Interestingly the deviation from both values increases low and high air flows significantly > 13 % up to > 27 % - For air flows at 6 l/min, the deviations accounts for > 27 % of the theoretical value and for 25 l/min > 21 %. The higher sigma values at an air flow of 4 l/min can be mainly accounted for by a systematic error in the particle size determination process. At higher air flows,  $\geq 25$  l/min blow-off and re-entrainment effects also come into play, see Chapter 3.2.1.

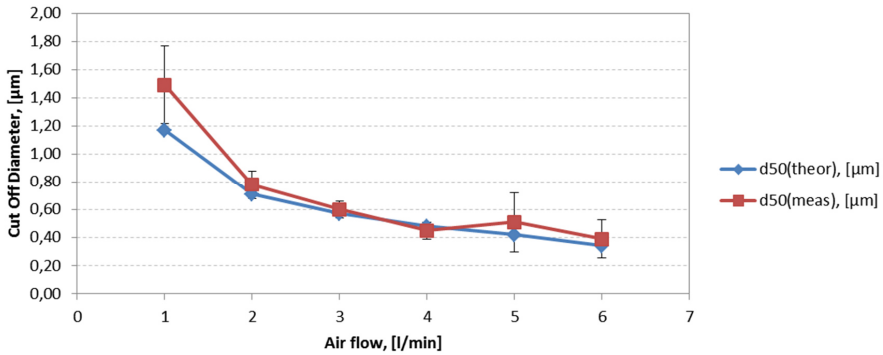


**Figure 28: Comparison of theoretical and measured cut-off diameters for the one-stage inertial impactors used at IAEA and FZJ.**

These values indicate the limitations of this investigation the accounted systematic and intrinsic errors are significant. At larger particle sizes, the efficiency curves reach a saturation plateau which is differs about 8 % between 4 l/min and 35 l/min. Figure 28 depicts the theoretical cut-off diameters in direct comparison with the measured cut-off diameters and the corresponding deviation. Figure 28 also confirms the forecast that the cut-off diameter actually decreases with in increasing air-flows.

### 5.1.2 Modified Inertial Impactor

The modified inertial impactor (MII) is a derivative of the one stage inertial impactor. The development of the MII was caused by the need to prepare suitable reference substrates with comparable size distributions which were used for  $\mu$ -Raman analysis which were performed at CEA and TUW. The MII is a two stage inertial impactor which is designed to be operated at a set air flow rate of 4 l/min. Stage 1 is designed to retain particles bigger than  $2\mu\text{m}$  (nozzle diameter is 2.2 mm,  $d_{50(\text{theor})} = 2.14\ \mu\text{m}$ ). Additionally, Stage 1 was coated with a layer of a PIB-Nonane.

The existing nozzle of Stage 2 was re-adjusted to a diameter of 1.6 mm – which results in a theoretical cut-off diameter “ $d_{50(\text{theor})}$ ” of  $d_{50(\text{theor})} = 1.73\ \mu\text{m}$ . Stage 2 was used for the collection of particles  $\ll 2\ \mu\text{m}$ . Both modified stages were assembled and glued together, see Figure 29. For this investigation polydisperse glass bed particles were used (Retsch Technology, Typ S 10 – 100  $\mu\text{m}$ ).

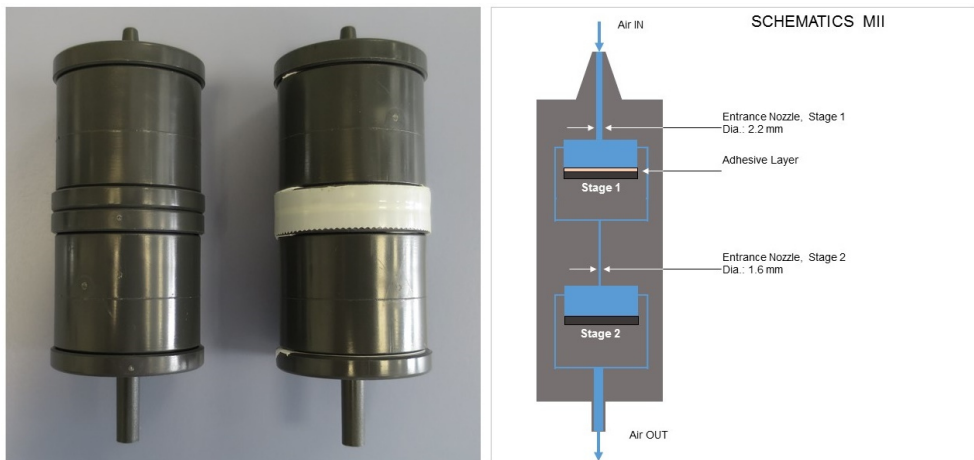


**Figure 29: Left: Photo of modified inertial impactor designed at SGAS-ESL; Right: Scheme of MII.**

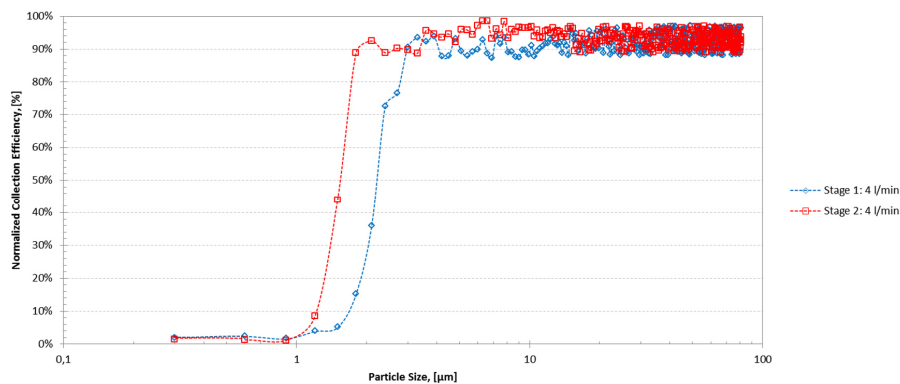


**Figure 30: Normalized collection efficiency curves of Stage 1 and 2.**

The particles were ground and carefully placed onto a cotton swipe. The feret diameter was used as a measure for the particle size due to the erratic shape of the polydisperse particles. Pre-cleaned glassy carbon disks (1" diameter, Ted Pella Inc.) were used to collect the particles. The first stage was covered with a thick adhesive layer consisting of high viscosity silicone grease (Merck, Germany) and Stage 2 was left uncoated. Particle size distribution was measured by performing the particle analysis plug-in in Fiji from stitched images. The same parameters as in Chapter 5.1.1 were used: the investigated area accounted for approximately  $7.07 \cdot 10^3 \mu\text{m}^2$ . Particle retention was similar to Chapter 5.1.1. The cut-off diameters were measured by plotting the normalized and integrated signal of the collection efficiency against the measured particle size. The measure cut-off diameters " $d_{50(\text{meas})}$ " ranged from 7.13 % for Stage 1 to 25.06 % for Stage 2, see Table 10.

The normalized functions are depicted in Figure 30 do not depict the relation of measured signal. For Stage 1 the signal was much higher due to the heavy loading of the substrate. Therefore, the function for Stage 2 is blurred and less distinct. On Stage 2, the number of particles collected was much lower, about a factor of 10. Stage 1 was heavily covered with particles caused by the adhesive layer. Multiple layers of microparticles stacked on top of one another, thus not all particle sizes could be evaluated. Stage 2 was less loaded and showed an expected particle size distribution. A small but noticeable increase of the particle collection efficiency could be observed for particle sizes  $> 6 \mu\text{m}$ . The phenomenon may be caused by a systemic property of this particular impactor stage. The radial distribution was evaluated by investigating stitched images over a mean area with a radial distribution of 15 mm from the disk center, see Figure 31.

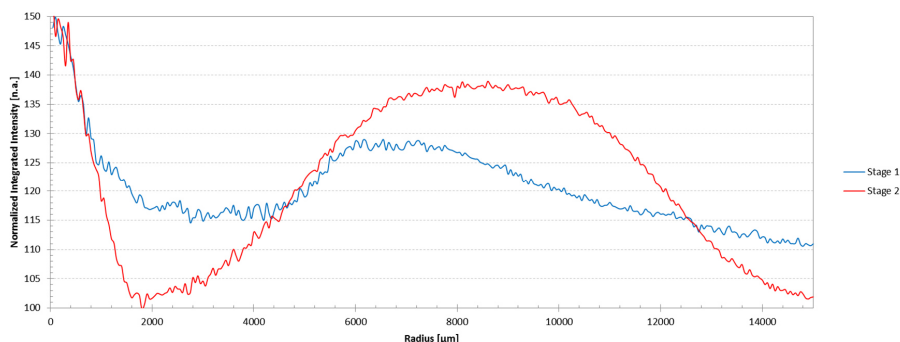


**Figure 31: Radial profile distribution over 360° for Stage 1 and 2 – Intensities are normalized and not equivalent.**

**Table 10: MII-stage properties and corresponding theoretical and measured cut-off diameters.**

	Nozzle Dia. [mm]	$d_{50(\text{theor})}$ , [ $\mu\text{m}$ ]	$d_{50(\text{meas})}$ , [ $\mu\text{m}$ ]	$\Delta$ , [%]
Stage 1	2.20	2.14	2.30	7.13%
Stage 2	1.60	1.30	1.73	25.06%

The estimated total collection yield for Stage 1 was about 23.06 % and for Stage 2 about 2.11 %. These values are heavily biased due to the high uncertainty caused by the heavy loading of Stage 1 and the insufficient area relocation of the target substrate.

### 5.1.2.1 Sample Preparation for $\mu$ -Raman Spectroscopy

The MII was used for the sample preparation of the  $\mu$ -Raman investigations which were conducted at CEA, Ile-de-France and TU Vienna. All samples were prepared in the same manner: A modified two stage impactor was used to mimic the particle size distribution found on the uranium particles produced at Forschungszentrum Jülich. Two different batches produced at Jülich were evaluated: SG141027\_12A and SG140521\_02. Five different reference samples - including (1)  $\text{UO}_2\text{F}_2$ , (2)  $\text{U}_3\text{O}_8$ , (3)  $\text{UO}_2$ , (4) uranyl nitrate hexahydrate (UNH) and (5) ammonium diuranate (ADU) - were selected and carefully prepared. All reference samples were grinded and distributed on to cotton swipes. Particles were collected via inertial impaction with the modified inertial impactor (MII) at standard conditions: 4 - 4.5 l/min. The grinding of the reference material lead to polydisperse size distribution between 1 - 25  $\mu\text{m}$ . The MII offers the opportunity to narrow this distribution down to an acceptable level: The two stage impactor contains two stages: stage I is covered with Si-grease to catch most of the heavier particles with higher mass and higher aerodynamic diameter. The second stage is uncoated and contains a comparable size distribution - see Chapter 5.1.2.

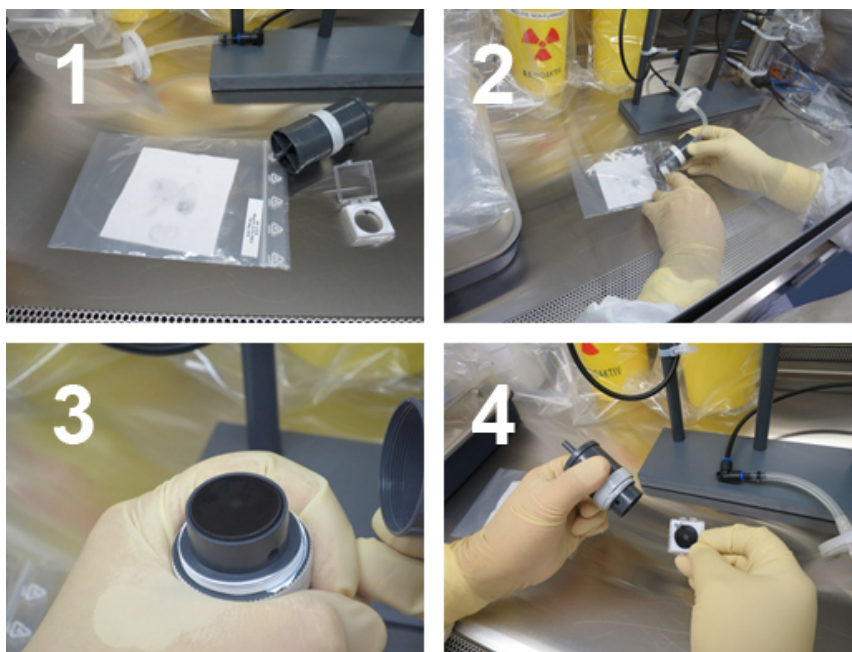


**Figure 32: Sequence of sample preparation for  $\mu$ -Raman measurements.**

### 5.1.3 Cyclone Impactor

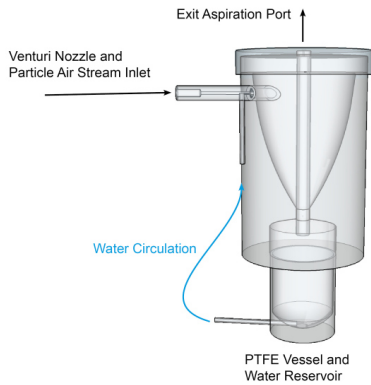


**Figure 33: Left: Schematics of Cyclone Sampler with Venturi Nozzle Inlet and right: Image of the Cyclone Sampler with Venturi Nozzle.**

In a cyclone impactor a jet of particles impinges tangentially on the surface of inner conically shaped structure. The air flow is diverted in downward directed spiral to the bottom where the exit aspiration port is located. Cyclones are generally used for high air flow measurements. The cyclone sampler was modified by attaching a Venturi nozzle as an inlet to the cyclone body. The Venturi nozzle was connected via PTFE tubing to the bottom PTFE vessel, see Figure 33. This inlet produces a fine aerosol water spray at air flows. This inlet produces a fine aerosol water spray at air flows ranging from 20 - 135 l/min. At higher air flows above 130 l/min, the turbulences and pressure increase and liquid is uncontrollably released through the exit aspiration port. Pretests showed a recommended operating range of 13 - 120 l/min. The collection vessels are commercially available PTFE vessel with a thread and variable volume. For this assessment, PTFE vials purchased from VWR, Germany ( $V = 20\text{ml}$ ) were used. The vessel contained 5 ml MilliQ water. The cyclone Sampler was developed very early on out of the necessity to improve the collection yield. At the time, the number of collected particles was  $\ll 1000$  per  $10 \times 10 \text{ mm}^2$ . Another advantage is the collection of micrometer sized particles as suspensions. Some precursor sampling devices had been developed using 3D printed prototypes. Finely ground certified soil matrix (Sigma Aldrich) was used to assess the collection efficiency by gravimetical means at different air flows between 0 - 130 l/min. The collection yield was assessed by gravimetical means.

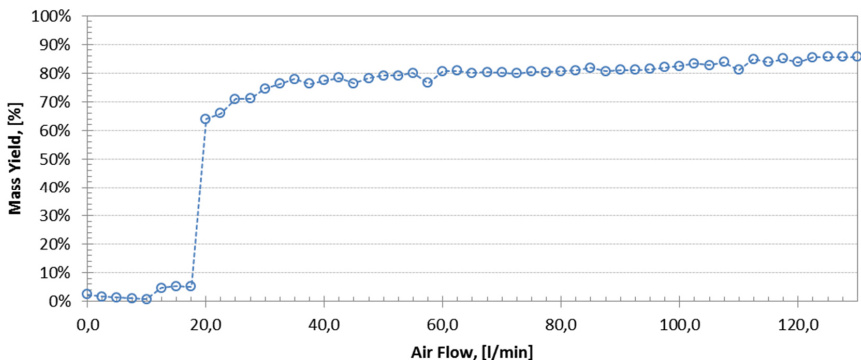


**Figure 34: Collection efficiency of the cyclone sampler at various air flows.**

Figure 34 indicates that the Venturi orifice does not work sufficiently at air flows  $\ll 20$  l/min. The yield for lower air flows ranging between 20 - 45 l/min increases slowly and respectively the yield from 64 % to 76 %. This is due to the fact that the establishment of the aerosol spray takes a few seconds to fully establish itself. Small quantities of soil are ejected out of the aspiration port. The collection efficiency is much higher for the cyclone sampler than for the inertial impactors. But it can just be operated at high air flows. It can be concluded that this cyclone impactor collects all investigated particle sizes with the same efficiency. This is an important advantage to against conventional inertial impactors.

Note: With the current setup, the cyclone impactor is not feasible because the air flow through the system is  $< 8$  l/min. At the time the cyclone impactor was developed it offered an effective alternative. Nevertheless, after re-adjustment of the entrance nozzle this system offers the opportunity to sample directly into aqueous / organic solution, which simplifies particle transfer to various substrates.

#### 5.1.4 Conclusion

One stage inertial impactors were routinely used for particle collection during this project. They are easy to handle and particle can be re-distributed and transferred onto different substrates quite easily. Also graphite planchets offer the advantage that they can be used in SEM- and SIMS analysis as well. The comprehensive assessment shows that the particle retention on the target graphite substrate at air flows of 4 l/min is the highest. And that the theoretical and the measured mean cut-off diameters are in good accordance. Only at lower air flows does the deviation become more pronounced.

The modified, two-stage, inertial impactor was used for the preparation of the  $\mu$ -Raman spectroscopy investigations. Existing CRMs were used as a control material for these investigations. These uranium compounds consisted of oxides, nitrates, fluorites and were of polydisperse nature and significantly bigger than SG140521\_02, SG141027\_12 and SG150401\_14A. So these compounds were ground and these particulates were deposited onto two different stages. Stage 1 acted as a catcher for bigger particles while Stage 2 was designed to mimic size distribution in the low micrometer range. The calculated and measured cut off diameters differ from 7.13 to 25.06 %.

All inertial impactors show a distinct collection pattern which can also be observed in Figure 31 in Chapter 5.2.1: underneath the nozzle is a strong deposition as well as a radial accumulation a few millimetres away. The radial distance is dependent on the air flow. The higher the air flow the further the radial distribution.

The cyclone sampler was initially developed to overcome the collection yield issues related to the one stage inertial impactor and it offers the advantage of collecting particles directly into a liquid which make the re-distribution much easier. It could be demonstrated that the cyclone design, which was developed at SGAS-ESL, can collect microparticles efficiently at air flows  $> 20$  l/min - 130 l/min.

## 5.2 Characterization of Particle Size and Morphology

### 5.2.1 Overview

This dissertation presents particle production runs conducted between May 2014 and April 2015. Most notable progress was made in the evolution of the particle morphology which is an important indicator of the performance of the production setup. Table 11 lists all six batches that were studied and the type of analyses that were performed. All particles were produced at IEK-6 in Germany and sent to the IAEA for further analysis. SG140521\_02 and SG141027\_12A were investigated intensively with a variety of techniques: from SEM-EDX to LG-SIMS. SG150401\_14A, SG150413\_03A and SG150429\_02A were produced in April 2015 and were examined with the SEM. Scanning electron microscopy investigations was performed on all six batches: SG140521\_02, SG141027\_12A, SG150312\_05A, SG150401\_14A, SG150413\_03A and SG150429\_02A. The aim was to investigate the particle size-distribution, shape descriptors, morphology. The presence of uranium was verified by energy dispersive X-Ray spectroscopy.

**Table 11: Overview of all batches of interest and analytical methodologies applied.**

#	Sample-ID	Technique				
		SEM/EDX	TOF-SIMS	SIMS	μ-Raman	TOFSIMS/FIB
1	SG140521_02	X	X	X	X	
2	SG141027_12A	X	X	X	X	X
3	SG150312_05A	X				
4	SG150401_14A	X			X	X
5	SG150413_03A	X				
6	SG150429_02A	X				

## 5.2.2 Particle Size Distribution

This chapter describes the particle size distribution of all six batches, particle size was determined by a combination of SEM images and image analysis tools. A quality criterion for particles produced as reference material is the monodispersity. The National Institute of Standards and Technology (NIST) defines the concept of monodispersity, see Hackley and Ferraris (2001) [154], as when particle size distribution is considered to be a monodisperse if 90 % of the particle population is within  $\pm 5\%$  from the mean value. Hackley and Ferraris (2001) [154] provide an alternative simple equation to evaluate monodispersity where “ $\sigma$ ” is the standard deviation of the size distribution and “ $\bar{d}$ ” is the mean diameter:

$$\text{Monodisperse: } 1.645\sigma/\bar{d} \leq 0.05 \quad (78)$$

$$\text{Polydisperse: } 1.645\sigma/\bar{d} \geq 0.05 \quad (79)$$

Particle size, geometry and morphology are significantly dependent on the precursor solutions and the conditions during droplet-to-particle conversion. That is why the batches are discussed in chronological order. Depending on the uranium concentration of the precursor solution, we expect to see different mean particle sizes for each batch. Additionally, we expect to see a decrease of size spread due to better adjustments of the aerosol production, to a real mono disperse size distribution.

The particle size distribution of each batch was derived from large areal SE-Images (see Chapter 5.2.2). These images were created by stitching multiple single, high resolution SEM images together. This procedure was necessary to obtain a statistical significant number of representative particles or respectively to investigate the entire specimen surface. These stitched images were used as a basis for an automatic particle analysis using image acquisition software such as ImageJ and FIJI to assess the size distribution and the corresponding uncertainty of each batch. The following sub-chapters will depict the process for each batch individually.

### 5.2.2.1 The First Evolution Step: SG140521\_02

SG140521\_02 was developed to produce monodisperse spherical particles. An automated particle analysis was done using SEM images and FIJI: a mean diameter of about  $1.25 \pm 0.60 \mu\text{m}$  was derived. SEM investigations further revealed the existence three distinct particle species: (A) a small number of “solid” uranium particles with a mean size of  $1.35 \pm 0.53 \mu\text{m}$ , (B) a larger number of intact, inflated particles with a size range of  $6.5 \pm 0.5 \mu\text{m}$  and (C) particle debris and agglomerations ranging from  $\sim 4.5 - 9.2 \mu\text{m}$ . The shape descriptors were also analyzed by investigation the aspect ratio of particles of interest: predominantly of population (A) and (B). The following paragraphs will depict the findings in detail.

Particle analysis was performed on a stitched image which covers almost the whole surface area of the planchet:  $a = 4.91 \cdot 10^8 \mu\text{m}^2$ . Single images were recorded with a Zeiss Z2 optical microscope at an effective magnification of  $\times 20$  and stitched together using the Axio Vision software. In Figure 35 the stitched image is named “Original”.

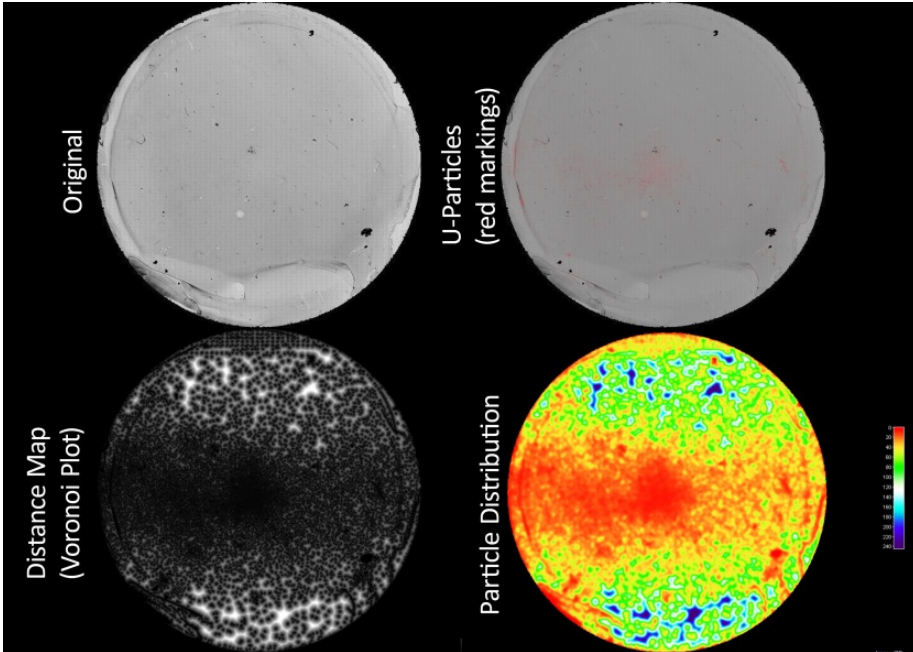


Figure 35: Particle analysis on SG140521\_02, depicting the particle distribution on a 1" glassy carbon disk.

This image was further processed by using the FIJI to remove unwanted artefacts and dust matrix. In total 7076 particles of interest were identified which were labelled red and named "U-Particles". The size of the red markings corresponds to the actual particle size. For a better graphical presentation, a mean inter particle distance profile was calculated using the Delaunay Voronoi plugin in. The "Distance Map" shows a typical distribution pattern of an inertial impactor. Since the sampling time was 30 min, blow-off effects at the bottom and top of the planchet can be observed. For a better representation, the distance map was colored and is named "Particle Distribution", see Figure 36.

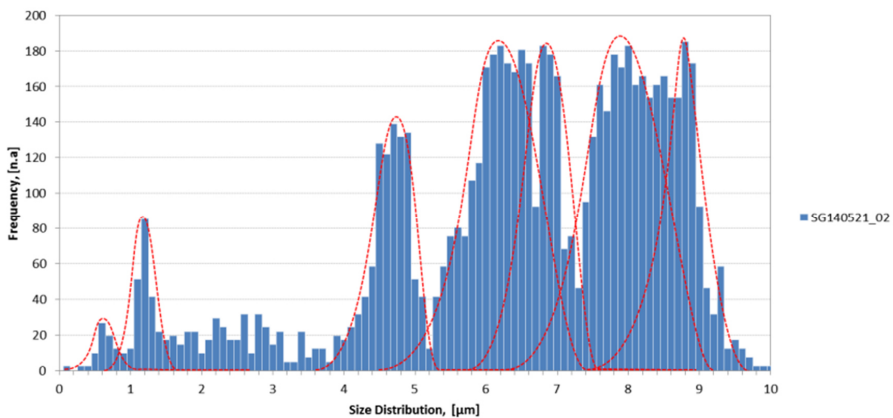
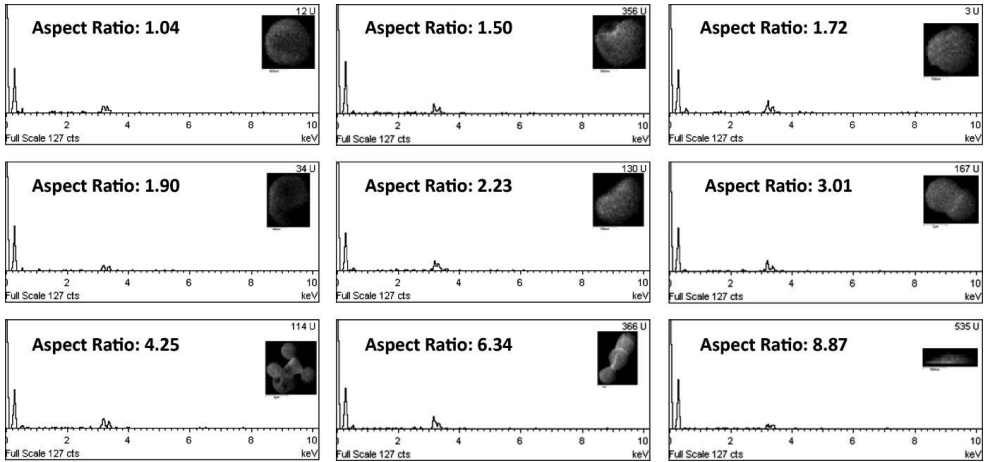


Figure 36: Particle size distribution for SG140521\_02.



**Figure 37: Aspect Ratio deviations due to particle deformations, agglomerations, artefacts and measurement errors.**

Five different particle species could be identified by using SEM-EDX (Jeol JSM 6610). All particle depicted in the following paragraph were identified as uranium containing particles. Several interesting sizes were observed: (1) a small number of debris with a mean size distribution of  $0.67 \pm 0.5 \mu\text{m}$ . Image processing with FIJI revealed that this species has an aspect ratio of  $0.95 \pm 0.05$ . According to image processing, these sub-micron particles are spherically shaped. Their signal is about 1/3 of species (2) which has a mean diameter of  $1.35 \pm 0.5 \mu\text{m}$ . Species (2) is in correspondence with the calculated particle diameter of  $1.25 \pm 0.60 \mu\text{m}$ . These particles seem to be solid and have a nearly spherical shape. The outer crust shows a lot of scores and dents. This fact is also represented in the mean aspect ratio of species (2) of  $0.77 \pm 0.19$ , see Figure 37. The signal intensity of species (2) is about 2.5 x smaller than the signal of species (3) which has a mean diameter of  $4.61 \pm 0.27 \mu\text{m}$ . This species could be identified as hollow, inflated particles; most of which are intact. The evaluation about the hollowness will be discussed in detail in Chapter 5.2.3.1. An additional intact hollow and inflated species (4) could be observed at a size  $6.50 \pm 0.53 \mu\text{m}$ . Both species (3) and (4) are spherical and show a similar mean aspect ratio of  $0.98 \pm 0.02$ , see Figure 37. Above  $6.7 \mu\text{m}$ , an additional species (5) could be identified. These particles are predominantly agglomerations of collapsed particle shell and debris of various particle species. Due to the large amount of debris of inflated particles, the mean diameter could not be determined satisfactory. SEM studies also showed a homogenous distribution of these all particle species throughout the entire area. Figure 35 depicts a distribution pattern which is typical for the IAEA inertial impactors, the radial distribution pattern acquired in Chapter 5.1.1 (Figure 26) and 5.1.2 (Figure 31) support this observation. No sharp distinction and radial separation between all species was seen: even a smooth transition of intact spheres and debris at a size range " $d$ " of  $6.0 \leq d \leq 9.0 \mu\text{m}$  could be observed. Shape descriptors: Species (4) and (5) showed the highest number of particles. The ratio of species (2) to species (4) and (5): 1.0 : 1.5 : 2.1. According to NIST (see equation 78 and 79), this batch shows a clear polydisperse distribution. The aspect ratio is a simple measure for the circularity of a particle. The following figure (Figure 37) depicts a wide range of particles originating from SG140521\_02 with aspect ratios ranging from 1.04 - 8.87 - the corresponding EDX spectra are included. The aspect ratio is a simple measure for the circularity of a particle. But for particles with an irregular shape, the aspect ratio is not the optimal solution to describe geometric shape factors. Therefore, the term circularity is introduced. The circularity " $C$ " is defined as:

$$C = 4\pi \frac{\text{Area}}{(\text{Perimeter})^2} \quad (80)$$

Meaning if a particle is spherically shaped its circularity " $C$ " is 1 or very close to 1. The more the circularity deviates from the value 1 the less it can be considered spherically shaped.

### 5.2.2.2 Towards Consistent Quality: SG141027\_12A

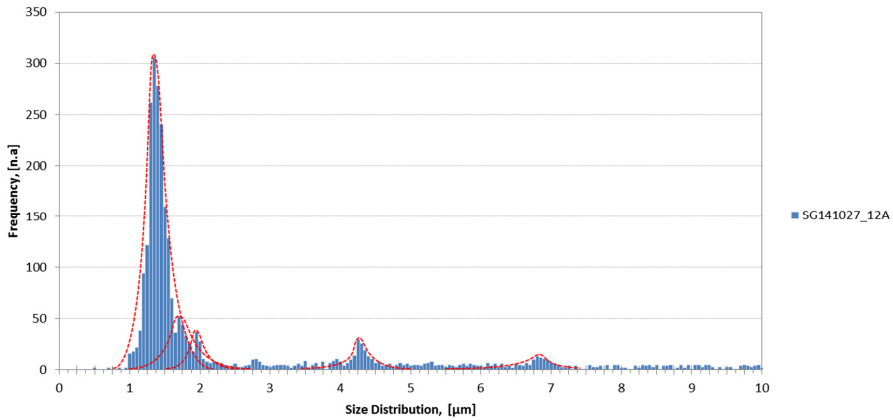


Figure 38: Particle size distribution for SG141027\_12A.

SG140521\_02 and SG141027\_12A were the first uranium oxide batches which were delivered to IAEA SGAS. All particles were designed to have a mean calculated particle size of around  $1.3 \pm 0.4 \mu\text{m}$ . The first assessments indicated good agreement with the theoretical values. In terms of particle production, the biggest change to its successor SG140521\_02 was the disposal of the furnace and the collection time was reduced to 5 min: the whole setup was less bulky due to dispensation of the furnace thus increasing the sampling yield. Particles were collected on an uncoated glassy carbon disk with the inertial impactor mounted up-side down. In total three different areas with a total net-area of  $4.6 \text{ mm}^2$  was investigated: each area totaling in  $1430 \times 1072 \mu\text{m}^2$ . 2689 particles identified using FIJI image processing. The derived mean particle size was  $1.37 \pm 0.19 \mu\text{m}$ . Four additional peaks could be identified which accounted for agglomerations: During the drying process or in the heat field of the furnace single particles can coagulate and form bigger entities. If two particles merge they are called a doublet, respectively three particles a triplet and so on. With each coagulation, the mean diameter of the newly formed doublet/triplet entity grows. For a doublet, this accounts to “ $d_2$ ”:  $d_2 = d_1 \sqrt{2}$  and for a triplet “ $d_3$ ” respectively:  $d_3 = d_1 \sqrt[3]{3}$ . The doublet peak at around  $1.73 \mu\text{m}$  is about 1/6 smaller than for the dominant  $1.37 \mu\text{m}$  peak and the triplet peak at around  $1.97 \mu\text{m}$  is smaller by a factor of approximately 1/8. A bigger inflated particle species at around  $4.25 \pm 0.22 \mu\text{m}$  appears. According to SEM investigations, these particles mostly appear at in the center area of the disk. Their intensity is about 1/10 smaller than for the dominant peak. One last weak peak could be observed at about  $6.80 \pm 0.31 \mu\text{m}$ .

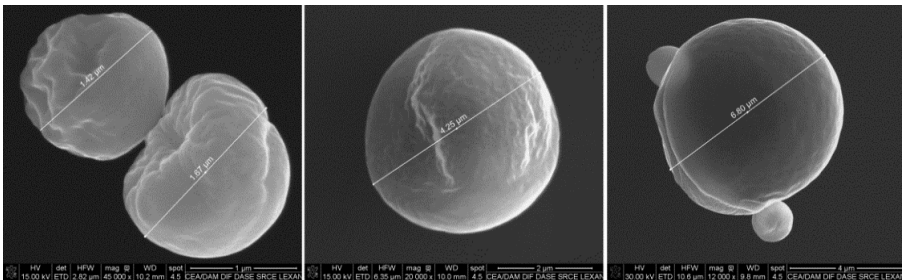
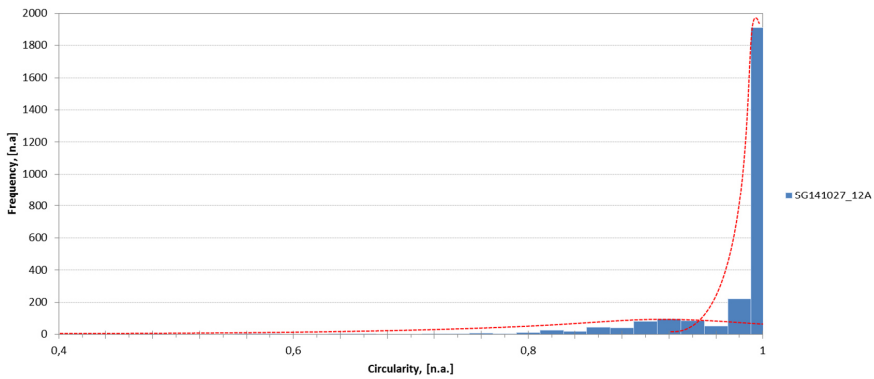


Figure 39: Three SE-images of particles originating from SG141027\_12A, courtesy of O. Marie from CEA/DAM.



**Figure 40: Circularity calculation of SG141027\_12A**

This signal is about 1/24 of the signal of  $1.37 \pm 0.19 \mu\text{m}$ . These particles belong to an even more extreme inflated species. It can be assumed that it might originate from doublet or triplet volumes. Its intensity is about 1/24 of the dominant peak. The majority of the particles investigated was found around the mean value. Nevertheless, according to equation 78 and 79 the calculated value accounts to  $0.23 > 0.05$  which means that SG141027\_12A does not fully fill the monodispersity criterion. SEM studies showed grooves and notches on the surface of the particles, similar to particle species (2) for SG140521\_02. Figure 39 shows that the particles are not perfectly spherically shaped. These SE- images were recorded at CEA - courtesy to Olivier Marie (CEA). The shape descriptors of all 2689 particles were also investigated. The circularity of all 2689 particles was investigated. Two distinct shapes were found, see Figure 40: one at  $0.92 \pm 0.02$  and a second one between  $0.99 \pm 0.01$ . About 71 % of all particles are within  $0.99 \pm 0.01$ . In total 93.22 % of all particles are within 0.9 - 1.0.

### 5.2.2.3 Consistency: SG150312\_05, SG150401\_14A, SG150413\_03A and SG150429\_02A

Particle sizes are in good accordance with the calculated values of  $1 \mu\text{m}$ . Particle shape is similar to the ones observed in SG141027\_12A. The size distribution of each mean particle species is depicted in Figure 41. SG150312\_05, SG150401\_14A, SG150413\_3A and SG1504229\_02A are similar in regard to their shape and outer structure the only characteristic that differed was the mean particle size.

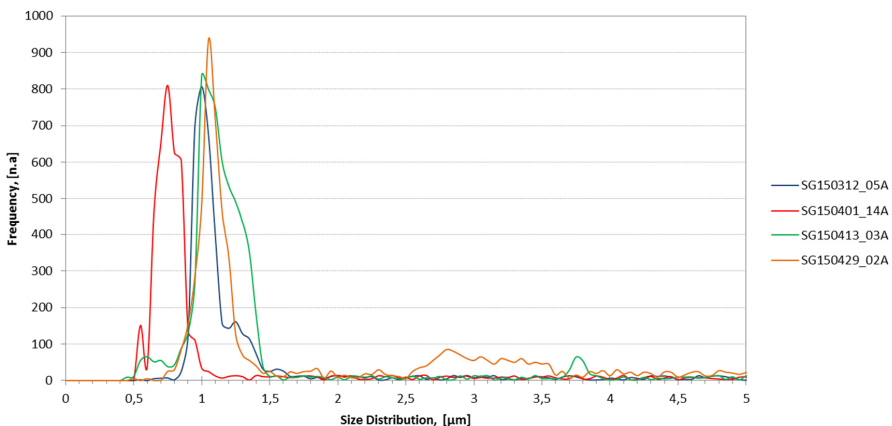


**Figure 41: Size distribution of SG150312\_05 (blue), SG150401\_14A (red) and SG150413\_03A (green).**

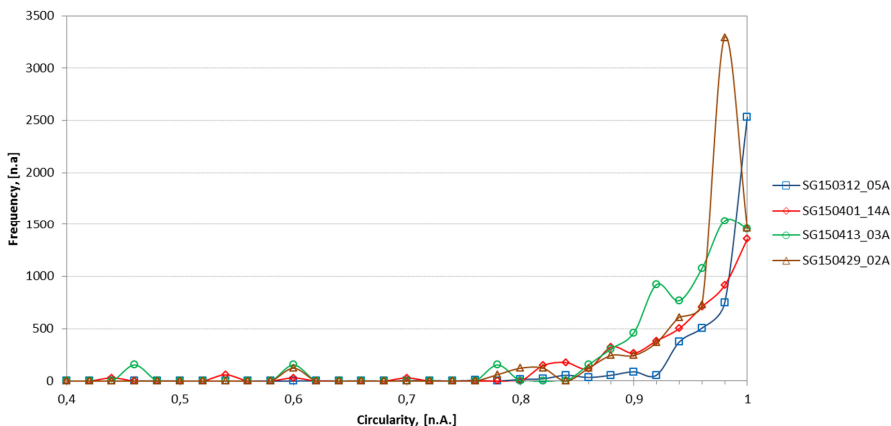


**Figure 42: Circularity of SG150312\_05 (blue), SG150401\_14A (red) and SG150413\_03A (green).**

Therefore, these four batches will be discussed in together in one chapter. For each of the three batches an area of about  $4700 \times 3500 \mu\text{m}^2$  was selected. Particle analysis was performed using FIJI. For these three batches particles looked almost spherical. In order to assess the geometric factor, the circularity was evaluated using FIJI.

For SG150312\_05 4497 particles were counted. The mean particle size was  $0.99 \pm 0.15 \mu\text{m}$ . A small doublet tailing was measured at  $1.25 \pm 0.13 \mu\text{m}$  with about 1/5 of the intensity of the main peak. The particle size distribution is not monodisperse according to Hackley and Ferraris (2001) [154]. But the distribution is much narrower: about 96% of all particles within 0.9 - 1.0 and 73% of all particles are within 0.98 - 1.0. A small tailing at 0.84 - these tailings can be associated to minor deformations which accounts to 1.22 % of the total particle population.

SG150401\_14A was investigated. In total 5043 particles were counted. The mean particle size was  $0.85 \pm 0.15 \mu\text{m}$ . A small doublet tailing at  $1.07 \pm 0.11 \mu\text{m}$  with a signal ratio of about 1/6 was recorded. The shape factor was evaluated by investigating the circularity: about 82% are within 0.9 - 1.0. In comparison, the number of particles which are nearly spherically shaped is lower than SG150312\_05. This may be caused by small changes to the system in particular to the orifice, see Figure 42.

For SG150413\_03A, 7142 particles were counted. The mean particle size was  $1.05 \pm 0.11 \mu\text{m}$ . No doublet tailing at  $d_2 = d_1\sqrt[3]{2}$  could be observed. Interestingly, the first peak appears at  $0.60 \pm 0.10 \mu\text{m}$  with a signal ratio of about 1/13 which accounts for  $\sim 0.9\%$  of the total population. The majority is to be found around the mean, 11.5%. A smaller at around  $3.75 \mu\text{m}$  with an intensity of about 1/13 of the dominant mean peak was observed. This is assumed to be due to an inflated coagulation of doublet or triplet particles; it accounts to 0.9 % of the total population. The shape factors show that 85.41 % are within 0.9 - 1.0 and are partially spherically shaped.

For SG150429\_02A 7505 particles were counted. The mean particle diameter was calculated to be  $1.02 \pm 0.10 \mu\text{m}$ . No doublet peaks could be identified. A small plateau between  $2.6 - 3.6 \mu\text{m}$  with max. 9 % intensity of the dominant peaks species. These particles were attributed to inflated species from various precursor droplets.

### 5.2.3 Characterization of Internal Particle Morphology

Two distinct particle populations were investigated: (1) hollow, inflated particles and (2) solid particles. The presence of an inflated, hollow species was predominantly found in SG140521\_02. The solid particle species can be found on all six batches. Particle morphology was assessed either by non-destructive and by destructive assay: SEM-EDX was used in combination with micromanipulation, as well as FIB in combination with TOF-SIMS.

#### 5.2.3.1 Hollow Species: SG140521\_02

The objective of this chapter is the morphology study of the inflated species found in SG140521\_02 and to show by non-destructive and destructive means the inner structure of these entities. A combination of SEM, Micromanipulation and SE-Image simulation revealed the presence of a hollow species. Investigations show that these particles have a thin, permeable outer structure with a mean thickness of about 20 - 50 nm and a second inner structure which are both made from  $U_3O_8$  but with different densities, a detailed study is presented in Chapter (5.2.3.1.1). In addition, the inflated hollow species exemplifies the complexity associated with the adjustment of the final morphology as described by Dash et al. (1999) [76] and Messing et al. (1993) [58] in Chapter (3.1.3).

The first species to be found has a mean diameter of  $1.35 \pm 0.5 \mu\text{m}$ . These particles seem to be solid and are outnumbered by the hollow, inflated species. The second species is far more interesting: inflated and hollow particles with a size range of  $4.61 - 6.50 \mu\text{m}$  could be observed. The formation of this species is controlled by surface kinetics due to the build-up of a semi permeable outer shell. During thermal conversion the trapped liquid and gases evaporate and expand the particle. The exact mechanics are still not fully understood. The expansion can lead to the deformation or total destruction of the particle. The existence of much debris and collapsed shells is a strong indication for this hypothesis. The following Figure 43 depicts the two main particle species which can be observed in SG140521\_02. Each entity was evaluated by SEM at different accelerating voltages (AcV) to see differences in the morphology.

The hollow species shows at very low AcV of 0.5 keV a smooth slightly structured surface with some dark artefacts on the surface which are suspected to be pores and give the outer structure permeable properties. At accelerating voltages above 2.0 keV, the inner cavity become more apparent. The best imaging results were obtained at accelerating voltages of 25 - 30 keV, see Figure 43. The inflated particles were investigated to assess their structure and morphology. According to intensive SEM studies, the particles are almost perfectly spherical and have a smooth surface. The surface shows several unique features: dark artefacts are all over the surface. These artefacts appear to be pores or small venting holes. Each of the inflated particles has a darker discoloration in the center. This area is located directly in the particle center is also spherically shaped and its diameter ranges between  $2.00 - 2.80 \mu\text{m}$ . Computational investigations will indicate the presence of a cavity thus resulting in an intensity loss, see Figure 44 upper left image.

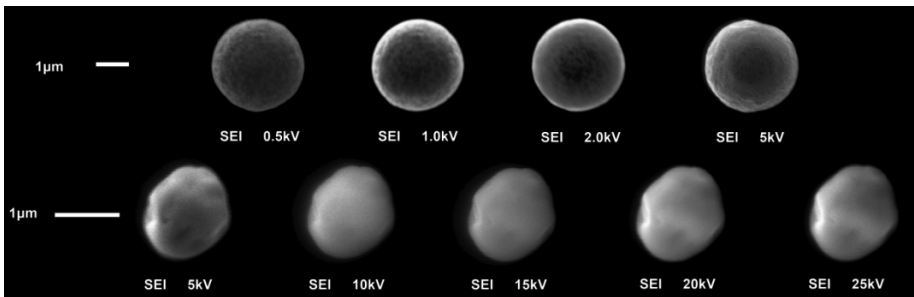


**Figure 43: Above: Inflated, hollow uranium particle at  $0.5 \leq \text{AcV} \leq 5 \text{ keV}$  (Dia.  $> 4 \mu\text{m}$ ) and Bottom: solid particle at  $5.0 \leq \text{AcV} \leq 25 \text{ keV}$  (Dia.  $> 1.35 \mu\text{m}$ ); both originate from SG140521\_02.**

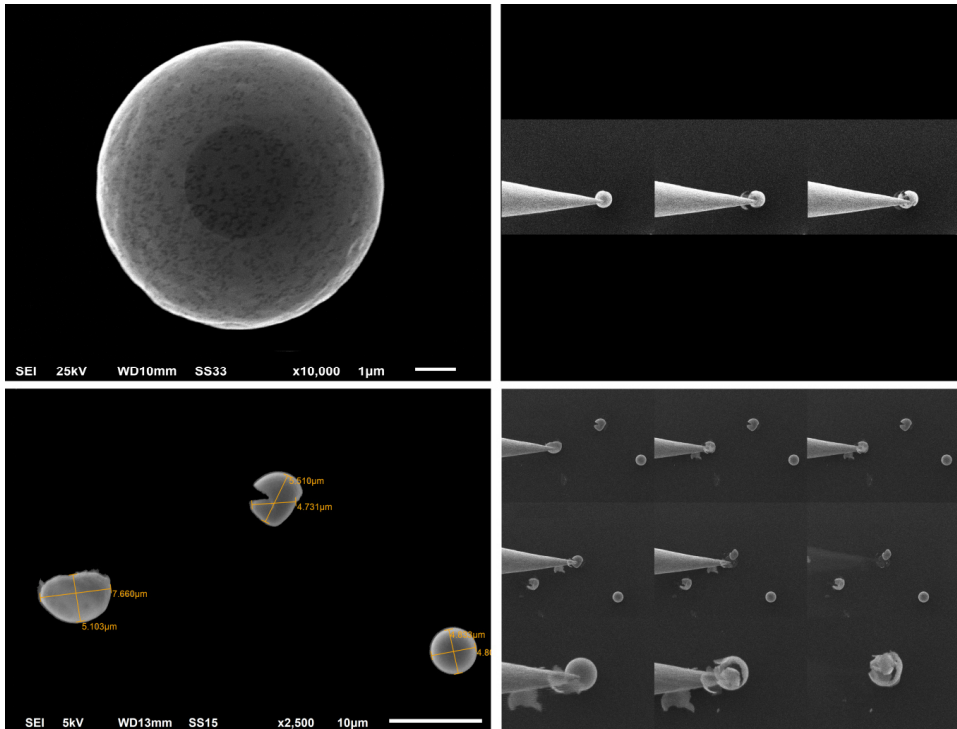


**Figure 44: Left: Inflated particle >6.0 µm diameter and Right: typical fragments and hollow particles on SG140521\_02 (Dia. > 4.8 µm).**

Four different particles were selected as representative samples for further analysis, by SEM/EDX. All particles were identified as uranium containing entities with EDX - the EDX data can be observed in the Appendix. For this investigation, single particles were transferred via micromanipulation and then destroyed with the same system to investigate their internal structure. In total, four different particles and fragments were evaluated by SEM/EDX. The EDX data can be observed in the Appendix. The following Figure 44 depicts four representative particles which are hollow or collapsed shells. Destructive assay was used to investigate the hollowness of these particles by destroying them inside a SEM with a tungsten needle. This tungsten needle was part of a micromanipulator system. SE images were taken before during and after the destruction. SEM investigations indicate that the intact spheres are actual spheres which are not damaged by the impactation. Before destruction, multiple SE-images were taken at inclination angles of 0°, +5° and +7°. For each inclination angle, a 360° view was processed. These image sequences indicate that the intact spheres are not damaged by the impact and that they are spherically shaped, see Figure 45.

An example of the destruction sequence is depicted in Figure 44, both images on the right side. They show two recorded sequences of the destruction of the particles. It can be observed how brittle this particle is, it breaks like a glass bulb. This observation can be extended to all four particles. Also after the destruction of all four particles multiple SE-images were recorded at inclination angles of -7°, 0° and +7°. Again a 360° view was generated for each inclination angle. The observations of these sequences indicate the presence of a hollow species with an outer shell in the range of a few tenths of nanometers. The inner structure cannot be derived with certainty, see Figure 45. The existence of a hollow core could not be sufficiently proven with SEM. In order to assess the morphology more thoroughly computational simulations were performed, see the following Chapter 5.2.3.1.1. For this investigation particle (1) from Figure 45 was used as a reference.

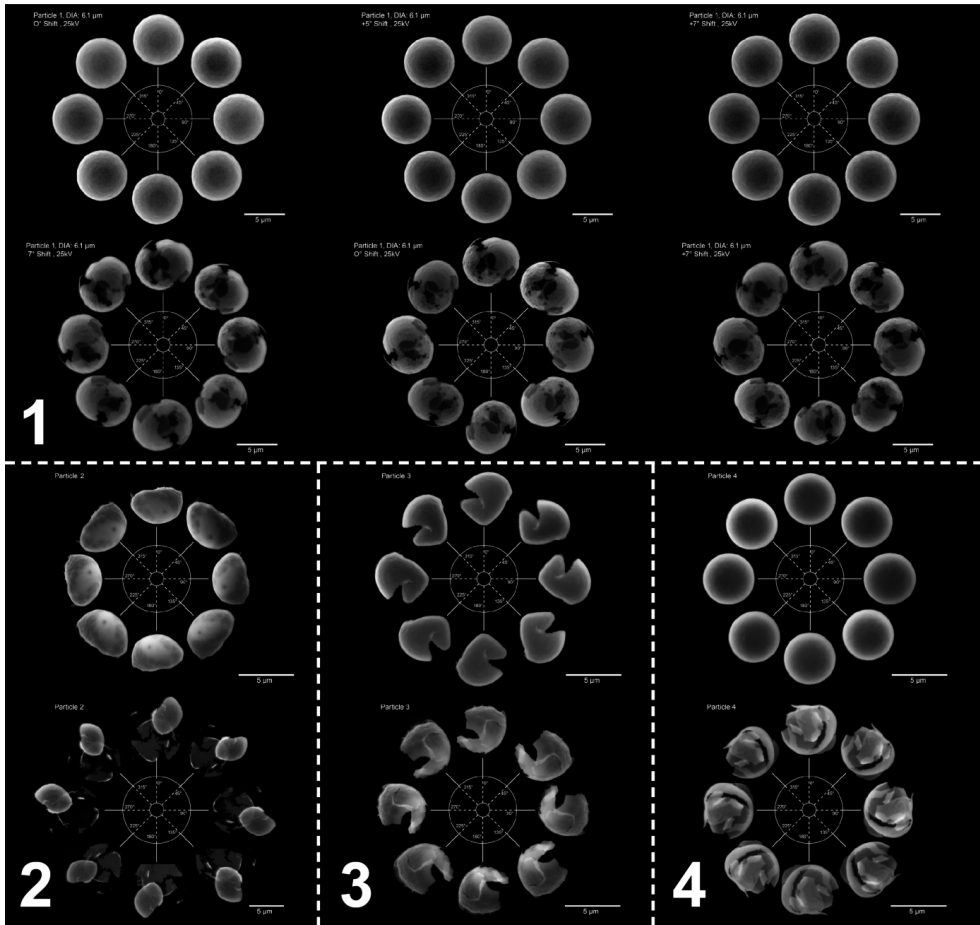


**Figure 45: Particles of Interest, (1) - (4), before and after destruction. Images recorded at different rotational- and inclination angles.**

### 5.2.3.1.1 Particle Morphology Evaluation: SE-Image Computation

The emergence of an unexpected particle species offered the opportunity to investigate the formation kinetics and subsequent morphological attributes of these particles by non-destructive means through Monte-Carlo computations. This sub-chapter reviews the idea of re-engineering three dimensional objects for Monte-Carlo-SE-image simulations that can be compared with the existing SE-images acquired at FZJ and IAEA in order to gain additional information regarding their morphology, solidity, shell thickness and elemental composition.

SE-Image computation was used as an additional tool to support SEM investigation of particles that did not meet the expected characteristics. These computational simulations offer a cost effective and easy alternative to destructive assays in order to investigate the outer and inner structure of microparticles. During this project, a limited number of particles was available to be investigated by destructive and non-destructive assays simultaneously. By setting up different inner compositions and densities, one can calculate the corresponding secondary electron (SE) signal and output it as a simulated SE-image. Figure 46 shows an overview of all simulated SE-images plus the actual SE-image in the bottom as a reference. The simulated SE-images are a two dimensional representation in XZ-plane of an actual three dimensional object.

## Simulated SE-Images with Casino 3.3.0.2

### Intensity Scan in XZ-Plane

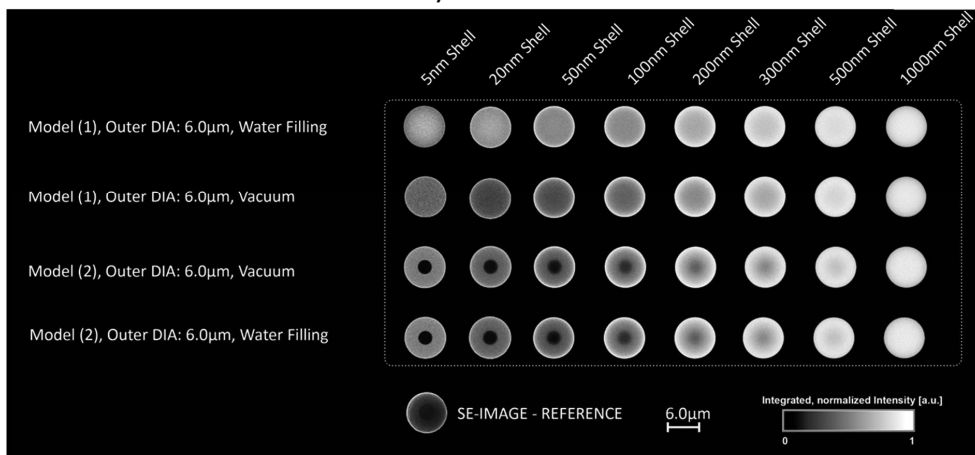


**Figure 46: Simulated SE-Images of 3D spheres, depicted in XZ-plane.**

In total, four different particles sets are displayed: two different models (1) and (2) and two variations of each model (with water filling and with no filling at all). With increasing shell thickness from 5 nm – 1000 nm, the intensity signal increases and at a shell thickness of around 300 nm no valid information regarding the inner structure can be drawn.

Model (1) and Model (2) particle-variations which were filled with water showed a slightly higher average intensity over a radial distribution of 360°. The deviation of the intensity signal between Model (1) and Model (2) is less than 4 %. The deviation at shell thicknesses > 300 nm decreases to about 2 %. According Figure 46 and Figure 47, Model (1) does not show any resemblance with the reference image. Particles which were calculated using Model (2) and which have a shell thickness of  $\geq 300$  nm can be excluded as well. The corresponding SE-Images and 3D surface plots show no distinct distribution due to interfering shielding effects originating from the outer structure. Thus putting the focus on particles which were simulated after Model (2) and which consist of a shell-thickness range of  $5 \text{ nm} \leq d \leq 100 \text{ nm}$ .

## Simulated SE-Images with Casino 3.3.0.2

### 3D-Surface Plots: Intensity Profile in XYZ-Plane

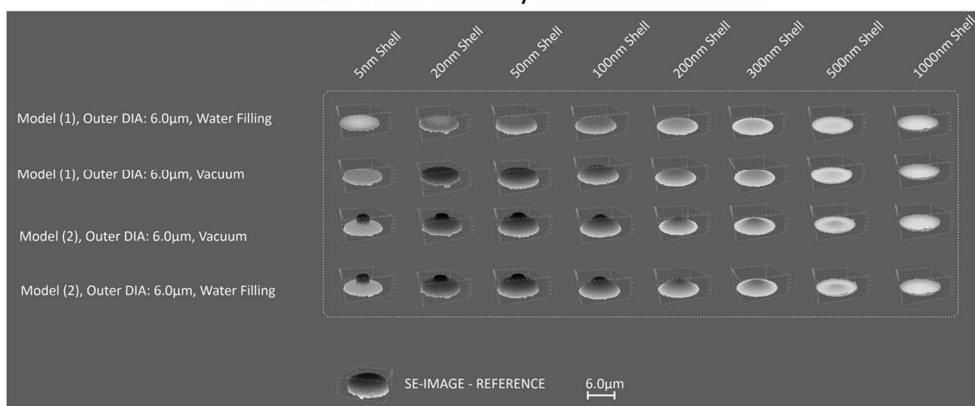


**Figure 47: Processed 3D-surface plots of the simulated images depicted in the previous Figure.**

For a more detailed analysis, the simulated SE-Images were further processed with ImageJ to generate a 3D surface plot: which is a signal intensity distribution as a function of three axes. Figure 47 shows the 3D surface plots of all particles in comparison with the reference image. Evaluation of Figure 47 narrows the shell thickness down to a range of  $5 \text{ nm} < d \leq 50 \text{ nm}$ . Evaluation of the 3D surface plots depicts a unique inherent attribute of all simulated SE-Images: these calculated particles are perfectly spherical and have no artefacts and defects on the surface or in the inner structure, therefore generating a very homogenous intensity profile depending on the radius. Modified particles with a thin shell of 5 nm show an intense peak in the middle. The contrast of the areas of the center cavity to the rest is very strong. The thicker the shell becomes, the more the signal blurs and decreases in the plots. This trend is in accordance with the radial intensity distribution depicted in Figure 48: the stronger the shell thickness, the less distinct the intensity profiles. Figure 48 depicts the stacked normalized and integrated signals as a function of the radius [ $\mu\text{m}$ ]. The radial intensity profiles (over an overall angle of  $360^\circ$ ) of a selected number of particles of interest were acquired with FIJI, using the “Radial Profile Angle” plugin.

The reference signal is plotted on top in a red dotted line. A relatively small but distinct increase in intensity at  $\sim 2.3 \mu\text{m}$  can be observed. As the distance to the center increases, the signal also slightly increases. This is due to electrostatic charging at the edges of the uranium oxide particle. Particles with 5 nm shell thickness (blue) show a very distinct increase at  $2 \mu\text{m}$  and a weaker intensity increase between  $5.6 - 6.0 \mu\text{m}$ . The intensity profile of 20 nm (grey) shell thickness shows a rather smoother profile. The same trend can be observed for higher shell thicknesses, see 50 nm (orange) and 100 nm (green). Particles with a shell thickness of 100 nm (green lines) show a very blurred profile. It is difficult to identify a sharp increase in intensity at a specific distance. After evaluating SE-images and their corresponding radial intensity profiles it can be concluded that the outer shell thickness of these Model (2) particles is very likely to be in the range of  $20 < d < 50 \text{ nm}$ . The outer shell is made of  $\text{U}_3\text{O}_8$  with a density  $\delta_{\text{OS}} = 8.4 \text{ g/cm}^3$ . The inner structure is also composed of  $\text{U}_3\text{O}_8$  but with a lower density  $\delta_{\text{IS}} = 6.6 \text{ g/cm}^3$ . Figure 49 shows a three dimensional reconstruction of particle (1), derived from the findings in this Chapter.

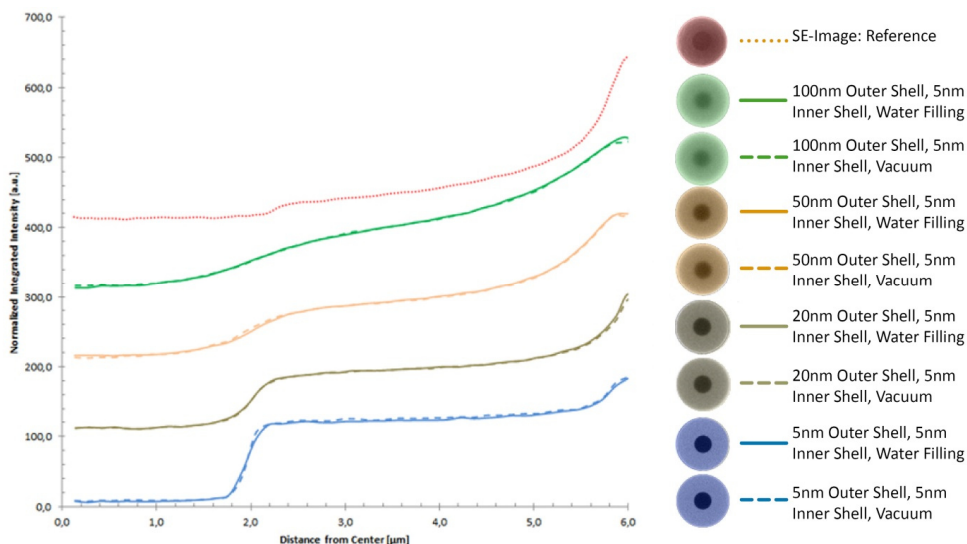


**Figure 48: Normalized integrated radial intensity distribution [arbitrary units].**

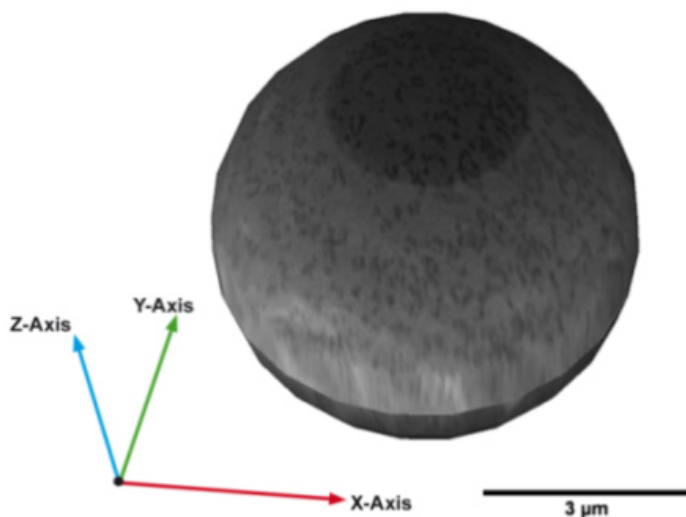


Figure 49: 3-D reconstruction of particle (A).

### 5.2.3.2 Solid Species: SG141027\_12A, SG150312\_05A, SG150401\_14A, SG150413\_03A, SG150429\_02A

Solid micro-particles are the preferred species. This chapter will discuss the morphology of these solid entities. SEM investigation already showed a strong resemblance in morphology and shape of all solid particles ranging from SG141027\_12A, SG150312\_05A, SG150401\_14A, SG150413\_03A to SG150429\_02A. The objective of this chapter is the assessment of the inner structure and morphology by focused ion beam in combination with time of flight SIMS. TOF-SIMS was also used to identify the elemental content of single uranium oxide micro-particles in order to look for possible contaminations.

#### 5.2.3.2.1 Internal Particle Morphology: TOF – SIMS / FIB Investigation

In total 31 particles (from SG141027\_12A) were investigated using FIB and Time of Flight SIMS (TOF-SIMS). SEM investigations revealed that all particles have a porous inner structure. The investigation was performed on a Lyra3 GM combined SEM/FIB / TOF-SIMS system; the TOF-SIMS detector is from TOFWERK, Switzerland. For mass identification, a representative particle was chosen to be discussed in detail. The particle was cut with a focused Gallium beam with positive polarity and a primary beam current of 577 pA and an  $AcV = 25$  keV. The dwell time was set at  $14 \mu s$  with a field of view of  $12 \mu m$ . Data was analyzed and processed with Mmass (Version 3) and TOF-Sims Explorer (Version 1.0.1.11). For the mass identification, the intensity as counts per second was plotted against the mass to charge ratio " $m/Q$ ". In the following chapter describes the mass identification process for one exemplary uranium microparticle.

#### 5.2.3.2.2 Mass Identification

For this thesis, one exemplary particle out of 31 uranium particles was chosen to be presented exemplarily for all consumed particles. For this investigation, a mass to charge ratio " $m/Q$ " in the range  $0 \leq m/Q \leq 350$  was recorded. The mean size for this particle was  $1.3 \pm 0.1 \mu m$ . In total, 25 ion species were identified plus two unidentified species. Figure 50 depicts the spectrum which was acquired and Table 12 shows the list of identified ion species – a more detailed version is depicted in the Appendix, see Figure 96 in Chapter 7.3.

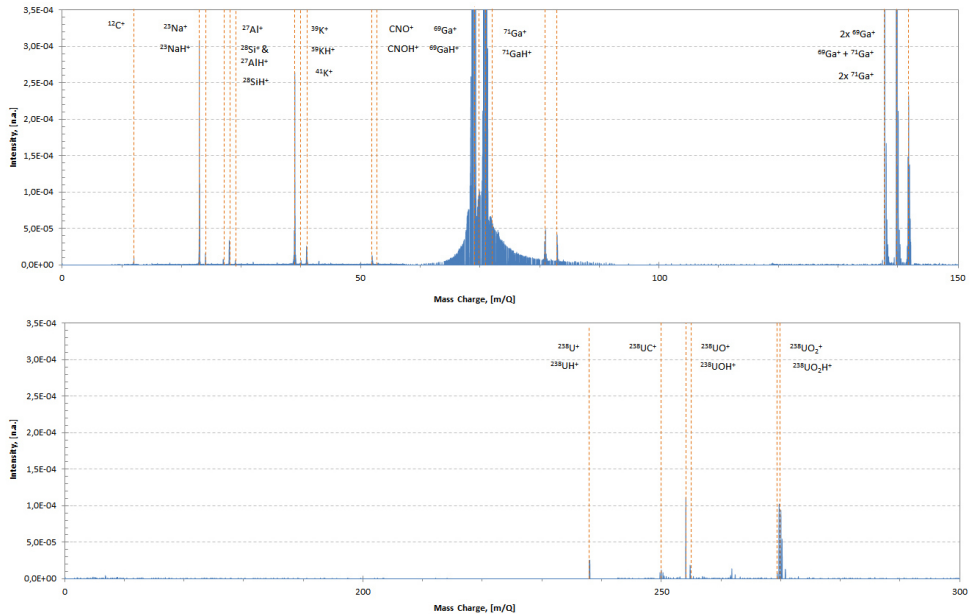


**Figure 50: Mass spectra of SG141027\_12A – Particle 1.**

The first signal to be identified belongs to the ion species at  $m/Q(12)$  and can be attributed to the carbon substrate. Since no adhesive layer was applied on the surface, we would expect a signal for the Ga-Ion source and the uranium-oxygen species. A few ion species appear which are not expected and they originate from cross contaminations. There are many possible sources for the introduction of these elements: (1) contaminated precursor aerosol solution through contaminated vessels or solutions and (2) cross contaminations due to insufficient cleanliness in the laboratory. Cross contaminations can be caused by airborne particles during the particle production procedure, either before or after introducing the substrate to the setup or shortly after the collection when the substrate is transferred into a sealed containment. The following elements and their  $m/Q$  ion species could be identified:  $m/Q(23)$  and  $m/Q(24)$  are caused by sodium and its hydride species; aluminum and silicon are identified at  $m/Q(28)$  and  $m/Q(29)$ ; potassium could be identified at  $m/Q(39)$ ,  $m/Q(40)$  and  $m/Q(41)$ ; and a pure organic species was found at  $m/Q(50)$  and  $m/Q(50)$  for  $CNO^+$  and  $CNOH^+$ . Two unidentified  $m/Q$  species could not be identified: (1)  $m/Q(52)$  and  $m/Q(53)$ . The strong peaks at  $m/Q(69)$ ,  $m/Q(70)$ ,  $m/Q(71)$  and  $m/Q(72)$  are associated with the Ga-ion source, as well as the complex ion species found at  $m/Q(138)$ ,  $m/Q(139)$  and  $m/Q(142)$ .

The uranium and uranium-oxide species occur at  $m/Q > 235$ . It has to be noted that the measured intensity for  $m/Q(235)$  was very low about  $m/Q(235) = 3.4 \cdot 10^{-6}$  [cts]. Which is due to the low amount fraction of  $n(235U)/n(U) = 0.320\%$ . The presence of the  $^{238}U$  species is significantly about 82 x higher - with  $m/Q(238) = 2.8 \cdot 10^{-4}$  [cts]. The ratio of the hydride species shows higher ratio of about 1 : 116 for  $m/Q(235+236) = 6.0 \cdot 10^{-4}$  [cts] than for  $m/Q(238+239) = 6.94 \cdot 10^{-2}$  [cts]. These ratios of  $^{235}U$  to  $^{238}U$  do not represent the initial ratio of IRMM-183. The discrepancy only be explained by the geometric constraints of the detector, the subsequent ion extraction efficiency and the detector sensitivity. The identification of the ion species showed the existence of two distinct uranium oxides species:  $^{238}UO^+ / ^{238}UOH^+$ ,  $^{238}UO_2^+ / ^{238}UO_2H^+$  at  $m/Q(254/255)$  and  $m/Q(270/271)$  respectively. Figure 51 shows the ablation process of Particle 1 and the signal of  $m/Q(16) = ^{16}O^+$ ,  $m/Q(28) = ^{28}Si^+$ ,  $m/Q(238) = ^{238}U^+$  and  $m/Q(239) = ^{238}UH^+$ . It shows a clear correlation of the  $m/Q(16)$  and  $m/Q(239)$  signals over the entire depth of the particle. In contrast, the signals for  $m/Q(16) = ^{16}O^+$  just shows a significant signal at the beginning. It decreases for all particles and no further information can be extracted.

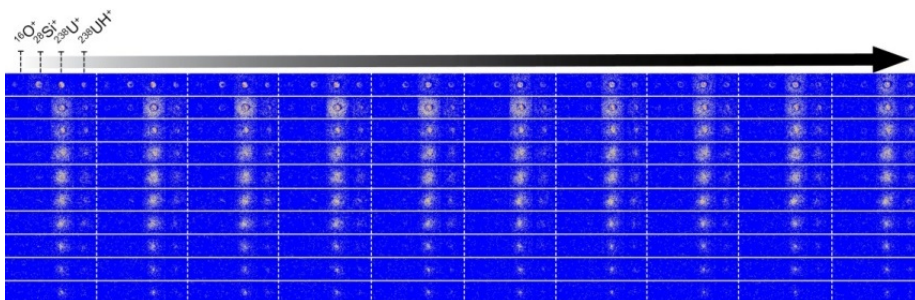


**Figure 51: Intensity evolution over 100 frames of  $m/Q(16)$ ,  $m/Q(28)$ ,  $m/Q(238)$  and  $m/Q(239)$  - Particle 1.**

The  $m/Q(28) = {}^{28}\text{Si}^+$  show a strong signal at the beginning and decreases much slower, thus indicating that  ${}^{28}\text{Si}^+$  is present in the entire particle. This ambiguity regarding the detector sensitivity towards each element, in particular for oxygen and silicon. It is possible that oxygen is harder to detect with the current settings. A possible explanation for the presence of Si can be derived that the precursor solutions were stored in glass vials and that precursor dilutions (Dilutions 1 and 2) were prepared in glass vessels as well. It is suggested to monitor the aerosol solutions for cross contaminations to contain the source of Si. Mass spectrometry of a single particle found indications of possible cross contaminations of Na, K, organic matrix as well as Si. There are multiple sources of origin for these contaminations. Almost throughout every step of the production- and evaluation process, cross contaminations may occur. These findings demonstrate the importance of clean production- and working environments.

**Table 12: Identification of ion species and their corresponding mass-to-charge ratio - Particle 1.**

#	m/Q	Ion Species	#	m/Q	Ion Species
1	12	${}^{12}\text{C}^+$	14	71	${}^{71}\text{Ga}^+$
2	23	${}^{23}\text{Na}^+$	15	72	${}^{71}\text{GaH}^+$
3	24	${}^{23}\text{NaH}^+$	16	138	$2 \times {}^{69}\text{Ga}^+$
4	27	${}^{27}\text{Al}^+$	17	139	${}^{69}\text{Ga}^+ + {}^{71}\text{Ga}^+$
5	28	${}^{27}\text{AlH}^+$ , ${}^{28}\text{Si}^+$	18	142	$2 \times {}^{71}\text{Ga}^+$
6	29	${}^{28}\text{SiH}^+$	19	238	${}^{238}\text{U}^+$
7	39	${}^{39}\text{K}^+$	20	239	${}^{238}\text{UH}^+$
8	40	${}^{39}\text{KH}^+$	21	250	${}^{238}\text{UC}^+$
9	41	${}^{41}\text{K}^+$	22	254	${}^{238}\text{UO}^+$
10	50	$\text{CNO}^+$	23	255	${}^{238}\text{UOH}^+$
11	51	$\text{CNOH}^+$	24	270	${}^{238}\text{UO}_2^+$
12	69	${}^{69}\text{Ga}^+$	25	271	${}^{238}\text{UO}_2\text{H}^+$
13	70	${}^{69}\text{GaH}^+$			

### 5.2.3.2.3 Particle Morphology Investigations Using Combined FIB TOF-SIMS data

The morphology was assessed using all data acquired from all 31 measurements. Particle 1 will be used as an example to discuss our findings. Figure 52 shows the intensity depth distribution of  $m/Q(238)$  and  $m/Q(239)$  over the entire depth of the particle. The top projection shows the presence of a few hot-spots indicating that the surface is not smooth. This observation is in correlation with SEM studies performed on comparable particles from the same batch. The front projections indicate the presence of a thin shell-like structure due to an increase of the intensity. The inside of the particle shows the presence of void, due to the lack of signal and much lower, inhomogeneous intensity distribution. This indicates the presence of a porous inner structure.

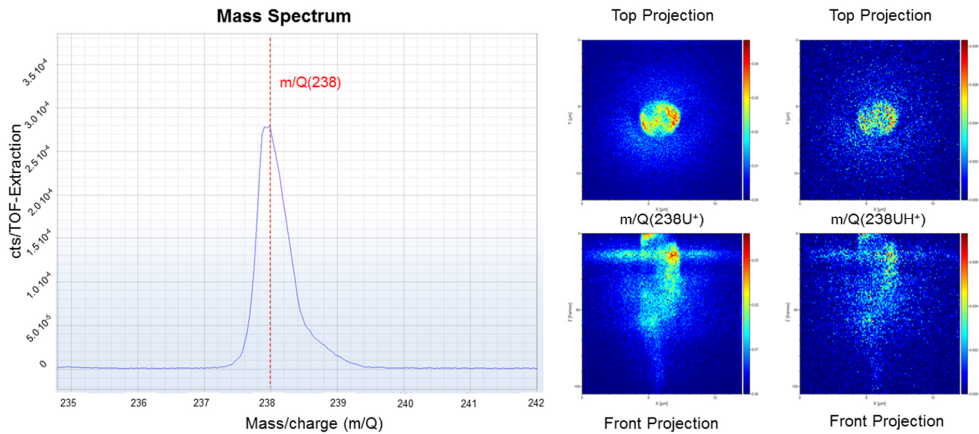


**Figure 52: Mass spectrum of m/Q(238) and m/Q(239) and the corresponding TOF signals in top- and front projection – Particle 1.**

Therefore, a depth profiling analysis was performed by plotting the normalized m/Q intensities in regard to the particle depth. Figure 53 depicts the depth profile of Particle 1 with the masses  $m/Q(16) = {}^{16}\text{O}^+$ ,  $m/Q(28) = {}^{28}\text{Si}^+$ ,  $m/Q(238) = {}^{238}\text{U}^+$  and  $m/Q(239) = {}^{238}\text{UH}^+$ . The signal for m/Q(16) is constant within  $1.15 \cdot 10^{-4} \pm 2.5 \cdot 10^{-5}$  and is an indication that oxygen is distributed throughout the entire particle. For silicon, the m/Q(28) signal drops within 12.5 nm and steadily decreases indicating that this signal might be associated to an external particle which contains Si. If Si was present in the outer structure of the particle we would expect to see a rise in the signal after  $\sim 0.9$  nm again. The deviation of the mean intensities of m/Q(16) to m/Q(28) is about 32.58 %. The signal evolution of m/Q(238) and m/Q(239) are directly correlated and it deviates by a factor of 7.4. The maximum of the measured peak intensity for m/Q(238) and m/Q(239) was about 180 nm in depth. The peak intensity indicates the presence of a denser shell with a mean thickness of  $< 200\text{nm}$ . This profile is typical for all particles measured. Subsequently, the mean intensity drops to about 45.76 % from the peak intensity. All single particles which were measured show a similar profile: the intensity rises between 100 – 200 nm to a maximum and then drops. Depending on the particle, the intensity rises again to similar intensity level or slightly lower. The intensity signals of m/Q(238) and m/Q(239) between 300 – 700 nm show a fluctuating intensity profile indicating a porous structure. SE images taken during the ablation process support the assumption that the inner structure is actually porous, to a certain degree small cavities can be observed. These SE-images were acquired during FIB ablation at different depths and are presented in the Appendix in Chapter 7.3.1 in Figure 99 - Figure 101, courtesy to Ronald Middendorp and Martina Klinkenberg at IEK-6.

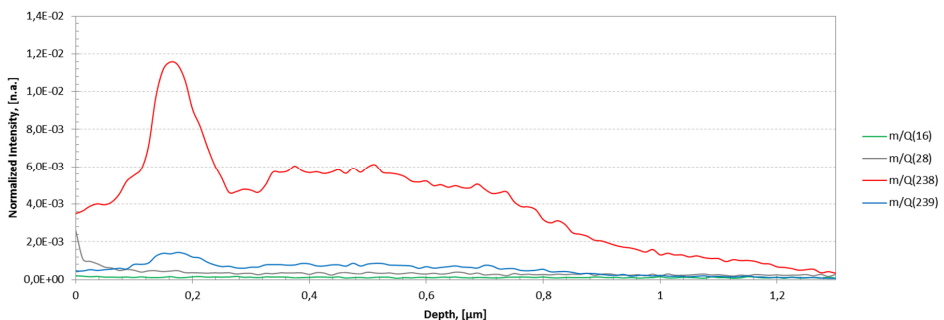


**Figure 53: Depth profiling of m/Q(16), m/Q(28), m/Q(238) and m/Q(239) of Particle 1.**

Investigations on 31 particles indicate comparable results, but the increase of the  $m/Q(238)$  signal appears between 180 – 260 nm, indicating that the denser outer shell is not homogenous. This can also be accounted for by the fact that each particle was aligned slightly different to the ion beam and the resulting sputter signal was slightly altered.

For Particle 1, the whole sequence is depicted in Figure 98 in the Appendix - Chapter 7.3 Figure 98. In order to highlight the ablation process, the ablation sequence was subsequently colored: red markings for the particle. Note: the change of background color due to the sputtering. Figure 54 clearly shows that the morphology changes over the length of the particle. Each frame corresponds to approximately 13.0 nm in depth. The structured surface with its grooves and notches can be seen as an intensity variation. After about 65 nm the first sign of a cavity becomes obvious. This sequence indicates the formation of a non-solid particle with a robust porous outer surface layer. According to our investigations, the outer layer does not have a homogenous thickness. SEM investigation of 105 slices during the ablation process revealed a porous inner structure. The outer shell (about 200 nm into the particle) shows no indication for pores. These morphological findings are in agreement with observation by Pratsinis and Vemury (1996) [63], Messing et al. (1993) [58] and Reuge et al. (2008) [66] [67]. After about frame 50 (row 5, column 50) the particle is almost ablated and a tailing pattern can be observed, see Figure 98.

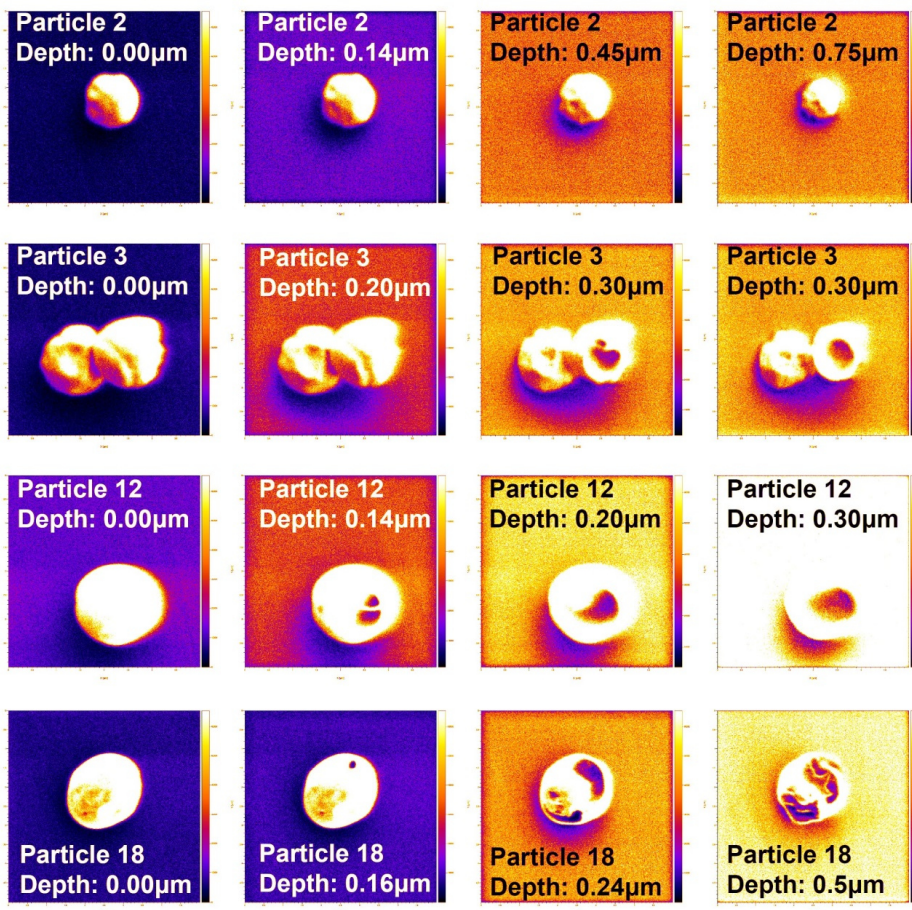


Figure 54: SE-image sequences at different ablation-depths of 4 selected particles (Particle 2, 3, 12 and 18) originating from SG141027\_12A.

This does not really give any substantial information regarding the morphology. Thus, the residue pattern may be attributed to the ablation specific behavior of the micro particle. But it can be derived that the particle density changes throughout the particle and cannot be considered homogenous. All investigated particles show a thin outer crust with a higher specific density than the inner structure.

This inner structure has a porous morphology thus resulting in a considerably lower density. The overall averaged density of a uranium microparticle is therefore much lower than of a naturally grown "uranium bulk material entity".  $U_3O_8$  has a mean density of  $8.3 \text{ g/cm}^3$  and  $UO_3$  depending on the modification  $5.5 - 8.7 \text{ g/cm}^3$ . Auxiliary FIB investigations on multiple particles were performed at IEK-6. These particles originate from SG150401\_14A and were produced in April 2015 in a comparable manner. The investigation revealed no significant changes: all particles show a corrugated, fissured outer structure and a porous inner structure for all particles. Three representative particles were selected to be displayed, see Appendix Figure 99 – Figure 101. All data show a consistent picture of the inner and outer structure of these particles.

FIB investigations proved the existence of a much less denser species. Further studies on the crystal structure using  $\mu$ -Raman investigations will give more information on the composition of these microparticles. But a thorough density assumption will be given in Chapter 5.4.3.1 which will be derived from the mean integrated  $^{238}\text{U}$ -intensity of a single uranium particle.

### 5.2.3.3 Elemental Analysis with Energy Dispersive X-Ray Spectroscopy (EDX)

EDX analysis was routinely applied during particle assessments to identify uranium in microparticles. This chapter presents the results obtained from EDX analysis performed on all six batches. Particles were either deposited on Si or on C substrates. The focus during EDX analysis was on the quantification of the C, Si and U amount and identification of their ratios and to demonstrate that microparticles can be easily identified and that solid particles show a much clearer signal than the hollow species.

SG140521\_02 is different to the other particle batches presented in this thesis. Morphological studies revealed the presence of a polydisperse distribution. Therefore, SG140521\_02 will be discussed in a separate sub-chapter, while the other particle batches SG141027\_12A, SG150312\_05A, SG150401\_14A and SG150429\_02A will be discussed in one chapter.

Elemental analysis was performed on several SEMs: Jeol JSM, Tescan TIMA and FEI Quanta 200 F SEM. All spectra presented in this work were acquired at  $\text{AcV} = 25 \text{ keV}$ .

#### 5.2.3.3.1 EDX on Polydisperse Species: SG140521\_02

Previous studies on the morphology revealed the existence of multiple species: (a) hollow, inflated particles, (b) debris and (c) solid particles. This chapter depicts the investigation of batch SG140521\_02. Two different studies were performed: (1) automated particle analysis including the analysis of over 170 particles and (2) the assessment of four representative particles. All particles were deposited on C-substrate.

This EDX analysis demonstrates that a quantitative EDX analysis at  $\text{AcV} = 25 \text{ keV}$  is significantly biased because at these accelerating voltages a lot of the signal originates from the substrate, this can be observed in Figure 55. Nevertheless a comprehensive attempt in quantitative characterization will be described in this chapter. An automated EDX-particle analysis was performed at  $\text{AcV} = 25 \text{ keV}$  on a Jeol SEM with INCA EDX software. A representative area of  $200 \times 200 \mu\text{m}^2$  was investigated containing 176 uranium bearing particles. The ternary diagram shown in Figure 55 depicts a strong spread of the U(M) and C(K) signal. This is due to the polydisperse nature of the particles and their position in relation to the BSE detector. This observation is in concurrence with the morphological studies performed in Chapter 5.2.3.1. Table 13 shows the mean C(K), O(K) and U(M) signals for all 176 particles. A mean C(K) values is  $65.02 \pm 23.97 \text{ wt-\%}$  was derived.

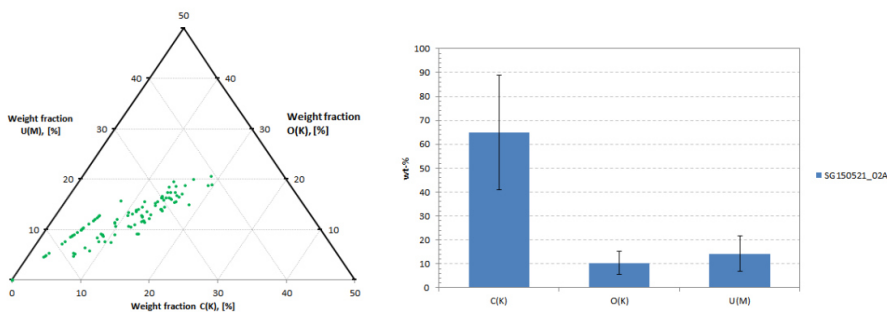


**Figure 55: Left: Ternary diagram depicting the significant variation of the C(K), O(K) and U(M)-ratio of 176 polydisperse particles from SG140521\_02 particle distribution. Right: Histogram depicting the mean wt% measured for 176 polydisperse particles originating from SG140521\_02.**

For oxygen, the mean O(K) value was derived to be  $10.43 \pm 10.43$  wt-% and U(M)  $14.17 \pm 7.47$  wt-%. The “ $w(O)/w(U)$ ” ratio ranges between  $0.23 \leq O/U \leq 1.44$ , see Table 13. EDX spectra were all collected in a low vacuum condition, therefore the presence of oxygen and carbon is expected, which is a possible explanation for the mean ratio of  $U/O = 0.72 \pm 0.24$ .

**Table 13: Mean values for C(K), O(K) and U(M) for 176 particles for SG140521\_02.**

SG150521_02A		
Element	wt%	$\Delta$ wt%
C(K)	65.02	23.97
O(K)	10.43	4.88
U(M)	14.17	7.43

Out of these 176 particles, four representative particles were selected for individual assessment. Figure 56 shows the wt-% distribution for each of the four particles. The dominant signal comes from the C-substrate. For the hollow species, intact and particle debris, over 98 % comes from C(K). The interaction of the electron beam with the porous and thin material is relatively low thus resulting in a high background signal. For the hollow species, no measurable proportion of oxygen could be detected. The U(M) signal varies between 0.97 - 1.70 w-%. For the solid species the U(M) signal can be 4.3 - 7.6 times higher than for the hollow species and reach up to 7.37 w-%.

**Table 14: Results EDX analysis of four selected particles from SG140521\_02.**

Hollow particle			Hollow particle - destroyed			Deformed Particle		
Element	Weight%	Atomic%	Element	Weight%	Atomic%	Element	Weight%	Atomic%
C(K)	98.44	99.92	C(K)	98.30	99.91	C(K)	98.98	99.97
O(K)			O(K)			O(K)		
U(M)	1.56	0.08	U(M)	1.70	0.09	U(M)	1.02	0.03
Particle Debris			Solid particle					
Element	Weight%	Atomic%	Element	Weight%	Atomic%			
C(K)	99.03	99.99	C(K)	75.38	84.98			
O(K)			O(K)	17.25	14.60			
U(M)	0.97	0.01	U(M)	7.37	0.42			

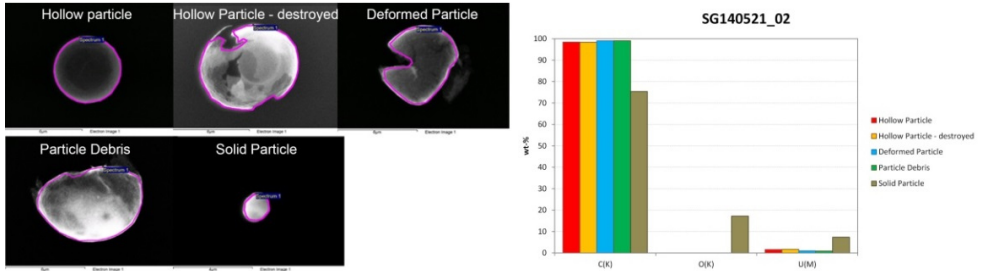


Figure 56: w-% of C(K), O(K) and U(M) on four selected particles from SG140521\_02 on C-substrate.

### 5.2.3.3.2 Uniform Particle Species: SG141027\_12A, SG150312\_05A, SG150401\_14A and SG150429\_02A

The second part describes the investigation of uniform, homogenous particles. EDX spectra were acquired at AcV = 25keV on the Jeol JSM 6610 and Tescan TIMA machine – particles were deposited either on C- or Si-substrates. First particle which were deposited on carbon substrate will be discussed: SG141027\_12A and SG150401\_14A. Both batches were produced during different stages of the setup evolution process. This chapter demonstrates that even with solid microparticles a quantitative elemental evaluation is significantly biased, at AcV = 25 keV. At lower accelerating voltages the signal originating from the micro sample insignificantly less biased due to the small size of the particle. The interaction volume of the electron beam is always much bigger than the measured microparticle itself.

SG141027\_12A was produced in October 2014 when the setup resembled more the schematics found in Figure (16) - No (2). An automated particle analysis with the Jeol JSM 6610 was performed and a total area of  $4.90E+05 \mu\text{m}^2$  was scanned and 639 uranium containing particles were identified. EDX analysis showed a mean values for C(K) =  $76.24 \pm 3.84$  wt-%, for O(K) =  $14.11 \pm 3.46$  wt-% and for U(M) =  $9.65 \pm 0.64$  wt-%. This corresponds to a “w(O)/w(U)” ratio of  $w(O)/w(U) = 1.46 \pm 1.60$ .

Batch SG150401\_14A was produced in April 2015 and the setup was significantly changed, see Figure (4), No (4). The biggest change was the increase in collection yield. For SG150401\_14A 150 particles were selected for EDX analysis. A mean value for C(K) =  $81.86 \pm 4.57$  wt-%, O(K) =  $13.52 \pm 2.64$  wt-% and U(M) =  $10.16 \pm 2.04$  wt-% was derived. A  $w(O)/w(U) = 1.33 \pm 0.30$  was derived. Table 15 depicts that there is no significant change in the wt-% between SG141027\_12A and SG150401\_14A.

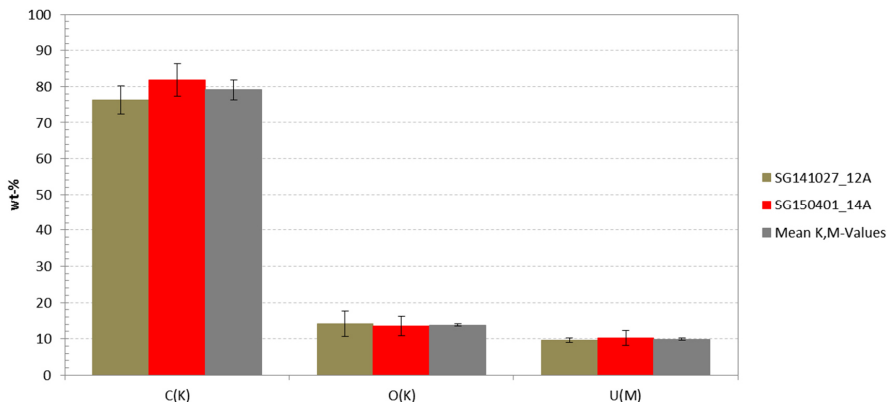


Figure 57: Comparison of EDX values of C(K), O(K) and U(M) in wt% from SG141027\_12A and SG150401\_14A – on C-substrates.

The calculated mean values for both batches show no significant deviation: C(K) = 79.05 ± 2.81 wt-%, O(K) = 13.82 ± 0.30 wt-% and U(M) = 9.91 ± 0.26 wt-%. The deviation between both batches for C(K) is about 6.9 %, for O(K) 4.2 % and for U(M) 5.0 %. Figure 57 depicts the measured data from SG141027\_12A and SG150401\_14A. Category two particles were deposited on a Si-wafer. For all three batches, just a limited number of 12 - 15 particles could be investigated. The following table (Table 15) depicts the mean values for C(K), O(K), Si(K) and U(M) lines.

**Table 15: Mean values for the C(K), O(K) and U(M) lines of solid particles deposited on glassy carbon substrates: SG141027\_12A and SG150401\_14A.**

SG141027_12A			SG150401_14A		
Element	wt%	Δwt%	Element	wt%	Δwt%
C(K)	76.24	3.84	C(K)	81.86	4.57
O(K)	14.11	3.46	O(K)	13.52	2.64
U(M)	9.65	0.64	U(M)	10.16	2.04
Mean K,M-Values					
	wt%	Δwt%			
Mean C(K)	79.05	2.81			
Mean O(K)	13.82	0.30			
Mean U(M)	9.91	0.26			

Both Table 15 and Figure 57 indicate that the deviation of each planchet for the corresponding elemental peak-signal is not significantly high. The derived mean value for U(M) matches about 98.4 % of the value for SG150413\_03A, for SG150312\_05A it is about 93.9 % and for SG140429\_02A it matches to about 95.7 %. The resulting “w(O)/w(U)” ratios are 0.34 for SG150312\_05A, 0.44 for SG150413\_03A and 0.25 for SG150429\_02A. EDX was used to investigate the uranium oxide species by comparing the measured weight ratios of oxygen and uranium with the values published by Morss et al. (2011) [92]. All spectra were measured in high vacuum mode. The resulting signals can be correlated to the uranium-oxide species. But it has to be noted that all particles were stored under ambient conditions: inside plastic boxes which were double bagged inside plastic backs. The w(O)/w(U)” ratios were derived from these measurements: for particles deposited on carbon substrates a ratio of w(O)/w(U) = 0.19 and w(O)/w(U) = 0.17 was measured which is close to the values for UO<sub>3</sub> published by Morss et al. (2011) [92].

For particles which were deposited on Si substrates, the ratios of w(O)/w(U) differed significantly w(O)/w(U) = 0.34 for SG150312\_05A, w(O)/w(U) = 0.44 for SG150413\_03A and w(O)/w(U) = 0.25 for SG150429\_02A, see Table 16.

**Table 16: Mean values for the C(K), O(K) and U(M) lines at solid particles deposited on Si wafer substrates: SG150413\_03A, SG150312\_05A and SG150429\_02A.**

SG150312_05A			SG150413_03A		
Element	wt%	Δwt%	Element	wt%	Δwt%
C(K)	2.38	0.76	C(K)	2.20	0.85
O(K)	4.25	0.87	O(K)	5.98	1.05
Si(K)	80.88	1.68	Si(K)	78.31	1.97
U(M)	12.49	0.89	U(M)	13.51	1.01
SG150429_02A			Mean K,M-Values		
Element	wt%	Δwt%		wt%	Δwt%
C(K)	2.86	0.91	Mean C(K)	2.48	0.16
O(K)	3.43	0.68	Mean O(K)	4.55	0.85
Si(K)	79.82	1.24	Mean Si(K)	79.67	0.79
U(M)	13.89	1.02	Mean U(M)	13.30	0.30

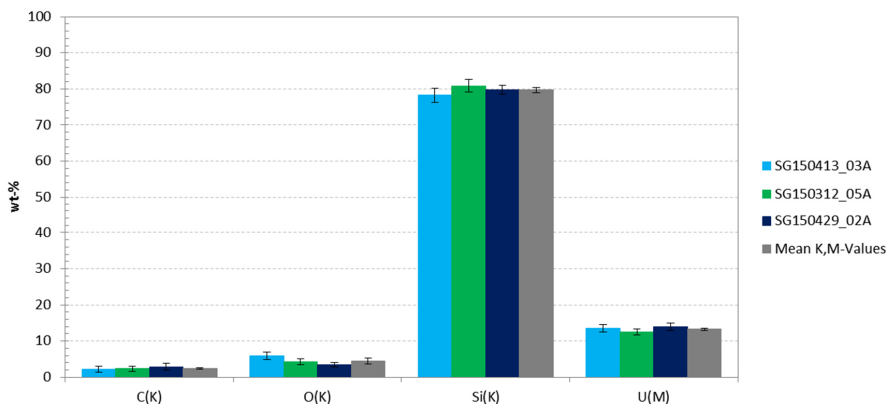


**Figure 58: Comparison of EDX values of C(K), O(K) and U(M) in wt% from SG150312\_05A, SG150413\_03A and SG150429A- all particles are deposited on Si wafer substrates.**

The presence of carbon inside the particles which are deposited on Si wafer substrates is interesting and was completely unexpected. There are two possible reasons for the emergence of carbon in the EDX spectra. (1) the presence of carbon can be an indication of an incomplete thermal conversion: the presence of carbon and uranium may also be an indication for a multiphase uranium species. Luan et al. (2015) [155] tested the long-term reduction of U(IV) species through the addition of ethanol and demonstrated its effects. Morss et al. (2010) [92] had already demonstrated the reduction of uranium species in the presence of carbon. Or (2) it can be attributed to an EDX specific artefact, because combined FIB/TOF-SIMS investigations, in Chapter 5.2.3.2.1, on the similar particles (SG141027\_12A) indicate the absence of carbon inside these particles. Further investigations on the chemical environment and oxidation state with extended X-ray absorption fine structure and X-ray absorption near edge structure (EXAFS and XANES) measurements have to be performed in order to investigate these effects. Further studies with  $\mu$ -Raman spectroscopy may give additional indication about the presence of carbon in single microparticles, see Chapter 5.3.

## 5.2.4 Conclusion SEM Characterization

### 5.2.4.1 Conclusion Particle Size Distribution

It can be shown that the particles size distribution became narrower and precise over the period of 12 months. The amount of tailings which can be associated to doublet or triplet droplet agglomerations decreases over the time. For all solid particles a similar shape and morphology could be observed, see Figure 59 which shows the particle size distribution for all six batches. So far no batch can be considered monodisperse yet, the variance became much smaller.

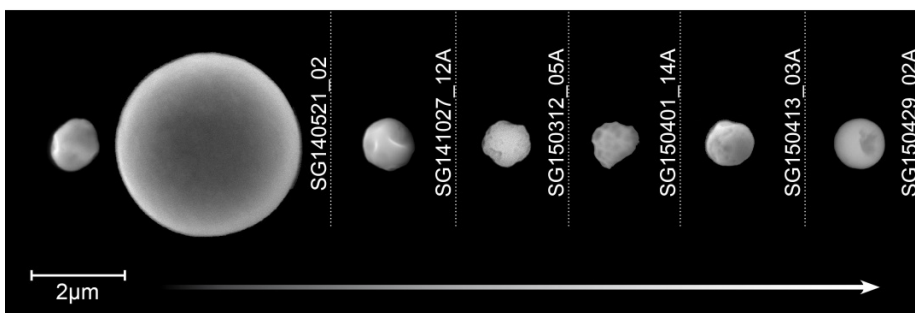


**Figure 59: Overview of the particle evolution since May 2014 to April 2015.**

This is a good indication that the control of the temperature and air flows is of utmost importance. We could demonstrate that the mean particle size can be adjusted precisely by the concentration of the precursor solution. Table 17 depicts the mean particle size and the corresponding temperature profile. It can be shown that the presence of the furnace is not needed. And that it rather introduces more disturbances and a decrease of the particle collection yield. The particle size is dependent on the characteristics such as the precursor aerosol solution concentration, the liquid feed rate and the frequency of the orifice. Particle morphology and density are controlled by the precipitation mechanics during solidification and can either be homogenous or surface controlled. The number of uranium atoms (see equation 10) is stable, but the density can vary significantly.

**Table 17: Overview of calculated diameters and heat parameters of the pre-heater and the furnace.**

Sample-ID	Mean Diameter [ $\mu\text{m}$ ]	$\Delta(\text{Mean DIA})$ [ $\mu\text{m}$ ]	Preheating [ $^{\circ}\text{C}$ ]	Furnace [ $^{\circ}\text{C}$ ]
SG140521_02	1.35	-	480	750
SG141027_12A	1.37	0.19	560	-
SG150312_05	0.99	0.15	400	480-900 [g]
SG150401_14A	0.85	0.15	500	-
SG150413_03A	1.05	0.11	500	-
SG150429_02A	1.02	0.10	500	-

### 5.2.4.2 Conclusions on the Particle Morphology Section

Scanning electron microscopy was used to assess the particle morphology of all six batches. Polydisperse particle originating from SG140521\_02 were useful to understand the formation processes from precursor droplets to particles. The final morphology is determined by the production environment and predominantly by the temperature. In the case of SG140521, a surface-controlled precipitation led to the generation of hollow particles. These particles were assessed by deliberate destruction with a micromanipulation needle inside a SEM. SEM investigations revealed that these microparticles are hollow and do not necessarily break on impact. To obtain further information and to prove that non-destructive computational means can deliver additional information, Monte Carlo simulations were performed to recreate the SE-images obtained in a SEM. Information regarding the density and shell thickness could be derived successfully from them. It can be concluded that the outer shell structure has a thickness in the range  $20 < d < 50$  nm and is made of  $\text{U}_3\text{O}_8$  with a density of  $\delta_{\text{os}} = 8.4$  g/cm<sup>3</sup>. The inner structure is also composed of  $\text{U}_3\text{O}_8$  but it has a lower density of  $\delta_{\text{is}} = 6.6$  g/cm<sup>3</sup>. According to our simulations the presence of a filling material did not play a significant role.

Furthermore, SEM investigation on the solid particle batches (SG141027\_12A, SG150312\_05, SG15040\_14A, SG150413\_03A and SG15429\_02A) provide confidence that the particle size can be adjusted precisely. Particle formation is controlled by an erratic internal solvent evaporation which leads to the formation of a high permeable solid entity, which is in accordance to the prediction of Reuge et al. (1961) [66] [67] and Messing et al. (1993) [58]. All solid particle batches show similar geometric features: particles are not perfectly spherical, instead the surface shows a lot of dents and grooves.

Combined FIB-TOF-SIMS, investigations on a selected number of particles demonstrated consistent quality within these batches. All microparticles which were investigated do not show a homogenous density distribution throughout the entire volume. According to FIB investigations, all single microparticles consist of two different parts which have significantly different densities: (1) a thin denser outer layer of about 0.2  $\mu\text{m}$  in thickness and (2) a porous inner structure which is far less dense. TOF-SIMS investigation proved the existence of Si cross-contaminations which might originate from the

[g] Temperature range of preheating system: 480  $^{\circ}\text{C}$  and furnace 900  $^{\circ}\text{C}$ .

application of glass vials in which the precursor solutions were stored. TOF-SIMS analysis also revealed that the inner structure was less dense and showed an erratic morphology. FIB analysis showed the existence of a porous inner structure. According to the recorded m/Q(238) signals a consistent amount of uranium can be assumed.

Elemental investigations using SEM-EDX verified the presence of uranium. SEM-EDX was already routinely used in automated particle analysis for the size determination: only uranium containing microparticles were selected for this analysis. Quantitative analysis using SEM-EDX on hollow and solid particles proved ineffective due to the small size of the particles. The main source of the signal originated from the background. This effect became more pronounced for the hollow entities of SG14521\_02.

## 5.3 Particle Characterization with Micro-Raman Spectroscopy

The aim of these measurements was to investigate the crystallinity, coordination- and chemical environment. One expects to see strong peaks associated to  $U_3O_8$  due to the production process used. SEM investigations on comparable micrometer sized particles which were also produced by spray pyrolysis were analyzed. These were: monodisperse Particles from ITU (20079), VTT and AWE. All particles were produced in a comparable manner, i.e. by spray pyrolysis – see Chapter 4.1. These particles were stored under ambient conditions or in aqueous solutions for several years and all batches showed significant ageing effects in form of crystal growth on the surface, formation of agglomeration, etc. This and reference research raised the question whether the particles produced at FZJ are thoroughly converted to the corresponding uranium oxide: preferably  $U_3O_8$  or  $UO_3$ . We expected to see no bands associated to uranium oxide-hydroxide compounds because we assumed that the calcination process is thorough.

For comparison reasons just the spectral range of 100 - 1400  $cm^{-1}$  is discussed in detail. Memorable bands will be dealt with at a later stage. All full spectra can be observed in the Appendix, Chapter 6.7 (except  $UO_2F_2$  which was solely measured at CEA thus having a spectral range of 100 - 1400 $cm^{-1}$ ). Three different notations are used for the peak identification to indicate the peak strength: “w” for weak, “m” for medium and “s” for strong. All five reference materials (1)  $UO_2F_2$ , (2)  $U_3O_8$ , (3)  $UO_2$ , (4) uranyl nitrate hexahydrate (UNH) and (5) ammonium diuranate (ADU) will be discussed one by one in detail before addressing SG140521\_02 and SG141027\_12A and SG150401\_12A.

### 5.3.1 Reference Raman Spectra on Particulate Material

#### 5.3.1.1 $U_3O_8$

Multiple samples containing  $U_3O_8$  particulates were measured by MRS at CEA and TUW. At CEA spectra were obtained in the energy range of 300  $\mu W$  – 15 mW. For an optimal result, a laser energy of 15 mW was selected with the Renishaw MRS. At CEA, particles were in the energy range of 300  $\mu W$  – 5 mW. A representative number of two spectra acquired with both instruments were selected for graphical comparison and discussion - in the spectral range of 100 - 1400  $cm^{-1}$ , see Figure 60. Nine different peaks were identified and could be matched with existing references, see Table 18.

**Table 18: Main Raman bands detected for  $U_3O_8$  in accordance with the following references.**

	Wavelength, [ $cm^{-1}$ ]		Reference
1	166	w	Stefaniak et al. (2008) (but with 514.5nm laser)
2	178	w	Pointurier et al. (2010) (185 $cm^{-1}$ )
3	244 - 260	w	Allen et al. (1987) (236 $cm^{-1}$ ) and Stefaniak et al. (2008)
4	342	w	Allen et al. (1987), Jégou et al. (2010), Palacios et al. (2000) - $\alpha$ - $U_3O_8$
5	420	m	Pointurier et al. (2010) (412 $cm^{-1}$ ), Palacios et al. (2000) - $\alpha$ - $U_3O_8$
6	453 - 493	m	Allen et al. (1987) for $U_4O_9$ , Palacios et al. (2000) - $\alpha$ - $U_3O_8$
7	485 - 514	s	Stefaniak et al. (2008) (480 $cm^{-1}$ )
8	809	m	Palacios et al. (2000), Jégou et al. (2010)
9	1313	s	Carbon substrate

The spectra were in good accordance to what Stefaniak et al. (2008) [138] and Allen et al. (1987) [117] measured. A weak and diffuse band at 166 - 178  $cm^{-1}$  could be identified: the Stefaniak et al. (2008) [138] measured a peak at 164  $cm^{-1}$  for  $U_3O_8$  but with a 514.5 nm – with the 785 nm no peak at 164  $cm^{-1}$  could be measured. Pointurier et al. (2010) [135] measured with the same MRS and a 785nm laser a small peak at 185  $cm^{-1}$ .

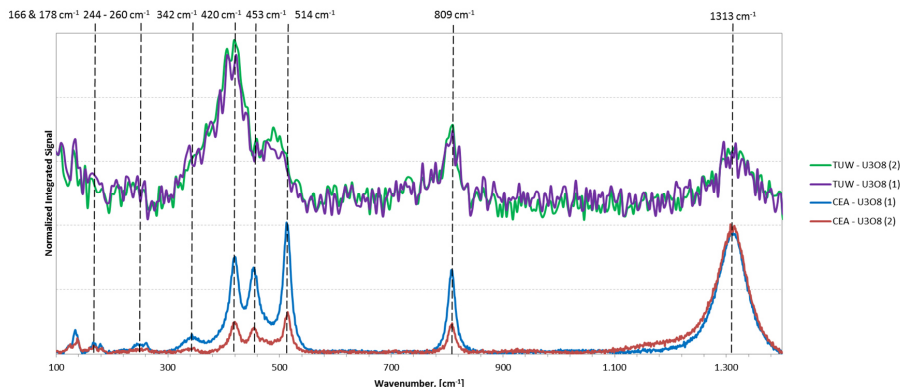


**Figure 60: Micro Raman spectra of  $U_3O_8$  acquired at CEA and TUW.**

Pointurier measured a weak peak at  $178\text{ cm}^{-1}$  – on the same MRS and with micrometer sized particulates. The shift may be accounted for difference in the  $U_3O_8$  material. According to Butler et al. (1988) [118], the band at  $224\text{ cm}^{-1}$  can be associated with  $a_{2u}$  U-O bending vibrations, while the peak at  $342\text{ cm}^{-1}$  is caused by  $a_{1g}$  U-O stretching vibration. The strong quadruple peak band between  $342 - 453\text{ cm}^{-1}$  is largely confirmed by Palacios et al. (2000) [126] and Jégou et al (2010) [140].

It can be concluded that the  $U_3O_8$  spectra measured can be associated with the  $\alpha$ - $U_3O_8$  modification. Senanayake et al. (2005) [94] and Jégou et al. (2010) [140] reported the following peaks for  $\alpha$ - $U_3O_8$ :  $340$ ,  $405$  and  $480\text{ cm}^{-1}$  due to  $A_{1g}$ ,  $A_{1g}$  and  $E_g$  U-O stretching. Peaks at higher wavenumbers:  $640$ ,  $795\text{ cm}^{-1}$  could be identified as overtones of the  $A_{1g}$  and  $E_g$  stretches. The measured peaks at higher wavelength of this quadruple band show a shift for the  $453\text{ cm}^{-1}$  peak to  $493\text{ cm}^{-1}$  for the spectra recorded at TUW. Stefaniak et al. (2008) [138] reports similar findings. The shift can be explained by the different measuring conditions and laser energies. The peak at  $809\text{ cm}^{-1}$  is in accordance to the findings of Palacios et al. (2000) [126] and Jégou et al. (2010) [140] and is an overtone or harmonic vibrational mode of the U-O stretch vibration band between  $340 - 550\text{ cm}^{-1}$ .

### 5.3.1.2 $UO_2$

Two bands were detected for  $UO_2$ :  $445\text{ cm}^{-1}$  and  $1147\text{ cm}^{-1}$ . These results are in accordance with various references from Pointurier et al. (2010) [135], Stefaniak et al. (2008) [138], Palacios et al. (2000) [126], Lue et al. (2014) [156] to Allen et al. (1987) [117].

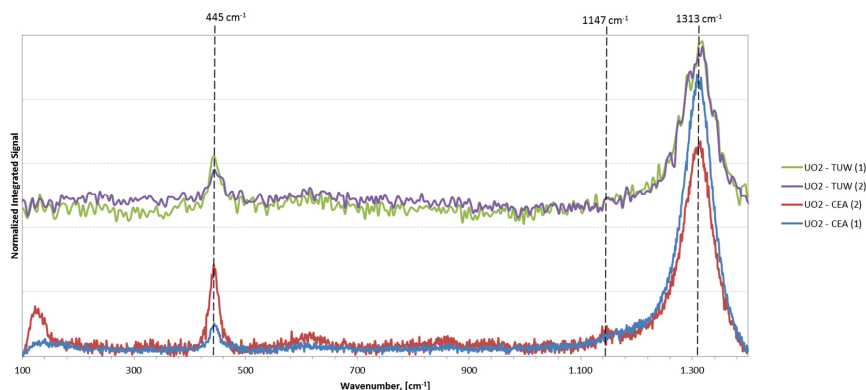


**Figure 61: Micro Raman spectra of UO<sub>2</sub> acquired at CEA and TUV.**

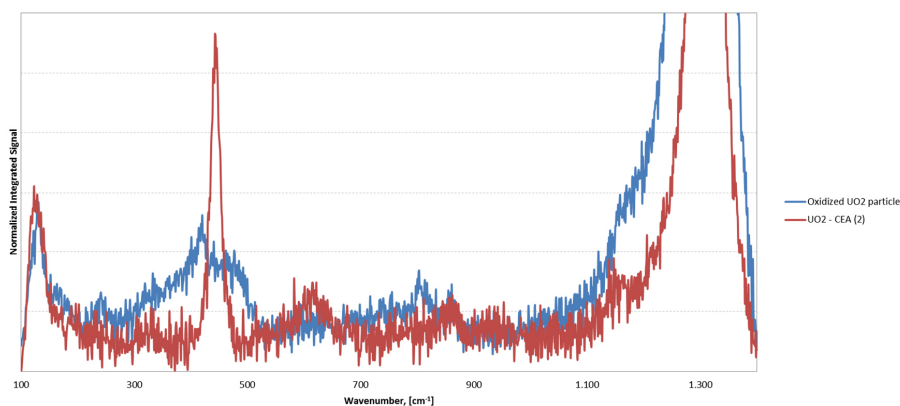


**Figure 62: Peak transition due to laser induced UO<sub>2</sub> oxidation; to U<sub>3</sub>O<sub>8</sub>.**

The same applies to the band around 1150 cm<sup>-1</sup>: Jégou et al. (2010) [140], Pointurier et al. (2010) [135], Stefaniak et al. (2008) [138], Senanayake et al. (2005) [94], Lue et al. (2014) [156] to Allen et al. (1987) [117], see Table 19.

If the laser energy is increased too much, UO<sub>2</sub> can oxidize to α-U<sub>3</sub>O<sub>8</sub>. The oxidation of UO<sub>2</sub> by the incident energy of the laser to U<sub>3</sub>O<sub>8</sub> is a well-documented process which is generated through an intermediate U<sub>3</sub>O<sub>7</sub> / U<sub>4</sub>O<sub>9</sub> step, see Pointurier et al. (2010) [135], Winer et al. (1986) [125], Armstrong et al. (1989) [157] and Hoekstra et al. (1961) [85], [127]. This oxidation phenomenon was observed during our measurements as well: the particle was exposed for 5s to a laser power of 150 mW, the spectra were acquired at 300 μW; see Figure 62.

**Table 19: Raman bands detected for UO<sub>2</sub> in accordance with the following references.**

	Wavelength, [cm <sup>-1</sup> ]		Reference
1	445	m	Stefaniak et al. (2008), Pointurier et al. (2010), Palacios et al. (2000)
2	1147	w	Jégou et al. (2000), Lue et al. (2014), Pointurier et al. (2010), etc.

### 5.3.1.3 Uranyl Nitrate Hexahydrate

Uranyl nitrate hexahydrate (UNH) was measured both at CEA and TUV. Data collected at CEA was measured from Stage (1) and Stage (2). Stage (1) contains bulk materials of UNH while Stage (2) contains micrometer sized particulates. The spectra differ significantly from those two substrates: bulk materials of UNH deliver a much more distinct peak resolution: 5 different bands for Stage (1) could be identified. A medium band at 205 - 230 cm<sup>-1</sup> a small band at 748cm<sup>-1</sup> and a strong signal at 872 cm<sup>-1</sup>. A distinct double peak at 1030 and 1040 cm<sup>-1</sup> was measured. In comparison, the peaks associated with Stage (2) which were obtained at CEA and TUV show a different band profile: the first band at 748 cm<sup>-1</sup> is rather weak and broadened and it merges into a medium band at 821 cm<sup>-1</sup>. The only strong band comes from the carbon substrate at 1310 cm<sup>-1</sup>. Khulbe et al. (1989) [158] present Raman spectra of uranyl nitrate hexahydrate at various temperatures. According to Khulbe et al. (1989) [158], the crystal structure was determined by neutron diffraction. UNH has orthorhombic space group C<sub>2v</sub><sup>12</sup> (Cmc2<sub>1</sub>). The following peaks for Stage 1 (bulk quantities) could be verified. Khulbe et al. (1989) [158] identified a strong band at 1622 cm<sup>-1</sup>. MRS measurements performed at TUV revealed a distinct peak at 1618 cm<sup>-1</sup>, see Figure (120) in the Appendix. The double band at 1030 and 1040 cm<sup>-1</sup> is in accordance to Khulbe et al. (1989) [158] findings (1039 - 1050 cm<sup>-1</sup>) as well as for 748 cm<sup>-1</sup> and 205 - 230 cm<sup>-1</sup>; the latter one not being so diffuse but distinct.

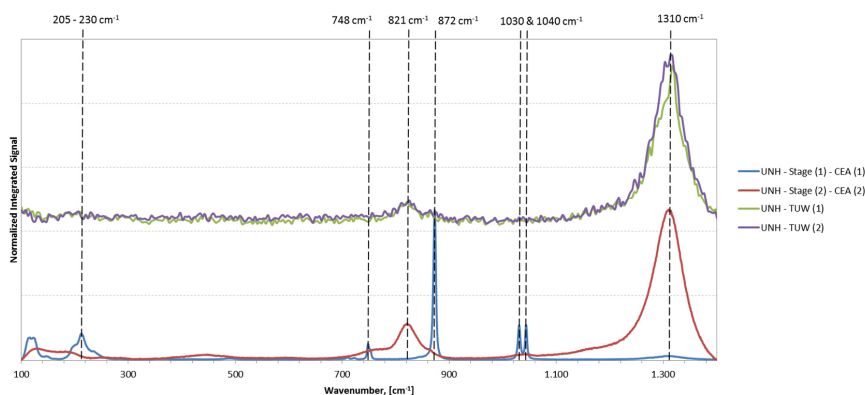


**Figure 63: Micro Raman spectra of UNH of Stage (1) and (2) acquired at CEA and TUW.**

For Stage 2, only minute quantities were measured on single micrometer sized particulates. Only one small-medium peak could be identified at 821  $\text{cm}^{-1}$ . This peak is in accordance with a peak identified from Khulbe et al. (1989) [158] at 830  $\text{cm}^{-1}$ .

**Table 20: Raman bands detected for UNH in accordance with the following references.**

Wavelength, [ $\text{cm}^{-1}$ ]		Reference
<b>Stage 1</b>		
1	205 - 230 w	Khulbe et al. (1989)
2	748 W	Khulbe et al. (1989)
3	872 S	Khulbe et al. (1989)
4	1030 & 1040 S	Khulbe et al. (1989)
5	1610 m	Khulbe et al. (1989)
<b>Stage 2</b>		
	821 w	Khulbe et al. (1989)

### 5.3.1.4 Ammonium Diuranate

Ammonium diuranate (ADU) was only measured at the TUW. ADU is part of the mixture that is commonly known as “Yellow Cake” (YC). YC is a precursor product for the nuclear fuel cycle. Uranium is leached from the ore and then purified and concentrated. The concentrated uranium solution is precipitated with reagents that can be ammonia or ammonium hydroxide, hydrogen peroxide, sodium peroxide thus forming the corresponding compounds. Drying and calcination processes lead subsequently to the corresponding oxides:  $\text{UO}_3$  and  $\text{U}_3\text{O}_8$ . The number of references concerning Raman spectra on ADU is very scarce. Ho et al. (2015) [159] investigated ADU compounds from different mines and geographical locations. Pointurier et al. (2010) [135] investigated ADU particulate with MRS. They found three distinct bands at 465, 810 and 1389  $\text{cm}^{-1}$ .

**Table 21: Main Raman bands detected for ADU.**

Wavelength, [ $\text{cm}^{-1}$ ]		Reference
1	716 - 755 w	No reference
2	814 m	Pointurier et al. (2010) (810 $\text{cm}^{-1}$ )
3	837 w	Ho et al. (2015)
4	1604 m	No reference

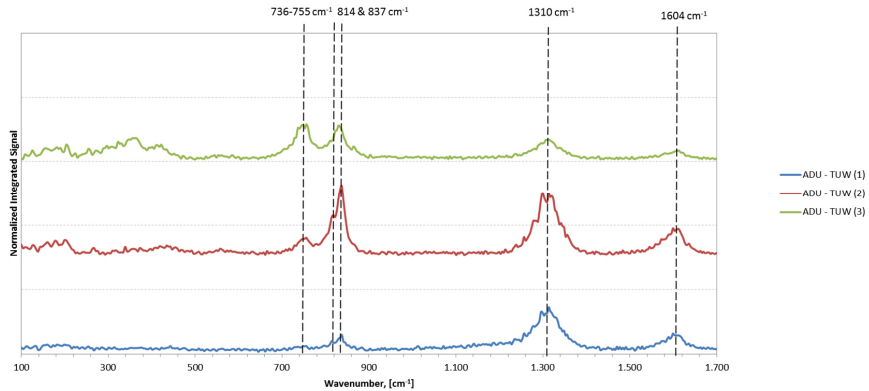


**Figure 64: Micro Raman spectra of ADU acquired at TUW.**

MRS revealed three distinct bands at 716, 814 and 1604  $\text{cm}^{-1}$ . The band at 716 – 755  $\text{cm}^{-1}$  is a broad and weak band. No reference to ADU could be found, but ammonium uranyl carbonate shows a deformation stretch of the uranyl ion in the region 727 – 816  $\text{cm}^{-1}$ . For the band at around 1600  $\text{cm}^{-1}$  no reference band could be identified, but it could be an overtone of the O-U stretch vibrational mode at 814 – 837  $\text{cm}^{-1}$ . Ho et al. (2015) [159] published a similar spectrum for ADU originating from Milliken Lake, Ontario Canada. Degradation effects on the ADU are possible reason for the discrepancy in the ADU spectra observed from Ho et al. (2015) [159] and Pointurier et al. (2010) [135].

### 5.3.1.5 $\text{UO}_2\text{F}_2$

$\text{UO}_2\text{F}_2$  was measured at CEA only. The  $\text{UO}_2\text{F}_2$  material was stored in a plastic vial for several years. Degradation and oxidation may occur. One distinct band could be identified at 867  $\text{cm}^{-1}$ . This accordance with Stefaniak et al. (2013) [160] and (2014) [139] and Pointurier et al. (2010) [135], Kips et al. (2009) [31] and Pidduck et al. (2008) [145]. The band between 800 and 900  $\text{cm}^{-1}$  can be associated with symmetric U-O vibrational modes. According to Stefaniak et al. (2013) [160] the exact wavenumber depends on the neighboring ions. They also presented spectra acquired from  $\text{UO}_2\text{F}_2$  particles which were stored under ambient conditions for months, in the same way as our particles: by gradual water absorption a Raman shift occurs and lead to a broadening of the signal which, see Figure 65 and Table 22.

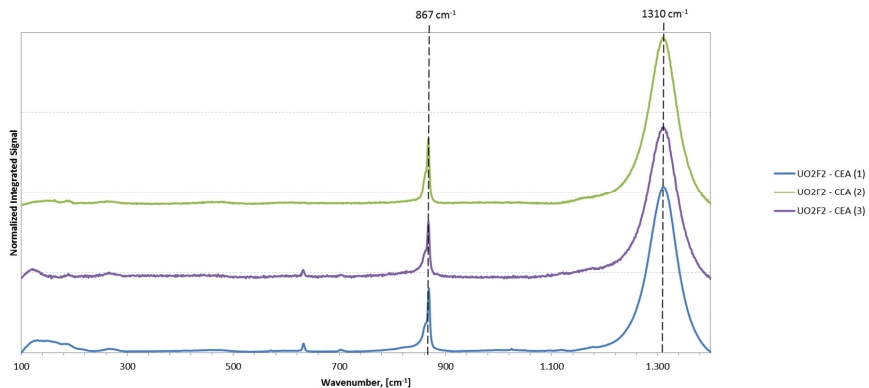


**Figure 65: Micro Raman spectra of  $\text{UO}_2\text{F}_2$  acquired at CEA.**

**Table 22: Main Raman bands detected for  $\text{UO}_2\text{F}_2$ .**

	Wavelength, [ $\text{cm}^{-1}$ ]	Reference
1	867	w
		Stefaniak et al. (2013), Pointurier et al. (2010)

The peak itself consists of a doublet band caused by water uptake. The measured peak at  $867 \text{ cm}^{-1}$  also shows tailing at the front. The well-established  $\text{UO}_2^{2+}$  stretching band had very probably shifted to a double band through the uptake of water (caused by humidity); this is the case when  $\text{UO}_2\text{F}_2$  reaches the water saturation equilibrium, see Figure 118 in the Appendix Chapter 7.5.3. This result is in direct accordance to Stefaniak et al. (2013) [160].

### 5.3.1.6 SG140521\_02

The polydisperse particles of SG140521\_02 were produced in May 2014. The precursor aerosol droplets were heat treated by the preheating system at  $480^\circ\text{C}$  and then calcinated at  $737 - 747^\circ\text{C}$  in the four-zone oven, see setup depicted in Figure 17. Under these production environment  $\text{U}_3\text{O}_8$  is expected. In this discussion a representative number of three spectra will be displayed, see Figure 66. All spectra acquired are depicted in the Appendix – Chapter 7.5.4: Figure 119.

Seven different bands could be identified using MRS at CEA:  $242 \text{ cm}^{-1}$  (w),  $377 \text{ cm}^{-1}$  (w),  $416 \text{ cm}^{-1}$  (m),  $481 \text{ cm}^{-1}$  (m) and  $607 \text{ cm}^{-1}$  (w). The first band was measured at  $242 \text{ cm}^{-1}$  can be associated with  $\alpha\text{-U}_3\text{O}_8$ : Allen et al. (1987) [117] measured on powdered solids a strong band at  $236 \text{ cm}^{-1}$ . Senanayake et al. (2005) [94] measured a band at  $235 \text{ cm}^{-1}$  for  $\alpha\text{-U}_3\text{O}_8$ . The band range between  $\sim 370$  and  $490 \text{ cm}^{-1}$  is a relatively strong, but very diffuse band area. The first identified peak of this allegedly triple peak can be found at  $377 \text{ cm}^{-1}$ . This band cannot be associated with a U-O stretching vibrational mode of  $\text{U}_3\text{O}_8$ . This band shows the biggest resemblance to a diffuse band from meta schoepite  $[(\text{UO}_2)_4\text{O}(\text{OH})_6 \cdot 5(\text{H}_2\text{O})]$  and uranium (IV) hydroxide  $[\alpha\text{-UO}_2(\text{OH})_2]$  measured by Sweet et al. (2013) [93] at around  $370 \text{ cm}^{-1}$ . The second peak at  $\sim 416 \text{ cm}^{-1}$  shows no distinct identification: Stefaniak et al. (2008) [138] measured a peak at  $405 \text{ cm}^{-1}$  for  $\text{U}_3\text{O}_8$ . Further references by Allen et al. (1987) [117], Palacios et al. (2000) [126] and Pointurier et al. (2010) [135] indicate the presence of  $\alpha\text{-U}_3\text{O}_8$ . The third peak was measured at around  $481 \text{ cm}^{-1}$ . This peak corresponds to a U-O vibrational mode of  $\text{UO}_3$  and was measured by Armstrong et al. (1989) [157], Sweet et al. (2013) [93] and Palacios et al. (2000) [126] on  $\gamma\text{-UO}_3$ . The peak at  $607 \text{ cm}^{-1}$  is very weak and phase identification is difficult. The biggest resemblance was to be found with a measurement acquired from measuring  $\text{UO}_2$  standard by Stefaniak et al. (2008) [138]. The peak at  $806 \text{ cm}^{-1}$  can be associated to an overtone mode of U-O by  $\text{U}_3\text{O}_8$ , see Jégou et al. (2010) [140], Palacios et al. (2000) [126], Stefaniak et al. (2008) [138] and Pointurier et al. (2010) [135], see Table 23.

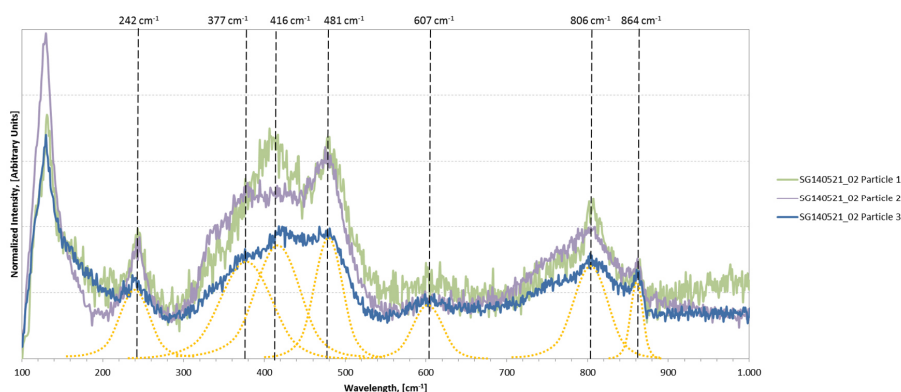


**Figure 66: Raman spectrum of polydisperse SG140521\_02.**

The last peak at around  $864\text{ cm}^{-1}$  shows the biggest resemblance to bands measured by Bastians et al. (2004) [161] and Pointurier et al. (2010) [135] on studite  $[\text{UO}_4 \cdot 4\text{H}_2\text{O}]$  and meta-studite  $[\text{UO}_4 \cdot 2\text{H}_2\text{O}]$ .

**Table 23: Main Raman bands detected for SG140521\_02.**

	Wavelength, $[\text{cm}^{-1}]$		Reference
1	242	w	$\alpha\text{-U}_3\text{O}_8$ Pointurier et al. ( $236\text{ cm}^{-1}$ )
2	377	w	Meta Schoepite, $\alpha\text{-UO}_2(\text{OH})_2$ , Sweet et al. (2013)
3	416	m	$(\alpha)\text{-U}_3\text{O}_8$ , Pointurier et al. (2010), Stefaniak et al. (2008)
4	481	m	$\gamma\text{-UO}_3$ , Armstrong et al. (1989), Sweet et al. (2013)
5	607	w	$\text{UO}_2$ , Stefaniak et al. (2008)
6	806	m	$\text{U}_3\text{O}_8$ , Pointurier et al. (2010), Stefaniak et al. (2008)
7	864	W	$\text{UO}_4 \cdot 4\text{H}_2\text{O}$ , $\text{UO}_4 \cdot 2\text{H}_2\text{O}$ , Bastians et al. (2004), Pointurier et al. (2010)

### 5.3.1.7 SG141027\_12A

All 15 spectra obtained on SG141027\_12A are shown in the Appendix in Chapter 7.5.5, Figure 120, all with the same comparable spectral range of  $100 - 1400\text{ cm}^{-1}$ . Spectra obtained at TUW have a wider spectral range. SG141027\_12A was produced without the furnace only with the pre-heating attached, at temperatures around  $560^\circ\text{C}$ . SG141027\_12A shows comparable Raman bands as SG140521\_02. It is obvious that the spectra for SG141027\_12A are less noisy and better resolved. The band at  $242\text{ cm}^{-1}$  can be identified as a U-O stretch vibration of  $(\alpha)\text{-U}_3\text{O}_8$ , see Allen et al. (1987) [117], Pointurier et al. (2010) [135] and Senanayake et al. (2005) [94]. A similar diffuse broad band between  $330 - 490\text{ cm}^{-1}$  was measured: The first band at  $339\text{ cm}^{-1}$  can be associated with multiple U-O species: Sweet et al. (2013) [93] measured band at  $339\text{ cm}^{-1}$  for  $\gamma\text{-UO}_3$  and for meta-schoepite and uranium (IV) hydroxide at around  $370\text{ cm}^{-1}$ . According to Allen et al. (2013) [117], this band can also be associated with  $\alpha\text{-U}_3\text{O}_8$  or according to Stefaniak et al. (2008) [138] to  $\text{U}_3\text{O}_8$ . The peak at  $386\text{ cm}^{-1}$  can be associated with meta schoepite and uranium (IV) hydroxide, see Sweet et al. (2013) [93]. Since this band is so diffuse it is difficult to identify it to a uranium species: Butler et al. (1988) [118] identified  $\text{U}_3\text{O}_8$ . The band at  $419\text{ cm}^{-1}$  is very likely to be associated with  $(\alpha)\text{-U}_3\text{O}_8$ , see Stefaniak et al. (2013) [138], Allen et al. (1987) [117], Palacios et al. (2000) [126] and Pointurier et al. (2010) [135]. The last peak of the strong diffuse band is  $481\text{ cm}^{-1}$ . As mentioned before this band was measured occurred at  $481\text{ cm}^{-1}$ . This peak corresponds to a U-O vibrational mode of  $\gamma\text{-UO}_3$  which was measured by Armstrong et al. (1989) [157], Sweet et al. (2013) [93] and Palacios et al. (2000) [126].

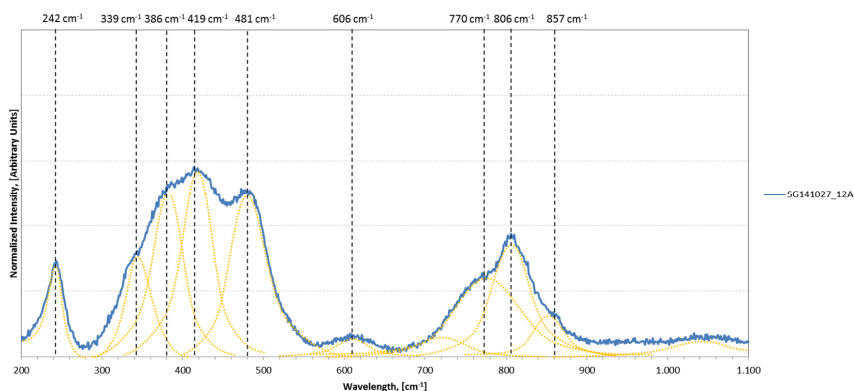


**Figure 67: Raman spectrum of selected particles from SG141027\_12A, measured at CEA.**

The peak at  $607\text{ cm}^{-1}$  is also very weak and it is difficult to make a meaningful statement: it is most likely that it is caused by  $\text{UO}_2$  modification which was also measured by Stefaniak et al. (2008) [160]. A band region between  $770$  and  $860\text{ cm}^{-1}$  was measured. Area fitting revealed the presence of three bands:  $770\text{ cm}^{-1}$ ,  $806\text{ cm}^{-1}$  and  $857\text{ cm}^{-1}$ . According to Sweet et al. (2013) [93] and Armstrong et al. (1989) [157], the band measured at  $770\text{ cm}^{-1}$  can be associated with  $\gamma\text{-UO}_3$ . The band at  $806\text{ cm}^{-1}$  is similar to SG140521\_02 and can be associated to an overtone mode of U-O vibrational modes of  $\text{U}_3\text{O}_8$ ; see Jégou et al. (2010) [140], Palacios et al. (2000) [126], Stefaniak et al. (2008) [138] and Pointurier et al. (2010) [135]. The peak measured at  $857\text{ cm}^{-1}$  is similar to SG140521\_02 as well; see by Bastians et al. (2004) [161] and Pointurier et al. (2010) [135] measurements on studite [ $\text{UO}_4 \cdot 4\text{H}_2\text{O}$ ] and meta-studite [ $\text{UO}_4 \cdot 2\text{H}_2\text{O}$ ]. Figure 120 depicts the variations between the measurements performed at CEA and TUW. It shows that the band discrimination is better with the spectra acquired at CEA and the overall intensity of those normalized bands is better resolved. On the other hand, the peak associated to the Si background is significantly more pronounced at the CEA acquired spectrum.

**Table 24: Main Raman bands detected for SG141027\_12A.**

	Wavelength, [ $\text{cm}^{-1}$ ]		Reference
1	242	m	$\alpha\text{-U}_3\text{O}_8$ Pointurier et al. (2010)
2	339	m	Possible matches to ( $\alpha$ -) $\text{U}_3\text{O}_8$ , Meta-schoepite and U(IV)hydroxide See Sweet et al. (2013), Allen et al. (2013), Stefaniak et al. (2008)
3	386	m	Meta Schoepite, $\alpha\text{-UO}_2(\text{OH})_2$ , Sweet et al. (2013) or $\text{U}_3\text{O}_8$ Butler et al. (1988)
4	419	m	( $\alpha$ -) $\text{U}_3\text{O}_8$ , Pointurier et al. (2010), Stefaniak et al. (2008)
5	481	m	$\gamma\text{-UO}_3$ , Sweet et al. (2013), Palacios et al. (2000)
6	606	W	$\text{UO}_2$ , Stefaniak et al. (2008)
7	770	m	$\gamma\text{-UO}_3$ , Sweet et al. (2013) and Armstrong et al. (1989)
8	806	m	$\text{U}_3\text{O}_8$ , Pointurier et al. (2010), Stefaniak et al. (2008)
9	857	w	$\text{UO}_4 \cdot 4\text{H}_2\text{O}$ , $\text{UO}_4 \cdot 2\text{H}_2\text{O}$ , Bastians et al. (2004), Pointurier et al. (2010)

### 5.3.1.8 SG150401\_14A

SG150401\_14A was solely measured at TUW. All spectra measured are depicted in the Appendix in Chapter 7.5.7 Figure 122.

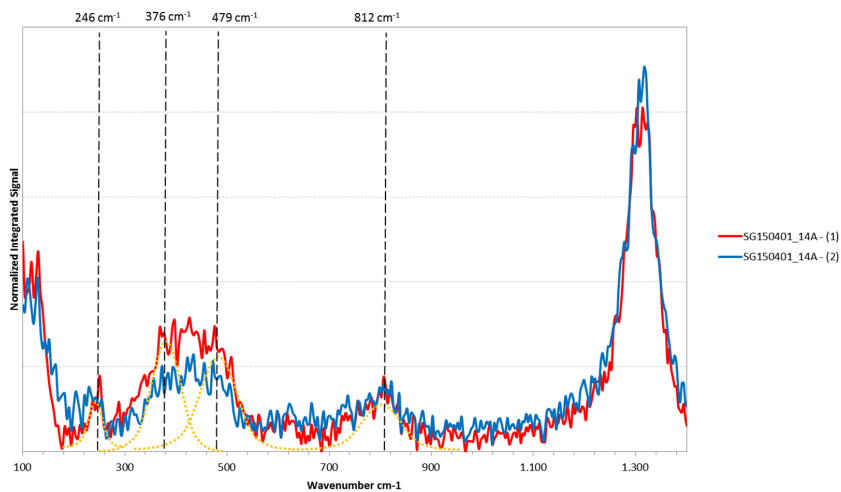


**Figure 68: Raman spectrum of selected particles from SG150401\_14A, measured at TUW.**

SG150401\_14A was produced in April 2015 under similar conditions to SG141027\_12A: no furnace and only pre-heating: at around 500°C. The spectra obtained are noisier than the spectra obtained at CEA thus making the identification of diffuser bands more challenging. This is due to a higher systematic signal to noise ratio. Four different bands were identified: 246  $\text{cm}^{-1}$ , 376  $\text{cm}^{-1}$ , 479  $\text{cm}^{-1}$  and 812  $\text{cm}^{-1}$ . The first band at 246  $\text{cm}^{-1}$  is comparable to “polydisperse” SG140521\_02 and “quasi-monodisperse” SG141027\_12A and can be associated to  $(\alpha\text{-})\text{U}_3\text{O}_8$ ; see Allen et al. (1987) [117], Pointurier et al. (2010) [135] and Senanayake et al. (2005) [94]. The band between 370 and 480  $\text{cm}^{-1}$  is very diffuse and noisy. The band measures at 376  $\text{cm}^{-1}$  is quite likely to be caused by meta schoepite  $[(\text{UO}_2)_4\text{O}(\text{OH})_6 \cdot 5(\text{H}_2\text{O})]$  and uranium (IV) hydroxide  $[\alpha\text{-UO}_2(\text{OH})_2]$ ; see Sweet et al. (2013) [93]. The second peak at 479  $\text{cm}^{-1}$  is also comparable to SG140521\_02 and SG141027\_12A and according to Armstrong et al. (1989) [157], Sweet et al. (2013) [93] and Palacios et al. (2000) [126] it can be associated with  $\gamma\text{-UO}_3$ . The last peak was measured at 812  $\text{cm}^{-1}$  and is according to Bastians et al. (2004) [161] and Pointurier et al. (2010) [135] caused by studite  $[\text{UO}_4 \cdot 4\text{H}_2\text{O}]$  and meta-studite  $[\text{UO}_4 \cdot 2\text{H}_2\text{O}]$ .

**Table 25: Main Raman bands detected for SG150401\_14A.**

	Wavelength, [ $\text{cm}^{-1}$ ]		Reference
1	246	w	$\alpha\text{-U}_3\text{O}_8$ Pointurier et al. (236 $\text{cm}^{-1}$ )
2	376	m	Meta Schoepite, $\alpha\text{-UO}_2(\text{OH})_2$ , Sweet et al. (2013)
3	479	m	$\gamma\text{-UO}_3$ , Armstrong et al. (1989), Sweet et al. (2013)
4	812	w	$\alpha\text{-U}_3\text{O}_8$ , Palacios et al. (2000), Pointurier et al. (2010) $\text{UO}_4 \cdot 4\text{H}_2\text{O}$ (Studite), Bastians et al. (2004)

### 5.3.1.9 Conclusion

Spectra acquired at CEA were recorded in a wavelength region of 100 – 1400  $\text{cm}^{-1}$  whereas spectra recorded at TUW had a much wider spectral bandwidth of 0 – 3200  $\text{cm}^{-1}$ . The strong peak at around 1310  $\text{cm}^{-1}$  is associated to the carbon substrate in all spectra. Figure 69 depicts the evolution of the particles from May 2014 to May 2015. It is apparent that the signal to noise ratio for spectra recorded at TUW is in general higher than for spectra acquired at CEA. This is an inherent systematic characteristic of the Vitec machine. Particle produced at FZJ show no significant changes in their spectra, see Figure 69. SG140521\_02 is due to its polydisperse characteristic the least well resolved spectrum. Furthermore, it is the only batch that was produced under significantly different conditions. Raman investigation revealed the presence of a non-distinct uranium-oxide species.

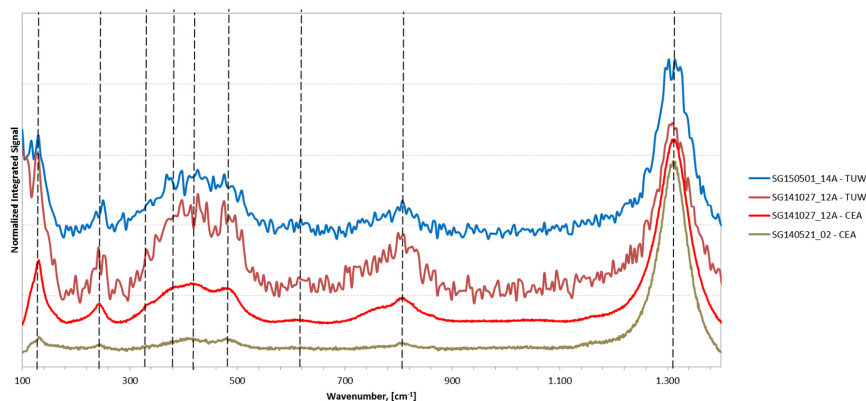


**Figure 69: Particle Evolution: Direct comparison of SG140521\_02 vs. SG141027\_12A and SG150401\_14A.**

The largest share is associated with  $U_3O_8$ . Small bands at around  $339\text{ cm}^{-1}$ ,  $377 - 386\text{ cm}^{-1}$  can be attributed to meta-schoepite and uranium (IV) hydroxide ( $\alpha\text{-}UO_3(OH)_2$  and meta-schoepite  $(UO_2)_4O(OH)_6 \cdot 5H_2O$ ) and  $812\text{ cm}^{-1}$  and  $857\text{ cm}^{-1}$  for (meta-) studite (studite  $[UO_4 \cdot 4H_2O]$  and meta-studite  $[UO_4 \cdot 2H_2O]$ ). This many matches deliver a strong indication that a multiphase uranium compound is present with varying amounts of uranium oxide and hydroxide - simultaneously present in a single microparticle. Additionally, small shares of  $\gamma\text{-}UO_3$  were identified as well, a weak and diffuse band at  $479 - 481\text{ cm}^{-1}$  was seen. Particles originating from SG140521\_02 were treated at higher temperature for a much longer time: for the preheating a dwell time of about 0.15 s was calculated and for the furnace a mean dwell time of 3.3 s at temperatures  $> 750\text{ }^\circ\text{C}$  were expected. SG141027\_12A and SG150401\_14A were only converted through the pre-heating system at temperature between  $500 - 560\text{ }^\circ\text{C}$ , see Table 5 and Table 6. Interestingly, no significant change of the recorded spectra could be observed. Therefore, all batches the quality is consistent. This observation can also be seen in Figure 119 - Figure 123 in the appendix chapter 7.5.4 - 7.5.8. It can be concluded that the furnace is not necessary to ensure proper thermal treatment but no indication about the presence of carbon was found during the  $\mu$ -Raman investigation. This leads to the assumption that the presence of carbon in the quantitative EDX analysis in Chapter 5.2.3.3. is associated with a detector specific artefact.

## 5.4 Particle Characterization with Secondary Ionization Mass Spectrometry

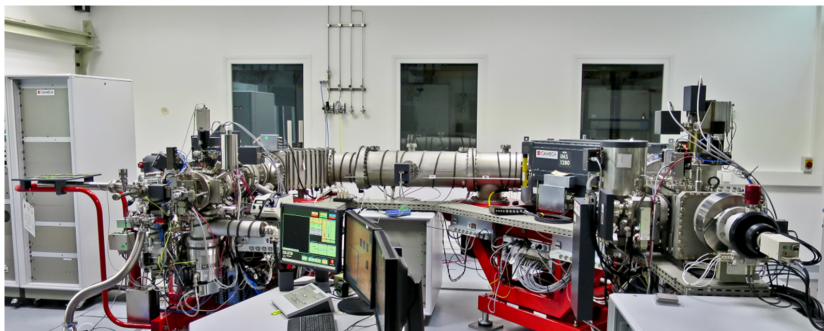


Figure 70: CAMECA 1280 LG-SIMS at SGAS-ESL.

All data presented in this chapter was recorded at an ion probe current (IP) of  $IP = 50\text{pA}$  and with a  $10\ \mu\text{m}$  beam raster size. All measurements were performed on a CAMECA 1280 large geometry SIMS (LG-SIMS) at IAEA SGAS-ESL. This chapter describes the results obtained on SG140521\_02 and SG141027\_12A with the LG-SIMS at SGAS-ESL. The aim of these measurements was to demonstrate the suitability of monodisperse microparticles over existing polydisperse bulk materials. Therefore, a series of measurements was performed, some of which are very specific for LG-SIMS. These investigations included the assessment of the isotopic content and the performance of monodisperse microparticles by evaluating the hydride formation, the useful yield, total evaporation and redistribution profiles and the effects of the ion beam on the  $^{238}\text{U}$  intensity profiles. Data presented in this chapter are obtained from analysis of single micrometer sized uranium oxide particles.

LG-SIMS reports raw data files. Appropriate particles of interest were identified with proprietary Cameca software called “APM” (Automated Particle Measurement). After data reduction, appropriate uranium microparticles [h] were selected and investigated with the micro-probe mode ( $10\ \mu\text{m}$  Beam Raster and an ion probe current IP of  $50\ \text{pA}$ ). The output data was collected as isotope abundances which were converted into isotope amount ratios, a quantity usually used in connection with metrological standards.

### 5.4.1 Isotopic Analysis

All particles discussed in this thesis were made from solutions with the uranium prepared from the CRM IRMM-183. According to Richter et al. (2005) [162], IRMM-183 was produced in 1987 along with a series of other uranium CRMs (IRMM183-187) ranging from 0.3 - 4.5 % enrichment levels. Richter et al. (2005) [162] re-certified the isotopic content of all these CRMs using more accurate measurement techniques than were available during the initial certification in 1987. Due to the progress in the development of mass spectrometers and measurement methods, the certified values had to be updated and the corresponding uncertainties of isotope mass fractions of  $^{234}\text{U}/^{238}\text{U}$  and  $^{236}\text{U}/^{238}\text{U}$  could be reduced significantly. For instance, the re-certified value for the minor abundance of  $n(^{234}\text{U})/n(^{238}\text{U})$  was revalued and a discrepancy of  $\sim 1.5\%$  to the old certified value was determined. The new value was derived to be  $n(^{234}\text{U})/n(^{238}\text{U}) = 1.975\ 5(22) \cdot 10^{-5}$ , see Table 26. The data was acquired using thermal ionization mass spectrometry (TIMS) (Thermo Fischer, Triton) on bulk materials of the CRM.

The aim of this investigation was to measure the isotopic content in order to see if anomalies from the certified values of the CRM occurred. Table 26 depicts the re-certified values by Richter et al. (2005)

[h] Appropriate particles: single uranium microparticles with a minimum distance of  $50\ \mu\text{m}$  to each other.

which were used as a direct comparison for the re-evaluation of the isotopic content by deriving the isotope amount ratios. The following paragraphs present results from measurements of the isotopic amount ratios of  $n(^{234}\text{U})/n(^{238}\text{U})$ ,  $n(^{235}\text{U})/n(^{238}\text{U})$  and  $n(^{236}\text{U})/n(^{238}\text{U})$ . The measured intensities, i.e. counts/particle can be directly correlated to the mass of uranium per particle, which will later on be discussed as well. In this chapter two different batches were analyzed: SG140521\_02A and SG141027\_12A. All particles were directly measured from the C-substrate. Since SG140521\_02A can be considered “worst-case scenario” for monodisperse particles it was useful to assess its performance in comparison to SG141027\_12A. The data sheet with all relevant data on  $n(^{234}\text{U})/n(^{238}\text{U})$ ,  $n(^{235}\text{U})/n(^{238}\text{U})$  and  $n(^{236}\text{U})/n(^{238}\text{U})$  is provided in the Appendix in Chapter (7.6.1) - Table 43 and Table 44.

**Table 26: Re-Certified Amount Ratios of IRMM-183, according to Richter et al. (2005).**

$n(^{234}\text{U})/n(^{238}\text{U})$	$1.9755(22) \cdot 10^{-5}$
$n(^{235}\text{U})/n(^{238}\text{U})$	$3.2157(16) \cdot 10^{-3}$
$n(^{236}\text{U})/n(^{238}\text{U})$	$1.48358(54) \cdot 10^{-4}$

### 5.4.1.1 Determination of Isotope Ratios

The isotope amount ratios of  $n(^{234}\text{U})/n(^{238}\text{U})$  from SG141027\_12A and SG140521\_02 will be discussed first. The following charts depict the abundance of  $^{234}\text{U}$  per particle as an isotope amount ratio of  $n(^{234}\text{U})/n(^{238}\text{U})$  against the number of particle being measured: for SG141027\_12A 21 particles were measured and for SG140521\_02 eight particles were measured. All relevant data is depicted in Table 27.

For SG141027\_12A, a mean isotope ratio of  $n(^{234}\text{U})/n(^{238}\text{U}) = 1.999 \cdot 10^{-5} \pm 1.333 \cdot 10^{-6}$  was measured. This corresponds to a relative standard deviation (RSD) of 6.67 %. As a comparison, Richter et al. (2005) measured an isotope ratio of  $n(^{234}\text{U})/n(^{238}\text{U}) = 1.976 \cdot 10^{-5} \pm 2.2 \cdot 10^{-7}$ . The deviation of SG141027\_12A to Richter’s value is about 1.22%. It has to be noted that Richter measured bulk materials of IRMM-183 with thermal ionization mass spectrometry (TIMS). As expected, the corresponding uncertainties for  $n(^{234}\text{U})/n(^{238}\text{U})$  on SG141027\_12A are higher, the deviation is about 16.5 %, see Table 27. A standard deviation of the mean of  $2.909 \cdot 10^{-7}$  was calculated.

SG140521\_02 shows a comparable mean isotope ratio intensity with  $n(^{234}\text{U})/n(^{238}\text{U}) = 2.1392 \cdot 10^{-5} \pm 4.4612 \cdot 10^{-6}$ . Due to the polydisperse nature of these particles, the scatter of the mean value is > 3.3 x and the deviation to Richter’s certified value accounts to 7.66 %. This trend is observable in higher standard deviation of the mean with  $1.577 \cdot 10^{-6}$  and higher RSD with 20.85 %. A direct comparison of SG141027\_12A and SG140521\_02 shows a deviation of the average values of  $n(^{234}\text{U})/n(^{238}\text{U})$  of 6.52% and a deviation of 70.12 % for the STD of the mean values.

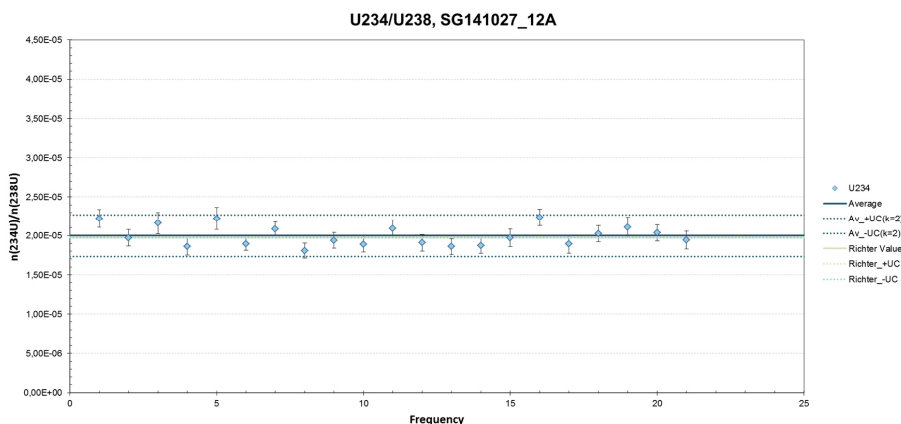


**Figure 71:  $n(^{234}\text{U})/n(^{238}\text{U})$  intensities of SG141027\_12A.**

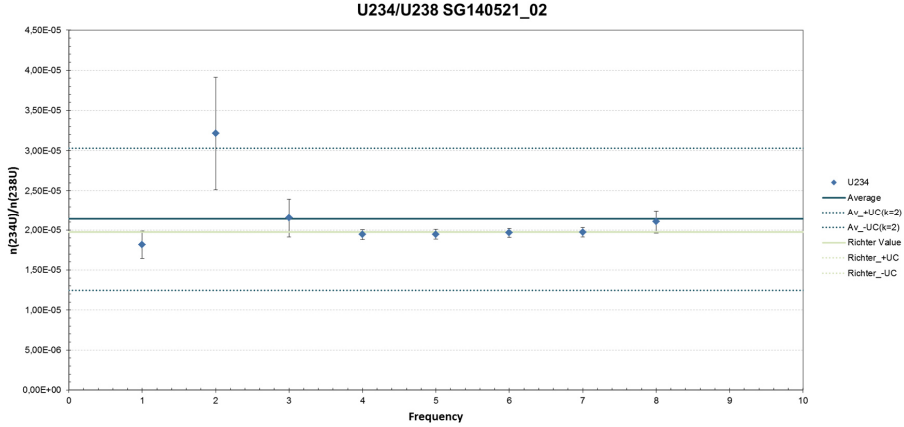


Figure 72:  $n(^{234}\text{U})/n(^{238}\text{U})$  intensities of SG140521\_02.

The isotope amount ratios for  $^{235}\text{U}$  of SG141027\_12A and SG140521\_02 were also measured. SG141027\_12 has an average intensity ratio of  $n(^{235}\text{U})/n(^{238}\text{U}) = 3.2189 \cdot 10^{-3} \pm 1.2991 \cdot 10^{-5}$  with a RSD of 0.40 %. The low RSD is accounted for the consistent quality of the monodisperse particle species and its resulting counting statistic. This trend is also reflected in a significantly low standard deviation of the mean of  $2.8350 \cdot 10^{-6}$ . The deviation to Richter's value is only 0.10 %.

Table 27:  $n(^{234}\text{U})/n(^{238}\text{U})$  ratios for SG141027\_12A and SG140521\_02.

$n(^{234}\text{U})/n(^{238}\text{U})$ (SG141027_12A)
Certified Value for $^{234}\text{U}/^{238}\text{U}$ ( $1.9755 \cdot 10^{-5} \pm 2.2 \cdot 10^{-7}$ ), $k = 2$
Average $^{234}\text{U}/^{238}\text{U}$ ( $1.9999 \cdot 10^{-5} \pm 1.3332 \cdot 10^{-6}$ ), $k = 2$ (STD, $n = 21$ )
Rel. Std. Dev.: 6.67 %, Rel. Bias: 1.22 %
$n(^{234}\text{U})/n(^{238}\text{U})$ (SG140521_02)
Certified Value for $^{234}\text{U}/^{238}\text{U}$ ( $1.9755 \cdot 10^{-5} \pm 2.2 \cdot 10^{-7}$ ), $k = 2$
Average $^{234}\text{U}/^{238}\text{U}$ ( $2.1393 \cdot 10^{-5} \pm 4.4612 \cdot 10^{-6}$ ), $k = 2$ (STD, $n = 8$ )
Rel. Std. Dev.: 20.85 %, Rel. Bias: 8.29 %

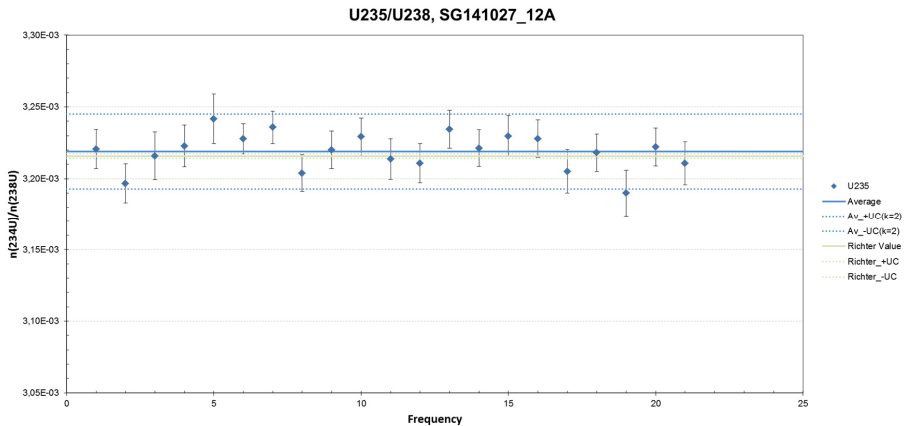


Figure 73:  $n(^{235}\text{U})/n(^{238}\text{U})$  intensities of SG141027\_12A.

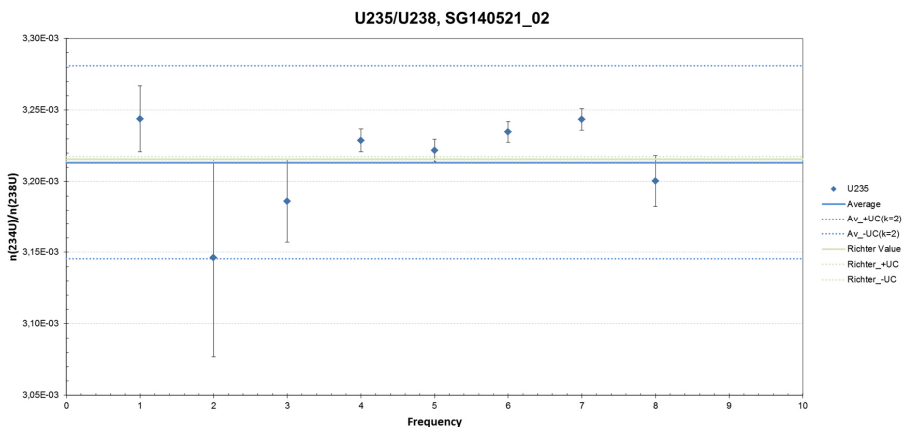


Figure 74:  $n(^{235}\text{U})/n(^{238}\text{U})$  intensities of SG140521\_02.

Again, SG140521\_02 shows a comparable mean value for the  $n(^{235}\text{U})/n(^{238}\text{U})$  intensity, but a significantly higher scatter:  $n(^{235}\text{U})/n(^{238}\text{U}) = 3.2132 \cdot 10^{-3} \pm 3.3806 \cdot 10^{-5}$  with a RSD of 1.05 % and a standard deviation of the mean of. Compared to Richter's value, the deviation account to -0.08 %, see Table 28.

Table 28:  $n(^{235}\text{U})/n(^{238}\text{U})$  ratios for SG141027\_12A and SG140521\_02.

$n(^{235}\text{U})/n(^{238}\text{U})$ (SG141027_12A)
Certified Value for $^{234}\text{U}/^{238}\text{U}$ ( $3.2157 \cdot 10^{-3} \pm 1.6 \cdot 10^{-5}$ ), $k = 2$
Average $^{234}\text{U}/^{238}\text{U}$ ( $3.2189 \pm 1.2991\text{E-}5$ ), $k = 2$ (STD, $n = 21$ )
Rel. Std. Dev.: 0.40 %, Rel. Bias: 0.10 %
$n(^{235}\text{U})/n(^{238}\text{U})$ (SG140521_02)
Certified Value for $^{234}\text{U}/^{238}\text{U}$ ( $3.2157 \cdot 10^{-3} \pm 1.6 \cdot 10^{-5}$ ), $k = 2$
Average $^{234}\text{U}/^{238}\text{U}$ ( $3.2132 \cdot 10^{-3} \pm 3.3806 \cdot 10^{-5}$ ), $k = 2$ (STD, $n = 8$ )
Rel. Std. Dev.: 1.05 %, Rel. Bias: -0.08 %

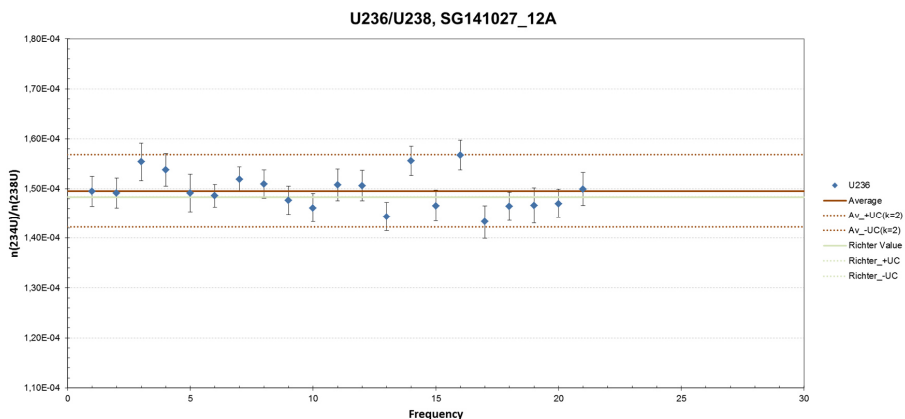
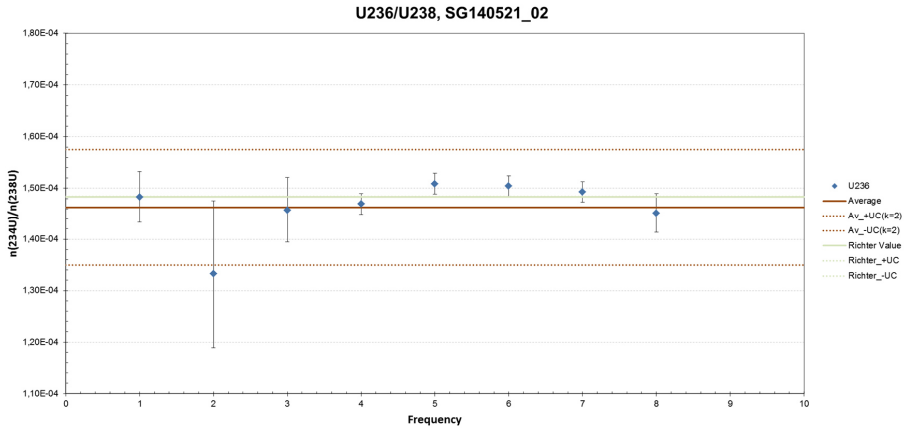


Figure 75:  $n(^{236}\text{U})/n(^{238}\text{U})$  intensities of SG141027\_12A.



**Figure 76:  $n(^{236}\text{U})/n(^{238}\text{U})$  intensities of SG140521\_02.**

The isotope ratios of  $^{236}\text{U}$  were measured for SG141027\_12A and SG140521\_02. A mean intensity of  $n(^{236}\text{U})/n(^{238}\text{U}) = 1.49521 \cdot 10^{-4} \pm 3.65118 \cdot 10^{-6}$  with a RSD of 2.44% and a standard deviation of the mean of  $7.96754 \cdot 10^{-7}$  was measured for SG141027\_12A. The deviation to Richter's value corresponds to 0.78%. The scatter and counting statistics for SG140521\_02 are poorer and account for  $n(^{236}\text{U})/n(^{238}\text{U}) = 1.46256 \cdot 10^{-4} \pm 5.64577 \cdot 10^{-6}$  with a RSD of 3.86 % and a standard deviation of the mean of  $1.99608 \cdot 10^{-6}$ . Compared to Richter's value, the deviation account to -1.42 %, see Table 29.

**Table 29:  $n(^{236}\text{U})/n(^{238}\text{U})$  isotope ratios for SG141027\_12A and SG140521\_02.**

<b><math>n(^{236}\text{U})/n(^{238}\text{U})</math> (SG141027_12A)</b>
Certified Value for $^{234}\text{U}/^{238}\text{U}$ ( $1.48358 \cdot 10^{-4} \pm 5.4 \cdot 10^{-7}$ ), $k = 2$
Average $^{234}\text{U}/^{238}\text{U}$ ( $1.4852 \cdot 10^{-4} \pm 3.6512 \cdot 10^{-6}$ ), $k = 2$ (STD, $n = 21$ )
Rel. Std. Dev.: 2.44 %, Rel. Bias: 0.78 %
<b><math>n(^{236}\text{U})/n(^{238}\text{U})</math> (SG140521_02)</b>
Certified Value for $^{234}\text{U}/^{238}\text{U}$ ( $1.48358 \cdot 10^{-4} \pm 5.4 \cdot 10^{-7}$ ), $k = 2$
Average $^{234}\text{U}/^{238}\text{U}$ ( $1.4626 \cdot 10^{-4} \pm 5.6458 \cdot 10^{-6}$ ), $k = 2$ (STD, $n = 8$ )
Rel. Std. Dev.: 3.86 %, Rel. Bias: -1.42 %

### 5.4.1.1 Conclusions

The measured values of the of the isotope amount ratio signals are a strong indication of the reproducibility or confidence of these data points. One can derive a qualitative assessment of these particles in terms of uranium amount per particle and density: smaller scatters and smaller uncertainties are favored.

For both batches, the original isotopic composition of IRMM-183 could be measured satisfactory. But inflated, hollow particles from SG140521\_02 show a significantly higher spread and uncertainty. This is due to their inhomogeneous properties and behavior during ion beam bombardment. The above-mentioned results prove that the measured mean values for  $n(^{234}\text{U})/n(^{238}\text{U})$ ,  $n(^{235}\text{U})/n(^{238}\text{U})$  and  $n(^{236}\text{U})/n(^{238}\text{U})$  of SG141027\_12A are in good accordance with the re-certified values determined by Richter et al. (2005) [162]. Since Richter's data was acquired using a TIMS on bulk material, we expect to see a significantly lower uncertainty for the isotope amount ratio signals in comparison to LG-SIMS results. The above mentioned results relate to the particle properties, e.g. amount of uranium per particle and density. But no quantitative statement can be made about these attributes. Results obtained

from SG141027\_12 indicate a consistent quality and the suitability as reference standard can be established with respect to isotope amount ratios.

SG140521\_02 shows a different picture. The variation in mean intensity values for the isotopic ratios vary is much greater. Table 30 depicts the deviation of the mean isotope ratio signals from SG141027\_12A and SG140521\_02. The deviation for the major isotopic ratio of  $n(^{235}\text{U})/n(^{238}\text{U})$  from SG140521\_02 is relatively low with 0.18 %. The difference of the minor abundances of  $n(^{234}\text{U})/n(^{238}\text{U})$  and  $n(^{236}\text{U})/n(^{238}\text{U})$  is significantly higher. The greater scatter and the resulting higher uncertainties caused by the poorer counting statistic due to the availability of only eight particles and thus their polydisperse attributes having an inconsistent amount of uranium/particle and density. This trend is also apparent in the Table 27 – Table 29, the mean values show a much stronger scatter and thus a greater uncertainty.

**Table 30: Comparison of SG141027\_12A and SG140521\_02.**

<b>Comparison SG141027_12A Vs SG140521_02</b>	
$n(^{234}\text{U})/n(^{238}\text{U})$	6.52 %
<b>Comparison SG141027_12A Vs SG140521_02</b>	
$n(^{235}\text{U})/n(^{238}\text{U})$	0.18 %
<b>Comparison SG141027_12A Vs SG140521_02</b>	
$n(^{236}\text{U})/n(^{238}\text{U})$	2.18 %

Due to the pronounced polydisperse character of SG140521\_02, it can be concluded that the performance of the scatter signals of  $^{234}\text{U}$ ,  $^{235}\text{U}$  and  $^{236}\text{U}$  does not meet the standards for a QC-material. The deviation is noticeably stronger than for SG141027\_12A. The spread or uncertainty of each measurement is a good indication for its inability to become a QC-material. SG141027\_12 on the other hand showed promising signal behavior the variance seems to be within tolerable limits and all 21 measurements performed within expected limitations. The consistency of its performance indicates a possible use as a QC-material in terms of isotope amount ratios signal intensity distribution. Finally, it can be concluded that the measured isotopic composition is independent of particle size and morphology. The initial isotopic composition of IRMM-183 could be verified in all batches.

#### 5.4.2 Direct Comparison to existing QC-Materials and CRMs

The performance of the monodisperse particles relative to the well-established CRM's was evaluated by measuring the  $^{238}\text{U}$  intensity profiles of each material over a defined period of time or so-called cycles. These  $^{238}\text{U}$ -intensity profiles were compared because it provides the highest signal output and the lowest corresponding uncertainties. IRMM-9073 and NBS-U010 were routinely used as an internal QC/calibration standard to calibrate the LG-SIMS m/Q(238)-signal for the analysis of the particles on the SG140521\_02 and SG141027\_12A samples. Sampling conditions for all four samples were kept constant (10  $\mu\text{m}$  beam raster, ion probe current 50 pA). All particles being analyzed were made in microprobe (MP) mode with 42 – 52 Cycles per particle.

**Table 31: Atom- and Weight Percent of NBS U010A.**

Atom-%	Weight-%
$^{234}\text{U}$ : 0.00541 $\pm$ 0.00005	$^{234}\text{U}$ : 0.00532
$^{235}\text{U}$ : 1.0037 $\pm$ 0.0010	$^{235}\text{U}$ : 0.9911
$^{236}\text{U}$ : 0.00681 $\pm$ 0.00007	$^{236}\text{U}$ : 0.00675
$^{238}\text{U}$ : 98.984 $\pm$ 0.001	$^{238}\text{U}$ : 98.997

So far, the existing CRMs were made from bulk materials of certified material which results in a very inhomogeneous and inconsistent  $^{238}\text{U}$ -profile. NBS U010 is a CRM containing  $\text{U}_3\text{O}_8$  and IRMM 9073 is a CRM made from Yellow Cake (YC). Both CRMs are finely grinded powders – chunky bulk materials with a polydisperse size distribution. A more predictable and consistent profile with a much lower

scatter is favored. Table 31 and Table 32 depict the certified values for NBS U010A and IRMM 9073. NBS U010A is a CRM from NIST with a chemical composition of  $U_3O_8$  and a certified molar mass of 238.02 g/mol. Copies of the certificates are deposited in the Appendix – Chapter 7.6.3 and 7.6.4, Figure 125 and Figure 126. IRMM 9073 is a CRM made of yellow cake (YC) with a certified molar mass of 238.028901 ± 0.0000012 g/mol.

**Table 32: Weight-, Amount- & Amount of Substance Fractions of IRMM 9073.**

Mass Fraction (·100)	Amount Fraction (·100)	Isotope Amount Ratio(s)
$m(^{234}U)/m(U)$ 0.005 325(42)	$n(^{234}U)/n(U)$ 0.005 415(76)	$n(^{234}U)/n(^{238}U)$ 0.000 054 55 (76)
$m(^{235}U)/m(U)$ 0.0711 51(36)	$n(^{235}U)/n(U)$ 0.720 54(36)	$n(^{235}U)/n(^{238}U)$ 0.007 258 1(36)
$m(^{236}U)/m(U)$ < 0.000 002	$n(^{236}U)/n(U)$ < 0.000 002	$n(^{236}U)/n(^{238}U)$ 0.000 000 02
$m(^{238}U)/m(U)$ 99.283 17(36)	$n(^{238}U)/n(U)$ 99.271 04(36)	

Figure 77 shows the combined  $^{238}U$  intensities of NBS U010A and IRMM 9073: NBS U010A data series 683278 - 683289 is depicted in green lines and IRMM 9073 data series 555615 - 555626 is depicted in grey lines. For each CRM, twelve particles were measured. Each  $^{238}U$  signal was composed of 42 cycles with 8 s integration time accounting for a total measurement time of 336 s. Generally the shape of the intensity is in a slight upward slope. The intensity of  $^{238}U$  of NBS U010A " $I_{NBS}$ " ranges between  $2.30 \cdot 10^4 < I_{NBS} < 1.03 \cdot 10^5$  with the exception of one outlier which was recorded 12 March, (Sample ID: 683287). This indicates the polydisperse nature of this CRM. The progression of each  $^{238}U$  intensity profile is consistent, see Figure 77 green lines for NBS U010A but the deviation of each profile is deviating significantly ( $> 2 \sigma$ ) from the mean  $^{238}U$  intensity value. For NBS U010A, a mean disintegrated  $^{238}U$  signal intensity of  $4.86 \cdot 10^4 \pm 5.62 \cdot 10^3$  was measured with a RSD 11.57 %. IRMM-9073 shows a different behavior.

**Table 33: Disintegrated and averaged  $^{238}U$  intensities for NBS-U010A and IRMM-9073.**

<b><math>^{238}U</math> Intensity for NBS-U010 (n=12)</b>
Average $^{238}U$ ( $4.8585 \cdot 10^4 \pm 5.6222 \cdot 10^3$ ), k = 2, RSD 11.57 %
<b><math>^{238}U</math> Intensity for IRMM-9073 (n=12)</b>
Average $^{238}U$ ( $7.3045 \cdot 10^4 \pm 8.1695 \cdot 10^3$ ), k = 2, RSD 11.18 %

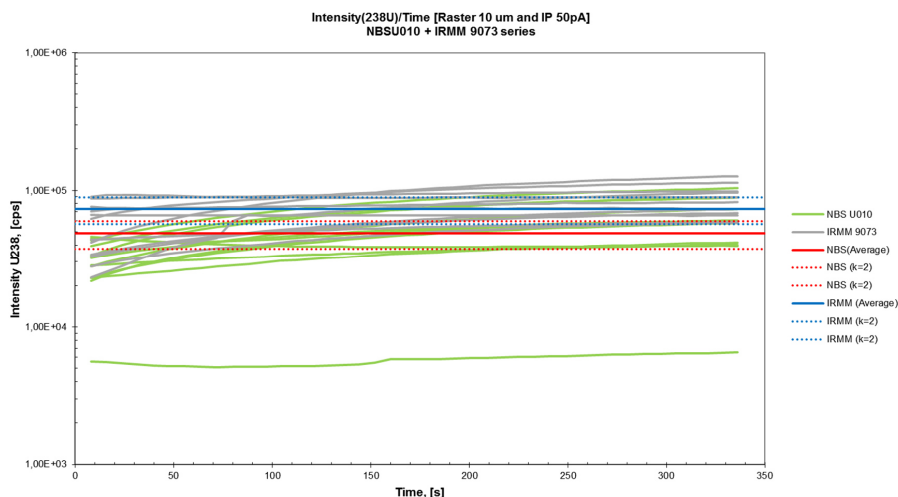


**Figure 77: Combined  $^{238}U$  intensities of NBS U010 series (green) and IRMM 9073 series (grey).**

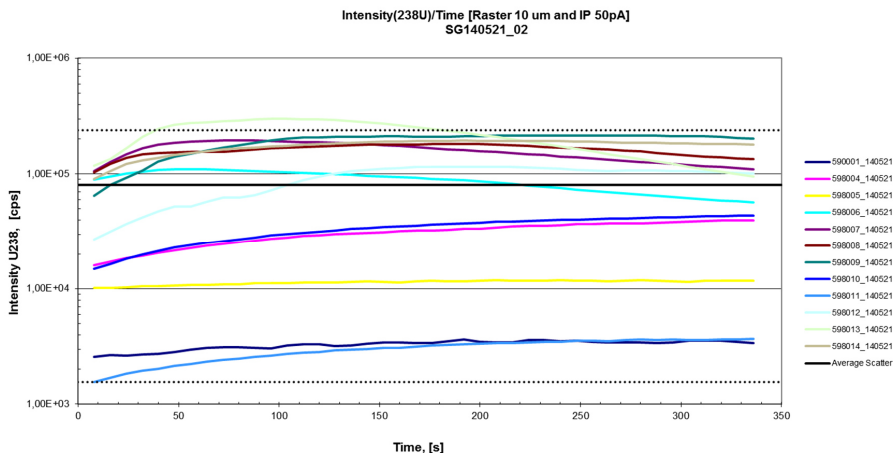


**Figure 78:  $^{238}\text{U}$  intensity plot of SG140521\_02.**

The mean disintegrated  $^{238}\text{U}$ -signal of IRMM-9073 is  $7.3045 \cdot 10^4 \pm 8.1695 \cdot 10^3$  with a RSD of 11.57 % and about 1.5 x higher than the mean disintegrated signal of NBS U010A, see Figure 77. The uncertainty of the disintegrated signal is comparable to NBS U010A. The scatter of IRMM-9073 is comparable to NBS-U010, see Table 33. For IRMM-9073, a mean scatter intensity of  $7.30 \cdot 10^4 \pm 8.17 \cdot 10^3$  with a RSD 11.18 % was measured and calculated. For SG140521\_02 12 different particles were analyzed. As expected the scatter for the polydisperse batch is significantly higher: for SG140521\_02 a mean  $^{238}\text{U}$  signal intensity of  $8.04 \cdot 10^4 \pm 7.89 \cdot 10^4$  was measured with a RSD 98.06 %, see Table 34 and Figure 78. This value accounts for the “poly-disperse” properties as well as for poorer counting statistics. The measured intensities vary almost by two orders of magnitude. But SG140521\_02 performed better than anticipated in direct comparison to IRMM-9073 and NBS-U030. The variations in  $^{238}\text{U}$  intensity make SG140521\_02 not applicable for use as a QC material and the mean values do not reflect the overall performance.

Figure 79 depicts the  $^{238}\text{U}$  scatter of SG141027. In total 28 particles were analyzed. SG141027\_12A has a mean disintegrated  $^{238}\text{U}$  intensity of  $5.5804 \cdot 10^4 \pm 2.1481 \cdot 10^4$  with a RSD of 38.49 %. The scatter profile shows a much homogenous, consistent and predictable profile and scatter. The intensity signal distribution is well within those of IRMM-9073 and NBS-U010. Interestingly, the uncertainties measured for SG141027\_12A look very promising in comparison to existing CRMs. SG141027\_12A performs better than the existing CRMs. This can be proved by comparing the scatter of the mean intensity: SG141027\_12A scatter was 2.6 % better than for NBS-U010 and 3.8 % better than for IRMM-9073.

In the Appendix in Chapter 7.6.2, all data collected was summarized into one Figure 124 and depicted more clearly. The intensities of SG140521\_02 are marked in red, for SG141027\_12A they are marked blue, for NBS-U010 in solid grey lines and for IRMM-9073 intensities are marked in grey dotted lines.

**Table 34: Mean disintegrated  $^{238}\text{U}$  intensities of polydisperse SG140521\_02 and monodisperse SG141027\_12A.**

<b><math>^{238}\text{U}</math> Intensity for SG140521_02 (n=12)</b>
Average 238U ( $8.0412 \cdot 10^4 \pm 7.8856 \cdot 10^4$ ), k = 2, RSD 98.06 %
<b><math>^{238}\text{U}</math> Intensity for SG141027_12A (n=28)</b>
Average 238U ( $5.5804 \cdot 10^4 \pm 2.1481 \cdot 10^4$ ), k = 2, RSD 38.49 %

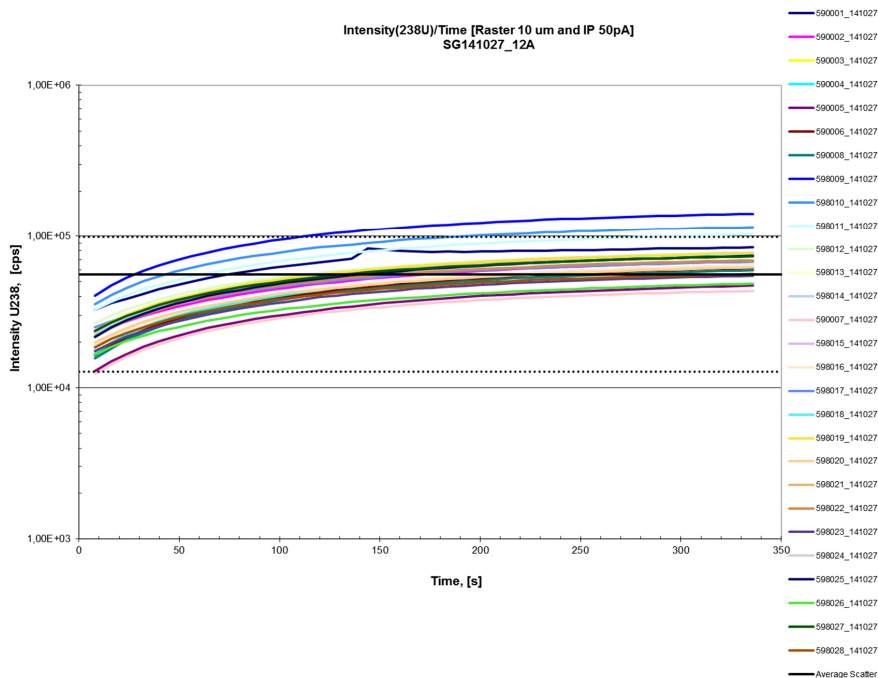


Figure 79:  $^{238}\text{U}$  intensity plot of SG141027\_12A.

#### 5.4.2.1 Conclusions

SG141027\_12A was evaluated directly against existing CRMs, (1) IRMM-9073 and (2) NBS-U010, which were used on routine bases for instrument calibrations and method validation. Due to the polydisperse nature of these CRMs, a wider spread in the measured mean disintegrated  $^{238}\text{U}$  could be observed in comparison to SG141027\_12A. Polydisperse particles from SG140521\_02 show a completely different behavior and indicate inconsistent and inhomogeneous uranium distribution, which is in accordance to the SEM investigations performed in Chapter 5.2.3.1. SG141027\_12A proved to be a consistent and reliable material a RSD of 38.48 % is an indication of this result.

#### 5.4.3 Assessment of Hydride Correction

The assessment of the hydride correction is another step forward in evaluating the capabilities of the monodisperse uranium particles towards the application as QC material. It gives also a qualitative feedback about the particle morphology. A consistent hydride formation with acceptable uncertainties is favored. The hydride correction plays an important role in the efficiency of collecting various ion-species and reducing its background: when sputtering a sample with the primary beam, a large variety of secondary ions is generated. These secondary ions range from mono-atomic to poly-atomic species and can manifest a variety of combinations between the atomic constituents. The atomic composition is independent of the valences, but it carries a specimen-inherent signature: from volatile gas molecules to primary ion beam species. These combinations present a potential risk of interference. Reducing the interference is always at the expense of transmission. Generally, there are two different ways to resolve interferences either (a) by mass resolution power or (b) by energy filtering. According to Sangely et al. (2014) [112], the interference can be considered resolved if the fraction of the interfering species is less than 1 % - i.e.  $m/\Delta m$  is similar to the mass resolution power which is defined at half maximum  $m/\Delta m_{50\%}$ . For hydride formation, the mass resolution power and energy filtering can be inefficient. In the high mass range, the mass resolution for the hydride formation is out of range even for large radius sector field instruments.  $m/Q(236)$  can be significantly biased due to the existence of  $^{235}\text{UH}^+$  instead of  $^{236}\text{U}$ .

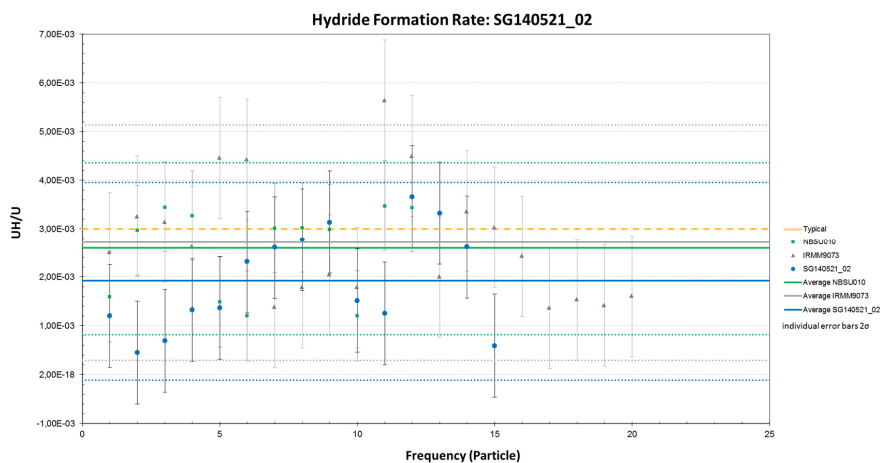


**Figure 80: Hydride formation rate for SG140521\_02.**

If the interference cannot be resolved, its share is subtracted from the peak of interest by measuring a QC-material with very similar properties; e.g. the fraction to the contribution for  $m/Q = 236$  from  $^{235}\text{UH}$  is usually evaluated by measuring the  $^{238}\text{UH}$  share. For uranium isotopic analysis, the fraction of the major isotope  $^{238}\text{U}$  to the measured minor isotope  $^{236}\text{U}$  is typically in the range of ppb-levels. Typically, for uranium isotopic analysis a  $\text{UH}/\text{U}$  value of less than 0.003 is considered acceptable, this value is empirically proven. All spectra were recorded with a  $10\ \mu\text{m}$  raster and an  $\text{IP} = 50\ \text{pA}$ . Figure 80 shows the hydride formation rate  $\text{UH}/\text{U}$  of each particle of interest from SG140521\_02 in direct comparison to IRMM-9073 and NBS-U010. SG140521\_02 shows acceptable scatter, especially for a polydisperse material. Both standards are also polydisperse materials, but are measured on bulk quantities and therefore have better counting statistics. But NBS U010 and IRMM 9073 show similar performance: the hydride formation rate for SG140521\_02 is  $1.92 \cdot 10^{-3} \pm 1.02 \cdot 10^{-3}$  with a RSD of 52.89 %, NBS, NBS-U010 has a mean formation rate of  $2.59 \cdot 10^{-3} \pm 8.85 \cdot 10^{-3}$  with a RSD of 34.18 %, and IRMM-9073 has a mean formation rate of  $2.72 \cdot 10^{-3} \pm 1.21 \cdot 10^{-3}$  with a RSD of 44.63 %.

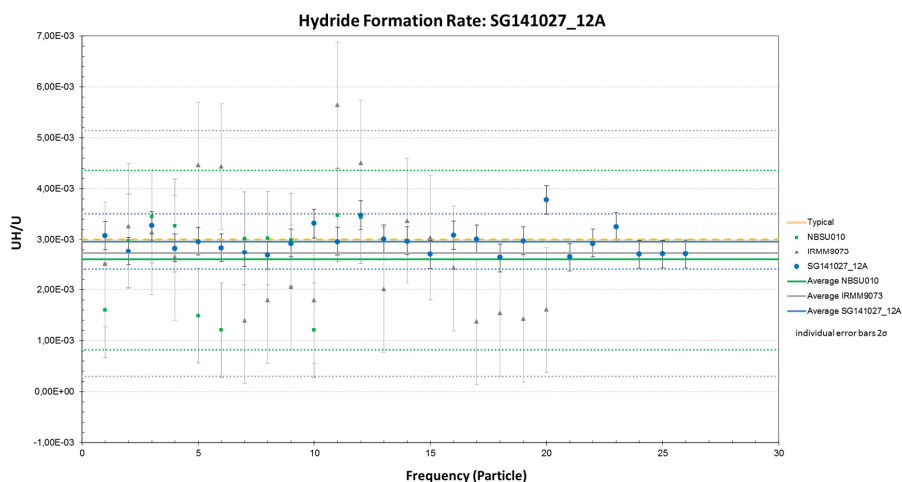


**Figure 81: Hydride formation rate for SG141027\_12A.**

**Table 35: Hydride formation rate UH/H on SG140521\_02 in comparison to NBS-U010 and IRMM-9073.**

Hydride Formation NB-U010, IRMM-9073, SG140521_02	
UH/U – NBS-U010	(2.5906E-3 ± 8.85464E-4), k = 2, RSD 34.18 %
UH/U – IRMM-9073	(2.7154E-3 ± 1.2119E-3), k = 2, RSD 44.63 %
UH/U - SG140521_02	(1.9219E-3 ± 1.0165E-3), k = 2, RSD 52.89 %

Due to the “quasi-monodisperse” properties of SG141027\_12A, the scatter of the hydride formation rate is significantly lower than for SG140521\_02. A mean formation rate of  $2.96 \cdot 10^{-3}$  with a corresponding level of uncertainty of  $2.75 \cdot 10^{-4}$  with a RSD of 9.32 % marks an outstanding performance. The performance is better than the ones measured for NBS U010 and IRMM 9073. The measured data points of SG141027\_12A indicate an erratic scatter around the limit of 0.003. Some of the data points exceeding 0.003. Still these particles performed very well and can be used as a QC-material to evaluate the hydrate formation, see Figure 81.

**Table 36: Hydride formation rate UH/H on SG141027\_12A in comparison to NBS-U010 and IRMM-9073.**

Hydride Formation SG141027_12A	
UH/U - NBSU010	(2.5906E-3 ± 8.85464E-4), k = 2, RSD 34.18 %
UH/U - IRMM9073	(2.7154E-3 ± 1.2119E-3), k = 2, RSD 44.63 %
UH/U - SG141027_12A	(2.9554E-3 ± 2.7535E-4), k = 2, RSD 9.32 %

### 5.4.3.1 Effects on Hydride Formation

The acquisition parameters play an important role in the evolution and formation of the hydride formation rate. This effect will be discussed briefly in this sub-chapter. A bigger raster of  $20 \mu\text{m}$  and higher load current  $IP = 20 \text{ pA}$  leads to an increase of the UH/U signal. To highlight this effect the polydisperse batch of SG140521\_02 was selected for this investigation. Figure 82 depicts the hydride formation rate at standard conditions (blue) and at altered conditions with a larger raster (red). The smaller uncertainty is due to better counting statistic – 14 particles in total. The mean intensity of the formation rate is about  $1.92 \cdot 10^{-3} \pm 1.05 \cdot 10^{-3}$  with an RSD of 54.75 % which is significantly higher than the mean intensity for UH/H, by about a factor of  $> 2.6$ , see Table 37.

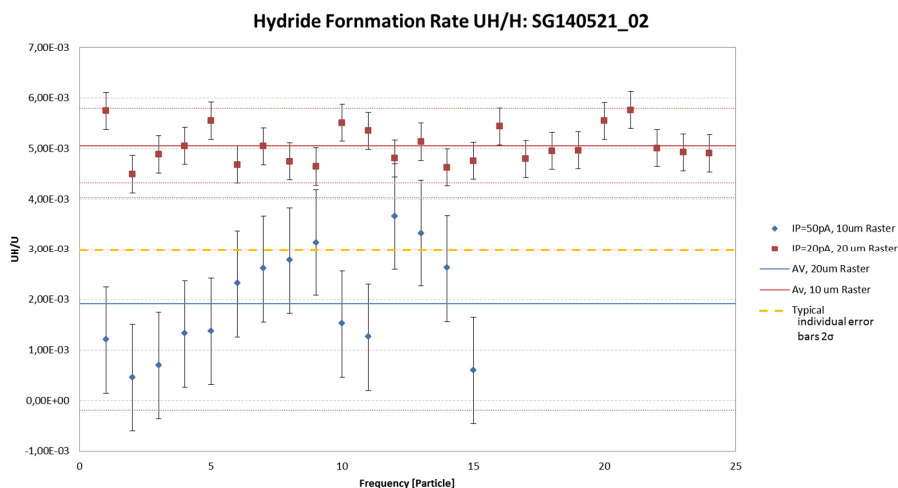


**Figure 82: Hydride Formation Rate UH/H of SG140521\_02 at IP = 50pA and 50 μm Raster in comparison to IP = 20pA and 20 μm Raster.**

**Table 37: Averaged values for the UH/H formation rate of SG140521\_02 at different acquisition conditions.**

<b>Hydride Correction SG140521_02</b>
Average Hydride Correction [IP = 50 pA, 10 $\mu\text{m}$ ] ( $1.9219\text{E-}3 \pm 1.0522\text{E-}3$ ), k = 2, RSD 54.75 %, n = 14
Average Hydride Correction [IP = 20 pA, 20 $\mu\text{m}$ ] ( $5.0576\text{E-}3 \pm 3.6778\text{E-}3$ ), k = 2, RSD 7.27 %, n = 27

#### 5.4.3.2. Conclusions

The formation of hydride species which can interfere with the measurement are an important aspect of all SIMS measurements and it serves as a measure for the collection efficiency of certain ion species. For this specific LG-SIMS instrument, an empirical threshold of UH/U = 0.003 was defined. The hydride formation rates of IRMM-9073, NBS-U010, SG140521\_02 and SG141027\_12A were compared at standard operating procedures (10  $\mu\text{m}$  raster and an IP = 50p). The hydride formation rates for the polydisperse CRMs is considerably different to monodisperse SG141027\_12A, see Table 36. The overall UH/H is bigger for SG141027\_12A but it has a significantly smaller uncertainty and an associated RSD of 9.32 % which indicates consistent performance and homogenous particle attributes during ion bombardment. But SG141027\_12A showed an overall higher mean UH/H intensity of about  $\text{UH/U}(\text{SG141027\_12A}) = 2.95 \cdot 10^{-3} \pm 2.75 \cdot 10^{-4}$  with a RSD of 34.18 %. But the UH/H-formation rate is still within acceptable limits.

Additionally, it could be demonstrated that variations in the acquisition parameters such as IP and raster size significantly determined the hydride formation rate. At lower IP = 20 pA and broader raster sizes of 20  $\mu\text{m}$ , an increase of the hydride formation rate of about 38.0 % could be observed to about:  $\text{UH/U}(\text{IP} = 20 \text{ pA}, 20 \mu\text{m}) = 5.06 \cdot 10^{-3} \pm 3.68 \cdot 10^{-3}$  with an RSD of 54.75 %.

#### 5.4.4 Total Evaporation Experiments

This chapter investigates a LG-SIMS specific behavior during MP-mode while a particle is partially or totally consumed. The aim was the direct comparison of the  $^{238}\text{U}$  intensity profiles of monodisperse particles against a small number of “monodisperse particles” produced with the same technique using spray pyrolysis of an aerosol at the Joint Research Center Institute of Transuranium Elements (JRC-ITU) and against polydisperse particles originating from IRMM-9073 and to demonstrate the advantages of monodisperse particles over existing CRMs and older “monodisperse” uranium microparticles.

Particle originating from JRC-ITU were produced in 2003 by a working group lead by Nicole Erdmann. She was the first person at ITU to use a spray pyrolysis system with a VOAG to produce uranium-oxide particles, see Erdmann et al. (2000) [6] [40], Stetzer (2001) [15], Ranebo et al. (2008) [43], (2009) [18] and (2010) [44] and Kraiem et al. (2012) [45]. The basic idea of the particle production setup in Jülich is based on JRC-ITU's approach. ITU particles have been stored under ambient conditions in double-bagged plastic bags, since 2003 at SGAS-ESL. The particles were collected on track etched polycarbonate filters: Nuclepore Filters. For further analysis, particles were transferred onto a glassy carbon substrate via inertial impaction. A selected number of six particles originating from SG141027\_12A was used for this investigation and compared against six particles from ITU (Series 20079-03-01) and 11 particles from IRMM-9073. Each particle was bombarded for 10.000 cycles (acquisition time for each cycle was 1.04 s) with an IP = 50 pA and a 10  $\mu\text{m}$  raster. The primary ion beam was “defocused” meaning it had a beam size  $\gg 1.0 \mu\text{m}$ . The mean particle size for ITU's particles is about 0.6  $\mu\text{m}$  - no real assessment on the size distribution was performed. For optimal measurement results the mean inter-particle distance should be around 50  $\mu\text{m}$  to minimize interferences.

This chapter is dedicated to the assessment of the performance of particle produced in Jülich in direct comparison to particles produced at ITU and to commonly used QC-/calibration material and helps to evaluate which material shows the most promising characteristics.

Figure 83 shows all  $^{238}\text{U}$  data sets in one graph: a common trend for all particles can be observed. There is a steep increase of intensity due to the consumption of the particle. Depending on the particle size and density, the intensity drops back gradually to a minimum. Fluctuation can be caused by particles

which are close by or due to particle movement caused by the ion beam bombardment, which rarely happens. Generally, particles reach the maximum after 1000 - 2000 s. The graph also shows that IRMM-9073 has one big outlier (Particle 5) the increase can be explained by the inadequate spatial distribution of particles; i.e. particles in the proximity were measured concurrently. Table 38 highlights the fact that the mean  $^{238}\text{U}$  intensity “ $I_{238\text{U}}$ ” depends on the specific uranium inventory of each particle respectively the  $m(\text{U})/\text{particle}$ . ITU particles which are the smallest in this assessment show a mean intensity of  $1.69 \cdot 10^7 \pm 6.29 \cdot 10^8$  which corresponds to a relative standard deviation of about 32.5 %.

ITU particles showed a relative consistent profile behavior but the counting statistics are much poorer than for the other samples. IRMM-9073 shows a more inconsistent profile behavior due to the polydisperse nature of the samples. One outlier can be explained due to the presence of another particle – see Particle 5 depicted in Figure 83. IRMM-9073 had the highest mean  $^{238}\text{U}$  intensity with  $1.54 \cdot 10^8 \pm 2.25 \cdot 10^8$ . The polydisperse nature is reflected in the significantly higher relative standard deviation of about >115 %. The most promising performance was evaluated from SG141027\_12A with a mean  $^{238}\text{U}$  intensity of  $2.42 \cdot 10^8 \pm 1.8 \cdot 10^7$ . Particle 7 showed some anomalies at the back tailing end at about 4500 - 5500 s which can be explained by particle movements or the collapse of the particle thus exposing the debris to the ion beam.

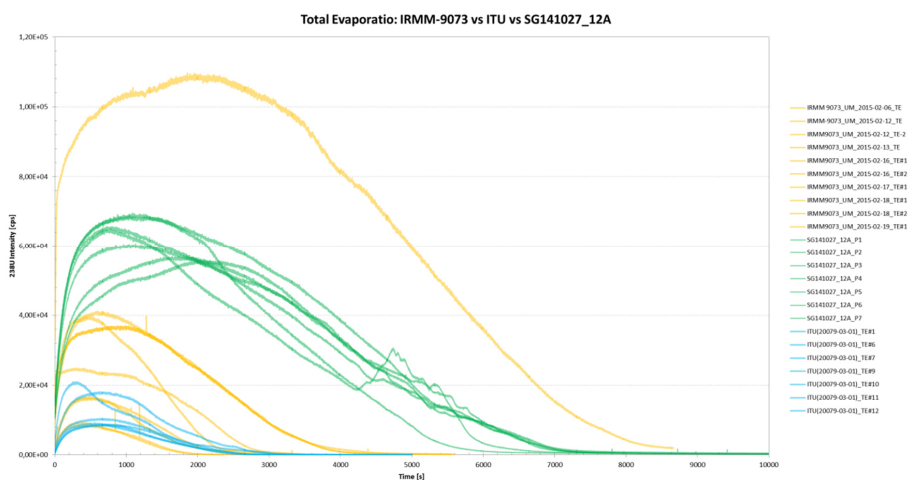


Figure 83: TE of IRMM-9073, ITU monodisperse (0.6  $\mu\text{m}$ ) and SG141027\_12A.

The intensity profiles are consistent, but small differences are observable. As SEM investigations revealed, the outer surface seems to form a denser thin crust which is erratically shaped with many curves and dents. This is a reasonable explanation for the differences in the profile shape and why certain particles reach the maximum intensity with a much lower slope. The monodisperse nature of SG141027\_12A is reflected in the lowest mean relative standard deviation of all measured samples with 6.14 %. The main message of this chapter is that it can be concluded that the homogeneity of the total evaporation experiments on SG141027\_12A indicate a consistent uranium mass distribution within this batch. Note: All individual TE intensity profiles of SG141027\_12A, ITU monodisperse and IRMM-9073 and their corresponding data set are displayed in the Appendix in Chapter 7.6.5; Figure 127 - Figure 129.

Table 38: Mean Intensities of SG141027\_12A, ITU monodisperse (0.6  $\mu\text{m}$ ) and IRMM-9073.

	SG141027_12A	ITU	IRMM-9073
$I_{238\text{U}}$ , [cts]	$2.425 \cdot 10^8$	$1.685 \cdot 10^7$	$1.540 \cdot 10^8$
$\Delta(I_{238\text{U}})$ , [cts]	$1.811 \cdot 10^7$	$6.291 \cdot 10^6$	$2.246 \cdot 10^8$
Mean Rel. Bias, [%]	6.14	32.50	115.35
$\Delta$ (Mean Rel. Bias), [%]	4.25	18.35	89.25

#### 5.4.4.1 Useful Yield and Density Assumption

The useful yield “X” is a very important parameter to assess the performance of the LG-SIMS. By assessing the useful yield, one can get an idea of the uranium mass per particle. We would expect monodisperse particles to be consistent in terms of elemental content. Also the determination of the useful yield is of particular importance for small particles. The useful yield is defined as the ratio of the integrated measured signal to the amount or number of sputtered / evaporated atoms originating from the sample, see Ranebo (2008) [43].

$$X = \frac{\int I(238U)}{N_{Droplet}} \quad (81)$$

The useful yield can be obtained by dividing the integrated  $^{238}\text{U}$ -signal “ $\int I(238U)$ ” with the amount of uranium atoms per particle. In order to assess a meaningful useful yield value multiple parameters have to be steered, e.g. the transmission of the system, the primary particle flux, detector calibration, etc.

Useful yield measurements were performed on monodisperse particles originating from ITU, SG141027\_12A. The  $^{238}\text{U}$  signal was measured in MP-mode and the integrated signal for the total evaporation or consumption was measured. Reuge et al. (2008) [66] [67] state that the measured density of particles which are produced by spray pyrolysis differs significantly from anticipated values. The measured values were compared against data acquired by Ranebo et al. (2009) [18] and therefore the acquisition parameters are set in the same way: for  $\text{O}_2^+$  a primary accelerating voltage of 13 kV and a secondary accelerating voltage of 8 kV was used. The total incident energy accounts to 5 keV. All measurements were performed with IP = 50 pA, 10  $\mu\text{m}$  raster and a spot size of 1  $\mu\text{m}$ . Monodisperse uranium particles from ITU (Series 20079-03-01) were compared against particles from SG141027\_12A. Ranebo et al. (2009) [18] measured the mean  $m(\text{U})$  per particle by isotope dilution mass spectrometry (IDMS): three planchets A, B and C were analyzed with an  $m(\text{U})$  per particle for  $m(\text{U}) = 2.41$  pg,  $m(\text{U})_B = 2.75$  pg and  $m(\text{U}) = 2.59$  pg. The  $m(\text{U})$  for SG141027\_12A was evaluated not by mass spectrometry but by careful assumptions and calculations. Since the particle is considered to be totally consumed, it can be deduced that all uranium atoms are consumed during the total evaporation experiments. With equation 10 in Chapter 3.1.2, the overall number of atoms per particle “N” was calculated:  $N = 2.067 \cdot 10^9$ . This value was derived from the VOAG-settings used for particle production and it was concluded from the assumption that the overall density is lower than the theoretical density value for uranium oxide, see Chapters 5.2.3.2.3 and from the assumption that the molar concentration “M” is constant. For  $c(\text{U})$  the ICP-MS verified concentration of with  $c(\text{U}) = 146.5 \pm 11$   $\mu\text{g/g}$  was used, see Table 5 and Table 6 in Chapter 4.1.2.6. The mass per particle can be derived from the “ $\rho$ ” density of the precursor solution taken from equation 10 and the volume of a 1  $\mu\text{m}$  microparticle. A uranium mass of  $2.89 \pm 0.9$  pg was derived.

$$m(\text{U}) = \rho * V_{1\mu\text{m}} = 2.89\text{pg} \quad (82)$$

The  $m(\text{U})$ /particle and the theoretical number of uranium atoms per particle can be calculated using equation 82. We assumed that we had  $\text{U}_3\text{O}_8$  with  $M(\text{U}_3\text{O}_8) = 842.08$  g/mol. Kraiem et al. (2012) [45] calculated a mean mass density for  $\text{U}_3\text{O}_8$  containing particles of  $\rho(\text{U}_3\text{O}_8) = 5.52 \pm 1.04$  g/cm<sup>3</sup> and for particles which are made from  $\text{UO}_3$ :  $\rho(\text{UO}_3) = 5.63 \pm 1.06$  g/cm<sup>3</sup>. The mass density was calculated from the measured uranium mass concentration which was determined by ID-TMS. Ranebo et al. (2010) [44] derived a mean mass density of  $\rho = 2.6 \pm 0.2$  g/cm<sup>3</sup>. Their derivation is also based on the uranium mass concentration based on IDMS-TIMS measurements rather than on the particle size. Ranebo et al. (2010) [44] state that the calcination process is not fully determined and that the droplet-to-particle conversion is dependent on many variables which affect the final particle morphology; thus leading to inconsistent mass density within a single microparticle and throughout an entire batch of particles. This is in accordance with Ranebo et al (2010) [44] and Kraiem et al. (2012) [45] as well as internal SEM and FIB investigations. The density varies significantly with the uranium stoichiometry and the conversion of droplet-to-particles has a considerable effect on the inner structure.

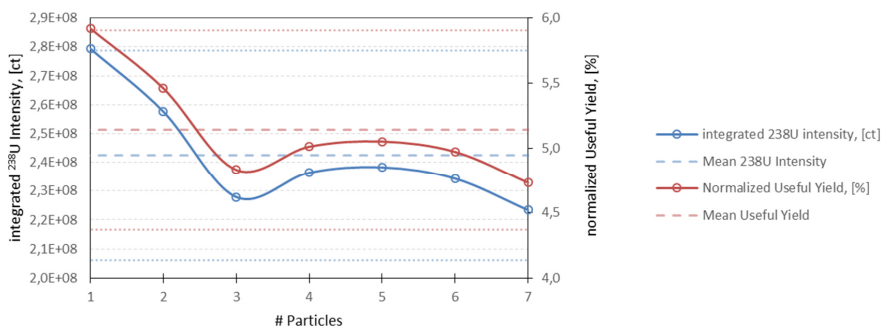


**Figure 84: Linear combination of the integrated  $^{238}\text{U}$  intensity [ct] on axis one and its correlated, normalized Useful Yield [%] with mean values and uncertainties with  $k=2$ .**

IRMM-9073 and NBS-U010 were used for mass calibration and mass bias determination. Particles SG141027\_12A were measured directly from the glassy carbon substrate not further preparations were necessary. Particles from ITU were received on Nuclepore filters. Particles were transferred to a glassy carbon substrate by inertial impaction: the surface was covered with an adhesive – PIB-nonane. After impaction the planchet was heated carefully to remove the organic matrix. Ranebo et al. (2008) [43] measured a useful yield for of  $X = 1.18 \pm 0.15 \%$  for  $\text{O}_2^-$  and for an  $\text{O}_2^+$  ion source  $X = 0.96 \pm 0.07 \%$ . Another study by Hedberg et al. in 2005 [163] determined a useful yield of 0.27 % for ITU particles. Hedberg et al (2005) [163] used a different raster size and assumed that all particles were made from  $\text{UO}_2$  which was homogeneously distributed. It has to be noted that the comparison values derived by Hedberg et al (2005) [163] and Ranebo et al. (2008) [43] are not very specific hence not really suitable as an example.

The useful yield depends significantly on the correct assumption of the particle density. The useful yield was calculated as the ratio of the integrated count rate of  $^{238}\text{U}$  to total number of particles. Table 39 depicts the integrated  $^{238}\text{U}$  intensities measured for all seven particles from SG141027\_12A and the corresponding useful yield “X”. A mean useful yield of  $5.14 \pm 0.38 \%$  was derived. This value is significantly higher than the values derived from Hedberg et al. (2005) [163] with 0.27 % and from Ranebo et al. (2009) [18] 0.96 %. The variances can largely be accounted for by the inaccurate density assumption. To overcome this issue, a thorough investigation should be carried out using SEM, mass determination (either by IDMS, ID-TIMS plus useful yield investigations using SIMS analysis).

Figure 84 shows clearly the direct correlation between the integrated  $^{238}\text{U}$  intensities [ct] of each particle and its associated normalized useful yield [%]. The mean values for the  $^{238}\text{U}$  intensity and the useful yield are shown in blue and red dashed lines; all uncertainties are depicted with  $k=2$ . The scale for the primary and secondary axis in Figure 84 chosen to depict the small variances. The useful yield is directly coupled to the integrated  $^{238}\text{U}$  intensity. On a larger scale, an almost linear dependency can be observed and a relative standard deviation of 3.22 %, which indicates that our assumptions are not significantly different from the measured and derived useful yield value. All values depicted in Figure 84 were taken from Table 39.

The density can be derived from the previously calculated uranium mass per particle and the overall mean particle size of SG141027\_12A which was  $1.3 \pm 0.4 \mu\text{m}$ . From this a mean density of  $2.51 \pm 1.0 \text{ g/cm}^3$  can be derived the associated uncertainty is significantly about 41.06 %. This result is highly biased and exemplifies the necessity to perform a thorough mass investigation using ICP-MS or ID-MS to derive a solid value for the uranium mass per particle. This value is not a good representation, since it shows only an average value. The density gradient throughout a single particle varies significantly from the outer structure to the porous inner structure. Therefore, it is advisable to correlate these findings with the FIB data acquired in Chapter 5.2.3.2.3 on solid particles originating from

SG141027\_12A. The measured  $m/Q(^{238}\text{U})$  signal gives a strong indication about the uranium distribution inside a microparticle. Figure 53 shows a strong peak at about 180 – 200 nm which indicates a denser structure with an overall thickness of  $< 0.2 \mu\text{m}$ . For the inner, porous structure, a decrease of about 45.8 % from the peak intensity was measured. Hence it can be concluded that the outer structure which only constitutes 39.42 % of the entire volume contributes a significant portion of the integrated  $^{238}\text{U}$  intensity while the porous inner structure, which accounts for 60.58 % of the entire particle volume contributes proportionally less to the integrated  $^{238}\text{U}$  intensity.

**Table 39: Useful Yield determination through TE of seven particles originating from SG141027\_12A.**

	Particle 1	Particle 2	Particle 3	Particle 4	Particle 5
$^{238}\text{U}$ counts, [cts]	$2.794 \cdot 10^8$	$2.576 \cdot 10^8$	$2.279 \cdot 10^8$	$2.364 \cdot 10^8$	$2.383 \cdot 10^8$
Useful Yield)	5.92 %	5.46 %	4.83 %	5.01 %	5.05 %
$\sigma$ (Useful Yield)	0.87 %	0.77 %	0.68 %	0.71 %	0.71 %
	Particle 6	Particle 7	Mean	STD(Mean)	RSD
$^{238}\text{U}$ counts, [cts]	$2.343 \cdot 10^8$	$2.234 \cdot 10^8$	$2.425 \cdot 10^8$	$7.814 \cdot 10^7$	3.22 %
Useful Yield)	4.97 %	4.73 %	5.14 %	0.38 %	
$\sigma$ (Useful Yield)	0.70 %	0.67 %			

#### 5.4.4.2 Primary Ion Beam Effects on the $^{238}\text{U}$ Intensity Profiles

The aim of this chapter is to document the changes in the  $^{238}\text{U}$  intensity on monodisperse microparticle due to changes to the ion beam. This demonstrates the importance of consistent measurement conditions – here the ion beam was focused which means that the primary beam diameter was about  $1 \mu\text{m}$ . A decrease in the smaller primary ion beam diameter was expected. But with the focused ion beam, a mean integrated intensity " $I(^{238}\text{U})$ " of  $I(^{238}\text{U}) = 3.038 \cdot 10^8 \pm 9.278 \cdot 10^7$ , with a RSD of 30.54 % was measured which is about 1.25 x bigger than the mean integrated intensity of the defocused total evaporation. The relative bias to the defocused species is 25.31%. All data is depicted in the following Figure 85 and Table 40.

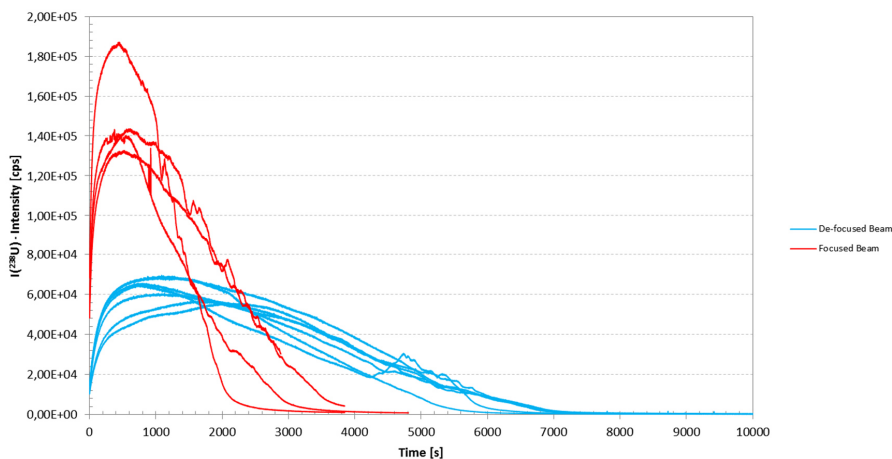


**Figure 85: Comparison of focused and de-focused ion beam on the  $^{238}\text{U}$  intensity profile.**

**Table 40: Comparison of integrated  $^{238}\text{U}$ -intensities with focused and defocused primary ion beam on SG141027\_12A.**

	Particle 5	Particle 6	Focused		
			Particle 7	Particle 8	Particle 9
$I(^{238}\text{U}), [\text{ct}]$	$2.219 \cdot 10^8$	$2.493 \cdot 10^8$	$2.788 \cdot 10^8$	$4.838 \cdot 10^8$	$2.853 \cdot 10^8$
	Mean	STD	RSD	Rel. Bias	
$I(^{238}\text{U}), [\text{ct}]$	$3.038 \cdot 10^8$	$9.278 \cdot 10^7$	30.54 %	25.31 %	
	Particle 1	Particle 2	Defocused		
	Particle 6	Particle 7	Mean	STD	RSD
$I(^{238}\text{U}), [\text{ct}]$	$2.794 \cdot 10^8$	$2.576 \cdot 10^8$	$2.279 \cdot 10^8$	$2.364 \cdot 10^8$	$2.383 \cdot 10^8$
$I(^{238}\text{U}), [\text{ct}]$	$2.343 \cdot 10^8$	$2.234 \cdot 10^8$	$2.425 \cdot 10^8$	$1.811 \cdot 10^8$	7.47 %

#### 5.4.4.3 Redisposition

The aim of this investigation was the measurement of the residual microparticle debris after total evaporation measurements and an SEM investigation on the residues. Once a particle is just partly or totally consumed, a deposition pattern around the artefact develops, such as Figure 86. A cone like shape becomes visible. The shape depends on the inclination angle of the primary ion beam to the sample. The size and shape of the redisposition depends upon the particle size, its morphology and the primary ion beam characteristics such as IP, inclination angle, etc.

After total evaporation, particles were rescanned with a  $50 \mu\text{m}$  raster, a primary ion beam current of  $1.5\text{nA}$  and a total area of  $2500 \mu\text{m}^2$  was covered. Particles originating from SG141027\_12A were compared against IT4U (20079-series) particles. Figure 86 shows the redisposition pattern of the  $^{238}\text{U}$  intensity of five particles from SG141027\_12A in comparison to one particle originating from ITU (20079). Particle 6 from SG141027\_12A (blue) is an outlier. Its untypical intensity profile can be explained by the presence of an un-sputtered particle which was measured simultaneously. Apart from Particle 6, all redisposition measurements were acquired within  $< 800$  cycles (acquisition time for each cycle was  $1.04 \text{ s}$ ).

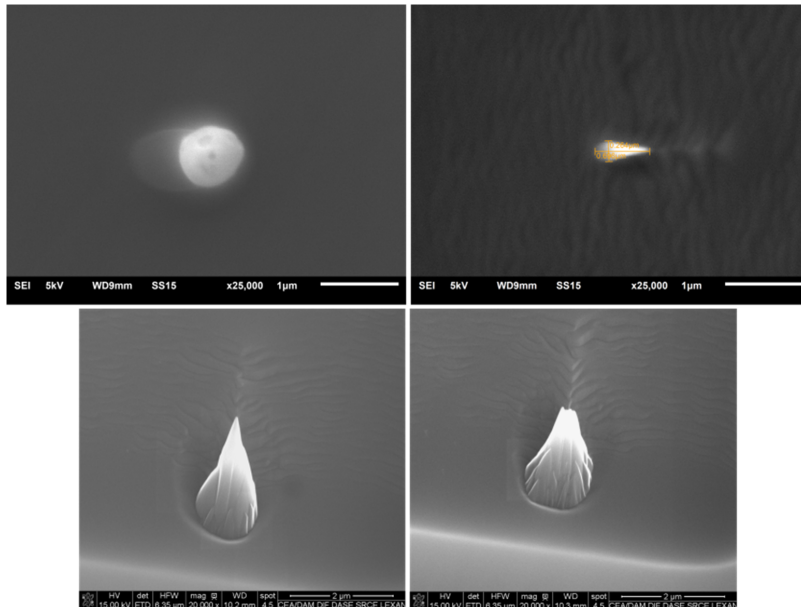


**Figure 86: Redisposition pattern of partially consumed particle (left) and total consumed particles, Image on the left were taken at CEA-DAM Ile-de-France, courtesy of O. Marie (CEA).**

It has to be noted that no sufficient data on ITU particles was available, not enough ITU particles could be identified on the substrate. After the redistribution measurements, a full SEM investigation was started. The typical redistribution shape significantly decreases within 150 - 200 cycles. The actual mass of the particle played an important role. Since the quantities are very small, they are consumed in less than 10 min. This time is dependent on the amount or the particle quantity. The larger a particle, the more debris is produced and the longer and distinct the redistribution profile becomes. ITU's particles which are about a factor of 2.28 x smaller produce a significantly smaller  $^{238}\text{U}$  intensity distribution, but measurements revealed a comparable slope and shape. The mean integrated  $^{238}\text{U}$  intensity of the five redistribution is  $2.425 \cdot 10^8 \pm 1.811 \cdot 10^7$  which is about 11.7 % higher than the intensity measured for ITU. The deviation in the redistribution intensities of the mean  $^{238}\text{U}$ -intensities between SG141027\_12A and ITU (20079) accounts for 2.55 %. This is also a strong indication, that the diameter of this particle batch from JRC-ITU are significant smaller than SG141027\_12A. Since the particles produced at FZJ are about 1.3  $\mu\text{m}$  in diameter, it can be assumed that the mean diameter of ITU's particles is  $\ll 1.0 \mu\text{m}$ , see Table 41.

**Table 41: Redistribution of SG141027\_12A and ITU (20079).**

	SG141027_12A_P2	SG141027_12A_P3	SG141027_12A_P4
Total Counts $^{238}\text{U}$	$2.576 \cdot 10^8$	$2.279 \cdot 10^8$	$2.364 \cdot 10^8$
Redispotion	$1.526 \cdot 10^7$	$1.461 \cdot 10^7$	$1.500 \cdot 10^7$
	5.92 %	6.41 %	6.35 %
	SG141027_12A_P6	SG141027_12A_P7	ITU (20079)_P1
Total Counts $^{238}\text{U}$	$2.343 \cdot 10^8$	$2.234 \cdot 10^8$	$2.825 \cdot 10^7$
Redispotion	$1.261 \cdot 10^8$	$1.714 \cdot 10^7$	$9.611 \cdot 10^5$
	53.82 %	7.67 %	3.40 %

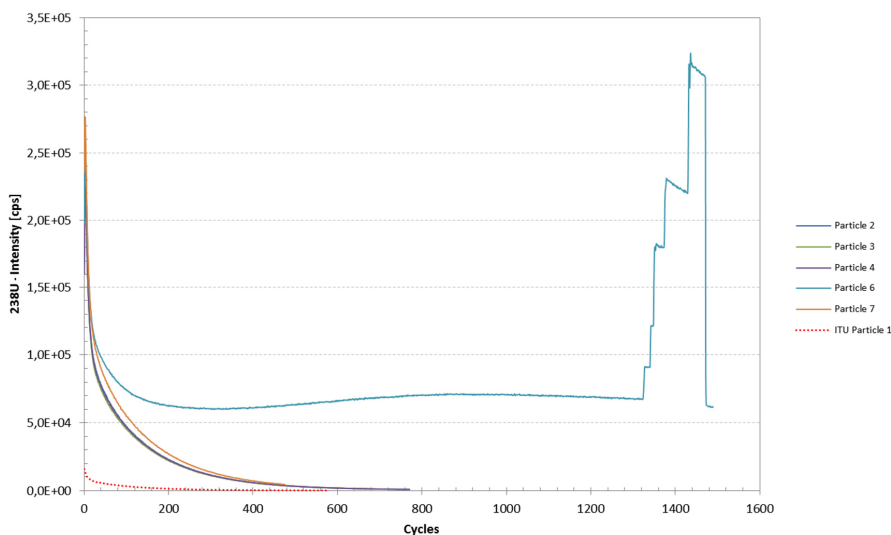


**Figure 87: Redistribution profile of SG141027\_12A in comparison to ITU (20079).**

#### 5.4.4.4 Conclusion

These results depict signatures which are specific to the instrument. SG140521\_02 and SG141027\_12A were compared against IRMM-9073 and ITU (20079) particles. These “total evaporation” experiments are a good indication for the homogeneity each microparticle and the entire batch. Again SG141027\_12A proved to be a much more reliable, predictable and consistent material than the polydisperse SG1400521\_02 and IRMM-9073. ITU particles showed a significantly lower signal due

to the size discrepancy – according to SEM investigations the mean size of these particles was about 0.6  $\mu\text{m}$ . measured  $^{238}\text{U}$  intensity was about 144 x higher than for ITU (20079). IRMM-9073 had the strongest  $^{238}\text{U}$  intensity of  $1.54 \cdot 10^8 \pm 2.25 \cdot 10^8$  and an RSD of 89.25 %. ITU particles are monodisperse, but their RSD is significantly higher. This can be accounted for by poorer counting statistics, see Table 38. SG141027\_12A had a mean  $^{238}\text{U}$  intensity of  $2.42 \cdot 10^8 \pm 1.8 \cdot 10^7$  and a RSD of 4.25 %. This result is a strong indication for a consistent uranium mass distribution per particle and per batch.

The useful yield and a density assumption were derived from the measured mean  $^{238}\text{U}$  intensity. A uranium mass per particle of  $m(\text{U})/\text{particle}$   $2.89 \pm 0.9$  pg was derived and a mean density of  $2.51 \pm 1.0$  g/cm<sup>3</sup>. This value depicts an averaged value which is not representative. FIB investigations indicate that the thin outer layer is far denser than the porous inner structure which contributes most to the particle volume. But an overall RSD of 3.2 % for the useful yield measurements indicates accordance with the expected values. This result underlines the need to perform a thorough mass investigation using ICP-MS or IDMS.

Redispersion experiments on particles which were previously “totally evaporated” showed a distinct ablation pattern under with SEM. These experiments also indicate consistent behavior and microparticle attributes for SG141027\_12A, see Figure 86 and Figure 87. As previously stated, changes to the acquisition parameters affect the outcome of the measurements: a smaller beam diameter of about 1  $\mu\text{m}$  was used and a stronger  $^{238}\text{U}$  intensity was measured than with a defocused beam:  $I(^{238}\text{U}_{1\mu\text{m}}) = 3.038 \cdot 10^8 \pm 9.278 \cdot 10^7$ , with a RSD of 30.54 %.

## 6. Conclusions and Outlook

This dissertation project had two major objectives: (1) to develop a setup for production of monodisperse uranium microparticles and (2) to characterize the particles with respect to their physico-chemical properties and assessing their usability as quality control and reference materials. Particle properties were evaluated: including geometry, morphology, composition, crystal structure, elemental- and isotopic content, properties such as homogeneity and consistency of the  $m(U)/particle$ , and size distribution to gain a sound indication whether these particles are fit for use as future QC materials. They were tested using various instruments and special focus was put on SIMS analysis using a Cameca IMS 1280 LG-SIMS. The particle performance was investigated by measuring their isotopic composition and performance in direct comparison to existing "bulk" reference materials. The following paragraphs will summarize these successful work carried out.

The development of the particle-production setup comprised an assessment of the vital components. Particle collection turned out to be a complex issue. Initially, both the particle size and yield were low and insufficient. After adjusting the air currents inside the setup, the yield improved significantly. The one-stage inertial impactor was routinely used for particle sampling. Because this device was never characterized a brief and comprehensive assessment was made, see Chapter 5.1.1. The calculated, theoretical values for the mean cut-off diameter " $d_{50}$ " were in good agreement with the measured values; however, at lower air flows the degree of uncertainty and deviation was almost 27.5 %, see Table 9 and Figure 27. Cut-off diameters, retention ability and deposition pattern were as predicted, see Figure 26.

The modified inertial impactor (MII) in Chapter 5.1.2 was used to collect particles for  $t \mu$ -Raman spectroscopic investigation. The MII is a two-stage inertial impactor with performance similar to the one-stage inertial impactor. Modification of the acceleration nozzle resulted in altering the corresponding cut-off diameters to a theoretical cut-off diameter of 2.20  $\mu\text{m}$  for Stage 1 and 1.30  $\mu\text{m}$  for Stage 2, see Table 10. The deviation of the measured cut-off diameters from the theoretical values (for Stage 1 and 2) is between 7.13 - 25.06 %, see Figure 30, Figure 31 and Table 10. Both stages showed performance in terms of yield and cut-off diameters as expected. Also, a similar deposition pattern to the one stage impactor such as in Chapter 5.1.1 was observed, see Figure 31. Two distinct accumulation areas were detected: (1) in the center and a circular accumulation towards the edge of the collection substrate. The radial distance from the center is dependent upon the air flow: the higher the air-flow the further away the second accumulation.

The cyclone sampler in Chapter 5.1.3 was initially developed to overcome the collection yield issues related to the on-stage inertial impactor. Due to the high air flow, the collection efficiency was  $> 0.1$  %. It could be demonstrated that the cyclone impactor can sample efficiently at high air flows; ranging from  $> 20$  l/min up to 130 l/min, see Figure 34.

We demonstrated the efficiency of laser micro dissection for the preparation of substrates for particle relocation. A three-point algorithm from Admon et al. (2009) [147] was used to relocate single particles with a high degree of accuracy ( $< 5 \mu\text{m}$ ) in different instruments.

A microparticle production setup was successfully implemented at Forschungszentrum Jülich GmbH. A significant amount of time and effort were spent on evolving the first particle production attempts into a working setup. The entire history is described in 4.1.2.4. A representative selection of six particle batches was chosen to be discussed in further detail. These batches were produced between May 2014 and April 2015.

The most important conclusion is that the final particle size can be precisely controlled by means of the initial uranium concentration of the precursor aerosol solution and the settings of the aerosol generator (such as frequency and liquid feed rate), see equation 12, leading to production of particles with a consistent uranium content per particle " $m(U)/particle$ ", see equation 10. The final geometry and

morphology is controlled by the precipitation mechanics during the conversion from aerosol droplets to solid particles. However, the density of these microparticles can vary significantly.

Scanning electron microscopy was used extensively to assess the particle size distribution, morphology and elemental composition of individual batches. All six particle batches were analyzed using SEM-EDX. This technique was also routinely used in automated particle assays to determine the presence of uranium containing microparticles and to assess their mean size. Table 42 lists all six particle batches, their derived mean size as well as the corresponding uranium concentration for the precursor solution (before dilution with water to 1 : 1 mixture).

**Table 42: Analyzed samples with the c(U) of the aerosol solution and the corresponding mean particle size.**

Sample-ID	Mean DIA [ $\mu\text{m}$ ]	$\Delta$ (Mean DIA) [ $\mu\text{m}$ ]	C(U) [ $\mu\text{g}$ ]	$\Delta$ c(U), [ $\mu\text{g}$ ]
SG140521_02	1.35	-	123.0	2.2
SG141027_12A	1.37	0.19	157.0	4.7
SG150312_05	0.99	0.15	107.0	1.1
SG150401_14A	1.07	0.11	104.6	1.0
SG150413_03A	1.05	0.11	59.9	1.8
SG150429_02A	1.02	0.10	120.0	4.3

SEM investigations revealed a number of interesting characteristics of the size distributions and morphology of individual batches, see Chapter 5.2.2 and 5.2.3. The first batch SG140521\_02 which was produced in May 2014 showed some significant deviations from the expected size and morphology. This particle batch was found to be polydisperse. Three distinct particle species could be identified: (1) a proportion of “solid” uranium particles with a mean size of  $1.35 \pm 0.53 \mu\text{m}$ , (2) significantly more inflated, hollow particles with a size range of  $6.5 \pm 0.5 \mu\text{m}$  and (3) particle debris and agglomerations ranging from  $\sim 4.5 - 9.2 \mu\text{m}$ . Even though SG140521\_02 did not meet our criteria in terms of size, geometry, morphology, consistency and homogeneity, it proved to be very helpful in order to understand the mechanics associated with the formation process from precursor droplets to final particles. Final particle morphology is strongly dependent upon the conversion conditions. Parameters such as dwell time, solution concentration, temperature profile play an important role in the formation process. SG140521\_02 is a good example on how the formation conditions lead to a surface controlled precipitation resulting in inflated, hollow particles. SEM investigations revealed that the particles are actually hollow and are destroyed by the impact energy. In order to assess the inner structure, selected particles were broken with a tungsten needle on the SEM stage. In Chapter 5.2.3.1 computational simulations of these hollow particles provided the missing information regarding the shell-thickness and confirming the presence of a hollow species, also giving indication about a density gradient within the particulates itself. A series of two different three-dimensional models were developed to simulate SE-images that were similar to the SE-images taken from non-typical uranium oxide particles. Further conclusions can be drawn with regard to the shell thickness, elemental composition and density. By direct comparison of the simulated SE-images with a reference SE-image, it can be concluded that the outer shell structure has very likely a thickness in the range  $20 < d < 50 \text{ nm}$  and is made of  $\text{U}_3\text{O}_8$  with a density of  $\delta_{\text{os}} = 8.4 \text{ g/cm}^3$ . The inner structure is also composed of  $\text{U}_3\text{O}_8$  and has a lower density of  $\delta_{\text{is}} = 6.6 \text{ g/cm}^3$ . According to our simulations, the simulated spheres were hollow and no filling material (such as water) was present and can be therefore neglected, see Figure 48.

The other five particle batches showed a much more coherent picture. The homogeneity of the size distribution within a batch was sufficient, but did not meet the criteria for a monodisperse particle distribution as defined by Hackley and Ferraris (2001) [154].

For solid microparticles, a thorough investigation was also performed, see Chapter 5.2.3.2. SEM investigations revealed that the particle size can be adjusted precisely by the precursor solution

concentration, see Figure 59. SEM investigations of the size and geometry revealed that these solid particles are not spherical. The outer surface shows many dents and cavities. Combined SEM-FIB/TOF-SIMS investigations revealed the inner structure of single microparticles. All measurements performed at SGAS-ESL and IEK-6 showed a coherent picture for these solid uranium microparticles of a thin outer layer and a porous inner structure. Based on TOF-SIMS measurements, the outer structure had a significantly higher density than the inner structure and overall thickness of a few nanometers (about 20 nm), see Figure 53. However, the same measurements revealed that the inner structure of these solid particles have a porous morphology with an overall inhomogeneous density distribution; Figure 53 shows the depth profiling of selected m/Q values (m/Q(16), m/Q(238) and m/Q(239)). SE-images recorded during the ablation process showed a significant number of cavities and venting holes, see Figure 54 and Figure 98 - Figure 101. These cavities vary in size and shape. It can be concluded that the porous inner structure is rather heterogeneous and no distinct density gradient could be observed. This observation is in accordance with Messing et al. (1993) [58] and Reuge et al. (1961) [66] [67] – the final morphology is controlled by a homogenous precipitation mechanism.

TOF-SIMS confirmed the presence of certain unexpected atomic species:  $^{23}\text{Na}$ ,  $^{27}\text{Al}$ ,  $^{28}\text{Si}$ ,  $^{39/41}\text{K}$ . These chemical species were probably introduced as cross-contamination during the preparation of the feed solutions by leaching of glass storage vessels.

SEM-EDX investigations were performed to measure elemental contents of the particles. Measurements of solid particles were much more precise than for the hollow, polydisperse species. This can be attributed to their higher density and resulting stronger signal. A quantitative investigation proved to be difficult because most of the “reflected” signal originated from the substrate – these findings apply both for the hollow and the solid species. For SG140521\_02 the effect is more pronounced; see Table 14 versus Table 15 and Table 16, as the interaction volume of electrons with a kinetic energy of 25 keV is larger than the actual specimen size. It is recommended that a quantitative investigation be carried out of SEM combined with wavelength dispersive X-Ray spectroscopy (SEM-WDX). SEM-EDX investigations revealed the presence of carbon, even in particles which were deposited onto Si substrates. This phenomenon indicates a detector specific artefact. This issue was addressed by carrying out  $\mu$ -Raman spectroscopy experiments on the same particles.

SEM investigations raised the question as to whether the oxidation of these particles was complete and the uranium converted completely to  $\text{U}_3\text{O}_8$ . Density variations within the microparticles are also an indication for an inhomogeneity in the uranium composition. Therefore,  $\mu$ -Raman spectroscopy measurements were carried out at two different institutions: (1) CEA DAM Ile de France and (2) at Vienna University of Technology (TUW).  $\mu$ -Raman spectroscopy investigations helped to identify the crystal structure of single microparticles produced at IEK-6. It can be concluded that all investigated particle batches (from SG140521\_12 to SG150401\_14A) show significant similarities with regard to their identified Raman bands. Different proportions of uranium compounds could be attributed to a number of single microparticles. The largest number of identifiable bands can be associated with  $\text{U}_3\text{O}_8$ .  $240\text{ cm}^{-1}$ ,  $340\text{ cm}^{-1}$ ,  $380\text{ cm}^{-1}$ ,  $420\text{ cm}^{-1}$ ,  $805\text{ cm}^{-1}$ , see Table 23 - Table 25. Meta-schoepite and U(IV)-hydroxide indicate residual water left in the crystal structure and suggest an insufficient oxidation or the uptake of water through ambient humidity; the following bands were identified:  $\sim 340\text{ cm}^{-1}$ ,  $\sim 380\text{ cm}^{-1}$ . Bands at  $\sim 860\text{ cm}^{-1}$  and indicate the presence of a studite/meta-studite species, see Bastians et al. [161]. Further indication of  $\text{UO}_3$  was found with bands at  $\sim 480\text{ cm}^{-1}$  and  $770\text{ cm}^{-1}$ . The smallest fraction could be associated with  $\text{UO}_2$ , with a single band at  $\sim 606\text{ cm}^{-1}$ .

These results underlay the assumption that a multiphase uranium oxide was created that has different areas within a particle associated with different oxidation states. The outer surface is much denser, which is the case for both the solid and the hollow species, see Figure 48 (for SG140521\_02) and Figure 53 (for SG141027\_12A). This part is more likely to be made of  $\text{U}_3\text{O}_8$  because it was exposed directly to the heat field of the furnace. The inner porous structure on the other hand is more likely to consist of uranium-hydroxide species.

Furthermore,  $\mu$ -Raman analysis could not detect any indication of the presence of carbon inside single particles. This leads us to conclude that the emergence of carbon in the EDX spectra is an indication of a detector specific artefact impacting a quantitative EDX analysis of microparticles.

The main aim of the characterization work was the isotopic composition and homogeneity as well as a consistent uranium content per particle. This was accomplished by using the LG-SIMS at SGAS. The primary designated instrument is the LG-SIMS. In Chapter 5.4 LG-SIMS experiments were used to investigate the particle performance under operational conditions. A series of tests were performed: (1) identification of the original isotopic composition, (2) direct comparison to existing CRMs (IRMM-9073 and NBS-U010), (3) an assessment of the hydride formation and (4) an assessment of the total evaporation behavior. Apart from point (1), these results depict instrument specific value, but they are a good indication of the microparticles' homogeneity and a conclusion about the uranium content and particle density.

Firstly, the original isotopic content from IRMM-183 was identified. Two different particle batches from Jülich were investigated: (1) polydisperse SG140521\_02 and (2) "quasi" monodisperse SG141027\_12A. The variability in the isotope ratios of ( $^{234}\text{U}/^{238}\text{U}$ ), ( $^{235}\text{U}/^{238}\text{U}$ ) and ( $^{236}\text{U}/^{238}\text{U}$ ) were investigated and compared to -certified values by Richter et al. (2005) [162]. Richter's data was derived from TIMS measurements on bulk material. Hence, we expect to see a higher degree of accuracy and smaller associated uncertainties. All results obtained from SG140521\_02 and SG141027\_12A are presented in direct comparison to Richter's data. As expected, polydisperse SG140521\_02 show a significantly higher deviation to Richter's data of 0.08 - 8.29 % which can be correlated to the morphology and density differences. SG141027\_12A shows a much more consistent signal for all isotopes and its associated uncertainties are significantly lower than of SG140521\_02. The overall deviation of 0.10 - 1.22 % from the reference values reflects this trend, see Table 27 - Table 29. It can be concluded that the measured isotopic composition is independent of the particle size and morphology.

The second step was the evaluation of the SG140521\_02 and SG141027\_12A against existing reference materials (IRMM-9073 and NBS-U010) during which the averaged disintegrated  $^{238}\text{U}$  intensities were compared against each other. They are a measure for the homogeneity and consistency in size distribution of the measured particles. Since IRMM-9073 and NBS-U010 are bulk materials consisting of polydisperse particles, we expect to see a higher degree of variance in the disintegrated averaged  $^{238}\text{U}$  signal. NBS-U010 showed a disintegrated averaged  $^{238}\text{U}$  intensity of  $4.86 \cdot 10^5 \pm 5.62 \cdot 10^3$  with a relative standard deviation of 11.57 % and for IRMM-9073 a disintegrated  $^{238}\text{U}$  intensity of  $7.30 \cdot 10^4 \pm 8.17 \cdot 10^3$  with a relative standard deviation of 11.18 %; see Table 33. Polydisperse SG140521\_02 showed a more consistent and homogenous  $^{238}\text{U}$  signal of  $8.04 \cdot 10^4 \pm 7.89 \cdot 10^4$  was measured with a RSD 98.06 %. In comparison to SG141027\_12A which has a mean disintegrated  $^{238}\text{U}$  intensity of  $5.5804 \cdot 10^4 \pm 2.1481 \cdot 10^4$  and a RSD of 38.49 %. The variability in the isotope ratios is considerably smaller and can be related to the monodisperse properties such as morphology and uranium mass. The signal intensity is well within those of IRMM-9073 and NBS-U010. It can be concluded that SG141027\_12A performed better than the existing CRMs, see Figure 77 - Figure 79.

The next step in the assessment process leading to the application as a QC-material for isotopic measurements is the evaluation of the hydride formation rate " $\text{UH}/\text{U}$ ". Interfering hydride species can substantially distort the actual measurement. The hydride formation rate is a measure for the collection efficiency. For the LG-SIMS, an empirical value of  $\text{UH}/\text{U} = 0.003$  is considered acceptable. All spectra were recorded in microprobe mode (10  $\mu\text{m}$  raster and an IP = 50pA). The hydride formation rate for two existing reference materials - IRMM-9073 and NBS-U010 was measured:  $\text{UH}/\text{U}(\text{IRMM-9073}) = 2.59 \cdot 10^{-3} \pm 8.85 \cdot 10^{-3}$  and  $\text{UH}/\text{U}(\text{NBS-U010}) = 2.71 \cdot 10^{-3} \pm 1.21 \cdot 10^{-3}$ . For polydisperse SG140521\_02 the hydride formation rate was low:  $\text{UH}/\text{U}(\text{SG140521_02}) = 1.93 \cdot 10^{-3} \pm 1.02 \cdot 10^{-3}$  with a RSD of 52.89 %, SG141027\_12A showed a different performance, the overall mean  $\text{UH}/\text{U}$  intensity was higher as expected:  $\text{UH}/\text{U}(\text{SG141027_12A}) = 2.95 \cdot 10^{-3} \pm 2.75 \cdot 10^{-4}$  with a RSD of 34.18 %, see Table 38. A threshold level for  $\text{UH}/\text{H}$  of 0.003 was assigned. A non-significant number of measurement values exceeded this threshold level indicating that the overall formation rate was relatively high but still

acceptable. This effect of an increased UH/H of SG141027\_12A can be associated to a LG-SIMS specific reaction to the monodisperse properties. It can be concluded that the UH/H formation rate was higher than expected but within acceptable margins. The spread or variance of the UH/H values was significantly smaller and more consistent for SG141027\_12A than for NBS-U010 and IRMM-9073, see Table 35 and Table 36.

Chapter 5.4.3.1 describes briefly the influence of different acquisition parameters such as ion probe current (IP) and raster size on the hydride formation rate. It can be concluded that both acquisition parameters play an important role in the assessment process. Unexpectedly, a decrease of the IP (IP = 20 pA) in combination with a broader raster size (20  $\mu\text{m}$ ) lead to an increase of the UH/U formation rate of 38.0 %:  $\text{UH/U}(\text{IP} = 20 \text{ pA}, 20 \mu\text{m}) = 5.06 \cdot 10^{-3} \pm 3.68 \cdot 10^{-3}$  with an RSD of 54.75 % - see Table 37.

The evaluation of the total evaporation experiments in combination with the assessment of the useful yield is the most important parameter in the LG-SIMS based assessment because it allows to derive an approximation of the uranium mass per particle and of the overall mean particle density. Only SG141027\_12A was compared against IRMM-9073 and monodisperse particles from ITU (20079). ITU (20079) are monodisperse particles made from JRC-ITU, see Erdmann et al. (2000) [40]. In total 10.000 cycles (acquisition time per cycle was 1.04 s) were measured at IP = 50pA and a 10  $\mu\text{m}$  raster.

IRMM-9073 had the highest mean  $^{238}\text{U}$  intensity of  $1.54 \cdot 10^8 \pm 2.25 \cdot 10^8$  with an associated mean relative bias of 115.35 %, ITU particles showed a mean intensity of  $1.69 \cdot 10^7 \pm 6.29 \cdot 10^8$  with a corresponding mean relative bias of 32.5 %. The significantly smaller mean relative bias of ITU (20079) in comparison to polydisperse IRMM-9073 is already a strong indication of the homogenous nature of the ITU (20079) particles. But the mean  $^{238}\text{U}$  intensity indicated a smaller amount of uranium thus a smaller particle size. Belated SEM studies revealed a considerably smaller average particle size for ITU (20079) of  $\ll 1.0 \mu\text{m}$ . SG141027\_12A on the other hand showed a consistent  $^{238}\text{U}$  intensity profiles over 1000 cycles, see Figure 127. Just in one case an adjacent particle was simultaneously measured, which explains the rugged profile at around 4200 s. Since the  $^{238}\text{U}$  intensity signal correlates to the mass of uranium per particle, a significantly higher  $^{238}\text{U}$  intensity for SG141027\_12A in comparison to ITU (20079) was measured; by a factor of 144. The most promising performance was evaluated from SG141027\_12A with a mean  $^{238}\text{U}$  intensity of  $2.42 \cdot 10^8 \pm 1.8 \cdot 10^7$  and just a RSD of 4.25 %. This result indicates a high degree of homogeneity and is an indication of consistent quality and reproducible, predictable outcome; hence desired performance.

The useful yield "X" is an important performance characteristic. The useful yield is the ratio of the integrated signal which was measured against the number of atoms in the particle. Ranebo et al. (2009) [18] measured a useful yield  $X = 1.18 \pm 0.15\%$  for  $\text{O}_2^-$  and for an  $\text{O}_2^+$  ion source  $X = 0.96 \pm 0.07\%$ . In total, seven different particles were used to assess the useful yield. Measurements showed a mean useful yield of  $5.14 \pm 0.38\%$  which is significantly higher value than what Ranebo et al. (2009) [18], 0.96 %, and Hedberg et al. (2005) [163], 0.27 % derived. Their results were derived from the fact that all microparticles were made from the same uranium compounds and that their density was consistent throughout all particles of all measured specimen and also based upon a density assumption derived from mass spectrometric measurements. Figure 84 shows a linear dependency of the useful yield for all particles. The assessment of the useful yield builds on an estimated value: the particle density. A linear dependency can be observed and a relative standard deviation of 3.2 % was calculated, see Table 39. This indicates that the theoretical number of atoms per particle and the measured value only deviate by 3.2 %; which can be calculated using equation 10:  $2.067 \cdot 10^9$  uranium atoms per particle. A mean uranium mass per particle of  $2.89 \pm 0.9 \text{ pg}$  with an average density of  $2.51 \pm 1.0 \text{ g/cm}^3$  was derived. This result is also a strong indication for the homogeneity and the consistent quality of SG141027\_12A and opens up the possibility of using these particles as a uranium mass standard.

In Chapter 5.3.4.1, the changes of the mean integrated  $^{238}\text{U}$  intensity " $I(^{238}\text{U})$ " in dependence of the primary ion beam diameter were investigated. The primary ion-beam diameter was focused to about 1  $\mu\text{m}$ . It was expected to see a decrease for smaller primary ion-beam diameters. But the opposite was

observed; with the focused ion beam a mean integrated intensity " $I(^{238}\text{U})$ " of  $I(^{238}\text{U}) = 3.038 \cdot 10^8 \pm 9.278 \cdot 10^7$ , with a RSD of 30.54 % was measured which is about 1.25 x bigger than the mean integrated intensity of the defocused total evaporation. This effect demonstrates the need for consistent instrumental measurement conditions.

After total evaporation experiments, a distinct sputter-residue pattern is left behind, due to the ablation process a cone shaped residue was formed, see Figure 86. After the total evaporation experiments, the residue was re-scanned with a 50  $\mu\text{m}$  raster, a primary ion beam current of 1.5 nA and a total area of 2500  $\mu\text{m}^2$  was investigated. All residues showed a consistent and predictable behavior which is an indication for the homogeneity of the particles. One particle showed a deviant behavior which can be explained by the proximity of another particle measured simultaneously.

The evolution of the particle production setup is also of importance for this thesis. The current setup (as of May 2015) is sophisticated enough to produce a sufficient number of microparticles of consistent quality. Preliminary experiments and data evaluation on SG140521\_02 indicate that the presence of the furnace with temperature > 600 °C might facilitate the generation of unfavorable particle species. The final particle morphology is controlled by the precipitation mechanics, see Messing et al. (1993) [58] and Reuge et al. (1961) [66]. With the dismantling of the furnace, (a) the particle morphology could be controlled more easily and (b) the collection yield could be increased by two to three orders of magnitude. Monodisperse, homogenous microparticles show consistent quality and quantity of key features, important for nuclear forensics related work; e.g. enough particles for either non-destructive and destructive assays, consistent  $m(\text{U})/\text{particle}$ , homogenous morphology, consistent behavior during (non)-destructive assays (e.g. SEM, FIB, (TOF)-SIMS and Raman Spectroscopy).

Ultimately it can be concluded that microparticles produced in Jülich show great potential for use as a QC-material or even as a (C)RM: our investigations showed that the intended "solid" particles can be produced by rather mild production parameters and not fast and hot environments (>850 °C), see Chapter 4.1.2. By carefully selecting the optimal production parameters solid, consistent microparticles with an intended size distribution can be produced. SEM-EDX investigations demonstrated the inefficiency of a qualitative uranium determination. Due to the small particle size, the vast majority of the signal originated from the background. Nevertheless, SEM-EDX proved to be extremely efficient to easily verify the presence of uranium for automated, large scale particle counting procedures used to assess the size distribution, but were not suitable for a sound elemental quantification.  $\mu$ -Raman spectroscopy experiments indicated the presence of a multiphase uranium compound. This result is relevant for future studies on the chemical stability of these microparticles.

LG-SIMS experiments showed strong evidence for the applicability of the produced particles as a reference material. In particular SG141027\_12A proved to have consistent, homogeneous and reproducible behavior and result. The most important message from this work is that these total evaporation experiments, in Chapter 5.4.4, can be directly correlated to a consistent uranium mass per particle per batch. This also includes a consistent particle morphology which is determined by the precipitation mechanics during the conversion of aerosol droplets to solid entities. This implies that the density may vary significantly within a microparticle. This inhomogeneity in the particles' morphology can be observed for all investigated batches. It can be concluded that the most important thing is the uranium mass per particle, particle size and density are of subsidiary importance. Furthermore, all experiments indicate reasonable or outstanding performance.

## Outlook

The particle production setup can be further improved using an electronic pump to control the liquid feed rate more accurately. For future projects, it would be advisable to investigate the influence of different precursor solutions - instead of nitrate solutions, acetate and carbonate or chloride solutions.

One urgent issue is the question of the particle density and thorough uranium mass determination – especially in regard towards the implementation as a (certified) reference material. Several possible

approaches to determine the uranium content could be used: (a) similar to what Kraiem et al. (2012) [45] did using IDMS or ICP-MS measurements, (b) auxiliary Laser Ablation – ICP-MS (LA-ICP-MS) measurements would deliver comparable results with much less efforts in sample preparation or (c) if necessary fission-track TIMS (FT-TIMS) could deliver a more precise measurements result.

Further SIMS measurements have to be made on each particle batch. So far only SG141027\_12A was thoroughly investigated. And as of now only one isotopic composition has been used to produce microparticle. It would be interesting to see if the introduction of one or multiple uranium CRMs shows any memory effects and cross contamination in subsequent runs.

The identification of the physico chemical environment plays an important role but will be addressed more thoroughly in a different publication. In late 2015 combined EXAFS/XANES and XRD measurements were performed at Paul-Scherrer Institute (Micro XAS beamline), Switzerland, on bulk quantities [i] of microparticles as well as on single particles. One outcome can be derived from these experiments: it confirms the existence of a polymorphous uranium oxide/hydroxide species with oxidations states between U(V) and U(IV). This finding is in accordance with the measurement results that could be derived from the  $\mu$ -Raman spectroscopy investigation.

This work represents a first step towards the development of QC and RM microparticles application. Further studies have to be carried out in order to assess the thermodynamic stability of the created particles. If particles are thoroughly assessed it would be advisable to embed these artificial particles inside a well-defined matrix which resembles real-life samples. Particles could be measured in a more realistic manner and interferences could be ruled out much readily.

[i] “Bulk quantities” means in this context a few hundred microparticles on small area of a few mm<sup>2</sup>.

## 7. Appendix

### 7.1 Size Distribution Histograms

#### 7.1.1 SG150312\_05A, SG150401\_14A, SG150413\_03A and SG150429\_02A

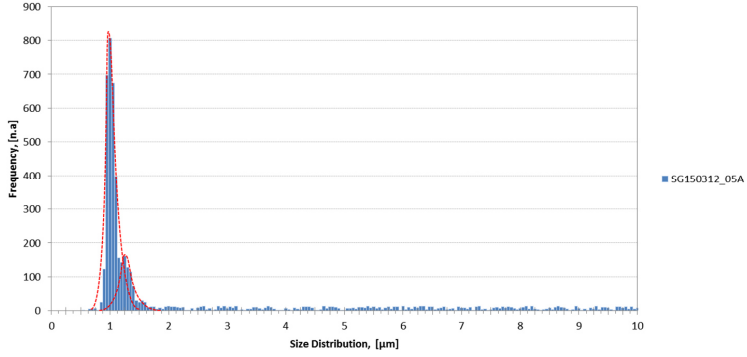


Figure 88: Size distribution of SG150312\_05A.

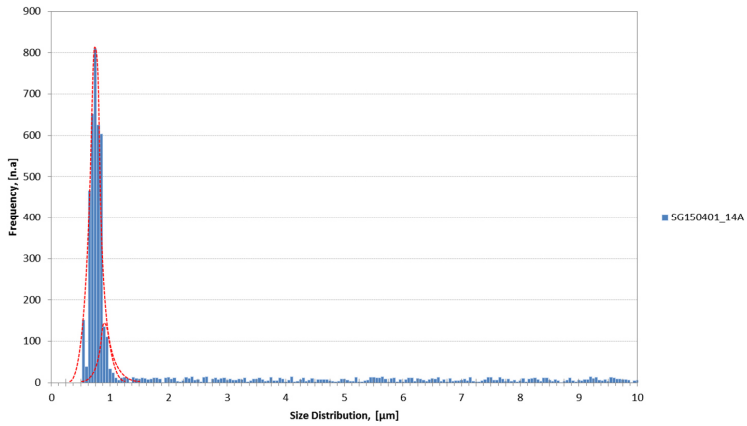
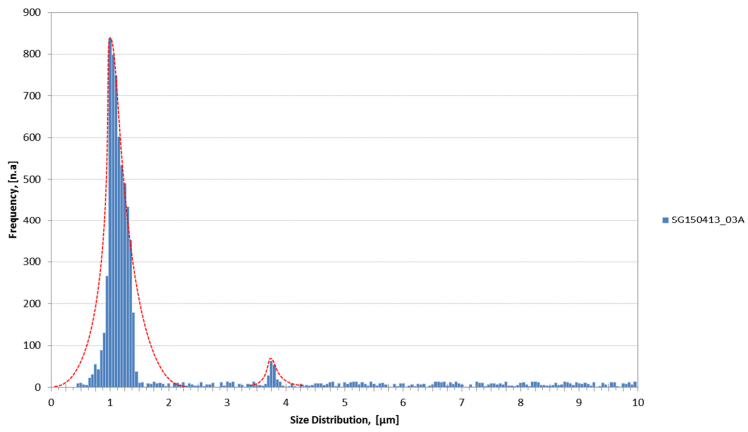
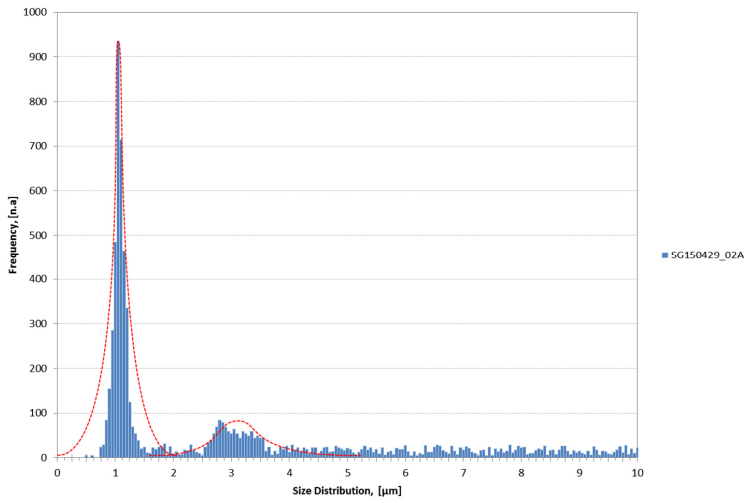


Figure 89: Size distribution of SG150401\_14A.



**Figure 90: Size distribution of SG150413\_03A.**



**Figure 91: Size distribution of SG150429\_02A.**

## 7.2 Shape Descriptors: Circularity

### 7.2.1 SG150312\_05A, SG150401\_14A, SG150413\_03A and SG150429\_02A

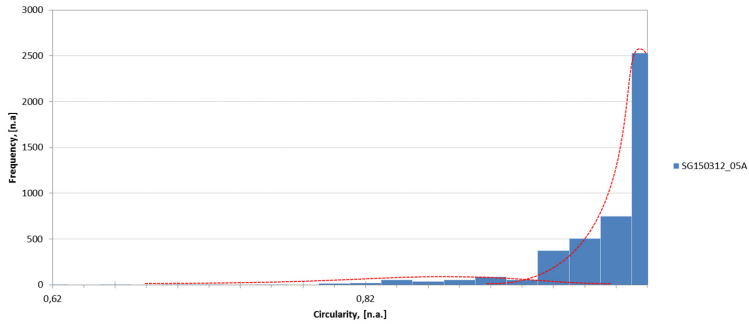


Figure 92: Circularity of SG150312\_05A.

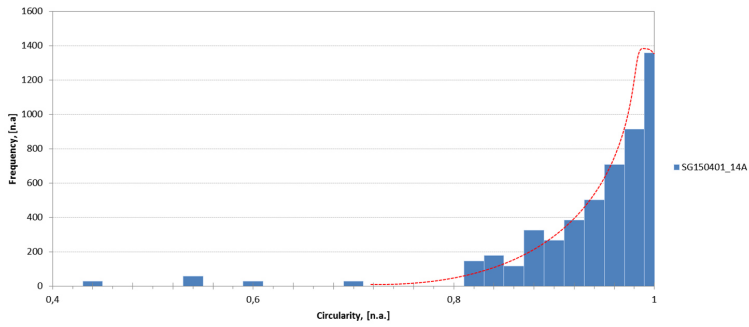


Figure 93: Circularity of SG150401\_14A

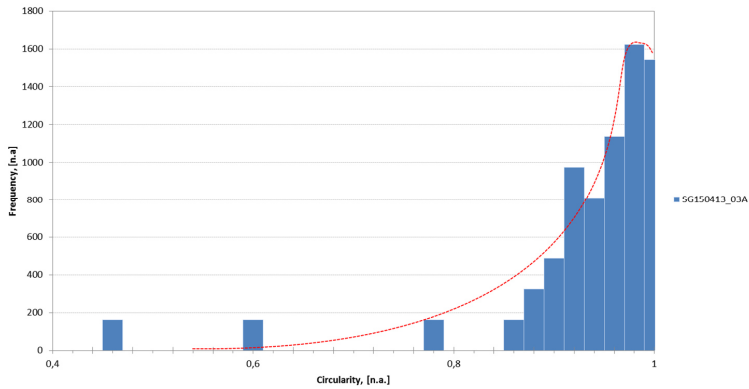
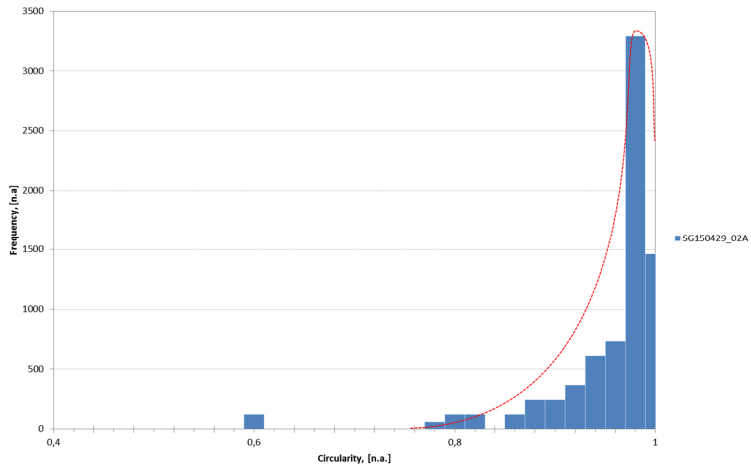


Figure 94: Circularity of SG150413\_03A



**Figure 95: Circularity of SG150429\_02A.**

### 7.3 Focused Ion Beam

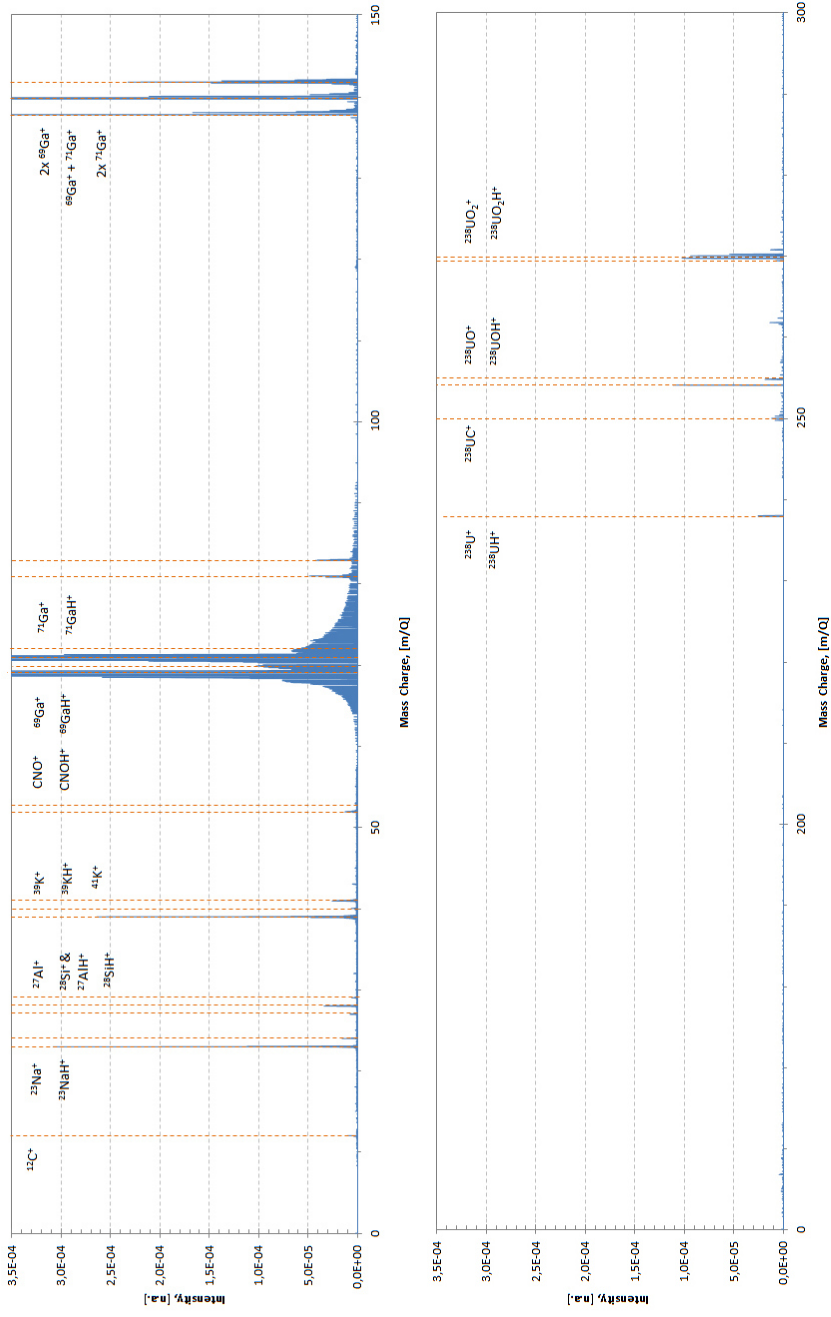


Figure 96: TOF Spectrum of selected particles originating from SG141027\_12A

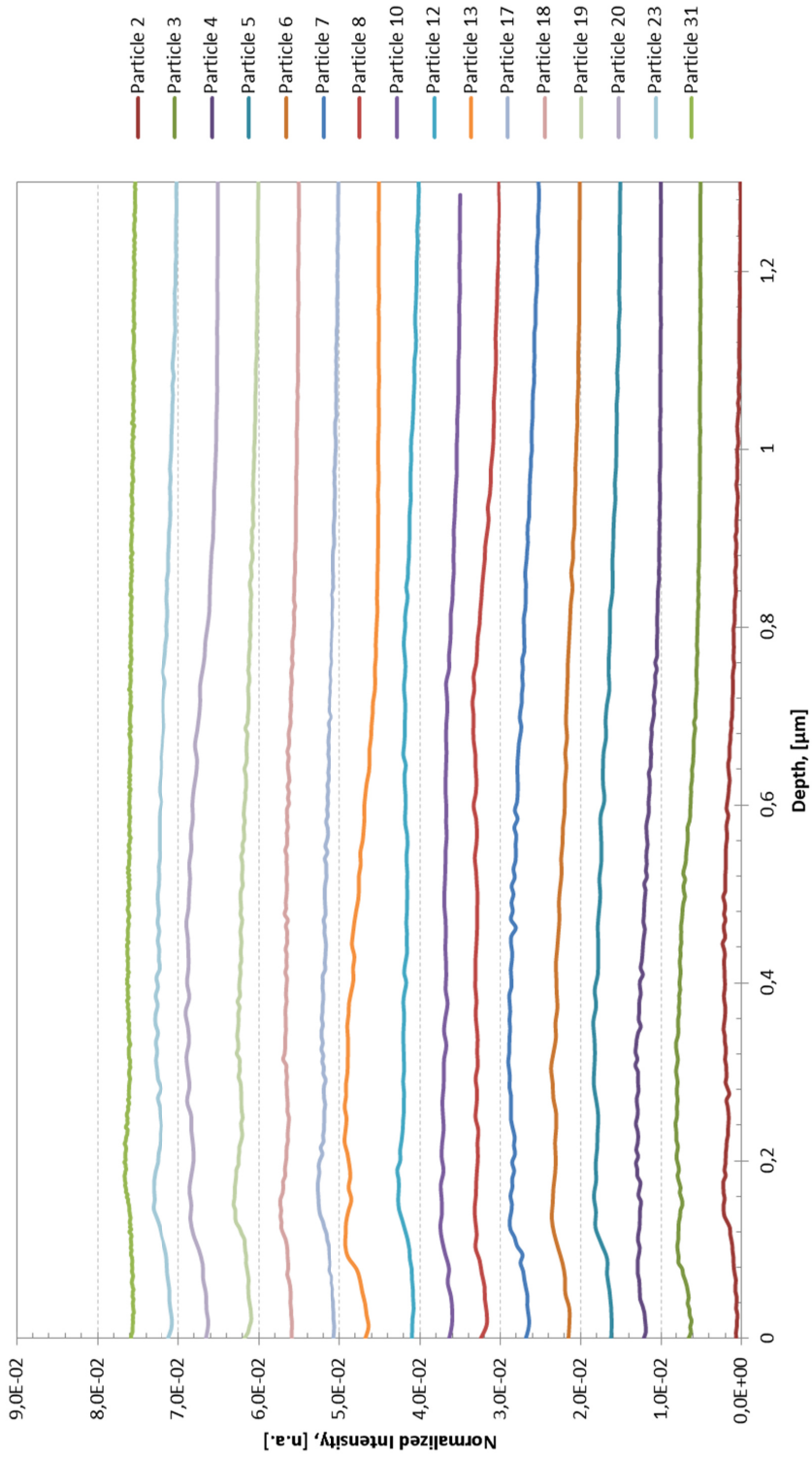


Figure 97: Depth profiles acquired from FIB-TOF-SIMS measurements – all intensities of  $m/Q(238)$  are normalized and plotted against the particle depth – all particles taken from SG141027\_12A.

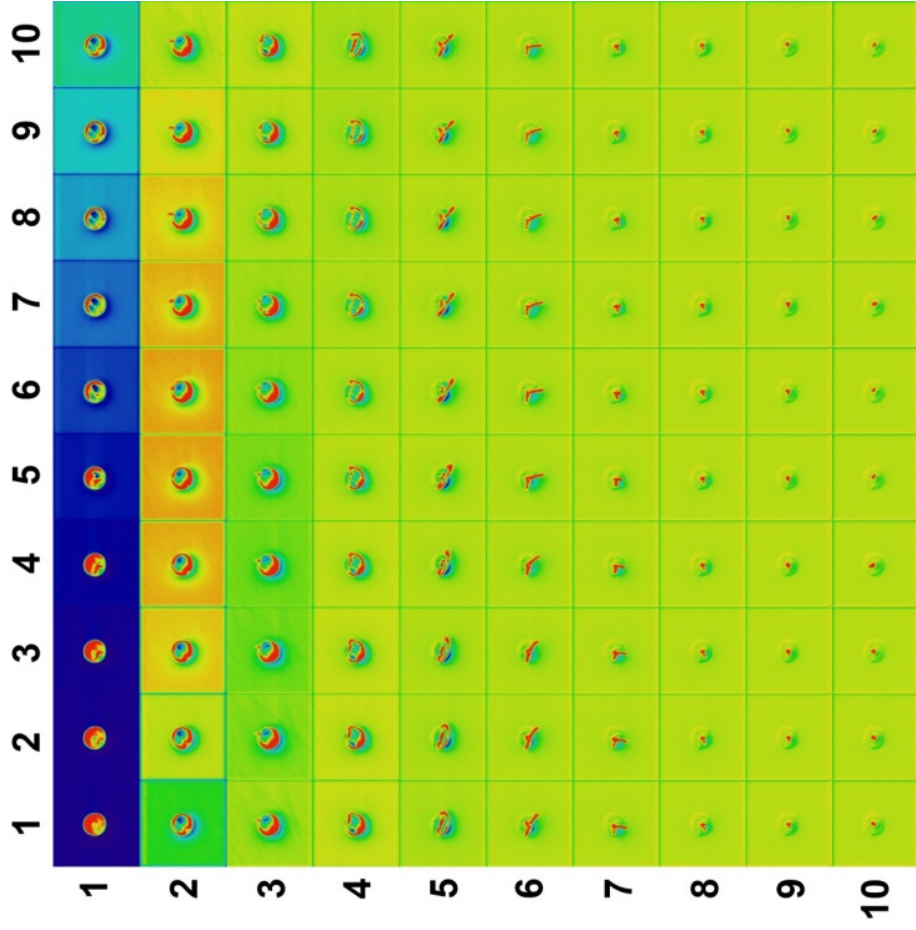


Figure 98: FIB ablation sequence of a micrometer sized uranium particle – Particle 1.

7.3.1 Auxiliary Focused Ion Beam analysis on SG150401\_14

Particle 4

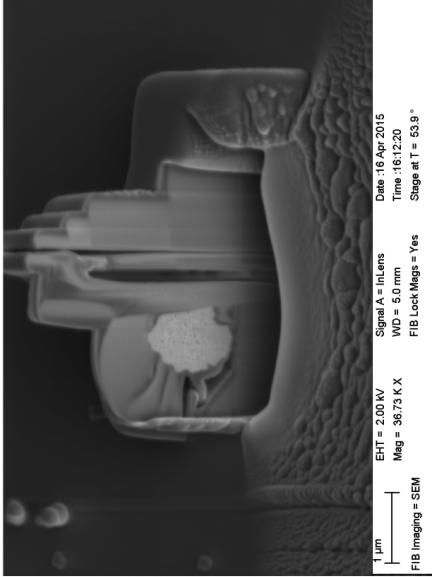
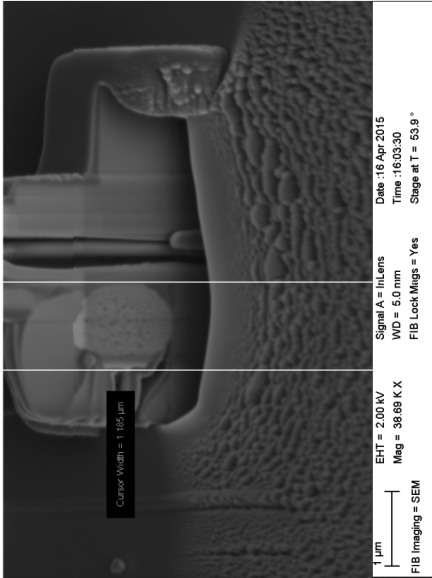
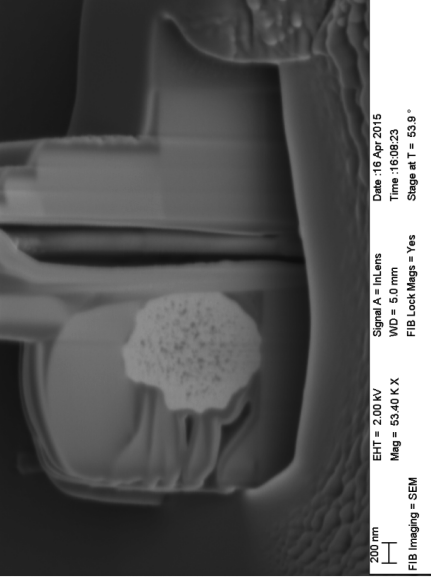
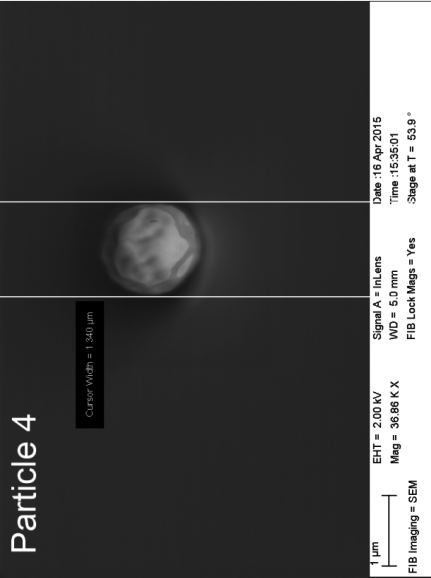


Figure 99: FIB-sequence of Particle 4 of SG150401\_1A.

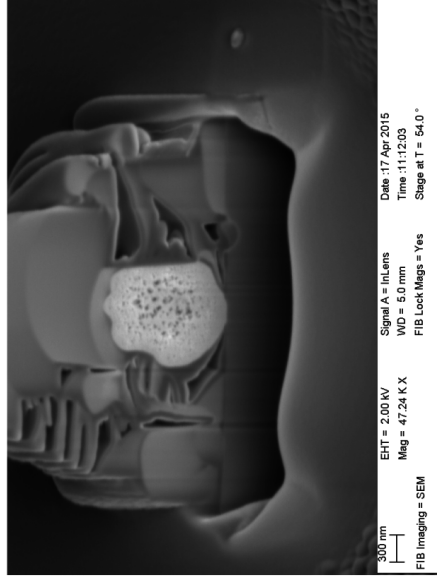
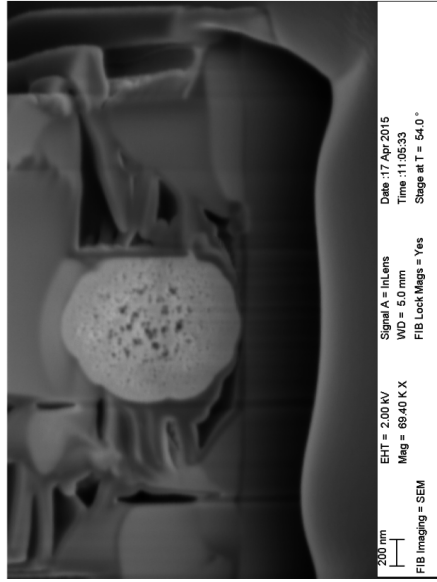
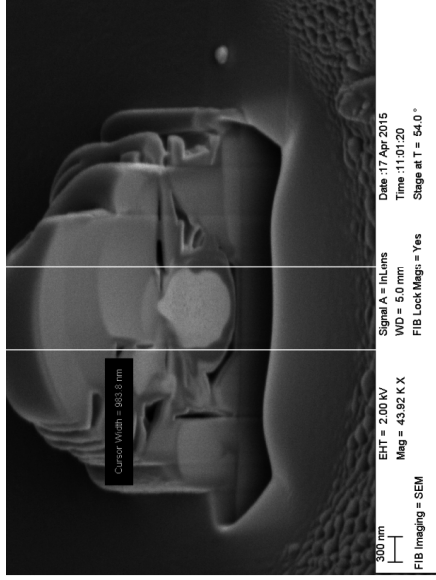
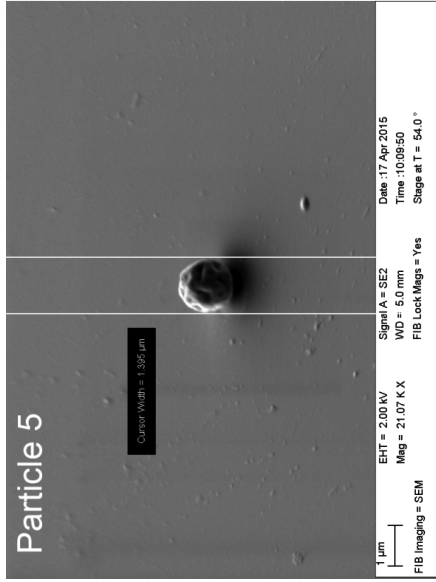
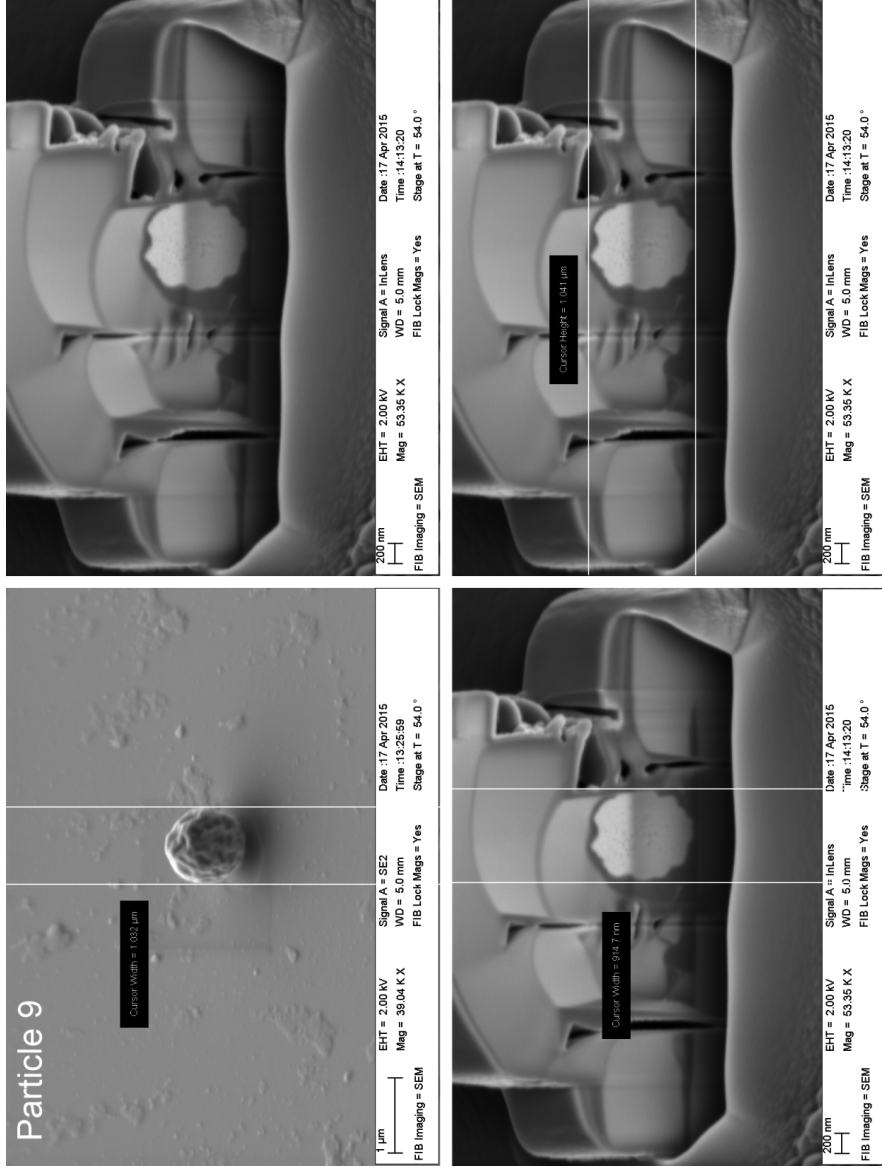


Figure 100: FIB-sequence of Particle 5 of SG150401\_1A.



**Figure 101: FIB-sequence of Particle 9 of SG150401\_1A.**

## 7.4 EDX-Spectra

### 7.4.1 Polydisperse Batch: SG140521\_02

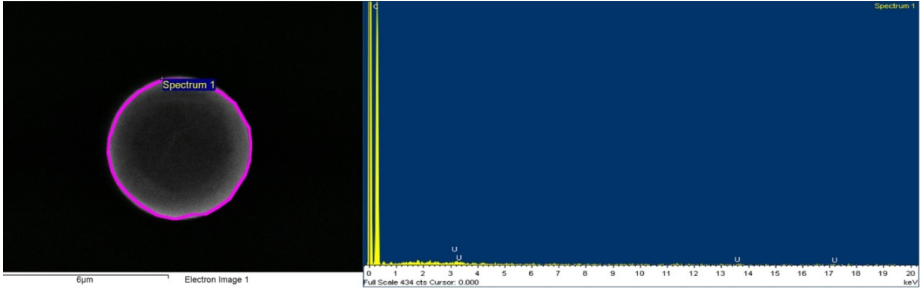


Figure 102: BSE-image and corresponding EDX spectrum of exemplary hollow particle on SG140521\_02.

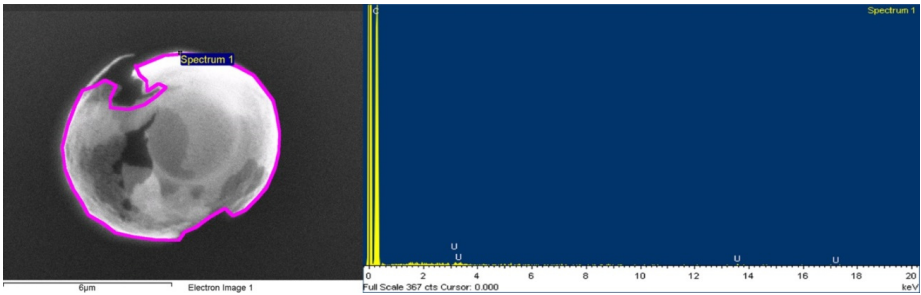


Figure 103: BSE-image and corresponding EDX spectrum of hollow particle after destruction.

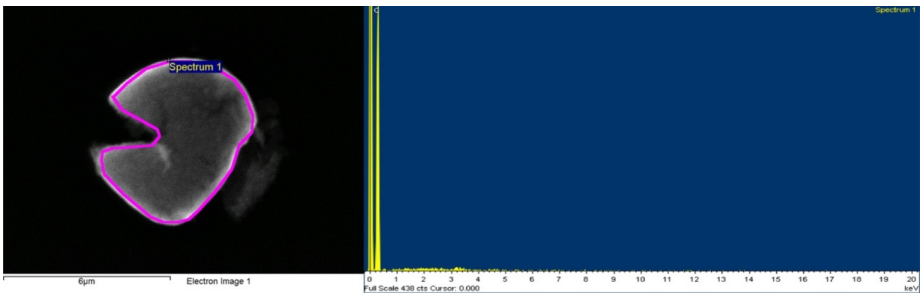


Figure 104: BSE-image and corresponding EDX spectrum of exemplary deformed particle on SG140521\_02.

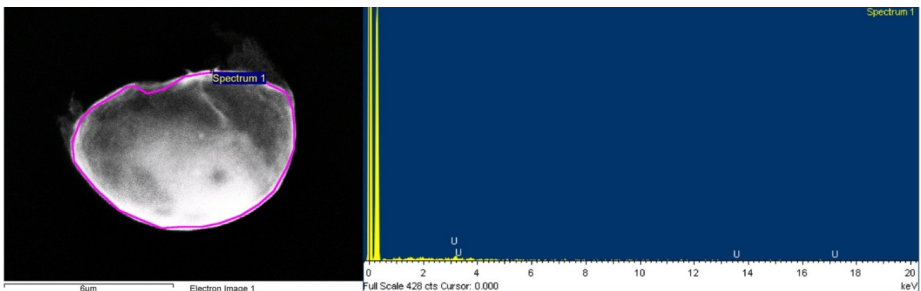


Figure 105: BSE-image and corresponding EDX spectrum of exemplary debris on SG140521\_02.

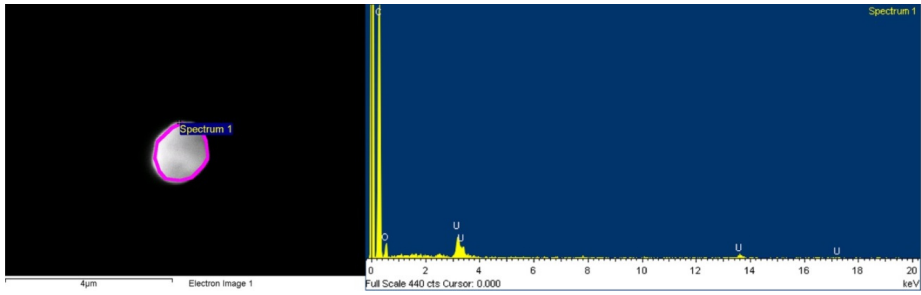


Figure 106: BSE-image and corresponding EDX spectrum of exemplary solid particle on SG140521\_02.

**7.4.2 Uniform Batches: SG141027\_12A, SG150312\_05A, SG150401\_14A, SG150413\_03A and SG150429\_02A**

**SG141027\_12A**

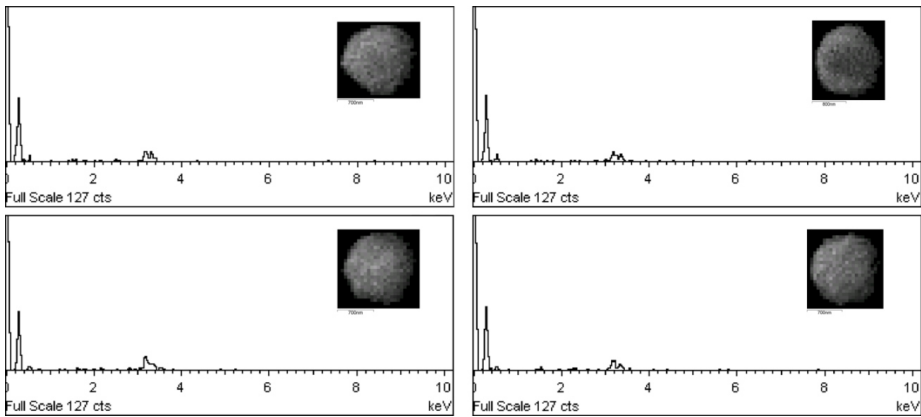


Figure 107: BSE image and corresponding EDX spectrum of exemplary solid particle SG141027\_12A.

**SG150312\_05A**

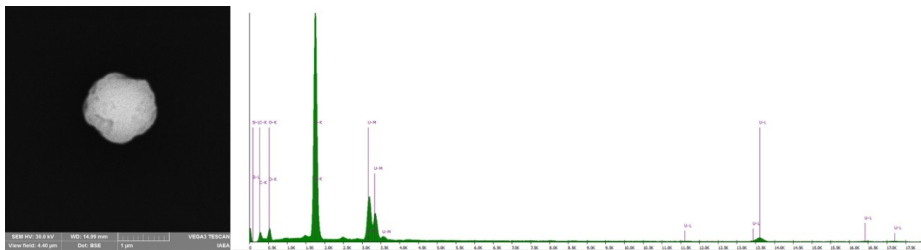
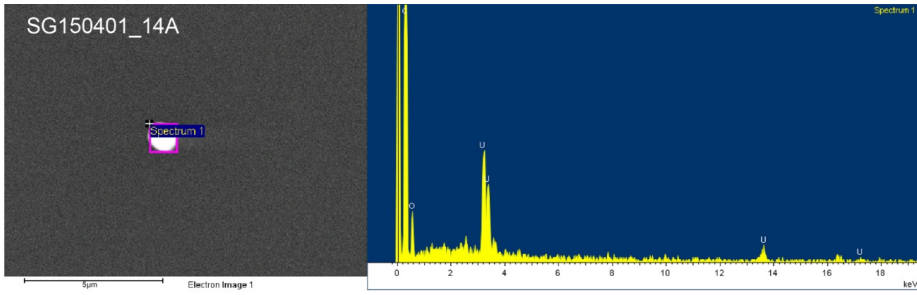


Figure 108: BSE image and corresponding EDX spectrum of exemplary solid particle SG150312\_05A.

**SG150401\_14A**



**Figure 109: BSE image and corresponding EDX spectrum of exemplary solid particle SG150401\_14A.**

**SG150413\_03A**

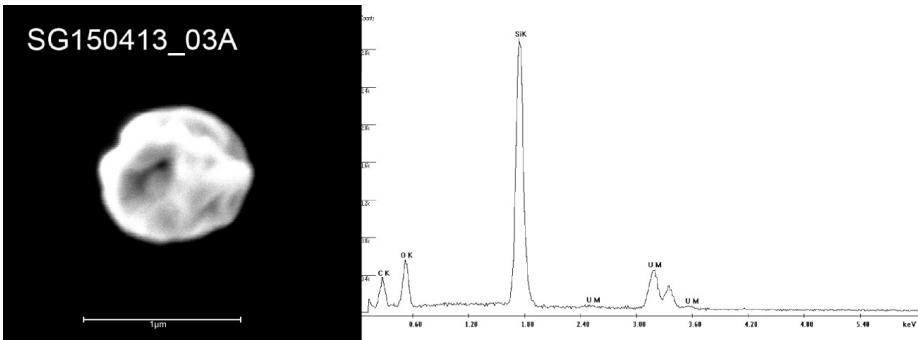


**Figure 110: BSE image and corresponding EDX spectrum of exemplary solid particle SG150413\_03A.**

**SG150429\_02A**

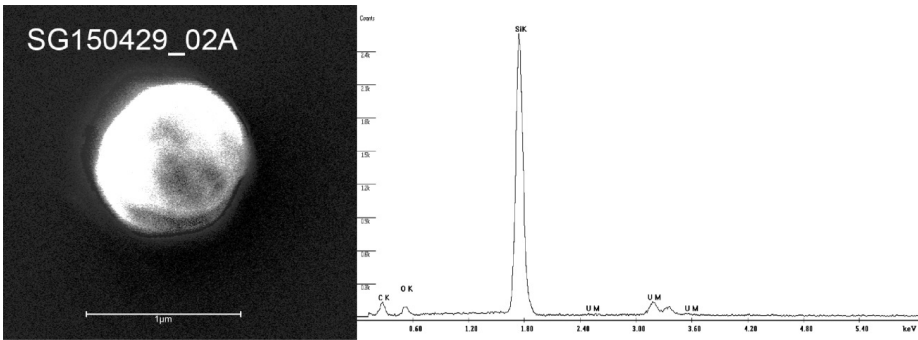


**Figure 111: BSE image and corresponding EDX spectrum of exemplary solid particle SG150429\_02A.**

## 7.5 Micro-Raman Spectroscopy

### 7.5.1 Uranyl nitrate Hexahydrate Spectra

#### UNH - CEA (Stage 1)

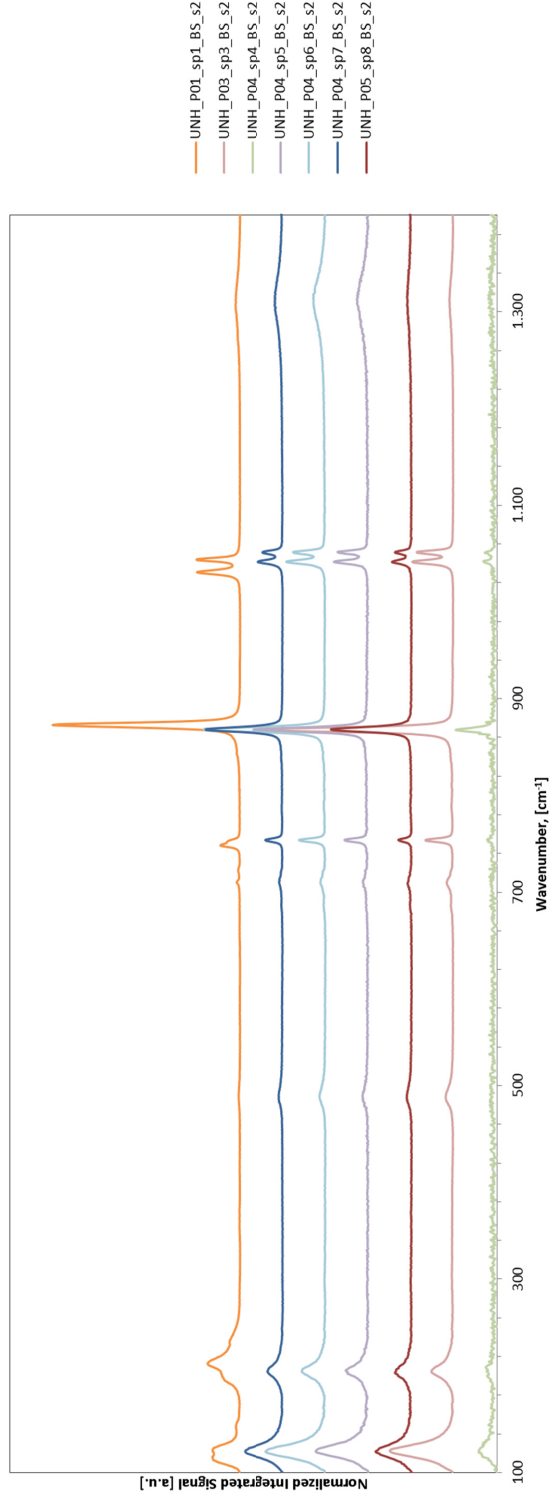


Figure 112: UNH spectrum on bulk material of Stage 1 - Spectra recorded at CEA-Ile-de-France.

## UNH - CEA (Stage 2)

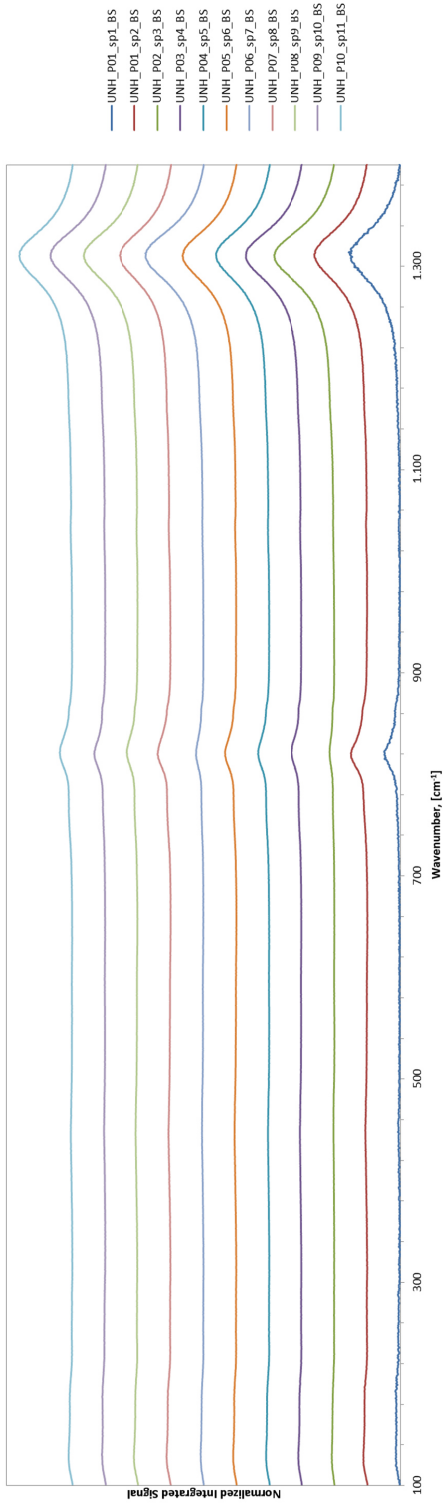


Figure 113: UNH spectrum on bulk material of Stage 2 – Spectra recorded at CEA-Ile-de-France.

## 7.5.2 Raman Spectra of selected number of particles originating from CEA and TUW with a total spectral range of 100-3200cm<sup>-1</sup>

U<sub>3</sub>O<sub>8</sub>

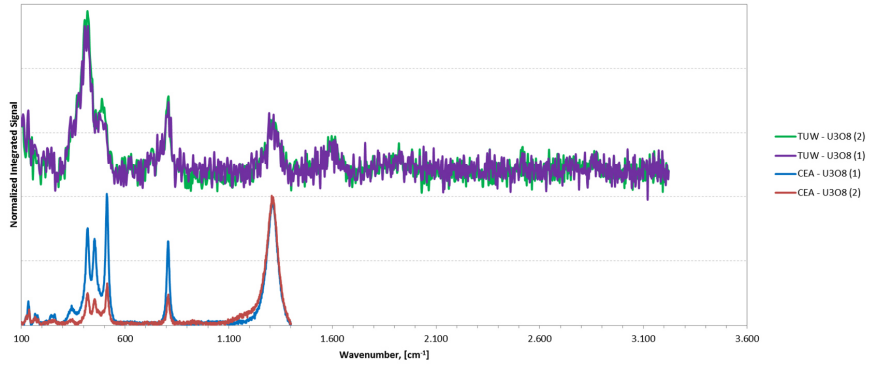


Figure 114: Micro Raman Spectra of selected U<sub>3</sub>O<sub>8</sub> samples originating from CEA and TUW. Spectra acquired at TUW have a wider acquisition range - 100-3200cm<sup>-1</sup>.

UO<sub>2</sub>

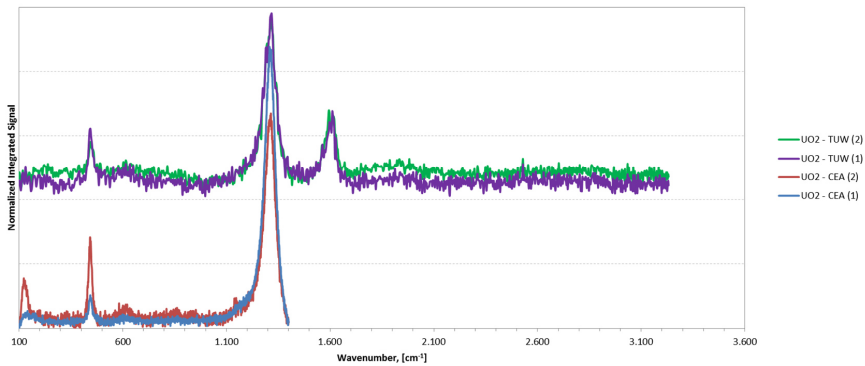
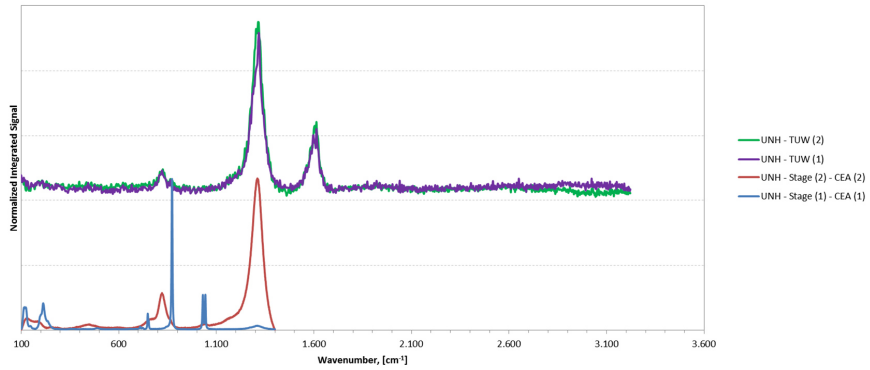


Figure 115: Micro Raman Spectra of selected UO<sub>2</sub> samples originating from CEA and TUW. Spectra acquired at TUW have a wider acquisition range - 100-3200cm<sup>-1</sup>.

## UNH



**Figure 116: Micro Raman Spectra of selected UNH samples originating from CEA and TUW. Spectra acquired at TUW have a wider acquisition range - 100-3200cm<sup>-1</sup>.**

## ADU

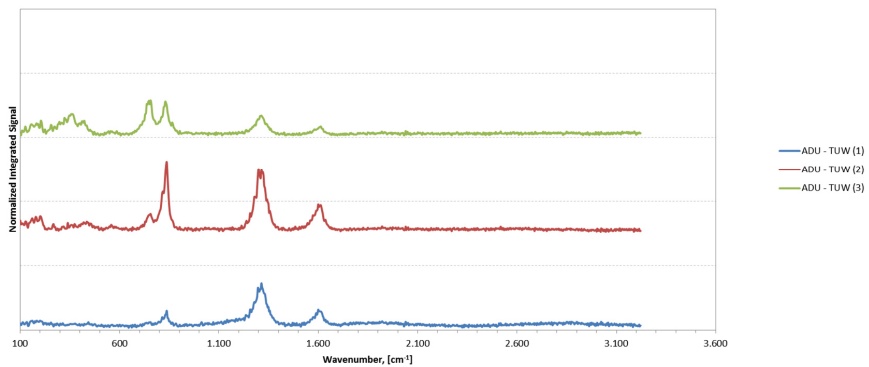


**Figure 117: Micro Raman Spectra of selected ADU samples originating from CEA and TUW. Spectra acquired at TUW have a wider acquisition range - 100-3200cm<sup>-1</sup>.**

### 7.5.3 Raman Spectra of $\text{UO}_2\text{F}_2$ - Double band at $867\text{cm}^{-1}$

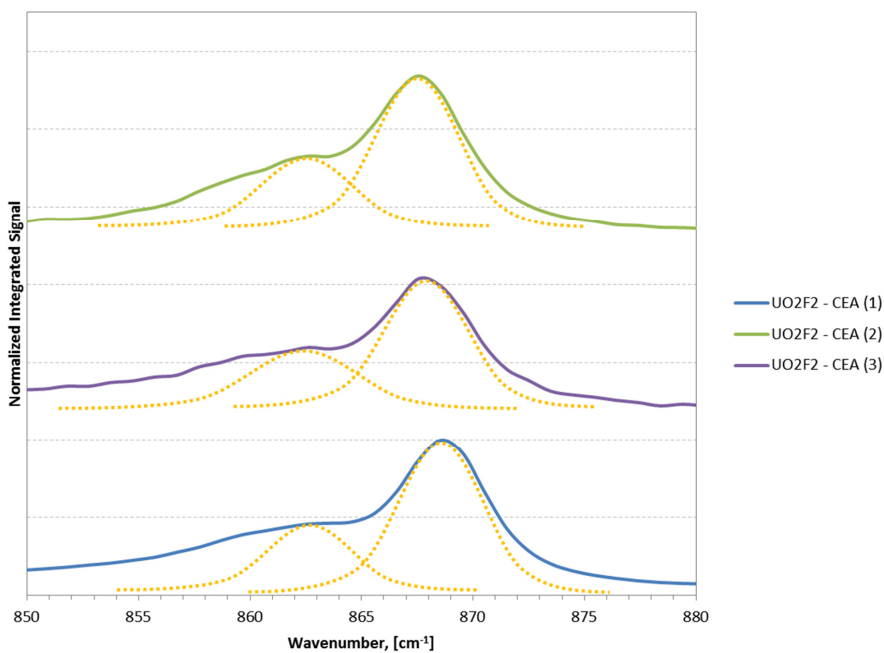


Figure 118: Observed double and at  $867\text{cm}^{-1}$  for  $\text{UO}_2\text{F}_2$ , in accordance with Stefaniak et al. (2013).

### 7.5.4 Raman Spectra of SG140521\_02

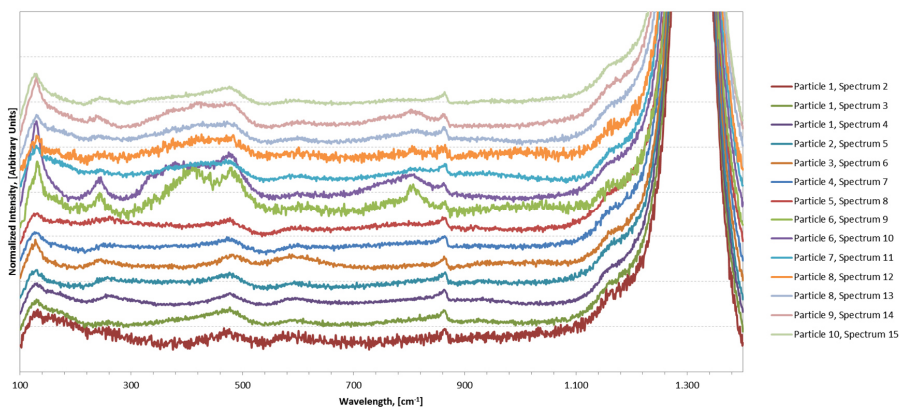


Figure 119: Raman Spectra of SG140521\_02 acquired at CEA.

### 7.5.5 Raman Spectra of SG141027\_12A

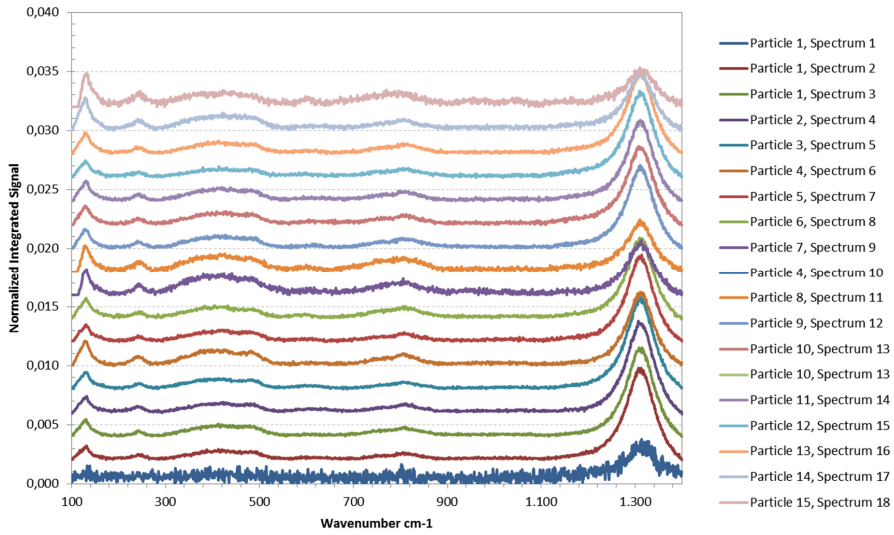


Figure 120: Raman spectra of 15 particles originating from SG141027\_12A.

### 7.5.6 Raman Spectra of SG141027\_12A from CEA vs TUW

Comparison CEA vs. TUW - SG141027\_12A

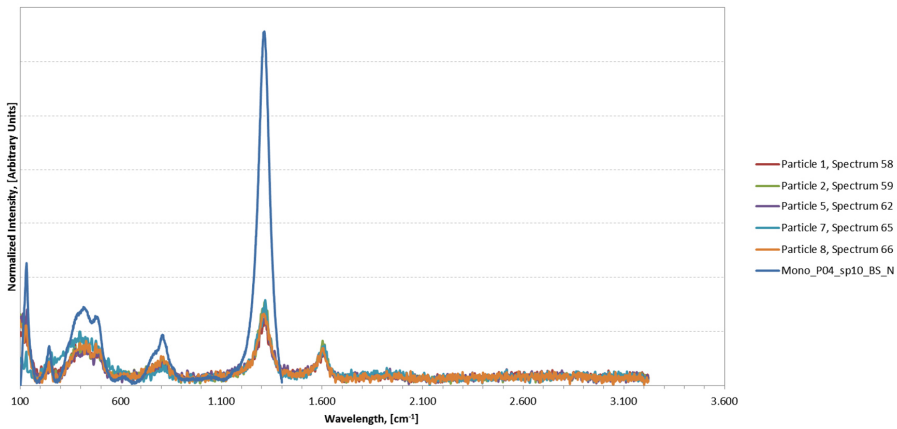


Figure 121: Raman Spectra acquired at CEA and TUW in direct comparison.

## 7.5.7 Raman Spectra of SG150401\_14A

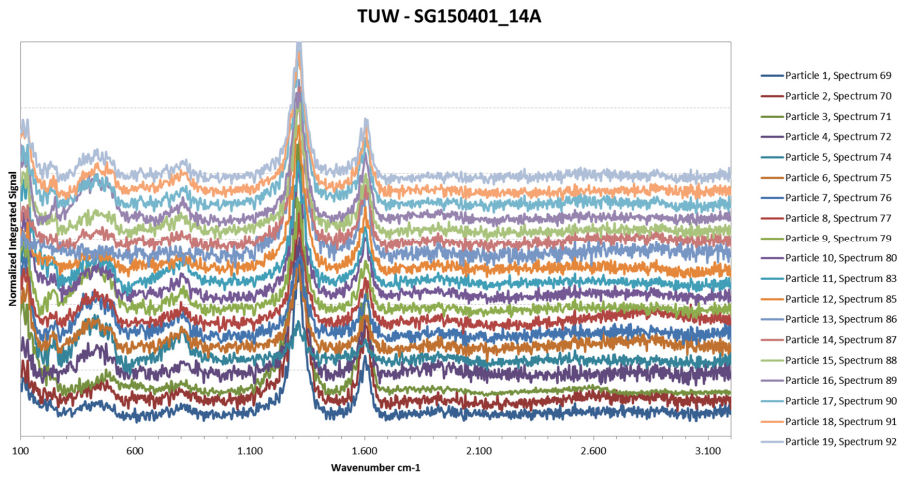


Figure 122: Collected Raman spectra of SG150401\_14A.

### 7.5.8 Direct comparison of selected uranium compounds to particles produced at FZJ

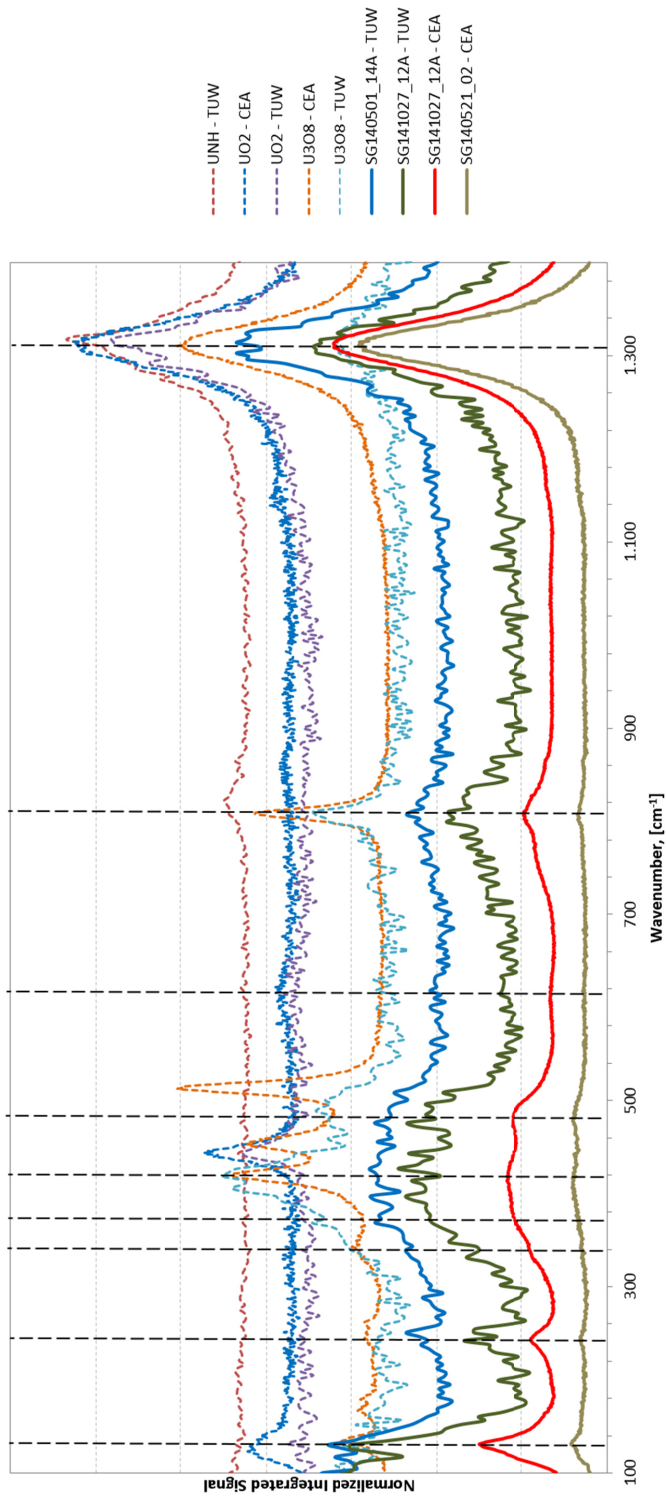


Figure 123: Micro Raman Spectra of selected uranium compounds in direct comparison to particle produced at Forschungszentrum Jülich GmbH: SG140521\_02, SG141027\_12A, SG140501\_14A.

## 7.6 SIMS spectra

### 7.6.1 Abundances of <sup>234</sup>U, <sup>235</sup>U and <sup>236</sup>U of particles originating from SG1040521\_02 and SG141027\_12A

Table 43: <sup>234</sup>U, <sup>235</sup>U and <sup>236</sup>U abundances on 24 micrometer sized uranium particles originating from SG141027\_12A.

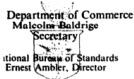
SG141027_12A														
Date	Sequence	Part. ID	234	234 (fs)	Final unc.	Rel. final unc.	235	235 (fs)	Final unc.	Rel. final unc.	236	236 (fs)	Final unc.	Rel. final unc.
10. Mrz15	SG141027_12A	590002	2,2149E-05	2,09974E-06	1,13992E-06	5.13%	3,22072E-03	1,82591E-05	1,3719E-05	0.43%	1,49475E-04	8,71631E-06	3,04137E-06	2.03%
10. Mrz15	SG141027_12A	590003	1,97189E-05	1,61078E-06	1,07540E-06	5.45%	3,19673E-03	1,97835E-05	1,36797E-05	0.43%	1,49131E-04	5,11875E-06	3,03169E-06	2.03%
10. Mrz15	SG141027_12A	590005	2,16011E-05	2,20113E-06	1,36706E-06	6.33%	3,21586E-03	2,23356E-05	1,66647E-05	0.52%	1,55388E-04	2,8922E-05	3,75755E-06	2.43%
10. Mrz15	SG141027_12A	590006	1,86182E-05	1,42372E-06	1,11153E-06	5.97%	3,22282E-03	1,87666E-05	1,46107E-05	0.45%	1,53757E-04	1,84496E-05	3,27862E-06	2.12%
10. Mrz15	SG141027_12A	590007	2,22425E-05	3,69014E-06	1,42933E-06	6.43%	3,24164E-03	2,96167E-05	1,72397E-05	0.53%	1,49153E-04	1,44945E-05	3,79845E-06	2.55%
10. Mrz15	SG141027_12A	590010	1,89117E-05	8,88165E-07	8,0025E-07	4.25%	3,22676E-03	2,30316E-05	1,04968E-05	0.33%	1,48585E-04	5,56400E-06	2,30897E-06	1.55%
11. Mrz15	SG141027_12A	598011	2,08762E-05	5,01690E-06	8,98474E-07	4.30%	3,23577E-03	2,27698E-05	1,11784E-05	0.35%	1,51858E-04	1,07171E-05	2,48895E-06	1.68%
11. Mrz15	SG141027_12A	598012	1,80827E-05	1,24339E-06	9,51892E-07	5.26%	3,20391E-03	1,94769E-05	1,26619E-05	0.40%	1,30907E-04	1,73490E-05	2,85513E-06	1.88%
11. Mrz15	SG141027_12A	598013	1,93808E-05	1,95214E-06	1,00820E-06	5.20%	3,22012E-03	3,14798E-05	1,29895E-05	0.40%	1,47691E-04	7,08060E-06	2,86106E-06	1.94%
11. Mrz15	SG141027_12A	598014	1,89094E-05	1,56788E-06	9,97855E-07	5.28%	3,22916E-03	2,63513E-05	1,30311E-05	0.40%	1,46149E-04	3,67956E-06	2,86909E-06	1.96%
11. Mrz15	SG141027_12A	598016	2,09082E-05	1,17153E-06	1,14266E-06	5.47%	3,21362E-03	1,92214E-05	1,41765E-05	0.44%	1,50775E-04	2,16546E-05	3,15732E-06	2.09%
11. Mrz15	SG141027_12A	598017	1,90773E-05	1,14428E-06	1,04731E-06	5.49%	3,21080E-03	2,16758E-05	1,35777E-05	0.42%	1,50641E-04	2,39924E-05	3,01552E-06	2.00%
11. Mrz15	SG141027_12A	598018	1,85840E-05	1,57426E-06	1,00676E-06	5.38%	3,23432E-03	1,80678E-05	1,31974E-05	0.41%	1,44332E-04	7,71023E-06	2,87321E-06	1.99%
11. Mrz15	SG141027_12A	598019	1,87115E-05	4,06213E-06	9,78520E-07	5.23%	3,22130E-03	1,89941E-05	1,28303E-05	0.40%	1,55591E-04	8,60921E-06	2,89794E-06	1.88%
11. Mrz15	SG141027_12A	598020	1,97161E-05	1,18336E-06	1,12926E-06	5.70%	3,22962E-03	1,97128E-05	1,43628E-05	0.44%	1,28012E-05	1,28012E-05	3,13812E-06	2.14%
11. Mrz15	SG141027_12A	598021	2,25632E-05	3,70109E-06	1,09374E-06	4.89%	3,22789E-03	1,79128E-05	1,31315E-05	0.41%	1,56727E-04	1,50318E-05	2,97240E-06	1.90%
11. Mrz15	SG141027_12A	598023	1,85239E-05	8,06770E-06	1,16948E-06	6.18%	3,20509E-03	1,94628E-05	1,52094E-05	0.47%	1,43250E-04	8,56744E-06	3,29952E-06	2.30%
11. Mrz15	SG141027_12A	598024	2,02682E-05	1,31407E-06	1,04097E-06	5.14%	3,21810E-03	1,78746E-05	1,31080E-05	0.41%	1,46426E-04	5,78836E-06	2,87645E-06	1.90%
11. Mrz15	SG141027_12A	598026	2,10755E-05	3,84302E-06	1,00915E-06	6.21%	3,18985E-03	1,95272E-05	1,60948E-05	0.50%	1,46603E-04	1,15463E-05	3,54009E-06	2.41%
11. Mrz15	SG141027_12A	598027	2,03646E-05	2,89730E-06	1,04330E-06	5.12%	3,22207E-03	1,78977E-05	1,31143E-05	0.41%	1,47004E-04	4,38362E-06	2,87469E-06	1.96%
11. Mrz15	SG141027_12A	598028	1,94215E-05	9,30161E-06	1,16290E-06	5.99%	3,21063E-03	2,10991E-05	1,49417E-05	0.47%	1,49911E-04	6,69670E-06	3,31163E-06	2.21%
Average			1,99986E-05				3,21894E-03					1,49521E-04		
STD			1,3332E-06				1,29914E-05					3,65118E-06		
RSD			6.67%				0.40%					2.44%		

Table 44: <sup>234</sup>U, <sup>235</sup>U and <sup>236</sup>U abundances on 8 micrometer sized uranium particles originating from SG104521\_02.

SG104521_02														
Date	Sequence	Part. ID	234	234 (fs)	Final unc.	Rel. final unc.	235	235 (fs)	Final unc.	Rel. final unc.	236	236 (fs)	Final unc.	Rel. final unc.
12. Mrz15	SG140521_02	590002	1,81462E-05	2,29716E-06	1,72480E-06	9.50%	3,24391E-03	2,53460E-05	2,30439E-05	0.71%	1,48283E-04	3,35236E-05	4,93638E-06	3.33%
12. Mrz15	SG140521_02	590003	3,21313E-05	1,34460E-05	7,00545E-06	21.80%	3,14631E-03	8,83224E-05	6,92667E-05	2.20%	1,33254E-04	4,96912E-05	1,43270E-05	10.75%
12. Mrz15	SG140521_02	598005	2,15395E-05	4,34381E-06	2,40470E-06	11.16%	3,18635E-03	3,93346E-05	2,92249E-05	0.92%	1,45776E-04	9,0743E-06	6,32510E-06	4.34%
12. Mrz15	SG140521_02	598007	1,94370E-05	1,05703E-06	6,17080E-07	3.17%	3,22281E-03	2,24052E-05	7,94733E-06	0.24%	1,46948E-04	4,42784E-06	2,00000E-06	1.36%
12. Mrz15	SG140521_02	598008	1,94584E-05	6,54618E-06	6,09518E-07	3.13%	3,22178E-03	2,91801E-05	7,83694E-06	0.24%	1,50896E-04	4,27410E-06	2,00000E-06	1.33%
12. Mrz15	SG140521_02	598009	1,96550E-05	6,27795E-07	6,64366E-07	2.99%	3,2316E-03	2,51700E-05	7,55000E-06	0.23%	1,50427E-04	7,44939E-06	2,00000E-06	1.33%
12. Mrz15	SG140521_02	598014	1,97419E-05	1,23233E-06	5,89469E-07	2.87%	3,24346E-03	2,76024E-05	7,25000E-06	0.23%	1,49284E-04	8,55766E-06	2,00000E-06	1.34%
Average			2,10360E-05		1,95105E-06	6.83%	3,20038E-03	2,68235E-05	1,77093E-05	0.55%	1,45175E-04	1,03891E-05	3,78500E-06	2.61%
STD			2,13932E-05				3,21321E-03					1,46256E-04		
STD			4,4612E-06				3,38059E-05					5,64577E-06		
RSD			20.85%				1.05%					3.86%		



### 7.6.3 Certificate: NBS U010



# National Bureau of Standards

## Certificate

### Standard Reference Material U-010

#### Uranium Isotopic Standard (Nominally 1% Enriched)

	<sup>234</sup> U	<sup>235</sup> U	<sup>236</sup> U	<sup>238</sup> U
Atom Percent	0.00541	1.0037	0.00681	98.984
	±0.00005	±0.0010	±0.00007	±0.001
Weight Percent	0.00532	0.9911	0.00675	98.997

This Standard Reference Material (SRM) is certified for use as an isotopic standard. The primary intended use is for the evaluation of mass discrimination effects encountered in the operation of a mass spectrometer.

The material is a highly purified uranium oxide, U<sub>3</sub>O<sub>8</sub>. The atomic weight of the material is calculated to be 238.020, using the nuclidic masses 234.0409; 235.0439; 236.0457; and 238.0508.

The values for <sup>234</sup>U and <sup>236</sup>U were calculated from measurements at the National Bureau of Standards. The samples were spiked with high-purity <sup>233</sup>U to approximate the <sup>234</sup>U concentration, the ratios <sup>233</sup>U to <sup>234</sup>U and <sup>233</sup>U to <sup>236</sup>U were measured on a triple-filament equipped surface ionization mass spectrometer with ion-multiplier amplifier circuits.

The values for <sup>235</sup>U and <sup>238</sup>U were calculated from measurements of the <sup>235</sup>U to <sup>238</sup>U ratio made at the National Bureau of Standards on a triple-filament, surface ionization mass spectrometer equipped with d-c amplifier circuits. The observed ratios were corrected for mass discrimination effects by intercomparison with synthetic mixtures prepared at the 1 percent <sup>235</sup>U level from high-purity <sup>235</sup>U and <sup>238</sup>U.

The indicated uncertainties for the isotopic concentrations are at the 95-percent confidence limits for a single determination, and include allowances for inhomogeneities in the material as well as analytical error. The <sup>235</sup>U to <sup>238</sup>U ratio for this standard, 0.010140, is known to at least 0.1 percent.

Measurements leading to the certification of this SRM were made by E. L. Garner and L. A. Machlan.

The overall direction and coordination of the technical measurements leading to certification were performed under the chairmanship of W. R. Shields.

The technical and support aspects in the preparation, certification, and issuance of this Standard Reference Material were coordinated through the Office of Standard Reference Materials by J. L. Hague.

NOTE: In many industries traceability of their quality control process to the national measurement system is carried out through the mechanisms of SRM's. It may be therefore of interest to know the details of the measurements made at NBS in arriving at the certified values of this SRM. An NBS Special Publication, 260-27, is reserved for this purpose and is available from the NBS Office of Standard Reference Materials upon request.

Washington, D.C. 20234  
April 6, 1981  
(Editorial revision of  
Certificate dated 7-30-70)

George A. Uriano, Chief  
Office of Standard Reference Materials

Figure 125: Certificate for NBS-U010.

7.6.4 Certificate: IRMM 9073



**IRMM**

Institute for Reference Materials and Measurements

**CERTIFICATE OF ISOTOPIC COMPOSITION**

B-2440 Geel, 1997-05-30

1. Applicant: Dr. Stein Deron  
IAEA-Seibersdorf  
P.O.Box 100, Wagramerstrasse 5  
A-1400 Vienna

2. Sample Identification: 9073-01-B

3. Isotopic composition:

	isotope amount ratio(s)
$n(^{234}\text{U})/n(^{238}\text{U})$	0.000 058 92(82)
$n(^{235}\text{U})/n(^{238}\text{U})$	0.007 255 7(3 6)
$n(^{236}\text{U})/n(^{238}\text{U})$	< 0.000 000 02

amount fraction (x 100)		mass fraction (x 100)	
$n(^{234}\text{U})/n(\text{U})$	0.005 849(82)	$m(^{234}\text{U})/m(\text{U})$	0.005 751(80)
$n(^{235}\text{U})/n(\text{U})$	0.720 30(36)	$m(^{235}\text{U})/m(\text{U})$	0.711 27(36)
$n(^{236}\text{U})/n(\text{U})$	< 0.000 002	$m(^{236}\text{U})/m(\text{U})$	< 0.000 002
$n(^{238}\text{U})/n(\text{U})$	99.273 85(36)	$m(^{238}\text{U})/m(\text{U})$	99.282 98(36)

molar mass: 238.028 891(12) g·mol<sup>-1</sup>

4. Reference number: SMS 7275

5. Remarks:

This sample will be stored for a minimum period of six months from the date of this certificate.

Request received at laboratory: 1994-12-09  
Sample received: 1994-12-09  
Measurement achieved: 1996-02-09  
Oral communication:

All uncertainties indicated are ISO/BIPM expanded uncertainties  $U = k \cdot u_c$  where  $u_c$  is the combined standard uncertainty. They are given in parentheses and include a coverage factor  $k=2$ . They apply to the last two digits of the value. The values certified are traceable to the SI.

Mass spectrometric measurements were performed by W. De Bolle [ $n(^{235}\text{U})/n(^{238}\text{U})$  amount ratio by UF<sub>6</sub>] and R. Ovaskainen by TIMS on sample(s) chemically prepared by R. Ovaskainen.

c. W. De Bolle, R. Wellum  
P. De Bièvre, K. Mayer

*R.W.*

*Allo*

*Raisa Ovaskainen*  
Raisa Ovaskainen  
Stable Isotope Measurements

B-2440 GEEL (Belgium)  
Tel. +32-14-571 211 - Fax + 32-14-591 978

European Commission - JRC

Figure 126: Certificate for IRMM-9073.

### 7.6.5 TE-Spectra of SG141027\_12A, ITU and IRMM-9073

#### Total Evaporation - SG141027\_12A

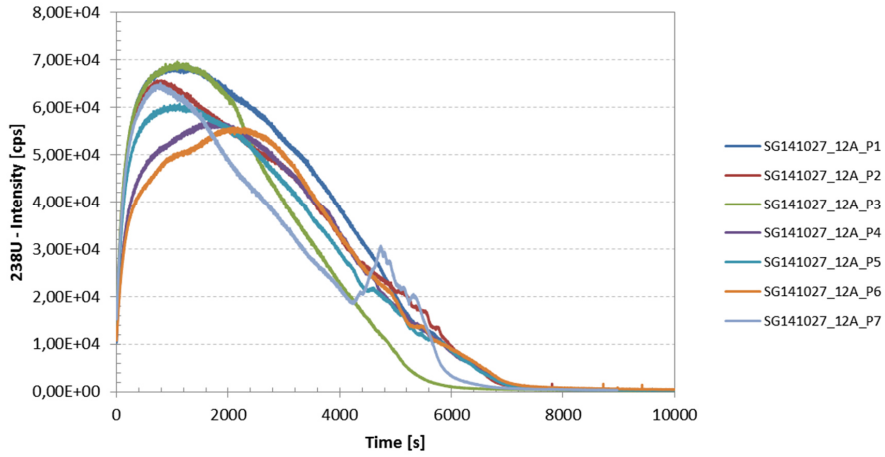


Figure 127: TE-profile of SG141027\_12A.

#### Total Evaporation - ITU (20079-03-01)

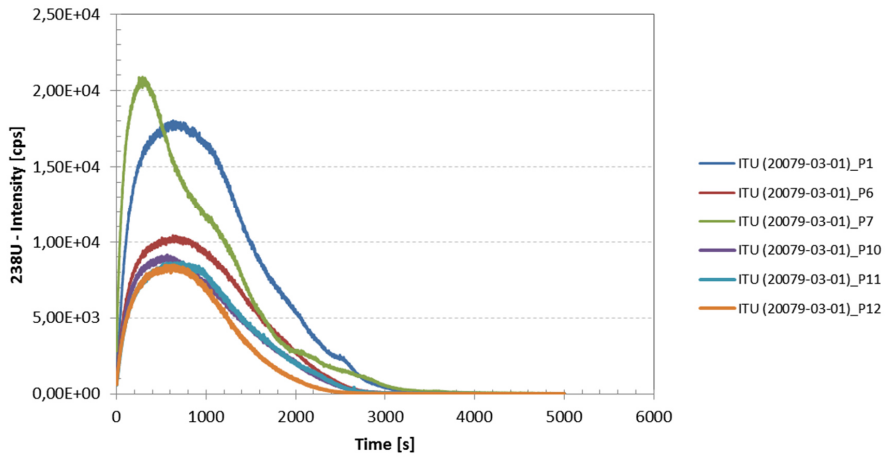


Figure 128: TE-profile of ITU monodisperse – Mean DIA: 0.6µm.

### Total Evaporation, IRMM-9073

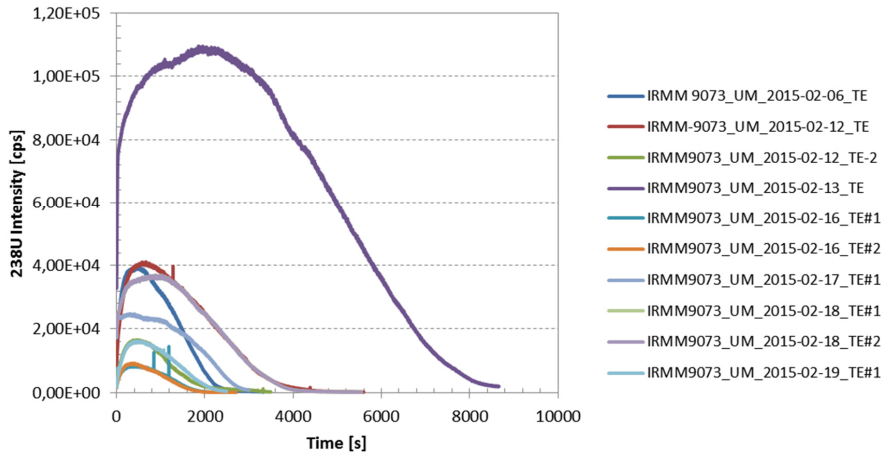


Figure 129: TE-profile of IRMM-9073, polydisperse distribution.

## 7.6.6 Total Evaporation

Table 4-5: Table 1:  $^{238}\text{U}$  intensities for  $^{238}\text{U}$  of SG141027; ITU-monodisperse (20079 Series) and IRMM-9073.

Series	Sample-ID											
	Particle 1	Particle 2	Particle 3	Particle 4	Particle 5	Particle 6	Particle 7	Particle 8	Particle 9	Particle 10	Particle 11	Particle 12
<b>SG141027_12A</b>	Total $^{238}\text{U}$ , [cts]	2.79419E+08	2.57624E+08	2.27876E+08	2.36358E+08	2.38250E+08	2.34269E+08	2.23379E+08				
	Mean $^{238}\text{U}$ , [cts]	2.42455E+08										
	U(Mean $^{238}\text{U}$ ), [cts]	1.81056E+07										
<b>ITU</b>	Particle 2	Particle 6	Particle 7	Particle 9	Particle 10	Particle 11	Particle 12					
	Total $^{238}\text{U}$ , [cts]	2.82477E+07	1.57940E+07	2.46346E+07	1.31982E+07	1.27397E+07	1.26307E+07	1.07363E+07				
	Mean $^{238}\text{U}$ , [cts]	1.68545E+07										
U(Mean $^{238}\text{U}$ ), [cts]	6.29095E+06											
<b>IRMM-9073</b>	Particle 1	Particle 2	Particle 3	Particle 4	Particle 5	Particle 6	Particle 7	Particle 8	Particle 9	Particle 10		
	Total $^{238}\text{U}$ , [cts]	5.62641E+07	9.2029E+07	2.14620E+07	5.53641E+08	9.98340E+06	9.81078E+06	4.70122E+07	8.70805E+07	6.42712E+08	2.20100E+07	
	Mean $^{238}\text{U}$ , [cts]	1.54018E+08										
U(Mean $^{238}\text{U}$ ), [cts]	2.24637E+08											

## 8. Eidesstattlich Erklärung

Hiermit versichere ich eidesstattlich, dass ich die Dissertation selbständig verfasst habe und alle Referenzen und Hilfen in der Dissertation korrekt angegeben habe.



---

Köln, 08.05.2016

## 9. Disclaimer

This dissertation which is titled "*Production and Characterization of Monodisperse Uranium Particles for Nuclear Safeguards Applications*" does not include any proprietary or classified information obtained as part of the experimental work pursued in the Office of Safeguards Analytical Services Laboratory. It was granted permission by the IAEA to be published. The results and interpretations published in this work are not be regarded as representing the views of or endorsement by the IAEA.

# I. Table of Figures

Figure 1:	Schematics of the core unit of the vibrating orifice aerosol generator. ....	10
Figure 2:	Diagram of liquid jet break up cycle induced by piezo electric disturbance. ....	11
Figure 3:	Schematic of spray pyrolysis: evolution of droplet-to-particle conversion in a heated flow reactor. ....	13
Figure 4:	Precipitation schematics for homogenous and surface controlled precipitation.....	15
Figure 5:	Schematics of droplet-to-particle morphology evolution during thermolysis, see Messing et al. (1993) [58] and Reuge et al. (2008) [66] [67].....	16
Figure 6:	UNH dehydration and decomposition by Dash et al. (1999) [76]. ....	18
Figure 7:	Left: Phase diagram of the O-U system. Right: U-O phase diagram in O/U ratio range 2.0-3.0 in dependence of the pressure, see Morss et al. (2011) [92]. ....	19
Figure 8:	JKR model depicting particle deformation in contact area. ....	23
Figure 9:	DMT-model depicting adhesion forces with the affected zones and contact area (marked grey). ....	24
Figure 10:	Contact relations for the Hertz-, DMT- and JKR-models. ....	25
Figure 11:	Particle with radius "r" adherent on surface with a contact area "a". Several forces act on the particle including: gravitational force " $F_G$ ", adhesion force " $F_A$ ", external tangential to surface " $F_T$ " and external force normal to surface " $F_N$ ". ....	26
Figure 12:	Left: Jet trajectories for an inertial impactor (see Marple et al. (1976) [107]), Right: Schematics of inertial impactor used at SGAS-ESL.....	27
Figure 13:	Determination of the cut-off diameter by plotting the collection efficiency curve. ....	28
Figure 14:	Layout of a Scanning Electron Microscope. ....	30
Figure 15:	Schematics of Cameca's IMF1280 LG-SIMS, courtesy of CAMECA.....	31
Figure 16:	Image of the particle production setup at IEK-6 at Forschungszentrum Jülich GmbH, as of December 2014. ....	42
Figure 17:	No (1): First setup with neodymium precursor particles (wet); No(2): First fully operational setup to produce dry neodymium oxide particles; No(3) Uranium oxide particles from SG140521_02; No(4) latest evolution step of the setup as from December 2014. ....	43
Figure 18:	SE-image of a corroded high grade steel orifice used to produce uranium particles. ....	44
Figure 19:	Particle analysis and re-location scheme, see Admon et al. (2009). ....	47
Figure 20:	Top: SURUGA-Particle manipulation system at SAL and bottom: SE-images depicting the transfer of single micrometer sized particles, recorded with Jeol JSM 6610.....	48
Figure 21:	Left: Vector diagram representing the triangulation method. A, B, C are reference marks, P is the particle of interest, O the source instrument and O' the target instrument. (See Admon, et al. 2005 [9]); Right: Reference marks: (left hand side) either by scratching with a tungsten needle or (right hand side) by LMD. ....	49
Figure 22:	Left: Model (1) simple $U_3O_8$ sphere with variable shell thickness. Right: Model (2) modified $U_3O_8$ sphere with variable outer shell thickness and constant inner cavity. ....	51
Figure 23:	Basic scheme of a confocal microscope and Layout of a confocal Raman Spectrometer. ....	54
Figure 24:	Target surface after vacuum impaction, with visible score marks.....	57
Figure 25:	Histogram depicting the number of particles per size-iteration for each batch from 4 - 35 l/min.....	58
Figure 26:	Radial profile distribution over 360° for all six air flows: 6-35 l/min.....	58
Figure 27:	Normalized collection efficiency curves for each air flow: 4-35 l/min. ....	59
Figure 28:	Comparison of theoretical and measured cut-off diameters for the one-stage inertial impactors used at IAEA and FZJ.....	60
Figure 29:	Left: Photo of modified inertial impactor designed at SGAS-ESL; Right: Scheme of MII. ....	60
Figure 30:	Normalized collection efficiency curves of Stage 1 and 2.....	61

Figure 31:	Radial profile distribution over 360° for Stage 1 and 2 – Intensities are normalized and not equivalent. ....	61
Figure 32:	Sequence of sample preparation for $\mu$ -Raman measurements.....	62
Figure 33:	Left: Schematics of Cyclone Sampler with Venturi Nozzle Inlet and right: Image of the Cyclone Sampler with Venturi Nozzle. ....	63
Figure 34:	Collection efficiency of the cyclone sampler at various air flows. ....	63
Figure 35:	Particle analysis on SG140521_02, depicting the particle distribution on a 1" glassy carbon disk.....	66
Figure 36:	Particle size distribution for SG140521_02.....	66
Figure 37:	Aspect Ratio deviations due to particle deformations, agglomerations, artefacts and measurement errors. ....	67
Figure 38:	Particle size distribution for SG141027_12A.....	68
Figure 39:	Three SE-images of particles originating from SG141027_12A, courtesy of O. Marie from CEA/DAM. ....	68
Figure 40:	Circularity calculation of SG141027_12A.....	69
Figure 41:	Size distribution of SG150312_05 (blue), SG150401_14A (red) and SG150413_03A (green). ....	69
Figure 42:	Circularity of SG150312_05 (blue), SG150401_14A (red) and SG150413_03A (green). ....	70
Figure 43:	Above: Inflated, hollow uranium particle at $0.5 \leq \text{AcV} \leq 5 \text{ keV}$ (Dia. $> 4 \mu\text{m}$ ) and Bottom: solid particle at $5.0 \leq \text{AcV} \leq 25 \text{ keV}$ (Dia. $> 1.35 \mu\text{m}$ ); both originate from SG140521_02.....	71
Figure 44:	Left: Inflated particle $>6.0 \mu\text{m}$ diameter and Right: typical fragments and hollow particles on SG140521_02 (Dia. $> 4.8 \mu\text{m}$ ).....	72
Figure 45:	Particles of Interest, (1) – (4), before and after destruction. Images recorded at different rotational- and inclination angles. ....	73
Figure 46:	Simulated SE-Images of 3D spheres, depicted in XZ-plane.....	74
Figure 47:	Processed 3D-surface plots of the simulated images depicted in the previous Figure.....	74
Figure 48:	Normalized integrated radial intensity distribution [arbitrary units].....	75
Figure 49:	3-D reconstruction of particle (A).....	76
Figure 50:	Mass spectra of SG141027_12A – Particle 1.....	77
Figure 51:	Intensity evolution over 100 frames of m/Q(16), m/Q(28), m/Q(238) and m/Q(239) – Particle 1.....	78
Figure 52:	Mass spectrum of m/Q(238) and m/Q(239) and the corresponding TOF signals in top- and front projection – Particle 1.....	79
Figure 53:	Depth profiling of m/Q(16), m/Q(28), m/Q(238) and m/Q(239) of Particle 1. ....	79
Figure 54:	SE-image sequences at different ablation-depths of 4 selected particles (Particle 2, 3, 12 and 18) originating from SG141027_12A.....	80
Figure 55:	Left: Ternary diagram depicting the significant variation of the C(K), O(K) and U(M)-ratio of 176 polydisperse particles from SG140521_02 particle distribution. Right: Histogram depicting the mean wt% measured for 176 polydisperse particles originating from SG140521_02.....	82
Figure 56:	w-% of C(K), O(K) and U(M) on four selected particles from SG140521_02 on C-substrate. ....	83
Figure 57:	Comparison of EDX values of C(K), O(K) and U(M) in wt% from SG141027_12A and SG150401_14A – on C-substrates. ....	83
Figure 58:	Comparison of EDX values of C(K), O(K) and U(M) in wt% from SG150312_05A, SG150413_03A and SG150429A– all particles are deposited on Si wafer substrates.....	85
Figure 59:	Overview of the particle evolution since May 2014 to April 2015.....	85
Figure 60:	Micro Raman spectra of $\text{U}_3\text{O}_8$ acquired at CEA and TUW.....	89
Figure 61:	Micro Raman spectra of $\text{UO}_2$ acquired at CEA and TUW.....	90
Figure 62:	Peak transition due to laser induced $\text{UO}_2$ oxidation; to $\text{U}_3\text{O}_8$ . ....	90
Figure 63:	Micro Raman spectra of UNH of Stage (1) and (2) acquired at CEA and TUW. ....	91

Figure 64:	Micro Raman spectra of ADU acquired at TUW.....	92
Figure 65:	Micro Raman spectra of UO <sub>2</sub> F <sub>2</sub> acquired at CEA.....	92
Figure 66:	Raman spectrum of polydisperse SG140521_02.....	93
Figure 67:	Raman spectrum of selected particles from SG141027_12A, measured at CEA.....	94
Figure 68:	Raman spectrum of selected particles from SG150401_14A, measured at TUW.....	95
Figure 69:	Particle Evolution: Direct comparison of SG140521_02 vs. SG141027_12A and SG150401_14A.....	96
Figure 70:	CAMECA 1280 LG-SIMS at SGAS-ESL.....	98
Figure 71:	n( <sup>234</sup> U)/n( <sup>238</sup> U) intensities of SG141027_12A.....	99
Figure 72:	n( <sup>234</sup> U)/n( <sup>238</sup> U) intensities of SG140521_02.....	100
Figure 73:	n( <sup>235</sup> U)/n( <sup>238</sup> U) intensities of SG141027_12A.....	100
Figure 74:	n( <sup>235</sup> U)/n( <sup>238</sup> U) intensities of SG140521_02.....	101
Figure 75:	n( <sup>236</sup> U)/n( <sup>238</sup> U) intensities of SG141027_12A.....	101
Figure 76:	n( <sup>236</sup> U)/n( <sup>238</sup> U) intensities of SG140521_02.....	102
Figure 77:	Combined <sup>238</sup> U intensities of NBS U010 series (green) and IRMM 9073 series (grey).....	104
Figure 78:	<sup>238</sup> U intensity plot of SG140521_02.....	105
Figure 79:	<sup>238</sup> U intensity plot of SG141027_12A.....	106
Figure 80:	Hydride formation rate for SG140521_02.....	107
Figure 81:	Hydride formation rate for SG141027_12A.....	107
Figure 82:	Hydride Formation Rate UH/H of SG140521_02 at IP = 50pA and 50 μm Raster in comparison to at IP = 20pA and 20 μm Raster.....	108
Figure 83:	TE of IRMM-9073, ITU monodisperse (0.6 μm) and SG141027_12A.....	110
Figure 84:	Linear combination of the integrated <sup>238</sup> U intensity [ct] on axis one and its correlated, normalized Useful Yield [%] with mean values and uncertainties with k=2.....	112
Figure 85:	Comparison of focused and de-focused ion beam on the <sup>238</sup> U intensity profile.....	113
Figure 86:	Redisposition pattern of partially consumed particle (left) and total consumed particles, Image on the left were taken at CEA-DAM Ile-de-France, courtesy of O. Marie (CEA).....	114
Figure 87:	Redisposition profile of SG141027_12A in comparison to ITU (20079).....	115
Figure 88:	Size distribution of SG150312_05A.....	i
Figure 89:	Size distribution of SG150401_14A.....	i
Figure 90:	Size distribution of SG150413_03A.....	ii
Figure 91:	Size distribution of SG150429_02A.....	ii
Figure 92:	Circularity of SG150312_05A.....	iii
Figure 93:	Circularity of SG150401_14A.....	iii
Figure 94:	Circularity of SG150413_03A.....	iii
Figure 95:	Circularity of SG150429_02A.....	iv
Figure 96:	TOF Spectrum of selected particles originating from SG141027_12A.....	v
Figure 97:	Depth profiles acquired from FIB-TOF-SIMS measurements – all intensities of m/Q(238) are normalized and plotted against the particle depth – all particles taken from SG141027_12A.....	vi
Figure 98:	FIB ablation sequence of a micrometer sized uranium particle –Particle 1.....	vii
Figure 99:	FIB-sequence of Particle 4 of SG150401_1A.....	viii
Figure 100:	FIB-sequence of Particle 5 of SG150401_1A.....	ix
Figure 101:	FIB-sequence of Particle 9 of SG150401_1A.....	x
Figure 102:	BSE-image and corresponding EDX spectrum of exemplary hollow particle on SG140521_02.....	xi
Figure 103:	BSE-image and corresponding EDX spectrum of hollow particle after destruction.....	xi
Figure 104:	BSE-image and corresponding EDX spectrum of exemplary deformed particle on SG140521_02.....	xi
Figure 105:	BSE-image and corresponding EDX spectrum of exemplary debris on SG140521_02.....	xi

Figure 106:	BSE-image and corresponding EDX spectrum of exemplary solid particle on SG140521_02. .....	xii
Figure 107:	BSE image and corresponding EDX spectrum of exemplary solid particle SG141027_12A.	xii
Figure 108:	BSE image and corresponding EDX spectrum of exemplary solid particle SG150312_05A.	xii
Figure 109:	BSE image and corresponding EDX spectrum of exemplary solid particle SG150401_14A.	xiii
Figure 110:	BSE image and corresponding EDX spectrum of exemplary solid particle SG150413_03A.	xiii
Figure 111:	BSE image and corresponding EDX spectrum of exemplary solid particle SG150429_02A.	xiii
Figure 112:	UNH spectrum on bulk material of Stage 1 – Spectra recorded at CEA-Ile-de-France.....	xiv
Figure 113:	UNH spectrum on bulk material of Stage 2 – Spectra recorded at CEA-Ile-de-France.....	xv
Figure 114:	Micro Raman Spectra of selected U <sub>3</sub> O <sub>8</sub> samples originating from CEA and TUW. Spectra acquired at TUW have a wider acquisition range – 100-3200cm <sup>-1</sup> .....	xvi
Figure 115:	Micro Raman Spectra of selected UO <sub>2</sub> samples originating from CEA and TUW. Spectra acquired at TUW have a wider acquisition range – 100-3200cm <sup>-1</sup> .....	xvi
Figure 116:	Micro Raman Spectra of selected UNH samples originating from CEA and TUW. Spectra acquired at TUW have a wider acquisition range – 100-3200cm <sup>-1</sup> .....	xvii
Figure 117:	Micro Raman Spectra of selected ADU samples originating from CEA and TUW. Spectra acquired at TUW have a wider acquisition range – 100-3200cm <sup>-1</sup> .....	xvii
Figure 118:	Observed double and at 867cm <sup>-1</sup> for UO <sub>2</sub> F <sub>2</sub> , in accordance with Stefaniak et al. (2013)..	xviii
Figure 119:	Raman Spectra of SG140521_02 acquired at CEA. ....	xviii
Figure 120:	Raman spectra of 15 particles originating from SG141027_12A.....	xix
Figure 121:	Raman Spectra acquired at CEA and TUW in direct comparison.....	xix
Figure 122:	Collected Raman spectra of SG150401_14A.....	xx
Figure 123:	Micro Raman Spectra of selected uranium compounds in direct comparison to particle produced at Forschungszentrum Jülich GmbH: SG140521_02, SG141027_12A, SG140501_14A.....	xxi
Figure 124:	Comparison of 238U intensities of SG140521_02 (red), SG141027_12A (blue), NBS-U010 (solid grey lines) and IRMM-9073 (dotted grey lines).....	xxiii
Figure 125:	Certificate for NBS-U010.....	xxiv
Figure 126:	Certificate for IRMM-9073. ....	xxv
Figure 127:	TE-profile of SG141027_12A.....	xxvi
Figure 128:	TE-profile of ITU monodisperse – Mean DIA: 0.6µm.....	xxvi
Figure 129:	TE-profile of IRMM-9073, polydisperse distribution.....	xxvii

*“The truth is, most of us discover where we are heading when we arrive.”*

Calvin and Hobbes

## II. References

- [1] INFCIRC-153; The structure and content of agreements between the agency and states required in connection with the treaty on the non-proliferation of nuclear weapons; International Atomic Energy Agency; **1972**.
- [2] INFCIRC-140; Treaty on the non-proliferation of nuclear weapons; International Atomic Energy Agency; **1970**.
- [3] INFCIRC-540; Model Protocol Additional to the Agreement(s) between State(s) and the International Atomic Energy Agency for the Application of Safeguards INFCIRC-540 corrected; International Atomic Energy Agency; **1997**.
- [4] Betti, M.; Tamborini, G. and Koch, L.; Use of Secondary Ion Mass Spectrometry in Nuclear Forensic Analysis for the Characterization of Plutonium and Highly Enriched Uranium Particles; *Anal. Chem.*; **71**; **1999**; p. 2616-2622.
- [5] Pajo, L.; Mayer, K.; Koch, L.; Investigation of the oxygen isotopic composition in oxidic uranium compounds as a new property in nuclear forensic science; *Fresen. J. Anal. Chem.*; **371**; **2001**; p. 348-352.
- [6] Erdmann, N.; Betti, M.; Kollmer, F.; Benninghoven, A.; Gruening, C.; Philipsen, V.; Lievens, P.; Silverans, R. E.; Vandeweert, E.; Resonance and Nonresonant Laser Ionization of Sputtered Uranium Atoms from Thin Films and Single Microparticles: Evaluation of a Combined System for Particle Trace Analysis; *Anal. Chem.*; **75**; **2003**; p. 3175-3181.
- [7] Baude, S.; Chiappini, R.; Isotopic Measurements on Micrometric Particles: The French Experience to Detect Fissile Material; IAEA Publication, **2005**.
- [8] Pointurier, F.; Pottin, A.-C.; Hubert, A.; Application of Nanosecond-UV Laser Ablation-Inductively Coupled Plasma Mass Spectrometry for the Isotopic Analysis of Single Submicrometer-Size Uranium Particles; *Anal. Chem.*; **83**; **2011**; p. 7841-7848.
- [9] Donohue, D. L.; Key tools for nuclear inspections. Advances in environmental sampling strengthen safeguards; *IAEA Bulletin*; **44**; **2002**, p. 17-23.
- [10] Donohue, D.; Ciurapinski, A.; III, J. C.; Ruedenauer, F.; Kuno, T., Poths, J.; Microscopic studies of spherical particles for nuclear safeguards; *Appl. Surf. Sci.*; **255**, **2008**; p. 2561-2568.
- [11] Pidduck, A. J.; Donohue, D. L.; Houlton, M.R.; Williams, G. M.; Micro-Analytical Characterization of Uranium Particles in Support of Environmental Sampling for Safeguards; 47th Annual Meeting INMM; **2006**; p. 1-8.
- [12] Shinonaga, T.; Esaka, F.; Magara, M.; Klose, D.; Donohue, D.; Isotopic analysis of single uranium and plutonium particles by chemical treatment and mass spectrometry; *Spectrochim. Acta B63*; **2008**; p. 1324-1328.
- [13] Kappel, S.; Uranium and Plutonium Isotopic Fingerprinting of Single Particles by Laser Ablation Multi Collector Inductively Coupled Plasma Mass Spectrometry; Universität für Bodenkultur Wien; **2012**.
- [14] Kappel, S.; Boulyga, S.; Dorta, L.; Guenther, D.; Hattendorf, B.; Koffler, D.; Laaha, G.; Leisch, F.; Prohaska, T.; Evaluation strategies for isotope ratio measurements of single particles by LA-MC-ICPMS; *Anal. Bioanal. Chem.*; **405**; **2013**; p. 2943-2955.
- [15] Stetzer, B. O.; Spaltspuranalyse von Uranoxidpartikeln; Johannes Gutenberg-Universität; Mainz; **2001**.
- [16] Kips, R.; Development of uranium reference particles for nuclear safeguards and non-proliferation control; University of Antwerp and EC-JRC-IRMM; **2007**.
- [17] Ihantola, S.; Surface sampling methods for non-destructive radionuclide analysis; Helsinki University of Technology; Faculty of Information and Natural Sciences; **2009**.
- [18] Ranebo, Y.; Hedberg, P. M. L.; Whitehouse, M. J.; Ingeneri, K.; Littmann, S.; Improved isotopic SIMS measurements of uranium particles for nuclear safeguard purposes; *J. Anal. At. Spectrom.*; **24**; **2009**; p. 277-287.
- [19] Ranebo, Y.; Physical Characterization of Actinide Particles - A Study on Novel Techniques for Radiological and Nuclear Safeguard Investigations, Department of Medical Radiation Physics, Clinical Sciences, Lund University, Sweden, **2009**.

- [20] Warneke, T.; High-precision isotope ratio measurements of uranium and plutonium in the environment; Faculty of Science; School of Ocean and Earth Science, Southampton Oceanography Center; **2012**.
- [21] Mácsik, Z.; Analysis of Actinides in Safeguards Swipe Samples by radiometric and mass spectrometric methods; Eoetvoes Loránd University of Sciences; Budapest Chemistry PhD School; **2013**.
- [22] Yetunde, A.; Jan, T.; Ruth, K.; Stephan, R.; Stefaniak, E.; Heinz, K.; Kraiem, M.; NUSIMEP-6: Uranium isotope amount ratios in uranium particles; JRC-IRMM; **2008**; p. 1-66.
- [23] Truyens, J.; Stefaniak, E.; Mialle, S.; Aregbe, Y.; NUSIMEP-7: Uranium isotope amount ratios in uranium particles; J. Env. Rad.; 125; **2013**; p. 50-55.
- [24] Raptis, K.; Ingelbrecht, C.; Wellum, R.; Alonso, A.; Bolle, W. D.; Perrin, R.; The preparation of uranium-doped glass reference materials for environmental measurements; Nucl. Instrum. Meth. A; 480; **2002**; p. 40-43.
- [25] Kappel, S.; Boulyga, S. F. and Prohaska, T.; Direct uranium isotope ratio analysis of single micrometer-sized glass particles; J. Environ. Radioactiv. 113; **2012**; p. 8-15.
- [26] Lux, C.J.; Evaluation of techniques for controlling UF<sub>6</sub> release clouds in the GAT environmental chamber; GAT-T-3116; Goodyear Atomic Corporation; Piketon Ohio ; **1982**.
- [27] Carter, J.A.; Hembree, D.M.; Formation and characterization of UO<sub>2</sub>F<sub>2</sub> particles as a result of UF<sub>6</sub> hydrolysis; Task A.200.3; K/NSP-777; Oak Ridge Gaseous Diffusion Plant; **1998**.
- [28] Kemp, R.S.; Technical note on the detectability of UO<sub>2</sub>F<sub>2</sub> aerosols produced by UF<sub>6</sub> released from clandestine uranium conversion plants; Princeton University; **2006**.
- [29] Kips, R.; Leenaers, A.; Gabriele, T.; Betti, M.; Van den Berghe, S.; Wellum, R.; Taylor, P.; Characterization of Uranium Particles Produced by Hydrolysis of UF<sub>6</sub> Using SEM and SIMS; Microsc. Microanal.; 13; **2007**; p. 156-164.
- [30] Kips, R.; Kristo, M.J.; Hutcheon, I.D.; Wang, Z.; Johnson, T.J.; Gerlach, D.C.; Amonette, J.E.; Olsen, K.B.; Stefaniak, E.; Measuring fluorine in uranium oxyfluoride particles using secondary ion mass spectrometry for nuclear forensics; Proc. Radiochim. Acta; 1; 7-11; **2011**; p. 7-11.
- [31] Kips, R.; Pidduck, A.; Houlton, M.; Leenaers, A.; Mace, J.; Marie, O.; Pointurier, F.; Stefaniak, E.; Taylor, P.; den Berghe, S. V.; Espen, P. V.; Grieken, R. V., Wellum, R.; Determination of fluorine in uranium oxyfluoride particles as an indicator of particle age; Spectrochim. Acta B64; **2009**; p. 199 – 207.
- [32] Kaerkelae, T.; Tapper, U.; Ziliacus, R.; Testing of the Experimental Facility for Uranium Particle Production; Research Report; VTT-R-07821-06; **2006**; p. 1-7.
- [33] Kaerkelae, T.; Tapper, U.; Ziliacus, R.; Improving the Experimental Facility for Uranium Particle Production; Research Report; VTT-R-03335-07; **2007**; p.1-12.
- [34] Ziliacus, R.; Hokkinen, J.; Kaerkelae, T.; Tapper, U.; Production of U- and U/Ce-particles; Research Report; VTT-R-10766-08; **2008**; p.1-8.
- [35] Hokkinen, J.; Taper, U.; Ziliacus, R.; Production of Plutonium Particles; VTT-R-100066-10; **2010**; p. 1-12.
- [36] Tushingam, J. W. A.; The preparation of a low-enriched uranium particle standard for environmental analysis; SRDP-R259; AEAT-3300; AEA Technology; **1998**.
- [37] Tushingam, J. W. A.; The Preparation of Low-Enriched Uranium Particle Standard for Environmental Analysis; SRDP-R275; AEAT/R/NS/0082; **1998**.
- [38] Tushingam, J. W. A.; Taylor, R.; The Preparation of a High-Enriched Uranium Particle Standard for Environmental Analysis; SRDP-R264; AEAT-5418; **2000**.
- [39] Tushingam, J. W. A.; The Preparation and Characterizations of Four Uranium Particle Standard for Application in Environmental Safeguards; SRDP-R275; AEAT/R/NS/0082; **2000**.
- [40] Erdmann, N.; Betti, M.; Stetzer, O.; Tamborini, G.; Kratz, J.; Trautmann, N.; Van Geel, J.; Production of monodisperse uranium oxide particles and their characterization by scanning electron microscopy and secondary ion mass spectrometry, Spectrochim. Acta B55; **2000**; p. 1565-1575.
- [41] Stetzer, O.; Betti, M.; van Geel, J.; Erdmann, N.; Kratz, J.-V.; Schenkel, R.; Trautmann, N.; Determination of the <sup>235</sup>U content in uranium oxide particles by fission track analysis; Nucl. Instrum. Meth. A; 525; **2004**; p.582-592.
- [42] Ranebo, Y.; Eriksson, M.; Tamborini, G.; Niagolova, N.; Bildstein, O.; Betti, M.; The Use of SIMS and SEM for the Characterization of Individual Particles with a Matrix Originating from a Nuclear Weapon; Microsc. Microanal.; 13; **2007**; p. 179-190.

- [43] Ranebo, Y.; Microparticles for environmental safeguards; Institute for Transuranium Elements; JRC-ITU-TN-2008/09; **2008**; p. 1-30.
- [44] Ranebo, Y.; Niagolova, N.; Erdmann, N.; Eriksson, M.; Tamborini, G. and Betti, M., Production and Characterization of Monodisperse Plutonium, Uranium, and Mixed Uranium-Plutonium Particles for Nuclear Safeguard Applications; *Anal. Chem.*; **82**; **2010**; p. 4055-4062.
- [45] Kraiem, M.; Richter, S.; Erdmann, N.; Kühn, H.; Hedberg, M.; Aregbe, Y. Characterizing uranium oxide reference particles for isotopic abundances and uranium mass by single particle isotope dilution mass spectrometry; *Anal. Chim. Act.*; **748**; **2012**; p. 37-44.
- [46] Berglund, R. N. and Liu, B. Y. H.; Generation of monodisperse aerosol standards; *Environ. Sci. Technol.*; **7**; **1973**; p. 147-153.
- [47] Patent: Berglund, R. N.; Liu, B. Y. H.; Method and Apparatus for Generating Monodisperse Aerosol; **1974**; p. 1-8.
- [48] Plateau, J.A.F.; *Statique experimentale et théorique des liquids soumis aux seules forces moléculaires*; Gauthier-Villars; 1873.
- [49] Rayleigh, L.; Strutt; J.W.; On the Instability of Jets; *Proc. London Math. Soc.*; **10**; **1878**; p. 4-13.
- [50] Rayleigh, L.; On the Capillary Phenomena of Jets; *Proc. Roy. Soc. (London)*, **29**; **1879**; p. 71-97.
- [51] Schneider, J. M.; Hendricks, C. D.; Source of Uniform-Sized Liquid Droplets; *Rev. Instrum.* **35**; **10**; **1964**; p. 1349-50.
- [52] Lindblad, N. R.; Schneider, J. M.; Production of uniform-sized liquid droplets; *J. Scient. Instr.*; **42**; **1965**; p. 635-638.
- [53] Sefiane, K.; Tadriss, L.; Douglas, M.; Experimental study of evaporating water-ethanol mixture sessile drop: influence of concentration; *Int. J. Heat Mass Transfer.*; **46**; **2003**; p. 4527-4534.
- [54] Tonini, S.; Cossali, G.; An exact solution of the mass transport equations for spheroidal evaporating drops; *Int. J. Heat Mass Transfer*; **60**; **2013**; p. 236-240.
- [55] Kudas, T.T.; Generation of complex metal oxides by aerosol processes: superconducting ceramic particles and films; *Adv. Mat.*; **6**; **1989**; p. 794-806.
- [56] Skillas, G.; Maisels, A.; Pratsinis, S.E.; Kudas, T.T; *Manufacturing of Materials by Aerosol Processes*; John Wiley & Sons Inc.; **2011**, p. 751-770.
- [57] Kingery, W.D.; Bowen, H.K.; Ulmann, D.R.; *Introduction to Ceramics*; Wiley NY; **1975**.
- [58] Messing, G. L.; Zhang, S.-C.; Jayanthi, G. V.; *Ceramic Powder Synthesis by Spray Pyrolysis* *Journal of the Am. Ceram. Soc.*; **76**; **1993**; p. 2707-2726.
- [59] Gurav, A.; Kudas, T.; Pluym, T.; Xiong, Y.; *Aerosol Processing of Materials*; *Aerosol Sci. Technol.*; **19**; **1993**; p. 411-452.
- [60] Xiong, Y.; Kudas, T.T.; Droplet evaporation and solute precipitation during spray pyrolysis; *J. Aerosol Sci.*; **24**; **1993**; p. 893-908.
- [61] La Mer, V. K.; Gruen, R.; A direct test of Kelvin's equation connecting vapor pressure and radius of curvature; *Trans. Faraday Soc.*; **48**; **1952**; p. 410-415.
- [62] Stebelkov, V.; Informativeness of morphology analysis of uranium microparticles from industrial dust at nuclear plants; *Proc. Int. Conf. GLOBAL 2005: Nuclear Energy Systems for Future Generation and Global Sustainability*; Japan; **2005**; p. 1-5.
- [63] Pratsinis, S.E.; Vemury, S.; Particle formation in gases: A review; *Powder Technol.*; **88**; **1996**; p. 267-273.
- [64] Hopkins, R. J.; Reid, J. P.; Evaporation of Ethanol/Water Droplets: Examining the Temporal Evolution of Droplet Size, Composition and Temperature; *J. Phy. Chem. A.*; **109**; **2005**; p. 7923-7931.
- [65] Schluender, E.; Temperatur- und Massenänderung verdunstender Tropfen aus reinen Flüssigkeiten und wässrigen Salzlösungen; *Int. J. Heat and Mass Transfer*; **7**; **1964**; p. 49-73.
- [66] Reuge, N.; Dexpert-Ghys, J.; Verelst, M.; Caussat, B.; Y<sub>2</sub>O<sub>3</sub>: Eu micronic particles synthesised by spray pyrolysis: Global modelling and optimization of the evaporation stage; *Chem. Eng. Process.*; **47**; **2008**; p.731-743.
- [67] Reuge, N.; Caussat, B.; Joffin, N.; Dexpert-Ghys, J.; Verelst, M.; Dexpert, H.; Modeling of spray pyrolysis—why are the synthesized Y<sub>2</sub>O<sub>3</sub> microparticles hollow?; *AIChE J.*; **54**; **2008**; p. 394-405.

- [68] Xiong, Y.; Kudas, T. T.; Droplet evaporation and solute precipitation during spray pyrolysis; *J. Aerosol Sci.*; 24; **1993**; p. 893-908.
- [69] Van der Lijn, J.; Simulation of Heat and Mass Transfer in Spray Drying; *Agric. Research Rep.*, 845; **1976**; p. 845.
- [70] Iwamoto, K.; Thermal Decomposition of Uranyl Nitrate Hexahydrate in the Presence of Graphite; *J. Nucl. Sci. Technol.*; 1; **1964**; p. 113-119.
- [71] Lodding, W.; Ojamaa, L.; Dehydration and thermal decomposition of uranyl nitrates in the presence of steam; *J. Inorg. Nucl. Chem.*; 27; **1965**; p. 1261-1268.
- [72] Smith, W. H.; Thermal dehydration of uranyl nitrate hydrates; *J. Inorg. Nucl. Chem.*; 30; **1968**; p. 1761-1768.
- [73] Rajagopalan, K.; Ravindran, P.; Radhakrishnan, T.; Thermal decomposition of uranyl nitrate hexahydrate; *J. Therm. Anal.*; 44; **1995**; p. 89-96.
- [74] Kozlova, R.D.; Matyukha, V.A.; Dedov, N.V.; Mechanism and Kinetics of Thermal Decomposition of Uranyl Nitrate Hexahydrate under the Nonisothermal Conditions; *Radiochem.*; 49; 2; **2007**; p. 130-134.
- [75] Ondrejcin, R. S.; Garrett, T. P.; The thermal decomposition of anhydrous uranyl nitrate and uranyl nitrate hydrate; *J. Phys. Chem.*; 65; **1961**; p. 470-473.
- [76] Dash, S.; Kamruddin, M.; Bera, S.; Ajikumar, P.; Tyagi, A.; Narasimhan, S.; Raj, B.; Temperature programmed decomposition of uranyl nitrate hexahydrate; *J. Nucl. Mat.*; 264; **1999**; p. 271-282.
- [77] Scott, K.; Harrison, K.; Some studies of the oxidation of uranium dioxide; *J. Nucl. Mater.*; 8; **1963**; p. 307-319.
- [78] Peakall, K.; Antill, J.; Oxidation of uranium dioxide in air at 350–1000° C; *J. Nucl. Mat.*; 2; **1960**; p. 194-195.
- [79] Wheeler, V.; Dell, R.; Wait, E.; Uranium trioxide and the UO<sub>3</sub> hydrates; *J. Inorg. Nucl. Chem.*; 26; **1964**; p. 1829-1845.
- [80] Cordfunke, E.H.P.; Book Review: The Chemistry of Uranium; *In Inorg. Chim. Act.*; 4; 1; **1970**.
- [81] Loopstra, B. O.; The Phase Transition on alpha-U<sub>3</sub>O<sub>8</sub> at 210°C; *J. Appl. Cryst.*; 3; **1970**; p. 94-96.
- [82] Loopstra, B.; The structure of beta-U<sub>3</sub>O<sub>8</sub>; *Acta Cryst.*; B26; **1970**; p. 656-657.
- [83] Labroche, D.; Dugne, O.; Chatillon, C.; Thermodynamic properties of the O–U system. II – Critical assessment of the stability and composition range of the oxides UO<sub>2+x</sub>, U<sub>4</sub>O<sub>9-y</sub> and U<sub>3</sub>O<sub>8-z</sub>; *J. Nucl. Mat.*; 312; **2003**; p. 50-66.
- [84] Felker, L.K.; Vedder, R.J. and Walker, E.A.; Product Conversion: The Link between Separations and Fuel Fabrication; ORNL O1-03; ATALANTE; **2008**.
- [85] Hoekstra, H.; Siegel, S.; The uranium-oxygen system: U<sub>3</sub>O<sub>8</sub>-UO<sub>3</sub>; *J. Inorg. Nucl. Chem.*; 18; **1961**; p. 154-165.
- [86] Grønvold, F.; High-temperature X-ray study of uranium oxides in the UO<sub>2</sub>-U<sub>3</sub>O<sub>8</sub> region; *J. Inorg. Nucl. Chem.*; 1; **1955**; p. 357-370.
- [87] Kulyako, Y.; Perevalov, S.; Trofimov, T.; Malikov, D.; Samsonov, M.; Vinokurov, S.; Myasoedov, B.; Shadrin, A.; Preparation of uranium oxides in nitric acid solutions by the reaction of uranyl nitrate with hydrazine hydrate; *Radiochem.*; 55; **2013**; p. 567-573.
- [88] Rand, M.; Ackermann, R.; Grønvold, F.; Oetting, F.; Pattoret, A.; Thermodynamic Properties of the Urania phase; *Rev. Int. Hautes Temper. Refract. Fr.*; 15; **1978**; p. 335-65.
- [89] Chevalier, P.-Y.; Fischer, E.; Cheynet, B.; Progress in the thermodynamic modelling of the O–U binary system; *J. Nucl. Mat.*; 303; **2002**; p. 1-28.
- [90] Guéneau, C.; Baichi, M.; Labroche, D.; Chatillon, C.; Sundman, B.; Thermodynamic assessment of the uranium–oxygen system; *J. Nucl. Mat.*; 304; **2002**; p. 161-175.
- [91] Labroche, D.; Dugne, O.; Chatillon, C.; Thermodynamics of the O–U system. I – Oxygen chemical potential critical assessment in the UO<sub>2</sub>–U<sub>3</sub>O<sub>8</sub> composition range; *J. Nucl. Mat.*; 312; **2003**; p. 21-49.
- [92] Morss, L.; Edelstein, N.; Fuger, J.; Katz, J.; The Chemistry of the Actinide and Transactinide Elements; (Set Vol.1-6); Springer; **2011**, p. 1-4514.
- [93] Sweet, L.E.; Blake, T.A.; Henager Jr., C.H.; Hu, S.; Johnson, T.J.; Meier, D.E.; Peper, S.M.; Schwantes, J.M.; Investigation of the polymorphs and hydrolysis of uranium trioxide; *J. Radioanal. Nucl. Chem.*; 296; **2013**; p. 105-110.

- [94] Senanayake, S.; Rousseau, R.; Colegrave, D.; Idriss, H.; The reaction of water on polycrystalline UO<sub>2</sub>: Pathways to surface and bulk oxidation; *J. Nucl. Mat.*; 342; **2005**; p. 179-187.
- [95] Mc Donald; A., Fox, R.; Introduction to fluid mechanics; John Wiley & Sons, 3rd Ed.; **1985**.
- [96] Johnson, K.; Kendall, K.; Roberts, A.; Surface Energy and the Contact of Elastic Solids; *Proc. R. Soc. Lond. A*; 324; **1971**; p. 301-313.
- [97] Derjaguin, B.V; Muller, V.M; Toporov Yu., P; Effect of contact deformations on the adhesion of particles; *J. Colloid Interface Sci.* 53; **1975**; p. 314-326.
- [98] Muller, V.; Yuschenko, M.; Derjaguin, D.; General theoretical consideration of the influence of surface forces on contact deformations and the reciprocal adhesion of elastic spherical particles; *Colloid Interf. Sci.*; 92; **1983**; p. 92-101.
- [99] Hertz, H.; Über die Grundgleichungen der Electrodynamik für bewegte Körper; *Annalen der Physik*; WILEY-VCH; 277; **1890**; p. 369-399.
- [100] R. Bowling; Particles on Surfaces 1 - A theoretical review of particle adhesion; Detection, Adhesion and Removal; II; Springer US; **1998**; p. 129-142.
- [101] Phares, D.; Smedley, G.; Flagan, R.; Effect of particle size and material properties on aerodynamic resuspension from surface; *J. Aerosol Sci.*; 31; **2000**; p. 1335-1353.
- [102] Corn, M. and Stein, F.; Re-entrainment of particles from a plane surface; *Am. Ind. Hyg. Assoc. J.*; 26; **1965**; p. 325-336.
- [103] Kousaka Y; Okuyama, K. E. Y.; Re-entrainment of small aggregate particles from a plane surface by air stream *J. Chem. Eng. Jpn.*; 13; **1980**; p. 143-147.
- [104] Smedley, G.; Phares, D.; Flagan, R.; Entrainment of fine particles from surface by gas jets impinging at normal incidence; *Exp. Fluids*; 26; **1999**; p.324-334.
- [105] Phares, D.; Smeldley, G.; Flagan, R.; The wall shear stress produced by the normal impingement of a jet on a flat surface; *J. Fluid Mech.*; 418; **2000**; p. 351-375.
- [106] Leighton, D.; Acrivos, A.; The lift on a small sphere touching a plane in the presence of a simple shear flow; *J. Appl. Math. Phys.*; 36; **1985**; p. 174-178.
- [107] Marple, A. V. and Willeke, K.; Impactor Design; *Atmos. Environ.*; 10; **1976**; p. 891-896.
- [108] Jurcik, B. and Wang, H.-C.; On the shape of impactor efficiency curves; *J. Aerosol Sci.*; 26; **1995**; p. 1139-1147.
- [109] Ensor, D.S.; *Aerosol Science and Technology, History and Reviews*, RTI International Press; **2011**; p. 1-21.
- [110] Boulyga, S.; Konegger-Kappel, S.; Richter, S.; Sangely, L.; Mass spectrometric analysis for nuclear safeguards; *J. Anal. At. Spectrom.*; 30; **2015**; p. 1469-1489.
- [111] Habfast, K.; Fractionation correction and multiple collectors in thermal ionization isotope ratio mass spectrometry; *Int. J. Mass Spectrom.*; 176; **1988**; p. 133-148.
- [112] Prohaska, T.; Lindemann, T.; Rottman, L.; Sector Field Mass Spectrometry for Elemental and Isotopic Analysis – New Developments in Mass Spectrometry; *Roy. Soc. Chem.*; **2014**; p. 1-664.
- [113] Dietzek, B.; Cialla, D.; Schmitt, M.; Popp, J., Confocal Raman Microscopy; Springer Berlin Heidelberg; 158; Chap. 2; **2011**; p. 22-42.
- [114] Manara, D.; Renker, B.; Raman spectra of stoichiometric and hyperstoichiometric uranium dioxide; *J. Nucl. Med.*; 321; **2003**; p. 233-237.
- [115] Mellini, M.; Riccobono, F.; Chemical and mineralogical transformations caused by weathering in anti-tank DU penetrators (“the silver bullets”) discharged during the Kosovo war; *Chemosphere*; 60; **2005**; p. 1246-1252.
- [116] Maya, L.; Begun, G.M.; Raman spectroscopy study of hydroxo and carbonato species of the uranyl (VI) ion; *J. Inorg. Nucl. Chem.*; 43; **1981**; p. 2827-2832.
- [117] Allen, G.C.; Butler, I.S.; Tuan, N.A.; Characterization of uranium oxides by micro-Raman spectroscopy; *J. Nucl. Mater.*; 144; **1987**; p. 17-19.
- [118] Butler, I.S.; Allen, G.C.; Tuan, N.A.; Micro-Raman spectrum of U<sub>3</sub>O<sub>8</sub>; *Appl. Spectrosc.*; 42; **1988**; p. 901-902.
- [119] Rao, B.S.M; Gantner, E.; Reinhardt, J.; Steinert, D.; Ache, H.J.; Characterization of the solids formed from simulated nuclear fuel reprocessing solutions; *J. Nucl. Mater.*; 170; 1; **1990**; p. 39-49.
- [120] Roeper, D.F.; Chidambaram, D.; Halada, G.P.; Clayton, C.R.; Development of an environmentally friendly protective coating for the depleted uranium–0.75 wt.% titanium alloy: Part V.

- Electrochemical impedance spectroscopy of the coating; *Electrochim. Acta*; 51; **2006**; p. 2130 - 2134.
- [121] Blumenroeder, S.; Brenten, H.; Zirngiebl, E.; Mock, R.; Guentherodt, G.; Thompson, J.D.; Fisk, Z.; Naegele, J.; Light scattering in heavy fermion compounds; *J. Magn. Magn. Mater.*; 76-77; **1988**; p. 331-334.
- [122] Amme, M.; Renker, B.; Schmid, B.; Feth, M.; Bertagnolli, H.; Doeblin, W.; Raman microspectrometric identification of corrosion products formed on UO<sub>2</sub> nuclear fuel during leaching experiments, *J. Nucl. Mater.*; 306; **2002**; p. 202-212.
- [123] Graves, P.R.; Raman Microprobe Spectroscopy of Uranium-Dioxide Single Crystals and Ion Implanted Polycrystals; *Appl. Spectrosc.*; OSA; 44; **1990**; p. 1665-1667.
- [124] Morris, D.E.; Allen, P.G.; Berg, J.M.; Chisholm-Brause, C.J.; Conradson, S.D.; Donhoe, R.J.; Hess, N.J.; Musgrave, J.A.; Tait, C.D.; Speciation of Uranium in Fernald Soils by Molecular Spectroscopic Methods: Characterization of Untreated Soils; *Environ. Sci. Technol.*; 30; **1996**; p. 2322-2331.
- [125] Winer, K.; Colmenares, C.; Smith, R.; Wooten, F.; On the stability of sub-stoichiometric uranium oxides; *Surf. Sci.*; 177; **1986**; p. 484-492.
- [126] Palacios, M.L.; Taylor, S.H.; Characterization of Uranium Oxides Using in Situ Micro-Raman Spectroscopy; *Appl. Spectrosc.*, OSA; 54; **2000**; p. 1372-1378.
- [127] Hoekstra, H.; Santoro, A.; Siegel, S.; The low temperature oxidation of UO<sub>2</sub> and U<sub>4</sub>O<sub>9</sub>; *J. Inorg. Nucl. Chem.*; 18; **1961**; p. 166-178.
- [128] Labroche, D.; Dugne, O.; Chatillon, C.; Thermodynamic properties of the O-U system. II - Critical assessment of the stability and composition range of the oxides UO<sub>2+x</sub>, U<sub>4</sub>O<sub>9-y</sub> and U<sub>3</sub>O<sub>8-z</sub>; *J. Nucl. Mater.*; 312; **2003**; p. 50-66.
- [129] Grønvold, F.; High-temperature X-ray study of uranium oxides in the UO<sub>2</sub>-U<sub>3</sub>O<sub>8</sub> region; *J. Inorg. Nucl. Chem.*; 1; **1955**; p. 357-370.
- [130] McEachern, R.; Taylor, P.; A review of the oxidation of uranium dioxide at temperatures below 400°C; *J. Nucl. Mater.*; 254; **1998**; p. 87-121
- [131] Thein, S.; Bereolos, P.; Thermal Stabilization of <sup>233</sup>UO<sub>2</sub>, <sup>233</sup>UO<sub>3</sub>, and <sup>233</sup>U<sub>3</sub>O<sub>8</sub>; ORNL/TM-2000/82; **2000**; p. 1-31.
- [132] Nipruk, O.; Knyazev, A.; Chernorukov, G.; Pykhova, Y.; Synthesis and study of hydrated uranium (VI) oxides, UO<sub>3</sub>·nH<sub>2</sub>O; *Radiochemistry*; 53; 2; **2011**; p. 146-150.
- [133] Biber, B.M.; Ebert, W.L.; Bates, J.K.; The Raman spectra of several uranyl-containing minerals using a microprobe; *J. Nucl. Mater.*; 175; **1990**; 188-193.
- [134] Pidduck, A.J.; Houlton, M.W.G.; Donohue, D.L.; A multi-technique approach to environmental particle analysis for nuclear safeguards; IAEA-CN 148/115; **2008**; p. 781-789.
- [135] Pointurier, F.; Marie, O.; Identification of the chemical forms of uranium compounds in micrometer-size particles by means of micro-Raman spectrometry and scanning electron microscope; *Spectrochim. Acta, Part B*; 65; **2010**; p. 797-804.
- [136] Pointurier, F.; Marie, O.; Use of micro-Raman spectrometry coupled with scanning electron microscopy to determine the chemical form of uranium compounds in micrometer-size particles; *J. Raman Spectrosc.*; 44; **2013**; p. 1753-1759.
- [137] Stefaniak, E.; Worobiec, A.; Potgieter-Vermaak, S.; Alsecz, A.; Török, S.; Grieken, R. V.; Molecular and elemental characterization of mineral particles by means of parallel micro-Raman spectrometry and Scanning Electron Microscopy/Energy Dispersive X-ray Analysis; *Spectrochim. Acta, Part B* 61; **2006**; p. 824-830.
- [138] Stefaniak, E. A.; Alsecz, A.; Sajó, I. E.; Worobiec, A.; Máthé, Z.; Török, S.; Grieken, R. V.; Recognition of uranium oxides in soil particulate matter by means of  $\mu$ -Raman spectrometry; *J. Nucl. Mat.*; **2008**; 381; p. 278-283.
- [139] Stefaniak, E.; Pointurier, F.; Marie, O.; Truyens, J.; Aregbe, Y.; In-SEM Raman microspectrometry coupled with EDX - a case study of uranium reference particles; *Analyst.*; 139; **2014**; p. 668-675.
- [140] Jégou, C.; Caraballo, R.; Peugeot, S.; Roudil, D.; Desgranges, L.; Magnin, M.; Raman spectroscopy characterization of actinide oxides (U<sub>1-y</sub>Pu<sub>y</sub>)O<sub>2</sub>: Resistance to oxidation by the laser beam and examination of defects; *J. Nucl. Mater.*; 405; **2010**; p. 235-243.

- [141] Dawson, J.K.; Wait, E.; Alcock, K.; Chilton, D.R.; Some aspects of the system uranium trioxide-water, *J. Chem. Soc.*; **1956**; p. 3531-3539.
- [142] Sobry, R.; Etudes des Uranates Hydrates – II; *J. Inorg. Nucl. Chem.*; **35**; **1973**; p. 2753-2768.
- [143] Weller, M.T.; Light, E.; Gelbrich, T.; Structure of U(VI) oxide dihydrate; synthetic meta-schoepite; *Acta Cryst. B56*; **1999**; p. 577-583.
- [144] Cordfunke, E.; New Fuel For Fast Reactors; *Atoomenergie Haar Toepass*; **11**; **1969**; p. 263-71.
- [145] Pidduck, A.J.; Wallis, D.; Williams, G.; SEM, TEM, Raman & SIMS Investigation of U test compounds: Summary report: Part 1 & Part 2; IAEA INMM Paper, **2006**, p. 1-69.
- [146] Canizarès, A.; Guimbretière, G.; Tobon, Y. A.; Raimboux, N.; Omnée, R.; Perdicakis, M.; Muzeau, B.; Leoni, E.; Alam, M. S.; Mendes, E.; Simon, D.; Matzen, G.; Corbel, C.; Barthe, M. F.; Simon, P.; In situ Raman monitoring of materials under irradiation: study of uranium dioxide alteration by water radiolysis; *J. Raman Spectrosc.*; **43**; **2012**; p. 1492-1497.
- [147] Admon, U.; Chinea-Cano, E.; Wegrzynek, D.; Aigner, H.; Markowicz A.; Donohue, D.L.; Ruedenauer, F.; Costin, W.; *Radioactive Particles in the Environment*; Springer Science & Business Media B.V.; 2<sup>nd</sup> Ed.; Chap. 2; **2009**; p. 15-55.
- [148] Drouin, D.; Couture, A.R.; Joly, D.; Tastet, X.; Aimez, V.; Gauvin, R.; CASINO V2.42 - A Fast and Easy-to-use Modeling Tool for Scanning Electron Microscopy and Microanalysis; *Scanning*; **29**; **2007**; p. 92-101.
- [149] Reimer, L.; Stelter, D.; FORTRAN 77 Monte-Carlo program for minicomputers using Mott cross-sections Scanning; *Wiley Periodicals, Inc.*; **8**; **1986**; p. 265-277.
- [150] Kotera, M.; Ijichi, R.; Fujiwara, T.; Suga, H.; Wittry, D.B.A.; Simulation of Electron Scattering in Metals; *Jpn. J. Appl. Phys.*; **29**; **1990**; p. 2277-2282.
- [151] Dieing T.; Hollricher, O. T. J.; *Confocal Raman Microscopy*; Springer Berlin Heidelberg; **158**, Chap.t. 1; **2011**; p. 1-18.
- [152] Ferreira, T.; Rasband, W.; *ImageJ User Guide - IJ 1.46r*; **2012**.
- [153] Misra, C.; Kim, S.; Shen, S.; Sioutas, C.; A high flow rate, very low pressure drop impactor for inertial separation of ultrafine from accumulation mode particles ; *J. Aerosol Sci.*; **33**; **2002**; p. 735-752.
- [154] Hackley V. A.; Ferraris, C. F.; *The Use of Nomenclature in Dispersion Science and Technology*; NIST SP 960-3; **2001**; p. 1-72.
- [155] Luan, F.; Zhang, G.; Senko, J. M.; Burgos, W. D.; Effects of supplemental organic carbon on long-term reduction and reoxidation of uranium; *RSC Adv.*; **5**; **2015**; p. 32210-32211.
- [156] Lue, J.-b.; Li, G.; Guo, S. I.; Raman and Infrared Spectra of Non-Stoichiometry Uranium Oxides; *Spectrosc. Spect. Anal.*; **34**; **2014**; p. 405-409.
- [157] Armstrong, D. P.; Jarabek, R. J.; Fletcher, W. H.; Micro-Raman Spectroscopy of Selected Solid U<sub>x</sub>O<sub>y</sub>F<sub>z</sub> Compounds; *Appl. Spectrosc.*; **43**; **1989**; p. 461-468.
- [158] Khulbe, P.K.; Agarwal, A.; Raghuvanshi, G. S.; Bist, H.D.; Hashimoto, H.; Kitagawa, T.; Little, T.S.; Durig, J.R.; Raman studies of the vibrational dynamics and phase transitions in uranyl nitrate hexahydrate; *J. Raman Spectrosc.*; **20**; **1989**; p. 283-290.
- [159] Ho, D. M. L.; Jones, A. E.; Goulermas, J. Y.; Turner, P.; Varga, Z.; Fongaro, L.; Fanghaenel, T.; Mayer, K.; Raman spectroscopy of uranium compounds and the use of multivariate analysis for visualization and classification; *Forensic Sci. Int.*; **251**; **2015**; p. 61-68.
- [160] Stefaniak, E. A.; Darchuk, L.; Sapundjiev, D.; Kips, R.; Aregbe, Y.; Grieken, R. V.; New insight into UO<sub>2</sub>F<sub>2</sub> particulate structure by micro-Raman spectroscopy; *J. Mol. Struct.*; **1040**; **2013**; p. 206-212.
- [161] Bastians, S.; Crump, G.; Griffith, W.P.; Withnall, R.; Raspite and studtite: Raman spectra of two unique minerals; *J. Raman Spectrosc.*; **35**; **2004**; p. 726-731.
- [162] Richter, S.; Alonso, A.; Bolle, W. D.; Kühn, H.; Verbruggen, A.; Wellum, R.; Taylor, P.; Re-certification of a series of uranium isotope reference materials: IRMM-183, IRMM-184, IRMM-185, IRMM-186 and IRMM-187; *Int. J. Mass Spectrom.*; **247**; **2005**; 37-39.
- [163] Hedberg, P.M.L.; Ingeneri, K.; Watanabe, M.; Kuno, Y.; Isotopic measurements of U particles by Secondary Ionization Mass Spectrometry; *Proc. of the 46<sup>th</sup> Institute of Nuclear Material Management (INMM) Annual Meeting*; Arizona; USA; **2005**.



Band / Volume 323

**Light induced water splitting using multijunction thin film silicon solar cells**

F. Urbain (2016), xi, 173, XLVI pp

ISBN: 978-3-95806-148-4

Band / Volume 324

**Properties of convective gravity waves derived by combining global modeling and satellite observations**

Q. T. Trinh (2016), 140 pp

ISBN: 978-3-95806-150-7

Band / Volume 325

**Feasible and Reliable Ab initio Atomistic Modeling for Nuclear Waste Management**

G. Beridze (2016), xix, 128 pp

ISBN: 978-3-95806-151-4

Band / Volume 326

**Sauerstoffspeicher für die oxidkeramische Batterie: Herstellung, Charakterisierung und Betriebsverhalten**

C. M. Berger (2016), XV, 128 pp

ISBN: 978-3-95806-154-5

Band / Volume 327

**Institute of Energy and Climate Research IEK-6: Nuclear Waste Management Report 2013 / 2014**

*Material Science for Nuclear Waste Management*

S. Neumeier, M. Klinkenberg, D. Bosbach (Eds.)

(2016), 219 pp

ISBN: 978-3-95806-155-2

Band / Volume 328

**Conductivity and Structure of Sputtered ZnO:Al on Flat and Textured Substrates for Thin-Film Solar Cells**

N. Sommer (2016), vii, 195, XIV pp

ISBN: 978-3-95806-156-9

Band / Volume 329

**Glaslotfügen von Festoxid-Brennstoffzellen durch Laseraufschmelzung**

M. Willberg (2016), 99 pp

ISBN: 978-3-95806-157-6

Band / Volume 330

**The Role of Natural Nanoparticles and Colloids for Phosphorus Binding in Forested Headwater Catchments**

N. Gottselig (2016), VIII, 116 pp

ISBN: 978-3-95806-160-6

Band / Volume 331

**Numerische Modellierung der thermomechanischen Fluid-Struktur-Interaktion im SOFC-Stack**

A. Al-Masri (2016), iii, 165 pp

ISBN: 978-3-95806-161-3

Band / Volume 332

**Analysis of biomixtures to determine the fate of pesticides**

S. Mukherjee (2016), xix, 136 pp

ISBN: 978-3-95806-163-7

Band / Volume 333

**Temperature Dependence of Carbon Kinetic Isotope Effect for The Oxidation Reaction of Ethane by Hydroxyl Radicals Under Atmospherically Relevant Conditions: Experimental and Theoretical Studies**

T. Piansawan (2016), 196 pp

ISBN: 978-3-95806-166-8

Band / Volume 334

**Konzeption von Membranmodulen zur effizienten Abtrennung von Kohlendioxid aus Gasgemischen**

S. Luhr (2016)

ISBN: 978-3-95806-170-5

Band / Volume 335

**Einfluss fehlpassungsinduzierter Spannungsfelder auf den Transportprozess bei ionischer Leitung**

J. Keppner (2016), viii, 171 pp

ISBN: 978-3-95806-171-2

Band / Volume 336

**Production and Characterization of Monodisperse Uranium Particles for Nuclear Safeguards Applications**

A. Knott (2016), A-H, 123, xxviii, xiii pp

ISBN: 978-3-95806-172-9



**Energie & Umwelt /  
Energy & Environment  
Band / Volume 336  
ISBN 978-3-95806-172-9**

